UNIVERSITÉ DE LIMOGES

ÉCOLE DOCTORALE Science - Technologie - Santé

FACULTÉ des SCIENCES et TECHNIQUES

XLIM - Département “O.S.A.”

Thèse N° [2008]

Thèse

pour obtenir le grade de

DOCTEUR DE L’UNIVERSITÉ DE LIMOGES

Discipline : Électronique des Hautes Fréquences et Optoélectronique

Spécialité : Télécommunications

Présentée et soutenue par

Rodrigo PONCE HEREDIA

le 18 juillet 2008

Contribution à la modélisation du rayonnemnet d’antennes conformées pour des applications C.E.M. en aéronautique

Thèse dirigée par Monsieur Alain REINEIX

JURY :

Rapporteurs :

Hervé AUBERT	**Professeur** *LASS CNRS, Groupe Micro et Nanosystèmes pour le Communications, Toulouse*
Lionel PICHON	**Professeur** *Université Paris-Sud, Université Pierre et Marie Currie, SUPELEC, Laboratoire de Génie Électrique de Paris, Gif-Sur-Yvette*

Examinateurs :

Thierry MONEDIERE	**Président du Jury, Professeur** *XLIM, Dép. “O.S.A.”, Limoges*
Gilles PERES	**Ingenieur** *EADS IW, Toulouse*
Alain REINEIX	**Directeur de Recherche CNRS** *XLIM, Dép. “O.S.A.”, Limoges*
Fabrice TRISTAN	**Ingenieur** *Dassault Aviation, DGT/STSPE, Saint-Cloud*

Preface

The present thesis work is the result of the collaboration between EADS Innovation Works (EADS IW) and the French National Research Centre (CNRS). The ellaboration of the thesis work took place partially at EADS IW in Toulouse and at the CNRS laboratory XLIM at the University of Limoges. The supervision at EADS IW has been done by the leader of the group "Physics of Electromagnetism", Gilles Peres. The academical supervision has been performed by the CNRS chief research director of XLIM, Alain Reineix.

I would like to thank my supervisor at EADS IW for the proposal of this disseration. Furthermore, I would like to thank the teams "Physics of Electromagnetism" and "Applied Mathematics" at EADS IW in Suresnes and Toulouse, which made my stay pleasant. From the staff of the site in Suresnes I am grateful to Eric Duceau for his support regarding laboral issues. I am also very grateful to my ex-colleague and very good friend Jesus Aspas Puertolas, with whom I share a lot of great memories inside and outside EADS IW. From the staff of the site in Toulouse I would like to thank Andrew Thain, who encouraged me concerning research material. I am also very grateful to Agnes Normand for her never-ending moral support even outside EADS-IW. I would like also to express my great gratitude to my ex-colleagues and friends Jean-Baptiste Welcome and Yannick Poire for the nice experiences beyond workaday life.

As next, I would like to thank my academical supervisor for the scientific contribution to the present thesis work. Moreover, I would like to thank the staff and my phd student fellows at the XLIM laboratory. My thanks goes particularly to Philippe Sin and David Bouygue, two exceptional student fellows who introduced me unconditionally to the French student life. I am also very grateful to my student fellows and very good friends Hicham Tarhini and Luis Delrio, with whom I shared the ups and downs of the PhD studies, and who cheered up my stay in Limoges. In addition, I am very greatful to Jorge Martinez Perez a post-doctoral student and very good friend, with whom I enjoyed great moments in Limoges during his one year stay.

Finally, my endless gratitude goes to my parents, Nelly and Felipe, who gave me all their support and encouragement even from my distant lying country Bolivia, and to my brother Albaro, who was always there for me and backed me in the most difficult moments of my PhD thesis work. Without them this dissertation would not have become reality.

Limoges, July 2008

Rodrigo Ponce Heredia

Contents

Introduction

In the recent years the use of planar antenna arrays in telecommunication systems has become an important issue. Such arrays are used for telecommunication tasks in civilian services like mobile telephone systems as well as in military applications like radar remote sensing. During the last decade the use of antenna arrays has become essential in the aerospace industry. For instance, the use of arrays is vital for different application systems in satellites. Furthermore, in the aircraft industry particularly the need of conformal antenna arrays for communication applications in fuselage has risen in order to diminish aerodynamic drag, to avoid the use of mechanical steering system and hence to reduce the weight of the antenna system.

Furthermore, due to the recent tendancy of the development of new aircraft architecture and new material applications, there is a need of performing fast and accurate electromagnetic compatibility (EMC) analyses in order to detect possible interactions between the antenna systems and the irregularly shaped antenna bearers. Consequently, parallel to the latter development the demand for robust but simple modelling techniques for such structure adaptable arrays has increased. There exist methods for modelling and analysing planar antenna arrays. Other procedures for handling curved arrays like approximating their behaviour with planar subarrays have been developed. Additionally, methods that calculate rigorously conformal antenna arrays exists. But all these existing methods have disadvantages like huge calculation times, high need in memory capacity, inaccurate correction factors,and so on, that retard the analysis of large conformal arrays in a fast and accurate way.

During the realization of a european project for satellite communication, the research department Innovation Works (IW) of the European Aeronautic Defence and Space Company (EADS) in France has been confronted with the latter constraints. The necessity of an adequate method for the analysis of large antenna array with the capability of handling conformal structured arrays due to fuselage integration has given origin to different research studies on that subject. The thesis work presented in this manuscript is embedded in one of such studies and its main goal is the contribution to the far field modelling of conformal arrays for EMC applications in aerospace industry.

The present thesis work comprises the development of a hybrid method for array analysis and synthesis. The basic concept of the conceived method is to analyse the radiating elements of an array by performing a decomposition of the active radiating region in smaller discrete regions that can be modelled by equivalent sources. These sources are described by electrical currents that are acquired by means of numerical techniques applied to volume, for instance FDTD or FIT, or by means of the cavity model. Furthermore, the method calculates the electromagnetic far field of an antenna array by applying analytical radiation formulae on the obtained active region of the entire array. The calculation of far field quantities like directivity and radiation

pattern have been implemented. Moreover, the developed method allows to analyse planar and conformal arrays as well as large arrays. In addition to that, the conceived method allows array synthesis by means of an optimization approach based on a versatile genetic algorithm.

Therefore, the thesis work is divided in three parts that are presented in six chapters. The first part handles the development of the array simulation tool and is presented in three chapters. The first chapter introduces the reader to antenna and array theory. There, different principles and equations, starting from electromagnetic wave theory and ending at antenna array theory, are presented. The second chapter comprises the existing numerical techniques for antenna and array analysis with main emphasis on numerical techniques for conformal antennas. In the third chapter the development of the hybrid method is presented and explained. There, the reader is introduced to the equivalent sources approach and its application to the array elements. Therefore, the applied formulae and the algorithms of the code functions are given. Moreover, the generation of the required currents by means of methods applied to volume and with the help of the cavity model is explained. This chapter includes some standard validation examples as well as the algorithm structure.

The second part of the thesis work concerns the realization of the array synthesis approach. This part is presented to the reader in two chapters, the fourth and fifth of this thesis work. In the fourth chapter several existing synthesis techniques for planar and conformal arrays are summarised. In this introduction to array synthesis main emphasis is placed on conformal arrays and on large arrays. Furthermore, the genetic algortithm approach is presented to the reader in detail. The respective implementation of the genetic algorithm by defining the probabilistic constants and the error function is described in the fifth chapter. In addition to that, standard validation examples are given to the reader.

The third part of this thesis work comprises the application of the developed analysis and synthesis method. It is presented in the sixth chapter. There, certain application cases in relation to future eletromagnetic compatibility studies in aircraft industry have been regarded. Several planar and conformal arrays, whose elements are based on a microstrip antennas proposed and used in aircraft industry, are modelled and simulated. The influence of the curvature on the radiation characteristics is observed. Moreover, the coupling between the array elements is regarded. Furthermore, optimization concerning source decomposition, beam-steering and beam-shaping have been performed. Focus has been given to the influence of the curvature on the optimization method. The yielded results are compared with the ones obtained by means of existing software.

Chapter 1

Theoretical foundations

The development of the method, algorithms and approximations in the present thesis work are based on theory concepts. This used theoretical background comes from different fields in physics and engineering. Specially from the domains electromagnetic theory and antenna theory several theorems, definitions and approaches have been used. Therefore, it is essential to review the theoretical foundations applied for a better understanding of the present thesis work.

1.1 Electromagnetic wave theory

The following fundamental concepts describe the electromagnetic phenomena from a "macroscopic" standpoint, which allows one to neglect the granular structure of matter and charge. The stationarity of matter in respect to the observer is also assumed. [1], [2] and [3] can be cited as main references.

1.1.1 The Maxwell Equations and the Equation of continuity

The Maxwell Equations are the basic principles of the electromagnetic wave theory. Electromagnetic wave functions obey these equations wherever they and their derivaties are continuous or discontinuous. The six quantities applied in the Maxwell Equations are the electric intensity $\vec{E}$, the magnetic intensity $\vec{H}$, the electric flux density $\vec{D}$, the magnetic flux density $\vec{B}$, the electric current density $\vec{J}$ and the electric charge density ρ.

1.1.1.1 The classical Maxwell Equations

The classical *Maxwell Equations in derivative form* have the following form

$$\nabla \times \vec{E} = -\frac{\partial \vec{B}}{\partial t} \tag{1.1}$$

$$\nabla \times \vec{H} = \frac{\partial \vec{D}}{\partial t} + \vec{J} \tag{1.2}$$

$$\nabla \cdot \vec{B} = 0 \tag{1.3}$$

$$\nabla \cdot \vec{D} = \rho \tag{1.4}$$

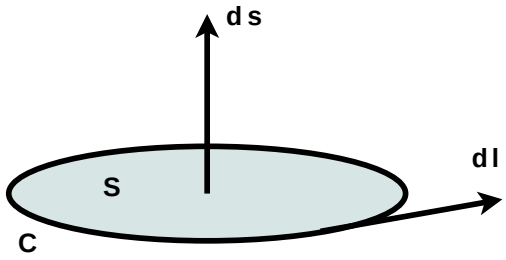

Figure 1.1 : *$d\vec{l}$ and $d\vec{s}$ on an open surface*

The first equation in the latter set defines any temporal change of the magnetic flux as an voltage induction in a path around the flux. The second expression of the set reveals that a temporal charge displacement in a path, represented by the temporally changing dielectric flux density plus an current density, induces a magnetic intensity arround it. The third expression states that the magnetic flux has no source: the magnetic flux lines have no beginning nor an end. The fourth and last equation expresses that the electric flux density has as a source: the electric flux density lines start and end on a electric charge.

More general and better known are some of the latter equations if they are integrated: the first equation becomes *Faraday's law*, the second *Ampere's law*, and the last ones *Gauss laws* for the magnetic and the electric field. Consequently, the following equations are the *Maxwell Equations in integral form*

$$\oint \vec{E} \cdot d\vec{l} = -\frac{\partial}{\partial t} \iint \vec{B} \cdot d\vec{s} \tag{1.5}$$

$$\oint \vec{H} \cdot d\vec{l} = \frac{\partial}{\partial t} \iint \vec{D} \cdot d\vec{s} + \iint \vec{J} \cdot d\vec{s} \tag{1.6}$$

$$\oiint \vec{B} \cdot d\vec{s} = 0 \tag{1.7}$$

$$\oiint \vec{D} \cdot d\vec{s} = \iiint \rho dv \tag{1.8}$$

In the first two equations $d\vec{l}$ stands for the path encircling the vector $d\vec{s}$ in an infinite open surface as illustrated in 1.1. In the other two equations $d\vec{s}$ points outward from a closed surface and dv is an infinite volume element enveloped by ds, as depicted in figure 1.2.

The latter equation set is valid also for quantities that are not necessarily "well-behaved". Therefore, the integral alternatives of the *Maxwell Equations* are more general then the differential ones.

1.1.1.2 Equation of continuity

The Maxwell Equations contain the information of conservation of charge, which is usually given by the following expression called *Equation of continuity*

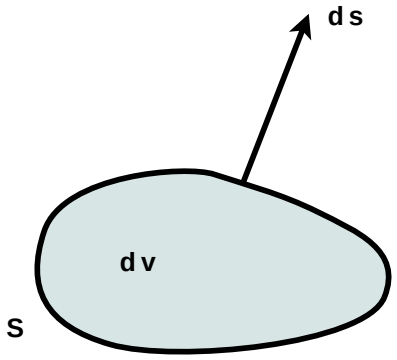

Figure 1.2 : *$d\vec{s}$ on a closed surface*

$$\nabla \cdot \vec{J} = -\frac{\partial \rho}{\partial t} \tag{1.9}$$

The latter equation states that charge can not be created, neither it can be destroyed. Consequently, charge can only be transported. The integral form of the *Equation of continuity* has the following form

$$\oiint \vec{J} \cdot d\vec{s} = -\frac{\partial}{\partial t} \iiint \rho dv \tag{1.10}$$

1.1.1.3 Time harmonic quantities

The quantities $\vec{E}$, $\vec{H}$, $\vec{D}$, $\vec{B}$ and $\vec{J}$ were specified as complex variables in this section. This handling assumes that their time variation is of harmonic kind. Furthermore, the harmonic time dependency can be expressed with the help of the complex exponential function. Thus each quantity has the following form

$$\vec{E}(\omega) = \vec{\mathrm{E}} e^{j\omega t} \tag{1.11}$$

In the latter expression $\vec{\mathrm{E}}$ represents the magnitude of the complex function. The product ωt forms the complex phase. Moreover, ω stands for the angular frequency and t for the time.

1.1.1.4 The generalized current concept

Due to the fact that in the present thesis work the Maxwell Equations will be applied on sources, it is necessary to generalize the current concept. Therefore, besides taking the electric displacement current $\vec{J}_d = \frac{\partial \vec{D}}{\partial t}$ and the conduction current $\vec{J}_c$ into account for the total electric current, this new concept will consider the impressed current $\vec{J}_i$. The same goes for the "magnetic currents": besides the "magnetic displacement current" $\vec{M}_d = \frac{\partial \vec{B}}{\partial t}$, the impressed magnetic current $\vec{M}_i$ is considered as contribution to the total magnetic current. In addition to that, it have to be said, that this impressed currents represent energy sources, which are seen as the cause of the field. The following expressions show the new current concept

$$\vec{J}_{total} = \frac{\partial \vec{D}}{\partial t} + \vec{J}_c + \vec{J}_i \tag{1.12}$$

$$\vec{M}_{total} = \frac{\partial \vec{B}}{\partial t} + \vec{M}_i \tag{1.13}$$

The latter currents can be found in any electric or magnetic circuit. For example in an electric circuit an impressed current $\vec{J}_i$ of the source produces a conduction current $\vec{J}_c$ through a resistor and a displacement current $\vec{J}_d$ through a capacitor. Similar happens in a magnetic circuit: an impressed magnetic current $\vec{M}_i$ of the circuit source generates an electric current that causes a magnetic displacement current $\vec{M}_d$ e.g. in a wired magnetic core.

1.1.1.5 The generalized harmonic Maxwell Equations

The latter new current concept enhances the generality of the Maxwell Equations. Furthermore, the definition of the tim-varying electromagnetic fields as time-harmonic ones symplifies the time derivatives in the Maxwell Equations. Consequently, the Maxwell Equations can be written in the following generalized way

$$\nabla \times \vec{E} = -j\omega\vec{B} + \vec{M}_i \tag{1.14}$$

$$\nabla \times \vec{H} = j\omega\vec{D} + \vec{J}_c + \vec{J}_i \tag{1.15}$$

$$\nabla \cdot \vec{B} = \rho_m \tag{1.16}$$

$$\nabla \cdot \vec{D} = \rho_e \tag{1.17}$$

In the latter equation set, ρ_m and ρ_e stand for the magnetic and electric charge density, respectively. Moreover, assuming that these volumic charges are time harmonic variant quantitues, the Equation of Continuity takes the following form

$$\nabla \cdot \vec{J} = -j\omega\rho_e \tag{1.18}$$

In the present thesis work all field quantities are of complex kind and their harmonic time dependency is understood. Consequently, the factor $e^{j\omega t}$ is omitted at all field equations and field functions.

1.1.2 Constitutive relationships

The *Constitutive relationships* together with the Maxwell Equations complete the information about the behaviour of electromagnetic waves in free space and in any homogeneous material. These relations specify the characteristic of the medium in which the electromagnetic wave functions exist. The *Constitutive relationships* are the following

$$\vec{D} = \varepsilon(\omega)\vec{E} \tag{1.19}$$

$$\vec{B} = \mu(\omega)\vec{H} \tag{1.20}$$

$$\vec{J} = \sigma_e(\omega)\vec{E} \tag{1.21}$$

$$\vec{M} = \sigma_m(\omega)\vec{H} \tag{1.22}$$

In this set of equations ε is the permittivity, μ the permeability, σ_e and σ_m the electric and magnetic conductivity of the medium. All these parameters are of complex kind and depend on the characteristic of the medium. The variable ω stands for the angular frequency. The relationship between the angular frequency and the frequency is given by the expression $\omega = 2\pi f$.

1.1.3 The wave equation for time-harmonic electromagnetic fields

The generalized Maxwell equations are first-order coupled partial differential equations, which describes the behaviour of time-harmonic electromagnetic fields. For each of these fields these equations can be uncoupled by certain transformations yielding a second order partial differential equation. The latter resulting equation is known as the wave equation. Consequently, the electromagnetic fields are solutions to the Maxwell equations and to their respective wave equations. Therefore, it is essential to define the different wave equations that describe time varying electromagnetism. Departure for this aiming are the Maxwell Equations set itself.

Furthermore, the solution for the resulting wave equations can be calculated by two different paths. The first path is to integrate directly the electric source current density $\vec{J}$ to obtain the electric field intensity $\vec{E}$ or alternatively the magnetic source current density $\vec{M}$ to get the magnetic field intensity $\vec{H}$. Although this procedure needs only one step to get the radiated field, the realization is rather complicated due to the difficulty in treating integrands. The other alternative, which is a two step procedure, is more like to be used due to the simpler handling of the integrands. In this second path the respective magnetic vector potential for an electric current source is calculated by integration as first. Sequentially, we obtain the electric field density via a differentiation of the vector potential. Alternatively, the vector potential for a magnetic current source can be obtained, and from it the respective magnetic field density can be calculated.

In the present thesis work the second version to obtain the electromagnetic fields has been used. Therefore, it is necessary to obtain the magnetic vector potential by solving the inhomogeneous wave equation stated before. The electric and magnetic intensities are calculated later on with it.

1.1.3.1 The homogeneous vectorial wave equation

The mathematically easiest way to obtain a wave equation from the Maxwell equations is by simplifying them with the following asumptions. The region where the wave should propragate is considered to be source free, linear and homogeneous. A source free region means that $\vec{J}$ and $\vec{M}$ are zero. In this region σ, ε and μ are independent of $|\vec{E}|$, $|\vec{H}|$ and of the geometrical position. In addition to that, the *Constitutive relationships*, equations (1.19) to (1.22), are applied to the Maxwell Equations. Thus the first and the second expression of the simplified equation set have now the following form

$$\nabla \times \vec{E} = -j\omega\mu\vec{H} \tag{1.23}$$

$$\nabla \times \vec{H} = j\omega\varepsilon\vec{E} \tag{1.24}$$

$$\nabla \cdot \vec{H} = 0 \tag{1.25}$$

$$\nabla \cdot \vec{E} = 0 \tag{1.26}$$

Using the curl operator on the first equation of the latter set, the following expression is obtained

$$\nabla \times \nabla \times \vec{E} = -j\omega\mu\nabla \times \vec{H} \tag{1.27}$$

In the right side of this equation the curl of $\vec{H}$ can be replaced by the second equation of the latter simplified equation set (1.24). Transfering the right side of this equation to the other afterwards, the following expression is gained

$$\nabla \times \nabla \times \vec{E} - \omega\mu\varepsilon\vec{E} = 0 \tag{1.28}$$

Finally, applying the mathematical simplification for the double curl expression and using the fourth expression in the simplified Maxwell equations (1.26), the homogeneous complex vector wave equation is acquired

$$\nabla^2\vec{E} + k^2\vec{E} = 0 \qquad \text{with} \quad k^2 = \omega\mu\varepsilon \tag{1.29}$$

k is the frequency dependant wave number. Furthermore, if the same procedure is done starting with the second simplified equation (1.24), afterwards replacing the right side of the resulting equation with first simplied expression (1.23) and simplifying with fourth expression (1.26), another homogeneous wave function is derived with $\vec{H}$ as equation variable.

$$\nabla^2\vec{H} + k^2\vec{H} = 0 \qquad \text{with} \quad k^2 = \omega\mu\varepsilon \tag{1.30}$$

1.1.3.2 The vector potential and the inhomogeneous wave equation

For the derivation of the inhomogeneous wave equation, the infinite region observed is considered to be field free and homogeneous and to have only a radiating source. This means that there exist no conduction current and no impressed magnetic currents. Consequently, the generalized Maxwell Equations have the following form, wherein $\vec{J}$ stands for the source or impressed current

$$\begin{aligned} \nabla \times \vec{E} &= -j\omega\vec{B} && (1.31)\\ \nabla \times \vec{H} &= j\omega\vec{D} + \vec{J} && (1.32)\\ \nabla \cdot \vec{B} &= 0 && (1.33)\\ \nabla \cdot \vec{D} &= \rho && (1.34) \end{aligned}$$

The vector potential is deduced mathematically from these Maxwell Equations. Due to the homogeneous media, the divergence of the magnetic flux in the third expression becomes zero. Hence the magnetic flux $\vec{B}$ can be represented by the curl of another vector function, which satisfies the non-divergence of $\vec{B}$.

$$\nabla \cdot \vec{B} = \nabla \cdot \nabla \times \vec{A} = 0 \tag{1.35}$$

This vector function is the magnetic vector potential $\vec{A}$. Hence the magnetic flux $\vec{B}$ can be defined by the following equation

$$\vec{B} = \nabla \times \vec{A} \tag{1.36}$$

Using $\vec{A}$ the magnetic $\vec{H}$ can be new defined like in the following expression

$$\vec{H} = \frac{1}{\mu}\nabla \times \vec{A} \tag{1.37}$$

If the new definition of the magnetic flux $\vec{B}$ is introduced in the expression (1.31) of the latter Maxwell Equations a new relationship is obtained

$$\nabla \times \vec{E} = -j\omega\mu\nabla \times \vec{A} \qquad \Rightarrow \qquad \nabla \times (\vec{E} + j\omega\mu\vec{A}) = 0$$

With the mathematical knowledge that any curl-free vector is the gradient of an scalar potential Φ_e, the latter relationship between the magnetic vector potential $\vec{A}$ and the electric field intensity $\vec{E}$ can be expressed by the following

$$\vec{E} + j\omega\mu\vec{A} = -\nabla\Phi_e \qquad \Rightarrow \qquad \vec{E} = -j\omega\mu\vec{A} - \nabla\Phi_e \tag{1.38}$$

Φ_e is an arbitrary electric scalar potential. Its definition is derived by means of the next steps. In the second expression of the Maxwell Equations set (1.32) the electric intensity $\vec{E}$ has to be replaced with the later expression. In addition to that, the magnetic intensity $\vec{H}$ has to be described with the magnetic vector potential $\vec{A}$. The respective mathematical transformations are shown via the next set of equations

$$\begin{aligned}
\nabla \times \vec{H} &= \vec{J} + j\omega\varepsilon\vec{E} \\
\nabla(\frac{1}{\mu}\nabla \times \vec{A}) &= \vec{J} + j\omega\varepsilon(-\nabla\Phi_e - j\omega\vec{A}) \\
\nabla(\nabla \cdot \vec{A}) - \nabla^2\vec{A} &= -\mu\vec{J} + j\omega\mu\varepsilon(\nabla\Phi_e + j\omega\vec{A}) \\
\nabla^2\vec{A} + k^2\vec{A} &= -\mu\vec{J} + \nabla(\nabla \cdot \vec{A} + j\omega\mu\varepsilon\Phi_e)
\end{aligned}$$

The defintion of the sought inhomogeneous wave equation is only possible if the scalar potential Φ_e is defined in the following way

$$\nabla \cdot \vec{A} + j\omega\mu\varepsilon\Phi_e = 0 \qquad \Rightarrow \qquad \Phi_e = -\frac{1}{j\omega\mu\varepsilon}\nabla \cdot \vec{A} \tag{1.39}$$

This condition that has to be fulfilled in order to obtain the inhomogeneous wave equation is called the *Lorentz condition*. The following expression shows the acquired inhomogeneious vectorial wave equation, wherein the factor k is the wave number as previously found in the homogeneous wave equation

$$\nabla^2\vec{A} + k^2\vec{A} = -\mu\vec{J} \tag{1.40}$$

The latter equation is also called the *Helmholtz Equation* or complex wave equation. The functions that solve this equation are known as *wave potentials*. Furthermore, the electric field can be calculated knowing the magnetic vector potential with

$$\vec{E} = -j\omega\vec{A} + \frac{1}{j\omega\mu\varepsilon}\nabla(\nabla \cdot \vec{A}) \tag{1.41}$$

1.1.3.3 Solution of the inhomogeneous vector potential wave equation

The *Helmholtz Equation* is an inhomogeneous partial differential equation of second order that can be separated in its components like in the following

$$\begin{aligned}\nabla^2 A_x + k^2 A_x &= -\mu J_x \\ \nabla^2 A_y + k^2 A_y &= -\mu J_y \\ \nabla^2 A_z + k^2 A_z &= -\mu J_z\end{aligned} \tag{1.42}$$

The set of differential equations can be solved separately. Depending on the boundary conditions in the respective medium the solutions for each component can differ. In the following case, it is assumed that the boundary conditions are the same for all components. Hence one of the inhomogeneous equation will be treated and solved.

Without loss of generality the third equation from the latter set will be solved in the following. Therefore, it is assumed that a z-directed dipole moment $I\vec{l}$, which is formed by a current I extending over an along the z-axis oriented length $\vec{l}$, is situated at the coordinates origin

$$\nabla^2 A_z + k^2 A_z = -\mu J_z \tag{1.43}$$

In order to find a solution to the inhomogeneous equation, the solution of the homogeneous case has to be calculated first. Consequently, the following equation is analysed

$$\nabla^2 A_z + k^2 A_z = 0 \tag{1.44}$$

Using spherical coordinates the ∇ operator in the latter equation can be reshaped into

$$\nabla^2 A_z + k^2 A_z = \frac{1}{r^2}\frac{\partial}{\partial r}\left[r^2 \frac{\partial A_z(r)}{\partial r}\right] + k^2 A_z = 0 \tag{1.45}$$

By realizing the derivations the following, the following differential equation is obtained

$$\frac{\partial^2 A_z(r)}{\partial r^2} + \frac{2}{r}\frac{\partial A_z(r)}{\partial r} + k^2 A_z = 0 \tag{1.46}$$

Mathematically, there exist two ansatz for that kind of differential equation based on exponential functions, these are

$$\begin{aligned}A_{z_1} &= c_1 \frac{e^{-jkr}}{r} \\ A_{z_2} &= c_2 \frac{e^{+jkr}}{r}\end{aligned} \tag{1.47}$$

Therein, k is the wave number, c_1 and c_2 are constants that can be found using the boundary conditions. The first ansatz represents an outward travelling wave, the second one an inward travelling wave. Due to the fact that waves should propagate finitely in the far field region ($r \to \infty$), the first ansatz is chosen

$$A_z = A_{z_1} = c_1 \frac{e^{-jkr}}{r} \tag{1.48}$$

In order to obtain the value of the constant c_1, the static case of the vector potential is regarded. In this case $k = 0$ and therefore equation (1.43) becomes

$$\nabla^2 A_z = -\mu J_z \tag{1.49}$$

The latter equation is equivalent to the Poisson's equation that can be solved by the following function

$$A_z = \frac{\mu}{4\pi} \iiint_V \frac{J_z}{r} dv' \tag{1.50}$$

Thus the value of the constant is $c_1 = \frac{\mu J_z}{4\pi}$ and the solution for equation (1.43) is after (1.48) the multiplication of the latter solution by the exponential component $\frac{e^{-jkr}}{r}$. Taking into account that the dipole's moment is described by the current I instead of the density J_z following transformations are done and at the end a line integral equation is obtained

$$\begin{aligned} A_z &= \frac{\mu}{4\pi} \iiint_V J_z \frac{e^{-jkr}}{r} dv' \\ &= \frac{\mu}{4\pi} \iint_S J_z^S \frac{e^{-jkr}}{r} ds' \\ &= \frac{\mu}{4\pi} \int_C I \frac{e^{-jkr}}{r} dl' \end{aligned} \tag{1.51}$$

In the latter transformation S stands for a surface wrapping the volume V and J^s is the current density flowing at each surface segment ds'. Furthermore, C is a path enclosing the surface S and I is the current in each infinite length element dl' over the path C. If the line integral in the latter formula is calculated and the dipole moment used, following result for the vector wave equation of a z-oriented dipole of length l excited by the current I is acquired

$$A_z = \frac{\mu I l}{4\pi} \frac{e^{-jkr}}{r} \tag{1.52}$$

The vectorial solution to the inhomogeneous differential equation in (1.40) is given by the following general equation

$$\vec{A} = \frac{\mu}{4\pi} \iiint_V \vec{J} \frac{e^{-jkr}}{r} dv' \tag{1.53}$$

This expression for the magnetic vector potential depending on the boundary and medium conditions has to be adapted.

1.1.3.4 General solution for a radiating source in free-space

The solution for the case of a in the cordinate origin situated source with a z-directed dipole moment in the latter paragraphs can be expanded to a general solution where the currents position described by $\vec{r}'$ is somewhere in the coordinate system. Therefore, the radiated electric

field is obtained with the help of the general magnetic vector potential by the following formula

$$\vec{E}(\vec{r}) = -j\omega\vec{A}(\vec{r}) + \frac{1}{j\omega\mu\varepsilon}\nabla(\nabla\cdot\vec{A}(\vec{r})) \qquad \text{with} \quad \vec{A}(\vec{r}) = \frac{\mu}{4\pi}\iiint_V \vec{J}(\vec{r}')\frac{e^{-jk|\vec{r}-\vec{r}'|}}{|\vec{r}-\vec{r}'|}dv' \tag{1.54}$$

$\vec{r}$ is the vector towards the observation point. This equation describes the fields in free-space caused by the source electric current $\vec{J}$.

1.1.4 Green's functions

Green's theorems (see Appendix A) have been used in order to solve field problems in mechanics and electromagnetics. Thereby the reciprocal problem of the concerned problem is solved and then reciprocity is applied. For example, a very common case is to find out the electric field $\vec{E}$ in a point $\vec{r}'$ in a certain region. Instead of finding the solution directly, a source point is positioned in $\vec{r}'$ and its radiated field is called a *Green's function* **G**. Substituating the field functions in *Green's theorem for vector functions* (see appendix A, (B.6)) like in the following $\vec{A} = \vec{E}$ and $\vec{B} = \mathbf{G}$, we obtain a formula in order to obtain $\vec{E}$ in $\vec{r}'$. The last steps denote that the reciprocal problem to the original one was found. Consequently, by solving it and using reciprocity, the solution to the original task will be found [3].

In electromagnetics, the solution to such and other problems is to solve second-order uncoupled partial differential equations that are derived form Maxwell's equations with appropriate boundary conditions. It would be desirable to obtain closed-form solutions, at least for some problems and associated regions, in order to know the behaviour of the whole systems specially at regions where rapid changes take place. The Green's function method allows to find out such solutions.

It can be said that the Green's function is the impulse response or the transfer function of a electromagnetic system. For a given problem it can take various forms: finite explicit functions, infinite series of suitably chosen orthogonal functions, integral forms. [2] and [3] are the main references for the following summary in the present thesis work.

1.1.4.1 General method

With the Green's function method a solution to the partial differential equation is obtained using an impulse function, mainly a Dirac delta, as the driving function. The solution to this driving function is given as the superposition of the impulse response solutions, the Green's function, with the Dirac delta source that in the limit simplifies itself to an integral.

The procedure for the generation of a Green's function for a three-dimensional scalar Helmholtz partial different equation like

$$\nabla^2\Phi(\vec{r}) + k^2\Phi(\vec{r}) = f(\vec{r}) \tag{1.55}$$

conditioned by a homogeneous boundary expressed by the following generalized function

$$c_1\Phi(\vec{r}_s) + c_2\frac{\partial\Phi(\vec{r}_s)}{\partial\vec{n}} = 0 \tag{1.56}$$

uses the *Green's theorems* (see appendix A) in order to obtain the desired Green's function. In the equation (1.56) that describes the boundary, $\vec{r}_s$ is the vector towards a point on the surface S and $\vec{n}$ stands for a normal vector in outward direction. Moreover, the wanted Green's function $\mathbf{G}$ has to satisfy the following partial differential equation

$$\nabla^2\mathbf{G}(\vec{r},\vec{r}') + k^2\mathbf{G}(\vec{r},\vec{r}') = \delta(\vec{r}-\vec{r}') \tag{1.57}$$

Furthermore, it has to fulfill the generalized homogeneous boundary condition in the following way

$$c_1\mathbf{G}(\vec{r}_s,\vec{r}') + c_2\frac{\partial\mathbf{G}(\vec{r}_s,\vec{r}')}{\partial\vec{n}} = 0 \tag{1.58}$$

In order to combine the available and obtained functions, they have to be transformed. First step is to multiply equation (1.55) by the Green's function $\mathbf{G}(\vec{r},\vec{r}')$ and then equation (1.57) by $\Phi(\vec{r})$. The following statements are obtained

$$\mathbf{G}\nabla^2\Phi + k^2\Phi\mathbf{G} = f\mathbf{G} \tag{1.59}$$
$$\Phi\nabla^2\mathbf{G} + k^2\Phi\mathbf{G} = \Phi\delta(\vec{r}-\vec{r}') \tag{1.60}$$

Substracting the latter equations from each other and integrating over a certain volume V the following new equation is created

$$\iiint_V \Phi\delta(\vec{r}-\vec{r}')dv - \iiint_V f\mathbf{G}dv = \iiint_V (\Phi\nabla^2\mathbf{G} - \mathbf{G}\nabla^2\Phi)dv \tag{1.61}$$

Calculating the integration scalar function Φ with the Dirac impulse the following statement is obtained

$$\Phi(\vec{r}') = \iiint_V f(\vec{r})\mathbf{G}(\vec{r},\vec{r}')dv + \iiint_V (\Phi(\vec{r})\nabla^2\mathbf{G}(\vec{r},\vec{r}') - \mathbf{G}(\vec{r},\vec{r}')\nabla^2\Phi(\vec{r}))dv \tag{1.62}$$

Applying the second identity (B.3) on the last expression, this function can be modified as it follows

$$\Phi(\vec{r}') = \iiint_V f(\vec{r})\mathbf{G}(\vec{r},\vec{r}')dv + \oint_S (\Phi(\vec{r})\nabla\mathbf{G}(\vec{r},\vec{r}') - \mathbf{G}(\vec{r},\vec{r}')\nabla\Phi(\vec{r}))ds \tag{1.63}$$

The last step to obtain the generalized formula for the development of a Green's function for a three-dimensional scalar Helmholtz equation is to interchange the the arbitrary point $\vec{r}'$ with the dummy variable $\vec{r}$

$$\Phi(\vec{r}) = \iiint_V f(\vec{r}')\mathbf{G}(\vec{r},\vec{r}')dv' + \oint_S (\Phi(\vec{r}')\nabla'\mathbf{G}(\vec{r},\vec{r}') - \mathbf{G}(\vec{r},\vec{r}')\nabla'\Phi(\vec{r}'))ds' \tag{1.64}$$

This formula can be simpified depending of the boundary conditions of Φ and $\mathbf{G}$, as well as thir derivatives in the surface S

1.1.4.2 The dyadic Green's function

According to Balanis [2], vectors and dyadics describe linear transformations with a given orthogonal coordinate system symplifying the manipulations of mathematical relations similar to the use of tensors. Dyads satisfy a number of mathematical identities like cross and dot products, differentiations, and integrations. Therefore, the use of dyadics for electromagnetic problems, wherein linear transformations take place between sources and fields, is of great benefit.

Due to the vectorial character of the linear transformations in Electromagnetics Dyads are used to represent the Green's function adequately. The solution for an electromagnetic problem is given frequently in the following form

$$\vec{h}(\vec{r}) = \iiint_V \vec{f}(\vec{r}) \bigotimes \overline{\overline{\mathbf{G}}}(\vec{r},\vec{r}')dv' \tag{1.65}$$

$\vec{h}$ is the solution function, $\vec{f}$ is the source function. Hence the dyadic Green's function $\overline{\overline{\mathbf{G}}}$ embraces all scalar Green's functions that transform the source field components. Consequently, the Dyadic Green's function has the following form

$$\overline{\overline{\mathbf{G}}} = \begin{bmatrix} \mathbf{G}_{xx} & \mathbf{G}_{xy} & \mathbf{G}_{xz} \\ \mathbf{G}_{yx} & \mathbf{G}_{yy} & \mathbf{G}_{yz} \\ \mathbf{G}_{zx} & \mathbf{G}_{zy} & \mathbf{G}_{zz} \end{bmatrix} \tag{1.66}$$

The elements $\mathbf{G}_{ij}$ of the dyad represent the scalar Green's functions. Furthermore, the fact that its elements show symmetry properties $\mathbf{G}_{ij} = \mathbf{G}_{ji}$ reflects the reciprocity theorem [3]. This is valid for the Dyadic Green's function in free-space or subjected to boundary conditions. In addition to that, the Green's theorems presented in appendix A are valid for the dyadic Green's function.

Moreover, the vector potential solution for the calculation of the free-space electric field in (1.54) can be taken as an example for the use of the dyadic Green's function. This equation can be expressed by means of the dyadic Green's function, this is

$$\vec{A}(\vec{r}) = \frac{\mu}{4\pi} \iiint_V \vec{J}(\vec{r}') \bigotimes \overline{\overline{\mathbf{G}}}(\vec{r},\vec{r}')dv' \tag{1.67}$$

The dyadic Green's functions are often sought, transformed or approximated in order to solve electromagnetic problems. Several publications like [43], [41] testify this.

1.1.5 The Equivalence Principle

The Equivalence Principle states that two sources producing the same field within a region of space are said to be *equivalent* within that region. That means that it is not necessary to know the actual sources to calculate a desired field in a given region, equivalent sources will serve as well [3]. This principle is the simplification of the Huygen's Principle for waves, which states that each point on an advancing wavefront can be considered as a new source for a new wave. And that the new wavefront can be regarded as the sum of all the new generated waves.

The Equivalence principle is also based on the uniqueness theorem. This theorem states that "*a field in a lossy region is uniquely specified by the sources within the region plus the tangential*

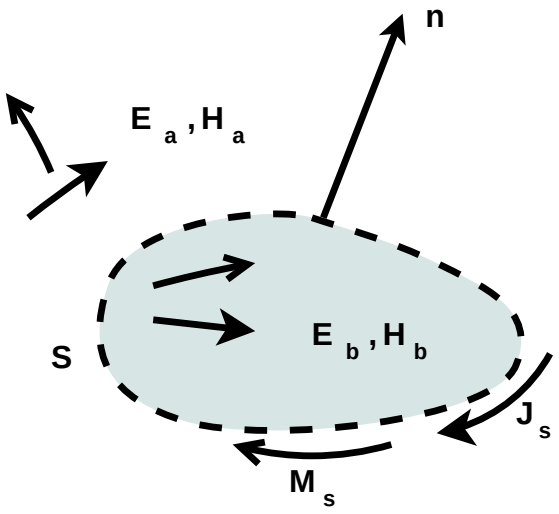

Figure 1.3 : *A general formulation of the Equivalence Principle*

components of $\vec{E}$ over the boundary, or the tangential components of $\vec{H}$ over the boundary, or the former over part of the boundary and the latter over the rest of the boundary". This means that a field in a lossless medium is considered to be the limit of the corresponding field in a lossy medium as the losses disappear. Furthermore, if the tangential field components of $\vec{E}$ and $\vec{H}$ over a boundary are completely known, then the fields over all the regions can be determined.

In order to illustrate this principle, the reader has to imagine himself a electric and a magnetic source (for example a transmitter with it's antenna) enclosed by an imaginary surface S that generates a field in free space (described by $\vec{E}$ and $\vec{H}$) as depicted in figure 1.3. The applied *Equivalence Principle* would mean that the field outside the imaginary surface would remain the same and would be generated by equivalent source currents $\vec{J}$ and $\vec{M}$ on the surface. Therefore, the field in the enclosed space would disappear becoming zero.

The equivalent sources are described by their surface currents, which can be of electric or magnetic kind, or even both. This current can be calculated by the following equations

$$\vec{J}_{surf} = \vec{n} \times \vec{H} \qquad \vec{M}_{surf} = -\vec{n} \times \vec{E} \tag{1.68}$$

$\vec{n}$ is the normal vector of the closed surface. Other conditions, which illustrates the Equivalence Principle more generally, are if it is assumed that inside the closed surface there exist fields $\vec{E}_a$, $\vec{H}_a$ as well as outside the fields $\vec{E}_b$, $\vec{H}_b$. In this case at the surface, which represents the boundary, there must exist electrical and magnetic sources with the following currents.

$$\vec{J}_{surf} = \vec{n} \times (\vec{H}_a - \vec{H}_b) \qquad \vec{M}_{surf} = -\vec{n} \times (\vec{E}_a - \vec{E}_b) \tag{1.69}$$

Harrington presents the Equivalence Principle for waves in detail in [3]. [2], [1] and [19] are additional references, which present this principle in an applied way to electromagnetic problems.

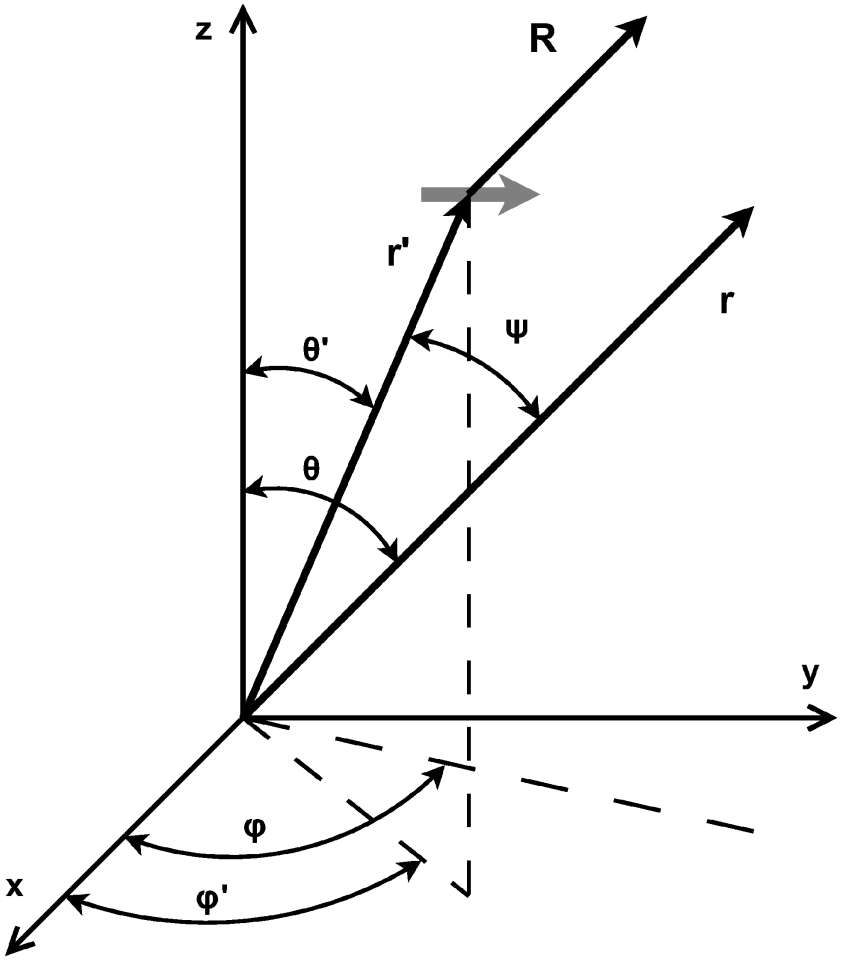

Figure 1.4 : *Infinitesimal dipole position for far field analysis*

1.2 Infinitesimal or Hertzian dipole

An infinitesimal dipole is a linear wire whose length and diameter are infinitesimal small compared to the wavelength in an electromagnetic system. Therefore, the dipole current is assumed to be constant all over the length of this elementary dipole.

1.2.1 Radiated Fields

The radiated field of an infinitesimal dipole can be calculated by handling it as a radiating source. Consequently, the field is approached by the dipole's magnetic vector potential and hence equation (1.54) from the last section is used. As aforementioned, this vector potential approach is mainly used due to a more simple solution proceeding from a mathematical point of view.

Hence the first step is to find the magnetic vector potential with the knowledge of the source current along the dipole. Therefore, the magnetic vector potential $\vec{A}$ that has been presented in the last section in equation (1.53) is applied. The threefold integral in the latter equation can be simplified like in the following: it can be transformed in a surface integral since the current

density is in general two dimensional. Furthermore, the twofold integral is converted to a simple integral by taking the current magnitude I plus its orientation instead of the current density $\vec{J}_s$. The latter can be achieved by assuming that the current does not change along the infinitesimal length. Hence the vector potential equation evolves like in the following

$$\begin{aligned}\vec{A} &= \frac{\mu}{4\pi}\iiint_V \vec{J}\frac{e^{-jkr}}{r}dv' \\ &= \frac{\mu}{4\pi}\iint_S \vec{J}_s\frac{e^{-jkr}}{r}ds' \\ &= \frac{\mu I}{4\pi}\frac{e^{-jkr}}{r}\int_C d\vec{r}'\end{aligned} \tag{1.70}$$

The following equation shows the resulting simplified solution for an infinitesimal dipole placed in the origin of the coordinates

$$\vec{A}(x,y,z) = \frac{\mu I\vec{l}}{4\pi}\frac{e^{-jkr}}{r} \tag{1.71}$$

In the more general case, wherein the elementary dipole lies somewhere in space, the dipole's magnetic vector potential is given by the next expression

$$\vec{A}(x,y,z) = \frac{\mu I}{4\pi}\int_C \frac{e^{-jkR}}{R}d\vec{r}' \qquad \text{with} \quad R = |\vec{r}-\vec{r}'| = r - r' \tag{1.72}$$

The vector $\vec{r}$ stands for the position vector of the observing point, r is the respective vector magnitude that is equivalent to the distance between origin and observing point. The position vector of the dipole is given by $\vec{r}'$ and its magnitude r' describes the distance between the origin and the position of the dipole. Hence R is the difference between both distances. Figure 1.4 illustrates the geometrical description of the infinitesimal dipole for the radiation analysis.

Due to the fact that elementary dipoles radiate spherical waves, the general solution for the electric field is in spherical coordinates. Therefore, $\vec{A}(x,y,z)$ is transformed to $\vec{A}(r,\theta,\phi)$ by means of a respective transformation matrix (see appendix A). Consequently, the function for electric field of an elementary dipole has the following form

$$\vec{E}(r,\theta,\phi) = -j\omega\vec{A}(r,\theta,\phi) + \frac{1}{j\omega\mu\varepsilon}\nabla_{r\theta\phi}(\nabla_{r\theta\phi}\cdot\vec{A}(r,\theta,\phi)) \tag{1.73}$$

$\nabla_{r\theta\phi}$ represents the divergence operator for field functions in spherical coordinates.

1.2.2 Far field approximation

The Maxwell Equations and the resulting function for the vector potential are valid inside a certain region that can be of infinite extension. The far field radiation is of primary interest for an antenna. This region of interest is where the distance between the source and the observing point are very big. Consequently, the following condition is valid: $r \gg \lambda$. This region, well-known as far field region, cause that certain values in the developed electromagnetic functions can be neglected or approximated by "simple-to-calculate" subtitutes [1].

It have be considered that complex harmonic functions can be regarded as "fussion" of a complex amplitude term and a complex phase term. Therefore, a segregation in applying the far field simplification is done: a far field approximation for the amplitude term and another for the phase term. In the next explanations r is the magnitude of the position vector of the observation point $\vec{r}$ and r' the magnitude of the position vector of the radiating source $\vec{r}'$. For the amplitude term the approximation that the distance R is a constant value is valid. This follows from the fact that the distance between the origin and the source r' is very small in comparison to the radius from the origin until the observer r. Thus the following expression is valid

$$r \gg r' \qquad \rightarrow \qquad R = r - r' \approx r \qquad \text{for the amplitude term} \tag{1.74}$$

The latter approximation can not be applied to the phase term, due to the fact that the phase term on the exponential function has a stronger influence on the values of the complex function than the amplitude term. The far field consideration for the phase term is done by approximating the spatial distance difference R as accurate as possible. Assuming that the observing point lies in the far field both the vectors $\vec{r}$ and $\vec{r}'$ will be aligned parallel to each other. Hence the distance difference R can be calculated by the following approximation

$$r \gg r' \qquad \rightarrow \qquad R = r - r' \cos\psi \qquad \text{for the phase term} \tag{1.75}$$

In the latter equation the angle ψ is the spatial angle enclosed by the vectors $\vec{r}$ and $\vec{r}'$

In order to simplify the evaluation of the vector potential equation, the far field approximation is applied on the equation for an elementary dipole lying in space. Moreover, the excitation current is assumed as constant at the dipole $I(x',y',z') = I_0$. The resulting expression for the vector potential is given by the following expression

$$\vec{A}(x,y,z) = \frac{\mu I_0 \vec{l}}{4\pi R} e^{-jkR} \simeq \frac{\mu I_0 \vec{l}}{4\pi r} e^{-jk(r - r'\cos\psi)} \tag{1.76}$$

$\vec{l}$ stands for the oriented length of elementary dipole pointing at a certain direction in space. In the following, the vector potential $\vec{A}(x,y,z)$ has to be transformed in its spherical coordinate form $\vec{A}(r,\theta,\phi)$

Furthermore, expression (1.73) is valid in order to obtain the electric field equation. Nevertheless, this function simplifies since the magnetic vector potential, in cartesian and in spherical coordinates as well, is a field function dependant of the term $\frac{e^{-jkr}}{r}$. Applying the two divergence operators to the latter, terms of higher-order of $\frac{1}{r^n}, n = 2,3,\ldots$ are obtained. For the far field case these terms are neglected since $\frac{1}{r^n}$ for $r \rightarrow \infty$. Consequently, the electric far field of an elementary dipole can be calculated taking into account only the term of (1.73). This is

$$\vec{E}(r,\theta,\phi) \simeq -j\omega\vec{A}(r,\theta,\phi) \tag{1.77}$$

Besides that, it has to be said that the latter expression is valid for the θ and ϕ components since the radial component of the electric field disappears for $r \rightarrow \infty$. This is due to its $\frac{1}{r^n}$ dependancy.

1.3 Finite length dipole

The techniques developed for the infinitesimal dipole can be used to model and to analyse the radiation characteristics of a linear dipole of any length. The elementary dipole, whose diameter and length are assumed to be very small compared to its wavelength, can be used as an element of the entire finite dipole. Consequently, the finite length dipole is modelled as a composition of several infinitesimal dipoles. Each elementary dipole is assigned with a current value according to a certain distribution for the entire finite length dipole. Detailed description of this procedure can be found at [1] and [15].

1.3.1 Current distribution

For the finite length dipole with a negligible diameter the current distribution can be approximated by mathematical equations based on harmonic functions. For instance, according to [1] for a dipole of length l positioned symmetrically on the z-axis, this means the geometrical centre of the dipole is at the origin of the coordinates, the current distribution can have the following form

$$I = \begin{cases} I_0 \sin[k(\frac{l}{2} - z)] & 0 \leq z \leq \frac{l}{2} \\ I_0 \sin[k(\frac{l}{2} + z)] & -\frac{l}{2} \leq z \leq 0 \end{cases} \tag{1.78}$$

Therein, I_0 stands for the current amplitude, k for the wave number, respectively. The function defined in the latter expression determines the current values of each elementary dipole used as a dipole element. This distribution assumes that the finite length dipole is fed at its centre. The desired current is supposed to be sinusoidal along the dipole length. The distribution function aims the current at the finite length dipole's ends to be zero.

1.3.2 Radiated field

Assuming the finite length dipole to be a composition of dipole elements excited with current values according to a current distribution, the radiated field of this dipole can be handled as an infinite summation of the field contributions of all its elements. Therefore, the total resulting field is an integration of the field contributions $d\vec{E}_{element}$ of all elements along the finite length of the dipole. This is

$$\vec{E}_{finite} = \int d\vec{E}_{element} \tag{1.79}$$

Furthermore, if we regard the aforementioned example of a finite dipole on the z-axis, the resulting far field function using the afore given current distribution and applying the latter expression is

$$\begin{aligned} E_r &= 0 \\ E_\theta &= jZ_0 \frac{I_0 e^{-jkr}}{2\pi r} \cdot \frac{\cos(\frac{kl}{2}\cos\theta) - \cos(\frac{kl}{2})}{\sin\theta} \\ E_\phi &= 0 \end{aligned} \tag{1.80}$$

In order to obtain the latter expression, wherein, Z_0 is the intrinsic or wave impedance,

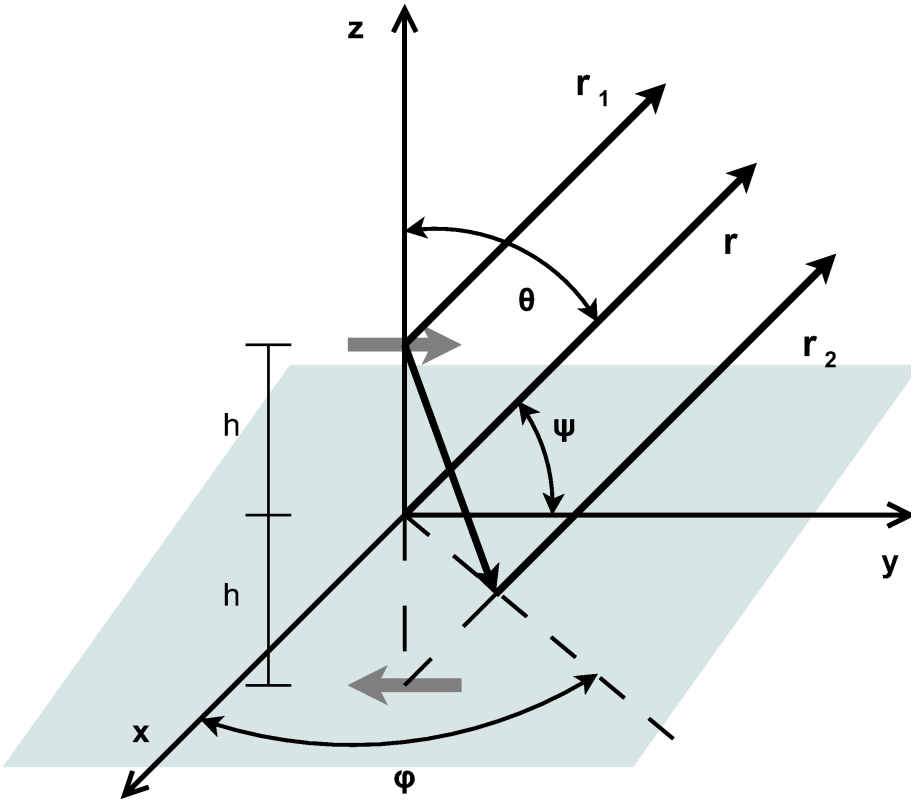

Figure 1.5 : *Horizontal elementary dipole positioned over a perfect conducting plane for far field analysis*

the far field approximations for magnitude and phase terms (see (1.74) and (1.75)) and some mathematical transformation have been applied. A detailed derivation for the latter is given in [1].

1.4 Horizontal dipole

Due to the frequency dependancy of the permittivity and the permeability as well as the conductivity a medium can change his characteristic in a certain frequency band. For example, a lossy medium becomes a very good conductor above certain frequencies. Therefore, it is necessary to analyse the behaviour of an antenna in presence of different materials. In the following paragraphs the interaction between a perfect electrical conductor (PEC) plate and a horizontally positioned dipole will be presented. This interaction has been analysed by different authors and is presented in [1], [2] and [3].

The relevance of this case for the present thesis work is the modelling of microstrip antennas. The radiating element of a microstrip antenna is positioned with a certain height over a grounded layer, namely the ground plane. The behaviour of the dipole in presence of a PEC plate will contribute to the modelling of the patch in a such configuration. Moreover, for this analysis the following configuration is regarded: a dipole placed horizontally over a infinite PEC surface as depicted in figure 1.5.

The field radiated by the dipole over the conducting plane will be reflected entirely by it.

This is, due to the fact that inside the conductor there can not exist a field. Consequently, on the other side of the perfect conducting plate exists no field. The PEC plate acts as a boundary dividing two regions. Hence the total field $\vec{E}_{total}$ received at an observation point in the far field zone is the sum of the contributions of the direct radiated field $\vec{E}_{direct}$ and of the reflected one $\vec{E}_{reflect}$. Furthermore, these far fields can be calculated by means of equation (1.77) using the vector potential expression in (1.76). The following expression describes the latter approach

$$\vec{E}_{total} = \vec{E}_{direct} + \vec{E}_{reflect} = \frac{j\omega\mu\vec{Il}}{4\pi}\frac{e^{-jkr_1}}{r_1} - \frac{j\omega\mu\vec{Il}}{4\pi}\frac{e^{-jkr_2}}{r_2} \tag{1.81}$$

In order to define the field contribution of the reflected waves, the image theory is applied. For it, the field contribution due to the reflection of the field coming from the dipole on the PEC surface can be represented by the field generated by a virtual equivalent source. This virtual dipole lies on the other region of the boundary. According to the image theory this ficticious dipole is oriented in opposite direction to real dipole, this is expressed by the minus sign in the latter equation. Moreover, for the calculation of the total field, according figure 1.5, the distance r_1 between the real source and the observation point is required. Furthermore, for computing the far field contribution of the virtual source, the distance r_2, which is the magnitude of the vector from its position towards the observation point, is needed. According to picture 1.5 r_1 and r_2 can be described by

$$r_1 = [r^2 + h^2 - 2rh\cos\xi]^{\frac{1}{2}} \tag{1.82}$$
$$r_2 = [r^2 + h^2 - 2rh\cos(\pi - \xi)]^{\frac{1}{2}} \tag{1.83}$$

With the help of far field approximations for the amplitude and the phase terms the distances r_1 and r_2 can be simplified and hence the total field calculation too. The applied far field aproximation for the amplitude term is

$$r_1 = r_2 \approx r \qquad \text{for the amplitude term} \tag{1.84}$$

The far field approximation for the phase term transforms expressions in equation set (1.83) into following equations

$$\begin{aligned} r_1 &= r - h\cos\xi \\ r_2 &= r + h\cos\xi \end{aligned} \qquad \text{for the phase term} \tag{1.85}$$

Therein, ξ is the angle formed by the distance r and the normal vector of the infinite PEC surface. Applying these attained approximations for the distances r_1 and r_2 in (1.81) and doing some mathematical transformations on them gives the following equation for the total electric far field

$$\vec{E}_{total} = \begin{cases} \vec{E}_{direct,origin} \cdot 2j\sin(kh\cos\xi) & \text{for} \quad -\frac{\pi}{2} < \xi < \frac{\pi}{2} \\ 0 & \text{else} \end{cases} \tag{1.86}$$

The resulting total field can be interpreted as a modulation of the field of a single dipole. Due to the fact that the image and the real source build an array of two elements, this sinusoidal function is called "array factor". In addition to formula (1.86) the values of the field under the ground plane have to be nulled since inside the perfect conductor there can not exist a field.

1.5 Far field quantities

The far field analysis of an antenna requires certain quantities that describe and characterize its radiation behaviour. The most used quantities are the radiation pattern and the directivity. Both analysis parameters are presented in the following paragraphs. For it, [1], [15] and [14] are used as references.

1.5.1 Radiation pattern

The radiation pattern shows the radiation performance of an antenna in dependency to the spacial angles in a certain coordinates system. This quantity describes the spatial distribution of the radiated energy as a function of the position of an observing point along a surface of constant radius. The radiation pattern can be calculated by means of the following formula

$$C(\theta,\phi) = \left.\frac{|\vec{E}(\theta,\phi)|}{|\vec{E}_{max}(\theta,\phi)|}\right|_{\substack{r=const \\ r\to\infty}} \tag{1.87}$$

1.5.1.1 Major lobe and minor lobes

The *major lobe*, also known as "main beam", is the desired lobe of the radiation pattern. This lobe contains the direction of the maximum radiation. Any other lobe besides the latter one is called *minor lobe*. Under the minor lobes there exist *side lobes* and *back lobes*. The side lobe is defined as a lobe in any direction than the intended major lobe. Commonly, the minor lobe adjacent to the main beam that points inside the hemisphere in direction of this major lobe is assumed as a side lobe. The back lobe is the minor lobe that points in the opposite direction of the major lobe. All these minor lobes are usually undesired and should be minimized.

1.5.2 Directivity and gain

The directivity of an antenna is the ratio between the radiation intensity from the antenna in a given direction and the averaged radiation intensity. Furthermore, the averaged radiation intensity is equal to the total power radiated by the antenna divided by 4π. The maximum of the directity can also be defined as the ratio between the maximal power density of the measuring antenna and the power density of an ideal isotropic radiator. According to [15] and [17], the following equation can be used to compute the directivity D

$$D = \frac{4\pi r^2 S_{rad}}{P_{rad}} \tag{1.88}$$

P_{rad} is the total radiation power of the isotropic radiator and r is the distance from the antenna to the measuring point. S_{rad} stands for the radiation density of the antenna and it is defined as

$$S_{rad}(r,\theta,\phi) = \frac{1}{2Z_0}|\vec{E}(r,\theta,\phi)|^2 \tag{1.89}$$

In the latter equation Z_0 stands for the free-space wave impedance or intrinsic impedance and $\vec{E}$ is the electric far field for an observing point (r,θ,ϕ). Moreover the total radiation power is given by

$$\begin{aligned} P_{rad}(r,\theta,\phi) &= \int_0^{2\pi}\int_0^{\pi} S_{rad} r^2 \sin\theta d\theta d\phi \\ &= \frac{r^2}{2Z_0}\int_0^{2\pi}\int_0^{\pi} |\vec{E}(r,\theta,\phi)|^2 \sin\theta d\theta d\phi \end{aligned} \tag{1.90}$$

In the latter expression the integration limits build a spatial area given by the spherical angles θ and ϕ. The resulting formula for the calculation of the directivity for an observing point (r,θ,ϕ) is consequently

$$D(r,\theta,\phi) = \frac{4\pi|\vec{E}(r,\theta,\phi)|^2}{\int_0^{2\pi}\int_0^{\pi}|\vec{E}(r,\theta,\phi)|^2 \sin\theta d\theta d\phi} \tag{1.91}$$

The following relation between the radiation pattern and the radiation density facilitates the calculation of the directivity if the radiation pattern is already known, this is

$$\begin{aligned} S_{rad}(r,\theta,\phi) &= \frac{1}{2Z_0}|\vec{E}(r,\theta,\phi)|^2 \\ &= C^2(r,\theta,\phi)\cdot\frac{|\vec{E}_{max}|}{2Z_0} \\ &= C^2(r,\theta,\phi)\cdot S_{rad,max} \end{aligned} \tag{1.92}$$

Therein, the integration limits are given by the spatial area given by the spherical angles θ and ϕ. The resulting formula for the calculation of the directivity is therefore

$$D(r,\theta,\phi) = \frac{4\pi C^2(r,\theta,\phi)}{\int_0^{2\pi}\int_0^{\pi} C^2(r,\theta,\phi)\sin\theta d\theta d\phi} \tag{1.93}$$

The gain G is a quantity describing the performance of an antenna taking into account the efficiency η of the antenna . Furthermore, the gain of an antenna is related closely to its directivity. The latter relation is given by the following equation

$$G = \eta D \tag{1.94}$$

1.6 Antenna arrays

For certain systems and applications like scanning at radars, antennas with very directive pattern are desired. A directive pattern is characterized by a slender main beam but with a high directivity value at the desired direction. Furthermore, a directive pattern can be generally reached by enlarging the antenna aperture or by building up several radiating elements into an array. Consequently, an antenna array can be seen as an "sampled" aperture that is excited at certain points or regions.

Moreover, depending on the distribution of the array elements in space, there exist two kind of arrays: linear arrays and a planar arrays. The elements of a linear array are put along a line in a row. The elements of a planar array are positioned along two dimensions describing a surface.

The distance between two array element positions is called "spacing". If the distances between neighbouring elements have the same value in the whole array, then the array has uniform spacing. For a two-dimensional array there can exist two spacing values if it is has uniform spaced elements.

For the following far field array analysis and the resulting quantities, at which [1], [6] and [15] are used as main references, the following preconditions are assumed. First assumption is that all array elements are identical. Second premise is that all array elements are equally oriented in space. And last supposition is that there exists no influence between the array elements.

1.6.1 Array Factor - linear array

The total radiated field of an array is the sum of the contributions of every single array element. Therefore, the electric far field for an array composed of N elements can be defined by the following equation

$$\vec{E}_{array} = \sum_{n}^{N} \vec{E}_n \tag{1.95}$$

Without invalidating the generality of the latter equation, elementary dipoles of length l_n positioned in space according to the vectors $\vec{r}_n$ and excited by respective currents I_n can be chosen as elements for the array. If it is assumed that the observation point $\vec{r}$ lies in the far field and that the sources are elementary dipoles are near the origin, then the calculation of the total radiated field can be transformed in the following way

$$\begin{aligned} \vec{E}_{array}(\vec{r}) &= \sum_{n=0}^{N-1} \kappa I_n \vec{l}_n \frac{e^{-jk(r-r_n\cos\psi_n))}}{r} \\ &= \kappa I_0 \frac{e^{-jkr}}{r} \sum_{n=0}^{N-1} \frac{I_n}{I_0} \vec{l}_n e^{jkr_n\cos\psi_n} \end{aligned} \tag{1.96}$$

Therein, $\vec{l}_n$ is the element oriented length, the fraction composed of the complex phase component e^{-jkr} and of distance from origin to observing point $|\vec{r}| = r$ is the green function, respectively. Furthermore, $r_n = |\vec{r}_n|$ and the current I_0 is a normalization value. ψ_n is the angle between the vectors $\vec{r}$ and $\vec{r}_n$, and comes from the afore given far field approximation in expression (1.75). The constant k stands for the wave number, $\kappa = \frac{j\omega\mu}{4\pi}$ stands for all remaining constants.

The resulting expression shows that the total radiated field depends mainly on the sum of the excitation currents and lengths of the dipoles. Moreover, the complex phase is determined by the position of the dipoles. The question arises, if this equation becomes more simple if the used array elements are equal. Adopting the latter case of an array composed of elementary dipoles and assuming similar elements, this means the dipoles have the same size $l_n = l$, equation (1.96) becomes

$$\vec{E}_{array}(\vec{r}) = \kappa I_0 \vec{l} \frac{e^{-jkr}}{r} \sum_{n=0}^{N-1} \frac{I_n}{I_0} e^{jkr_n\cos\psi_n} \tag{1.97}$$

Comparing the latter equation with expression (1.71) in the former section about elementary dipoles, the expression before the sum is the radiated field by a dipole being placed at the coordinates origin. Consequently, the total radiated field is the multiplication of the element field at the origin E_0 by the sum depending of the normalized excitations $\frac{I_n}{I_0}$ and the phase term that is described by the distances r_n towards the elements and the angles ψ_n

$$\vec{E}_{array}(\vec{r}) = E_0 \cdot \sum_{n=0}^{N-1} \frac{I_n}{I_0} e^{jkr_n \cos\psi_n} \qquad \text{with} \quad E_0 = \kappa I_0 \vec{l} \cdot \frac{e^{-jkr}}{r} \tag{1.98}$$

Furthermore, if all elements are excited with the same current $I_n = I_0$, then the latter equation simplifies by disappearing the excitation terms in the sum as follows

$$\vec{E}_{array}(\vec{r}) = E_0(\vec{r}) \cdot AF \qquad \text{with} \quad E_0(\vec{r}) = \kappa I_0 \vec{l} \cdot \frac{e^{-jkr}}{r} \tag{1.99}$$

and with

$$AF = \sum_{n=0}^{N-1} e^{jkr_n \cos\psi_n} \tag{1.100}$$

The latter expression is widely refered as the array factor AF of a linear array. It can be noticed that the derivation of the AF depends of the excitation current of each array element. Consequently and only under the preconditions stated before, the calculation of the far field $\vec{E}_{array}$ of an array composed by the same elements of any antenna kind reduces to a multiplication of the far field of the single element $\vec{E}_0$ in the origin by the respectively calculated Array Factor AF

1.6.1.1 Linear array with uniform current amplitude and spacing

The AF can be simplified for certain special cases, for instance for a linear array with equidistant distances and same excitations amplitude. Therefore, it is assumed that the linear array elements are positioned with a certain distance d in a row and that the equal elements are excited by currents with the same amplitude but with a progressive phase. Then from the expression (1.98) the AF is obtained as

$$AF = \sum_{n=0}^{N-1} e^{jn\alpha} e^{jkr_n \cos\psi_n} \tag{1.101}$$

α is the progressive phase that describes the phase shift by which the current in each element leads the current of the preceding element. Depending on the geometry, the phase component $e^{-jkr_n \cos\psi_n}$ in the AF can be expressed as a function of the variable d, known also as spacing.

For example, in the case of the geometrical constellation in figure 1.6, where the equal elements are positioned along the x-axis, the phase function in the phase term can be replaced by $r_n \cos\psi_n = nd \sin\theta \cos\phi$. Consequently, the array factor of this N-element linear array becomes

$$AF = \sum_{n=0}^{N-1} e^{jn\alpha} e^{jnkd \sin\theta \cos\phi} = \sum_{n=0}^{N-1} e^{jn\beta} \qquad \text{with} \quad \beta = kd \sin\theta \cos\phi + \alpha \tag{1.102}$$

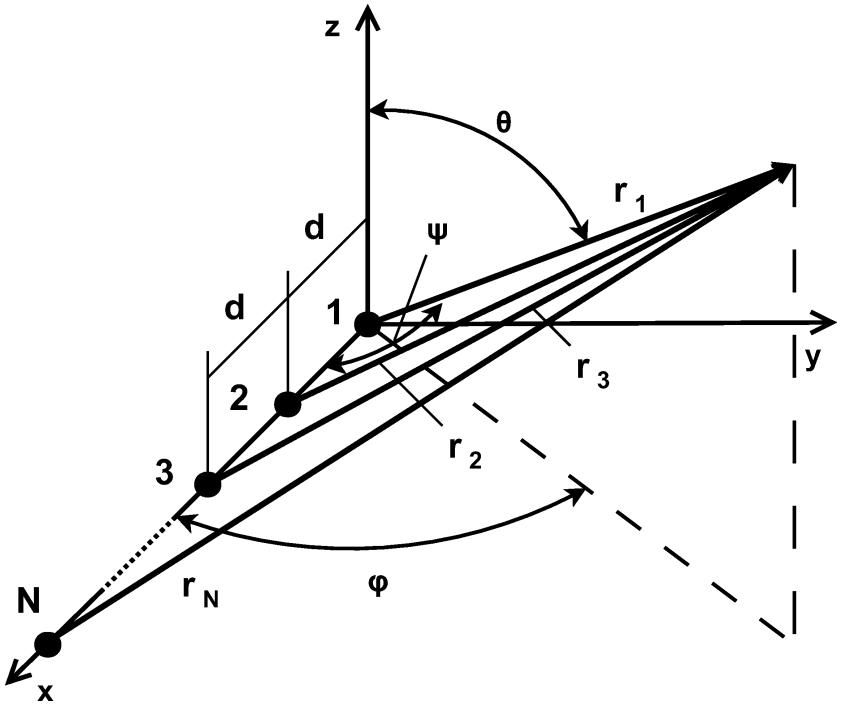

Figure 1.6 : *Geometry of a N-element linear array of isotropic sources for far field analysis*

As seen in the latter expression, the AF can be written in a more compact form with an all-embracing progressive phase β. It is immediately visible that this phase is a geometrical function, which depends on the distribution of the source elements and the excitations phases. Consequently, the AF for a linear array with equal elements, uniform spacing and uniform excitation amplitude can be generalized by means of a general defined phase function β as follows

$$AF = \sum_{n=0}^{N-1} e^{jn\beta} \qquad \text{with} \quad \beta = \beta(d, \alpha) \tag{1.103}$$

As aforementioned in the latter equation, β will change for the different array geometries, since it is a function of the spacing and of the progressive phase shift between the elements in the array. Furthermore, the latter generalized formula in, mathematically speaking, serial form can be simplified by transforming it into a closed form. Independant of the form of the function phase β, the *AF* can be regarded as a power series. These series can be developed in a closed form by means of the following mathematical relation

$$\sum_{n=0}^{N-1} q^n = \frac{q^N - 1}{q - 1} \qquad \text{for} \quad q \neq 1 \tag{1.104}$$

Applying the latter mathematical statement on the array factor, the series form AF is transformed in a closed form AF as in the following

$$AF = \sum_{n=0}^{N-1} e^{jn\beta} \tag{1.105}$$

$$= \frac{e^{jN\beta}-1}{e^{j\beta}-1} \tag{1.106}$$

$$= \frac{e^{j\frac{N}{2}\beta}}{e^{j\frac{1}{2}\beta}} \frac{e^{j\frac{N}{2}\beta}-e^{-j\frac{N}{2}\beta}}{e^{j\frac{1}{2}\beta}-e^{-j\frac{1}{2}\beta}} \tag{1.107}$$

$$= e^{j\frac{N-1}{2}\beta} \frac{\sin\left(\frac{N}{2}\beta\right)}{\sin\left(\frac{1}{2}\beta\right)} \tag{1.108}$$

If the physical centre of the linear array is chosen as reference point, the equation for AF for a uniform amplitude and spacing array of N elements has the following final form

$$AF = \frac{\sin\left(\frac{N}{2}\beta\right)}{\sin\left(\frac{1}{2}\beta\right)} \tag{1.109}$$

In order to normalize the AF so that the maximum value is equal unity, the latter expression can be divided by its maximum value that is the value N. A normalized array factor is obtained as follows

$$AF = \frac{\sin\left(\frac{N}{2}\beta\right)}{N\sin\left(\frac{1}{2}\beta\right)} \tag{1.110}$$

1.6.2 Array factor - two dimensional array

In order to obtain the two-dimensional array factor, the conditions for the linear array have been adopted. The total field of a planar array has to be also the sum of all element field contributions. Furthermore, considering the assumptions made already for the linear arrays, the total field must be a multiplication of the field of a single element multiplied by the respective array factor. Without invalidating the generalization of the following analysis, a two-dimensional array consisting of equal elementary dipoles positioned in lines and rows as depicted in figure 1.7 is observed.

The two-dimensional array can be seen as a series of linear arrays. Consequently, it is posible to use the acquired AF for linear arrays for the calculation of the field of a planar array. Deducing from equation (1.98), it can be stated that the total field of a $M \times N$ array is the multiplication of the element radiation $\vec{E}_0$ in the coordinates origin by the sum of the normalized excitations currents on the array elements. This yields in

$$\vec{E}_{array}(\vec{r}) = E_0 \cdot \sum_{m=0}^{M-1}\sum_{n=0}^{N-1} a_{mn} e^{jkr_{mn}\cos\psi_{mn}} \qquad \text{with} \quad E_0 = \kappa I_0 \vec{l} \cdot \frac{e^{-jkr}}{r} \tag{1.111}$$

Therein, I_0 is a normalization current, $\kappa = \frac{j\omega\mu}{4\pi}$ represents certain system constants, and k is the wavelength, respectively. Furthermore, $a_{mn} = \frac{I_{mn}}{I_0}$ is the complex amplitude of the excitation at element (m,n). Moreover, the complex phase term of the latter excitation depends of the

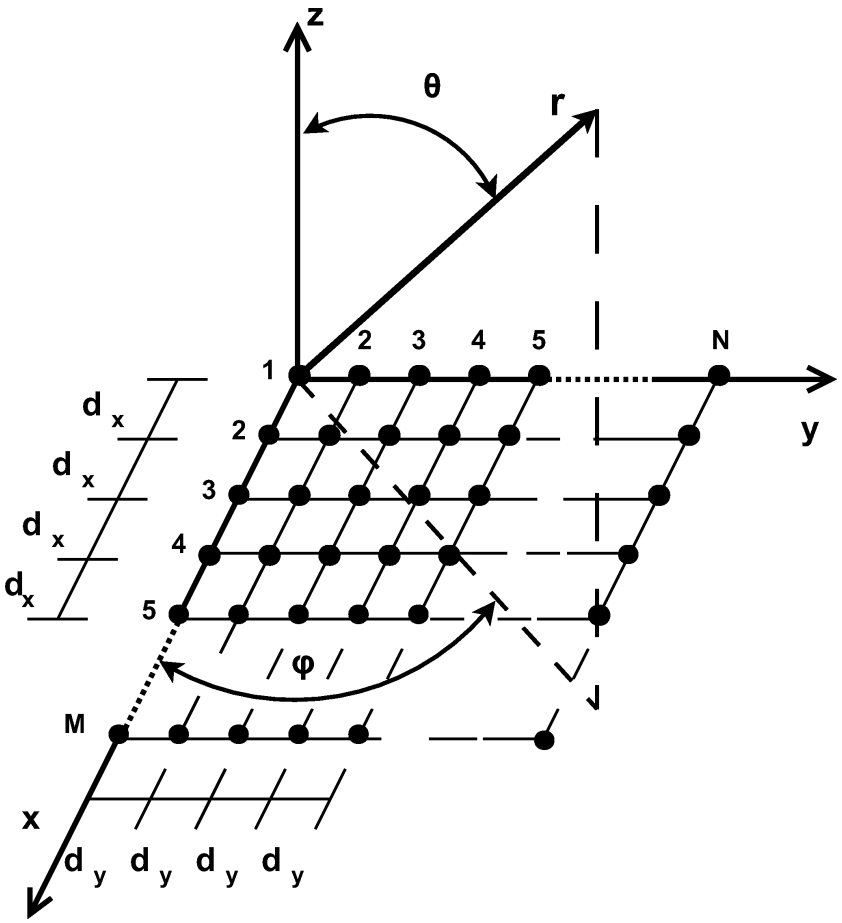

Figure 1.7 : *Geometry of a $M \times N$ array of isotropic sources for field analysis*

magnitude $|\vec{r}_{mn}| = r_{mn}$ of the position vector toward the element and the spatial angle ψ_{mn} enclosed by $\vec{r}_{mn}$ and the observing point vector $\vec{r}$. In addition, the phase function of the phase term can be approximated by $r_{mn}\cos\psi_{mn} \simeq r_m \cos\psi_m + r_n \cos\psi_n$. The vectors $\vec{r}_m$ and $\vec{r}_n$ are the positioning vectors along the rows and columns of the two-dimensional array. Furthermore, ψ_m and ψ_n are the spatial angles enclosed by the respective element position vector and the vector towards the observing point. In addition to the latter definition and assuming that for a rectangular array, a separable excitation amplitude distribution is chosen so that $a_{mn} = b_m \cdot c_n$, equation (1.111) can be rewritten as follows

$$\vec{E}_{array}(\vec{r}) = E_0 \cdot \sum_{m=0}^{M-1}\sum_{n=0}^{N-1} b_m c_n e^{jk(r_m\cos\psi_m + r_n\cos\psi_n)} = E_0 \cdot \sum_{m=0}^{M-1} b_m e^{jkr_m\cos\psi_m} \cdot \sum_{n=0}^{N-1} c_n e^{jkr_n\cos\psi_n} \tag{1.112}$$

Comparing each sum and the respective arguments to the sum in (1.98), similarities are found. If it is assumed that the excitations are at all elements the same then coefficient a_{mn} and hence b_m and c_n disappear. Moreover, if comparing the new sums, it is clear that these are the same sums as in the definition of the array factor in expression (1.100). This means, that the linear AF's for the columns AF_m and for the rows AF_n of the array are multiplied with the element radiated field E_0. Consequently, the total field for a two-dimensional array constituted

of equal elements excited with the same currents developes to

$$\vec{E}_{array}(\vec{r}) = E_0 \cdot \sum_{m=0}^{M-1} e^{jkr_m \cos\psi_m} \cdot \sum_{n=0}^{N-1} e^{jkr_n \cos\psi_n} = E_0 \cdot AF_m \cdot AF_n \tag{1.113}$$

As a consequence of the latter expression, the array factor of a two-dimensional array is the product of the linear AF's of its rows and columns elements

$$AF = AF_m \cdot AF_n \tag{1.114}$$

Moreover, the relationship between the field of an array element $\vec{E}_0$ and the far field of the entire array $\vec{E}_{array}$ remains for the linear and for two-dimensional array case the same, namely

$$\vec{E}_{array} = \vec{E}_0 \cdot AF \tag{1.115}$$

1.6.2.1 Planar array with uniform current amplitude and spacing

For the uniform amplitude and spacing case, the AF of a two-dimensional array can be simplified. Analogue to the linear uniform amplitude and spacing array, a progressive phase shift for the columns and arrows elements can be defined. The excitation coefficient $a_{mn} = \frac{I_{mn}}{I_0}$ with $I_{mn} = i_{mn} e^{\alpha_{mn}}$ becomes for the uniform current amplitude case $a_{mn} = e^{\alpha_{mn}}$. Assuming that this progressive phase can be decomposed in progressive parts for the row and column elements of the array like $\alpha_{mn} = \alpha_m + \alpha_n$, expression (1.116) becomes

$$\vec{E}_{array}(\vec{r}) = E_0 \cdot \sum_{m=0}^{M-1} e^{\alpha_m} e^{jkr_m \cos\psi_m} \cdot \sum_{n=0}^{N-1} e^{\alpha_n} e^{jkr_n \cos\psi_n} \tag{1.116}$$

Analogue to the linear case phase functions $\beta_m = \beta(d_m, \alpha_m)$ and $\beta_n = \beta(d_n, \alpha_n)$ are defined. As aforementioned for the linear array, these functions are dependent only on the geometry of the array. Consequently, the AF of the two-dimensional array becomes

$$AF = \sum_{m=0}^{M-1} e^{jm\beta_m} \cdot \sum_{n=0}^{N-1} e^{jn\beta_n} \tag{1.117}$$

Furthermore, using the mathematical definition in (1.104) and doing an analogue transformation as in (1.108) for the linear array case, the closed form for the AF of a planar array with uniform amplitude and spacing is

$$AF = \frac{\sin\left(\frac{M}{2}\beta_M\right)}{\sin\left(\frac{1}{2}\beta_M\right)} \cdot \frac{\sin\left(\frac{N}{2}\beta_N\right)}{\sin\left(\frac{1}{2}\beta_N\right)} \tag{1.118}$$

The latter expression includes in the array factor the influence of the progressive phase shifts α_m and α_m as well as of the spacing between row elements d_m and column elements d_n.

1.6.3 Radiation Pattern

The radiation pattern of the linear and of the two-dimensional array can be calculated by means of (1.87). For that, the relation between the total field of the array with the array factor and the field of a single element, expressed in (1.99) and (1.115) for the two-dimensional case, can be applied. Consequently, the following equation is gained

$$C_{array}(\theta,\phi) = \frac{|\vec{E}_{single}(\theta,\phi)\cdot AF|}{|\vec{E}_{single,max}(\theta,\phi)\cdot AF_{max}|} \tag{1.119}$$

$$= \frac{|\vec{E}_{single}(\theta,\phi)|}{|\vec{E}_{single,max}(\theta,\phi)|}\cdot\frac{|AF|}{|AF_{max}|} \tag{1.120}$$

The first fraction is equivalent to the single element radiation pattern, the second one is the radiation pattern of the array factor. Thus, knowing the radiation pattern of a single element C_{single} and the AF of an array, the radiation pattern of the array becomes

$$C_{array}(\theta,\phi) = C_{single}(\theta,\phi)\cdot C_{AF}(\theta,\phi) \tag{1.121}$$

In the latter expression C_{AF} is the radiation pattern of the array factor

1.6.4 Phased or Scanning Array

The radiated field of an array can have its maximum at a certain direction (θ_0,ϕ_0). Consequently, its pattern will have its maxima at the same point. An array, whose maximum radiated field and hence its main beam can be directed by controlling the phase of its element excitations, is called a phased or scanning array. As stated before, the far field of an array is built by the field of a single element and the AF of the array. Consequently, the main radiation lobe from the array element and therefore the major radiation of the array factor must be oriented in the direction (θ_0,ϕ_0). The latter is equivalent to a AF value of 1 for that direction. Regarding the general AF equation (1.103), the reader can deduce that for it the array factor's phase component $\beta(d,\theta,\phi)$ must dissapear in the direction (θ_0,ϕ_0). This is

$$\beta(d,\theta_0,\phi_0) = F(d,\theta_0,\phi_0)+\alpha = 0 \tag{1.122}$$

In the latter equation d stands for the element spacing and α for the progressive phase between the array element currents. The phase function $F(d,\theta,\phi)$ depends on the geometrical distribution of the element. The expression (1.122) concludes that in order to nullify the AF phase, the excitation phase α must compensate the phase function $F(d,\theta,\phi)$.

1.6.4.1 Broadside and end-fire array

According to [1], if the major lobe of the radiation pattern lies vertical to all elements and aligns with the normal vector of the array axis in the linear case or the surface's normal vector in the planar case, then this pattern is known as a *broadside* pattern. A pattern is called *end-fire* pattern when the main lobe is aligned with the array axis for the linear case or the surface expanding vectors for a two-dimensional case. These two pattern kinds can be seen as special cases in phased arrays. Furthermore, both are desirable pattern kinds in many applications and hence they are briefly presented in the following.

By means of the example of a linear array with uniform amplitude and spacing pictured in figure 1.6, the phase constellation for broad-side and end-fire pattern is derived. For it, the equation for the phase component in (1.103) is obtained. This is

$$\beta = kd\sin\theta\cos\phi + \alpha \tag{1.123}$$

At the latter expression k is the wavelength. Regarding the *broadside* case, the major lobe of the linear array pattern is vertical to the array's axis if $\phi_0 = 90°$. Introducing this value into the latter equation gives

$$\beta = kd\sin\theta|_{\theta_0=90°}\cos\phi|_{\phi_0=90°} + \alpha = 0 \qquad \rightarrow \qquad \alpha = 0 \tag{1.124}$$

This result means that for an phase shift of $0°$ for $\theta_0 = 90°$ and for $\phi_0 = 90°$ the pattern of the array becomes a broadside array pattern.

Taking the same array, the case of the *end-fire* pattern is regarded. This kind of pattern is achieved for $\theta_0 = 90°$ and $\phi_0 = 0°, 180°$. Introducing these two possible constellations in the phase equation (1.123) yields to

$$\beta = kd\sin\theta|_{\theta_0=90°}\cos\phi|_{\phi_0=0°,180°} + \alpha = 0 \qquad \rightarrow \qquad \alpha = 0, \pm kd \tag{1.125}$$

For an phase value of $\pm kd$, depending on the value θ, the main lobe is aligned to the arrays axis, hence an end-fire pattern is achieved.

1.6.5 Grating lobes

According to [15] and [14] the side lobes of arrays are also known as "grating lobes". They are defined as the lobes of an antenna array other than the major one, which originate when the element spacing is sufficiently large to permit in-phase addition of radiated fields in more than one direction. These lobes are in general not desired. Furthermore, from expression (1.122) and analysing equation (1.109) it can be deduced that for multiples of 2π the AF and therefore the pattern has additional maxima, namely grating lobes. This happens in any direction (θ, ϕ) for

$$\beta(d,\theta,\phi) = F(d,\theta,\phi) + \alpha = \pm 2p\pi \qquad \text{with} \quad p = 1,2,3,\ldots \tag{1.126}$$

To ensure that there are no gratings lobes the phase function $F(d,\theta,\phi)$ and the element excitation phases must be defined or steered so that the AF phase does not reach the 2π multiples.

The most common mean against grating lobes is to chose a proper value for the array spacing d in order to minimize or even avoid them. Therefore, the *end-fire* and *broadside* pattern cases for the linear array of figure 1.6 are analysed. According to (1.125) an end-fire pattern is obtained if $\alpha = \pm kd$. Consequently, the major lobes condition according expression (1.126) in this case is

$$kd\sin\theta|_{\theta_0=90°}\cos\phi|_{\phi_0=0°,180°} = \pm 2p\pi \qquad \rightarrow \qquad d = \tfrac{2p\pi}{k} \tag{1.127}$$

with $p = 1,2,3,\ldots$. Thus, in order to avoid these extreme angles, the lobe separation must be $d < \frac{2\pi}{k}$ that due to $k = \frac{2\pi}{\lambda}$ is equivalent to $d < \lambda$. For the broad-side case the statement in (1.124) results in the following relation for grating lobes

$$\beta = kd\sin\theta|_{\theta_0=90°}\cos\phi + \alpha = \pm 2p\pi \tag{1.128}$$

with $p = 1,2,3,\ldots$. According to the latter equation, the first side lobes appears for

$d = \frac{2\pi}{k} = \lambda$. Consequently, if the spacing is smaller than the wavelength, it is possible to avoid grating lobes. Moreover, Balanis suggests in [1] that under all these conditions and the avoidance of having two main lobes for the end-fire case the values for the spacing d must be chosen according to

$$d < \frac{\lambda}{2} \tag{1.129}$$

1.6.6 Directivity and Gain

In order to obtain the directivity and the gain of an array, the afore given equations (1.93) and (1.94) can be used. Due to the fact that the directivity and gain values of the main beam of an array are of high relevance, proper expressions for calculating them can be derived. In particular, for the uniform spacing and uniformly fed array case, the relation between the pattern and the array factor can be applied in order to reduce directivity or gain computation effort.

Consequently, the directivity and the gain of an array for an observing point (r, θ, ϕ) is calculated by introducing the respective far field function into equation (1.93). Since the field can be expressed by means of the AF the following formula is obtained

$$D_{array}(\theta_0, \phi_0) = \frac{4\pi[AF(\theta_0, \phi_0)][AF(\theta_0, \phi_0)]^*}{\int_0^{2\pi}\int_0^{\pi}[AF(\theta_0, \phi_0)][AF(\theta_0, \phi_0)]^* \sin\theta d\theta d\phi} \tag{1.130}$$

In the latter expression $(*)$ stands for the complex conjugate. For large planar arrays, with $(M \times N)$ elements that behave nearly broadside-like, the latter equation reduces to the following expression

$$D_{array}(\theta_0, \phi_0) = \pi \cos\theta_0 D_m D_n \tag{1.131}$$

Therein D_x stands for the directivity of a broadside linear array composed by M elements in one direction, D_y for the directivity of a broadside linear array composed by N elements in the other direction.

Furthermore, there exist a formula for the directivity maximum of an array. Assuming an array of identical elements with a major radiation in direction (θ_0, ϕ_0), then the maximum value of its AF in the latter direction is equivalent to the number of elements building the array. Consequently, in the case of an array with N_{elem} elements, the directivity and the gain are N_{elem} times greater in comparison to the directivity or gain of a single element in direction (θ_0, ϕ_0). This is

$$D_{array}(\theta_0, \phi_0) = N_{elem} \cdot D_{single}(\theta_0, \phi_0) \tag{1.132}$$

The product in this formula simplifies to a sum, if the logarithm is applied. The sought directivity is transformed in deciBell dB via the following equation [15]

$$D_{array,dB}(\theta_0, \phi_0) = 10\log(N_{elem} \cdot D_{single}(\theta_0, \phi_0)) = 10\log D_{single}(\theta_0, \phi_0) + 10\log N_{elem} \tag{1.133}$$

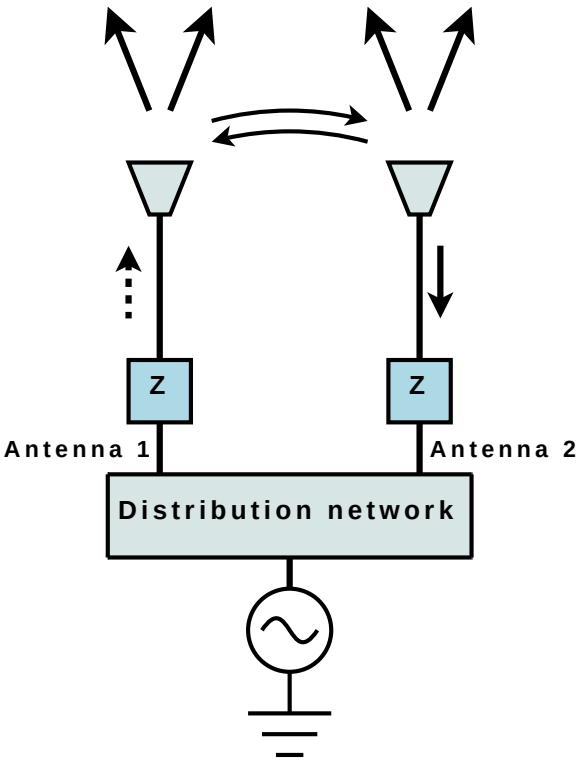

Figure 1.8 : *Mutual coupling scenario for the transmitting case*

1.6.7 Mutual coupling

The assumption that the array elements are independent from each other, which was made for the array analysis is not valid in practice. Hence the influence between the elements of the array, which is known as mutual compling, has to be taken into account. The mutual coupling effect is regarded in a general way in [9], [6] and [1]. References [20] and [21] show the mutual coupling consideration for a planar microstrip patch antenna array and for its conformal counterpart.

The interaction between neighbouring array elements is shown in figure 1.8. In the picture two neighbouring antennas during the emitting process are shown. The first antenna emits electromagnetic radiation that propagates into space. A certain fraction of the radiation arrives to the second antenna perturbating its emission by inducing currents in it. In a similar way this antenna is "hit" also by along the surface propagating currents, which are caused by surface leaking waves. Reflected currents generated by mismatch between the distribution network and the antennas reach also the neighbouring elements.

According to [9], in order to model the coupling between neighbouring array elements, the different coupling currents can be represented by one equivalent current. This mutual coupling current is then the summation of all coupling current contributions. The following equation displays the excitation of the N-th array element. The first addend is equivalent to the ideal current value composed of its magnitude term I_n and progressive phase term $e^{j\alpha_n}$, if coupling is neglected. The sum term components are the representation of the coupling currents i_{mn} from the n-th array element towards the m-th one that are two neighbouring array elements.

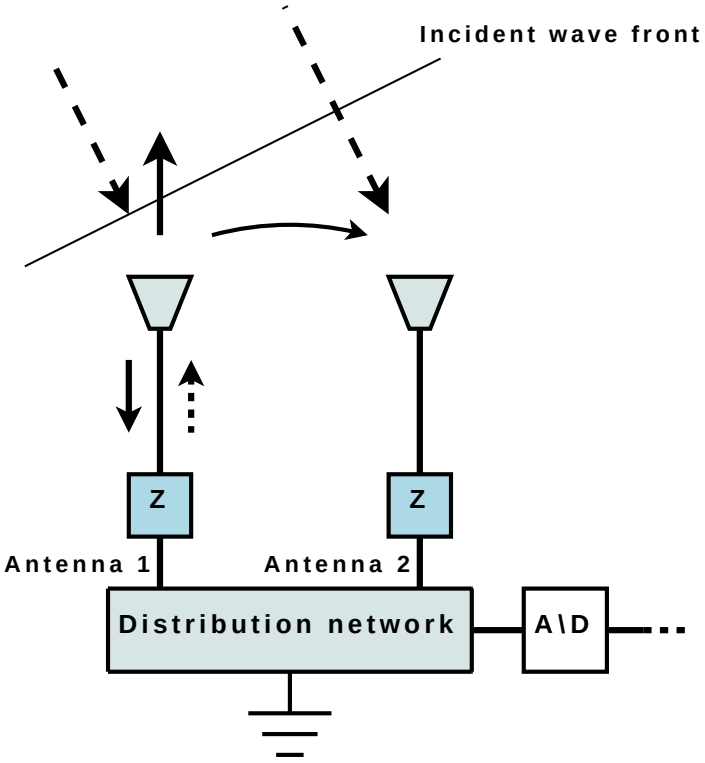

Figure 1.9 : *Mutual coupling scenario for the receiving case*

$$i_n = I_n e^{j\alpha_n} + \sum_m i_{mn} \tag{1.134}$$

Figure 1.9 visualizes the general coupling scenario in the reception case. Due to the fact that an antenna behaves similarly while transmitting and receiving, the mutual coupling current is for the reception process reciprocal.

Consequently, the excitation current for the whole array can be written like in the following equation

$$i_{total} = i_{design} + i_{coupling} \tag{1.135}$$

Therein, the total excitation current for the array is the design current i_{design}, which is composed by the independent feeding currents for each array element, in addition to the excitation current due to element's mutual coupling $i_{coupling}$. It can be deduced from the latter result that the actual current distribution at the elements depends on the mutual influence between the elements. Consequently, the positioning of the array elements at certain distances has an influence on the coupling effects. In other words the spacing value of the linear array, or both spacing values in the case of a planar array, can be chosen so that the coupling effects can be minimized.

Furthermore, Mailloux [6] and Balanis [1] suggest to model coupling by defining a mutual coupling matrix. For this simple approximation the current distribution of all array elements are assumed to be the same. In addition to that, three kind of impedances are defined. The first is the antenna impedance, which is the impedance of the single isolated element. The

second impedance, the passive driving impedance, is the impedance of one single array element regarded when the other elements are passively terminated in their normal generator impedance. The third one, the active driving impedance also known as the driving impedance, is the impedance of a single element when all other array elements are excited.

The mutual coupling relationships can be expressed by an impedance matrix. The latter matrix for a linear array can be calculated using the relation between the current excitations I_n and the terminal voltages V_m given in the following

$$[V_m] = [Z][I_n] \tag{1.136}$$

Consequently, the elements Z_{mn} are yielded with

$$Z_{mn} = \frac{V_m}{I_n} \tag{1.137}$$

The latter elements represent the passive driving impedance matrix. Nevertheless, in the usual array operation case a great number of elements are excited at the same time. Consequently, the coupling between the array elements behaves in another way. Therefore, the mutual coupling effect in this case are expressed with the driving impedance matrix.

Mailloux [6] states that the mutual coupling coefficients Z_{mn} in the driving impedance matrix have the form of integrals over the free-space scalar Green's function kernel . Hence they can be obtained by evaluating these integrals, which can be established for the different array cases like in [21] for a conformal microstrip patch array. Such integral evaluation is often rigorous, thus other possibilities for gaining these coefficients are proposed, like in [20], wherein the solutions for the mutual coupling impedance elements are approximated by series expansions. The latter reference considers the case of a microstrip patch array too.

In addition to that, Balanis [1] gives the formula for calculating the driving impedance Z_{Dmn} for the two dimensional array case assuming single-mode operation, uniform excitation, identical array elements and equidistant spacing values.

$$Z_{Dmn} = \frac{V_{mn}}{I_{mn}} \tag{1.138}$$

with

$$V_{mn} = \sum_p \sum_q Z_{mn,pq} I_{pq} \tag{1.139}$$

$Z_{mn,pq}$ are the mutual impedances defined by the terminal voltages V_{mn} and the currents I_{pq} in the passive impedance case.

1.6.8 Feed network

In order to feed signals with different amplitudes and phases to the different elements of an array a feed network is often required. There are two groups of feed networks for antenna arrays, these are series feeds and parallel feeds. Figure 1.10 shows the first type of feed network for an array composed of proximity feed microstrip patch antennas. In the series feed network

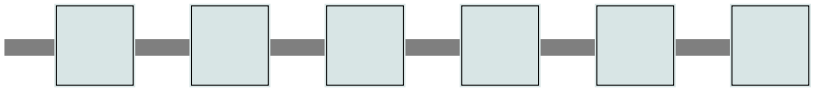

Figure 1.10 : *Series feed network*

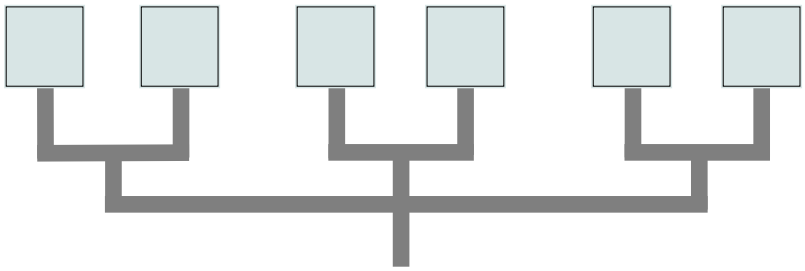

Figure 1.11 : *Parallel feed network*

the array elements are fed by a line: each element is fed in series of another element. This line can be terminated into a resistive load allowing only a forward waves to travel or causing resonances. This kind of network is simple to implement and provides a compact design. The series feed is limited to linear or planar arrays with a fixed beam or frequency-scanning beam.

In the parallel feed network, which is mainly known as corporate-feed network, each array element is fed in parallel with the other elements. Figure 1.11 depicts the possible parallel feed network for a group of proximity feed microstrip patch antennas. For the division of the input signal into several channels, several power dividers are required. Besides the disadvantages of the need of more space for the lines and dividers, corporate feed network allows the control of the feed of each array element. This enables the possibilities of realizing phase-scanning-beam, multi-beam and shaped-beam arrays.

The corporate-feed network allows in the case of aperture coupled patch arrays the sequential feeding technique for dual-polarisation. Here the mutual coupling effects between the patch elements due to the proximity of their apertures are lowered. This is done by placing the elements in groups of two patches with their feeds rotated such that the coupling is very small. Furthermore, a tapered feeding is possible with a parallel feed network. In the latter the different array elements with different amplitudes or "tapering" the radiation pattern of the array can be modified, eventually side lobes are suppressed.

[1], [14] and [10] present examples and further information about feed networks.

Chapter 2

Numerical Techniques and Analysis methods

This chapter introduces to existing numerical techniques used to model and analyse electromagnetic problems. These techniques are used nowadays to model and to simulate behaviour of antennas. Considering the framework of the present thesis work the modeling of conformal antennas will be regarded. Furthermore, existing approachs for analysing antenna arrays of planar and conformal kind will be presented. Therefore, some of the proposed methods of relevance for the present thesis work will be outlined.

2.1 Numerical Techniques in Electromagnetics

Through the years different numerical techniques thanks to extended and detailed research works have been developed. All these methods can be categorized into four groups: surface region methods, methods applied to volumes, asymptotical methods, and hybrid methods that combine mainly two methods each coming from the former three groups.

The first approach group includes the use of analytical functions, like the mixed-potential integral equation or the Green's function, and their transformations as well as approximations limited to the active region. The resulting solution procedure is done in frequency or space domain. Furthermore, the electromagnetic problems are solved using efficient mathematical ansatz and transformations, for instance the Method of Moments. The techniques of the second group discretize the volumic medium around the active zone with the goal to solve in time or in frequency domain by applying discretized Maxwell Equations or from it deriving wave equation. The Finite Difference Time Domain Method, the Finite Integral Technique and the Finite Element Method are part of this group.

The asymptotical methods, which embraces the Uniform Theory of Diffraction, are based on approximations of the Maxwell's Equations. Therefore, it is applied only for very high frequencies and it regards the active region as a pure radiation source (it does not take in account the form of the active region). In general, the techniques of this group are not used alone for antenna applications but combined with other methods. Consequently, the hybrid methods are in general combinations of the third group with the first or second group techniques, e.g Finite Element Method with Uniform Theory of Difraction. In addition, there exist other hybrid tech-

niques resulting from combinations between the approachs, like the Finite Element Boundary Integral Method (FE-BI). This hybrid derives from a combination of the Finite Element Method with the Method of Moment.

The approachs Method of Moments, Finite Difference Time Domain Method, Finite Integral Technique and Finite Element Method are frequently used as solvers in electromagnetical simulators. Although all these techniques are of relevance only the first three are regarded closer. The latter one is introduced shortly with the Uniform Theory of Diffraction.

2.1.1 Method of Moments (MoM)

The Method of Moments (MoM) is, more or less, a general concept for any approach (analytical or numercal) to solve a given problem by transforming its system transfer function to a matrix function in order to solve the latter with known techniques. Harrington was the first to use MoM in electromagnetics and his work [4] is a fundamental reference. Therefore, MoM is used frequently to model and to solve electromagnetical problems [22], [23], [41] and [47]. The latter two references will be presented in summerized form later in this chapter.

2.1.1.1 MoM Principle

The basic idea of Method of Moments is to reduce a functional equation to a matrix equation, which is solved by inverting the matricial operator. The found solution, depending on how the sought solution function was defined, will approximate or even be equivalent to the analytical solution of the functional equation. For the matrix inversion several known techniques are used.

The functional equation is usually of inhomogeneous kind, which has following form

$$L(f) = g \tag{2.1}$$

Herein L stands a linear operator, f is the unknown response or field that has to be determined, and g is the excitation or source that is described by a known function. The linearity of the operator allows to find a numerical solution with the following technique.

In order to obtain the unknown response function f, it is defined as a linear combination of a finite number of terms. This is represented by a series of chosen functions f_n, so-called *expansion functions* or *basis functions*, and by the constants c_n attributed to these functions, giving the unknown response function the following form

$$f = \sum_{n}^{N} c_n f_n \tag{2.2}$$

Therefore, the domain of the linear operator L and its range must be taken into account. The domain of the operator is restraint by the functions f on which it operates, the respective range is limited to the functions g. The unknown function is for $n \to \infty$ normally an exact solution. For a finite n, an approximation to the exact solution is obtained.

The new definition in (2.2) is introduced to equation (2.84). Since the operator is linear the latter system can be written as follows

$$\sum_{n}^{N} c_n L(f_n) = g \tag{2.3}$$

A new equation with the new task of calculating the c_n constants is obtained. In order to find the N coefficient values, N linearly independent equations are needed. A possible approach to solve the new equation is to evaluate for the expression (2.3) applying certain boundary contitions at N different points. This technique is known as *point-matching* and hence it converts the new equation to a linear matrix sytem. The latter is solved by inverting the obtained matrix.

Another way to find the solution function by means of the respective coefficients c_n and under the assumption that the inner product between f and g has been defined the inner product of all components of the equation in (2.3) with a series of *weighting functions* w_m is built. These testing functions are supposed to be in the range of the L. The equation changes to

$$\sum_{n}^{N} c_n \langle w_m, L f_n \rangle = \langle w_m, g \rangle \qquad \text{for} \quad m = 1,2,3,\ldots,M \tag{2.4}$$

The latter equation system can be paraphrased in the following matrix form

$$[l_{mn}][c_n] = [g_m] \tag{2.5}$$

wherein the matrix $[l_{mn}]$ is defined as

$$[l_{mn}] = \begin{bmatrix} \langle w_1, L f_1 \rangle & \langle w_1, L f_2 \rangle & \ldots & \langle w_1, L f_N \rangle \\ \langle w_2, L f_1 \rangle & \langle w_2, L f_2 \rangle & \ldots & \vdots \\ \vdots & \vdots & \ddots & \vdots \\ \langle w_m, L f_1 \rangle & \ldots & \ldots & \langle w_M, L f_N \rangle \end{bmatrix} \tag{2.6}$$

The coefficients vector $[c_n]$ in expression (2.5) has the following form

$$[c_n] = \begin{bmatrix} c_1 \\ c_2 \\ \vdots \\ c_N \end{bmatrix} \tag{2.7}$$

Similar form has the excitation vector $[g_m]$ in (2.5)

$$[g_m] = \begin{bmatrix} \langle w_1, g \rangle \\ \langle w_2, g \rangle \\ \vdots \\ \langle w_M, g \rangle \end{bmatrix} \tag{2.8}$$

Similar then in the *point-matching* technique, the new matrix equation can be solved by building the inverse of the matrix $[l_{mn}]$. This is only possible if the matrix is non-singular.In such a case the inverse matrix $[l_{mn}]^{-1}$ can be built and the coefficients vector $[c_n]$ can be calculated as follows

$$[c_n] = [l_{mn}]^{-1}[g_m] \tag{2.9}$$

Introducing the obtained coefficients in (2.2) the solution of the equation is found. Summing up the solution of the linear equation (2.3) is

$$f = [\tilde{f}_n][c_n] = [\tilde{f}_n][l_{mn}]^{-1}[g_m] \tag{2.10}$$

Herein the sum in expression (2.2) is described by the scalar product between the coefficients vector $[c_n]$ and the functions vector $[\tilde{f}_n]$. The latter is defined as

$$[\tilde{f}_n] = [f_1 \quad f_2 \quad \dots \quad f_N] \tag{2.11}$$

Depending of the choices of weighting functions w_m and basic functions f_n the solution may approximate or hit the exact solution. While chosing the basis functions, they should be linearly independent and they should ensure a reasonalbly well approximation of the response function f. For choice of the weighting functions the linear independency is necessary too. Furthermore, the desired advantage of computational simplicity, defined by the ease of evaluation of the matrix elements and the matrix inversion computational effort, affects the choice in both cases. The special case where the basic and the weighting functions are the same is known as *Galerkin's method*.

2.1.1.2 Appropriate basis functions

From the theoretically possible options for basis functions only certain ones are in practice used. They can be divided in two classes, the "subdomain functions" and the "entire domain functions"

The subdomain functions are structured in non-overlapping segments. These are not necessary to be collinear or of equal length, since each one is defined in conjunction with the limits of its neighbouring segment. The most common subdomain basis functions are the "pulse function" (or piecewise constant function) that is defined as

$$p(x) = \begin{cases} 1 & |x| < \frac{1}{2(N+1)} \\ 0 & |x| > \frac{1}{2(N+1)} \end{cases} \tag{2.12}$$

and the "triangle function" (or piecewise linear function)

$$t(x) = \begin{cases} 1 - |x|(N+1) & |x| < \frac{1}{N+1} \\ 0 & |x| > \frac{1}{N+1} \end{cases} \tag{2.13}$$

The latter functions are defined for a subdomain centered to one of the N equispaced points on the interval $0 \leq x \leq 1$. Other useful but more complicated subdomain basis functions are the "piecewise sinusoid" and the "truncated cosine" functions. The subdomain functions are often used as basis functions due to the fact that a priori knowledge about the nature of the sought response functions is not needed.

The entire domain functions are defined over the entire intervall. Consequently, segmentation is not necessary. They can be generated using Tschebyschev, Legendre and Hermite polynomials, or other convinient functions like cosine and sine functions. The representation of the unknown function by the latter functions is similar to the Fourier series expansion of arbitrary functions.

The entire domain functions are very useful in cases where the sought response function is supposed to have a similar behaviour to a known pattern. In these situations fewer terms or expansion functions for the unknown response are needed than in the case of subdomain functions. In cases of arbitrary or complicated unknown functions the entire domain functions are less apropiate.

2.1.1.3 Application to antennas

According to [4] and [22] the solution to an antenna problem is obtained by using *MoM* on an appropriate superposition integral equation. Due to calculation simplicity, the conventional retarded potential integral formulas are used herefor. These are

$$\vec{E}^s = -j\omega\vec{A} - \nabla\Phi_e \tag{2.14}$$

$$\vec{A} = \mu \iiint_C \vec{J}\frac{e^{-jkR}}{4\pi R}d\vec{v}' \tag{2.15}$$

$$\Phi_e = -\frac{1}{j\omega\mu\varepsilon}\nabla\cdot\vec{A} \tag{2.16}$$

$$\rho = -\frac{1}{j\omega}\nabla\cdot\vec{J} \tag{2.17}$$

These equations are derived in chapter 1 (see (1.18), (1.38) and (1.54) with $R = |\vec{r} - \vec{r'}|$) from the generalized harmonic *Maxwell Equations*. Besides, following boundary condition has to be fulfilled on the surface *S*, which separates the antenna and the propagating medium

$$\vec{n}\times(\vec{E}^s + \vec{E}^i) = 0 \qquad \leftrightarrow \qquad \vec{n}\times\vec{E}^s = -\vec{n}\times\vec{E}^i \tag{2.18}$$

$\vec{E}^i$ is the impressed or excitation field on the antenna, $\vec{E}^s$ is the respective scattered or radiated field from the antenna. The scattered field is produced by the currents $\vec{J}$ and the electric charge ρ.

The resulting operator equations contain derivatives as well as integrals. In order to ease the computation, the antenna is divided in small antenna segments that are connected together. Each end point of the segments define a pair of terminals, consequently a network is created.

The impedance matrix of this network is calculated by applying a current source to each port in turn and calculating the circuit voltages at each port. Once the impedance matrix is built the admittance matrix can be calculated. The latter is the inverse of the impedance matrix. Moreover, for any voltage excitation the port currents can be computed by means of a multiplication with the admittance matrix.

2.1.1.3.1 Example: Wire antenna An application example of MoM in electromagnetics is the radiation analysis of a wire antenna. In this case, which is depicted in figure 2.1, the segments of the wire antenna are small filaments along the wire axis. Each *n*-th segment has an starting point called n^+, a middle point referenced as *n* and a terminal point called n^-. The currents, which are supposed to flow only on the direction of the wire axis, and the charges are treated as constant over each segment. In addition, the integrals are approximated by the sums

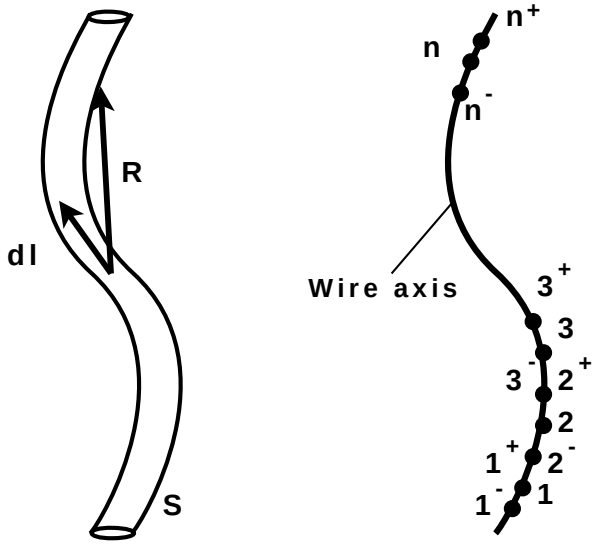

Figure 2.1 : *Discretization of a wire antenna*

for all segments. Derivatives are approximated by finite differences over the same intervals as for the integration. Following approximations are used

$$-\vec{E}_m^i \approx -j\omega\vec{A}_m - \frac{\Phi_{m^-} - \Phi_{m^+}}{\Delta l_m}\frac{d\vec{l}}{dl} \tag{2.19}$$

$$\vec{A}_m \approx \mu\sum_n^N I_n \int_{\Delta l_n} \frac{e^{-jkR}}{4\pi R} d\vec{l} \tag{2.20}$$

$$\Phi_{m^+} \approx \frac{1}{\varepsilon}\sum_n^N \sigma_{n^+} \int_{\Delta l_{n^+}} \frac{e^{-jkR}}{4\pi R} dl \tag{2.21}$$

$$\sigma_{n^+} \approx \frac{-1}{j\omega}\frac{I_{n+1} - I_n}{\Delta l_{n^+}} \tag{2.22}$$

Herein Δl_n is the n-th length increment between point n^+ and n^-. Δl_{n^+} and Δl_{n^-} represent the increment shift of half a segment along or against the length direction.

Defining a voltage vector, which describes the voltage values in every wire element, the impedance matrix can be found. Therefore, the voltage vector is approximated by the multiplication of the electric intensity E_n components at the wire elements with the length Δl_n of the respective segment.

$$[V] = \begin{bmatrix} E_1^i \cdot \Delta l_1 \\ E_2^i \cdot \Delta l_2 \\ \vdots \\ E_M^i \cdot \Delta l_M \end{bmatrix} \tag{2.23}$$

The necessary impedance components of matrix $[Z]$ are obtained by introducing the equations (2.20) to (2.1.1.3.1) in (2.1.1.3.1). An expression dependant on the currents is achieved,

which can be reshape in order to separate the current vector components and hence get the impedance matrix following the relation

$$[V] = [Z][I] \qquad \text{with} \qquad [I] = \begin{bmatrix} I_1 \\ I_2 \\ \vdots \\ I_N \end{bmatrix} \tag{2.24}$$

The acquired matrix equation can be solved by inverting the $[Z]$ matrix like in the following

$$[I] = [Y][V] \qquad \text{with} \quad [Y] = [Z]^{-1} \tag{2.25}$$

After acquiring the impedance matrix the current vector for any voltage excitation, which can be on one point or several points of the wire, can be obtained.

In order to calculate the far radiation field of the wire antenna, the electric dipole moment $I_n\vec{\Delta}l_n$ of each segment is computed applying the computed current vector $[I]$. In addition to that, they are introduced in the following vector potential equation for the far field case

$$\vec{A} = \frac{\mu e^{-jkr_0}}{4\pi r_0} \sum_{n}^{N} I_n \Delta\vec{l}_n e^{-jkr_n cos\xi_n} \tag{2.26}$$

In the latter expression r_0 stands for the magnitude of the vector to the origin to the observing point in the far field region, r_n for the magnitude for the radius vector to the source point. The electric far field is calculated by means of the following relation. With the help of the acquired vector potential, which is given, the electric far field is calculated.

$$\vec{E} \simeq -j\omega\vec{A} \qquad \rightarrow \qquad \begin{array}{l} E_r \simeq 0 \\ E_\theta \simeq -j\omega A_\theta \\ E_\phi \simeq -j\omega A_\phi \end{array} \tag{2.27}$$

In [4] another possibility for computing the impedance matrix departing also from the equations to is suggested.

2.1.2 Finite Difference Time Domain (FDTD)

The Finite Difference Time Domain method (FDTD) was introduced by Yee [24] and it has become since then a very popular technique for solving electromagnetic tasks. Furthermore, it has been generalized for different volume structures [25] and it has been used for antenna analysis [26], [27] and [54]. As its name indicates, the FDTD method is a temporal domain approach and it finds the solution to an electromagnetic problem by solving the differential form of the *Maxwell Equations*. Therefore, the regarded region is discretized resulting in a rectangular volumic grid composed of cubic cells. In each cell the fields are computed by means of the *Yee algorithm* with a second order accuracy in time and space. The following introduction to FDTD has [5] and [25] as main references .

2.1.2.1 FDTD Principle

Assuming that the analysed medium is homogene, isotropic, non-dispersive and without sources according to [5] the *Maxwell Equations* in differential form can be stated as follows

$$\nabla \times \vec{E} = -\mu \frac{\partial \vec{H}}{\partial t} \tag{2.28}$$

$$\nabla \times \vec{H} = \varepsilon \frac{\partial \vec{E}}{\partial t} + \sigma \vec{E} \tag{2.29}$$

σ is the electric conductivity of the media, ε and μ the permittivity and the permeability, respectively. In order to solve the latter equations, initial conditions as well as boundary conditions on the regarded object are needed. In general, the initial conditions for the FDTD method are zero, this means

$$\nabla \cdot \vec{B} = 0 \tag{2.30}$$

$$\nabla \cdot \vec{D} = 0 \tag{2.31}$$

In the exception cases the initial conditions must be stated in a self-consistent manner. This means that the charge must be taken into account in the second statement of the latter equation set. For the boundary conditions the relationships between the field and the media surfaces have to be taken into account.

The vectorial equations in (2.28) and (2.29) can be written as six scalar equations. These have the following form if the Cartesian coordinates are used

$$\frac{\partial H_x}{\partial t} = \frac{1}{\mu}\left(\frac{\partial E_y}{\partial z} - \frac{\partial E_z}{\partial y}\right) \tag{2.32}$$

$$\frac{\partial H_y}{\partial t} = \frac{1}{\mu}\left(\frac{\partial E_z}{\partial x} - \frac{\partial E_x}{\partial z}\right) \tag{2.33}$$

$$\frac{\partial H_z}{\partial t} = \frac{1}{\mu}\left(\frac{\partial E_x}{\partial y} - \frac{\partial E_y}{\partial x}\right) \tag{2.34}$$

$$\frac{\partial E_x}{\partial t} = \frac{1}{\varepsilon}\left(\frac{\partial H_z}{\partial y} - \frac{\partial H_y}{\partial z} - \sigma E_x\right) \tag{2.35}$$

$$\frac{\partial E_y}{\partial t} = \frac{1}{\varepsilon}\left(\frac{\partial H_x}{\partial z} - \frac{\partial H_z}{\partial x} - \sigma E_y\right) \tag{2.36}$$

$$\frac{\partial E_z}{\partial t} = \frac{1}{\varepsilon}\left(\frac{\partial H_y}{\partial x} - \frac{\partial H_x}{\partial y} - \sigma E_z\right) \tag{2.37}$$

The derivatives in equations (2.32)-(2.37) are approximated using the *Yee algorithm*. This algorithm is based on the *Leapfrog algorithm*, which is shortly presented in appendix A. According to *Yee* the partial derivative of a field function $F(x,t)$ is centered with respect to the two field values on the cell fronts. The space derivative valid for each space component and the time derivative become then

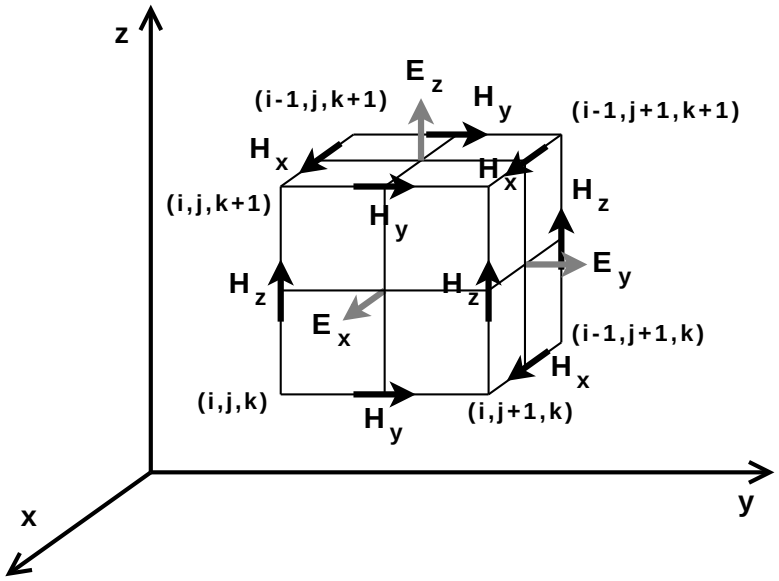

Figure 2.2 : *Position of the electric and magnetic field vector components about* Yee*'s cubic unit cell*

$$\frac{\partial}{\partial x}F(x+\tfrac{\Delta x}{2}) = \frac{F(x+\Delta x)-F(x)}{\Delta x} \tag{2.38}$$

$$\frac{\partial}{\partial t}F(t+\tfrac{\Delta t}{2}) = \frac{F(t+\Delta t)-F(t)}{\Delta t} \tag{2.39}$$

The latter definition is obtained by means of the definition of the derivative for a finite distance. The obtained equation approximates the derivation with a second order accuracy. Introducing this definition in the *Taylor series expansion* of the function F and neglecting the derivatives higher than the second order, following relationship is acquired

$$F(x) = \frac{F(x+\frac{\Delta x}{2})-F(x-\frac{\Delta x}{2})}{2}+o(\Delta x) \tag{2.40}$$

$$F(t) = \frac{F(t+\frac{\Delta t}{2})-F(t-\frac{\Delta t}{2})}{2}+o(\Delta t) \tag{2.41}$$

The latter equation show that the values of the function *F(x,t)* are centered. It can be shown that in both cases the accuracy of the values and the partial derivatives of the function are of second order

With the equations in (2.39) and (2.41) the equation set (2.32)-(2.37) can be approximated in the time domain. Therefore, the medium is discretized in a volumic grid composed of cells. In order to describe the cubic cells *Yee* defines its location with the indices (i, j, k) as depicted in figure 2.2 . These are related with the (x, y, z) coordinates as follows

$$x = i\Delta x \qquad y = j\Delta y \qquad z = k\Delta z \tag{2.42}$$

i,j and *k* are the coodinate indices for the respective coordinate directions. Similar goes for the time *t* with *n* as the time index

$$t = n\Delta t \tag{2.43}$$

Therefore, the time and space dependent function $F(x,t)$ takes the following form

$$F^n(i,j,k) = F(n\Delta t, i\Delta x, j\Delta y, k\Delta z) \tag{2.44}$$

Using the new indice nomenclature the statements in (2.39) can be generalized as follows

$$\frac{\partial F^n(i,j,k)}{\partial x} = \frac{F^n(i+\frac{1}{2},j,k) - F^n(i-\frac{1}{2},j,k)}{\Delta x} \tag{2.45}$$

$$\frac{\partial F^n(i,j,k)}{\partial t} = \frac{F^{n+\frac{1}{2}}(i,j,k) - F^{n-\frac{1}{2}}(i,j,k)}{\Delta t} \tag{2.46}$$

Yee's discretization and approximations are applied at the scalar Maxwell Equations given in expressions (2.32) - (2.37). Doing so, each field component is explicit given as a function of the past values. Reshaping the resulting equations, all components of the current fields can be calculated. In the following, the mathematical transformation for the x-component of the current magnetic field intensity in expression (2.32) is shown

$$\begin{aligned}\frac{H_x^{n+\frac{1}{2}}(i,j+\frac{1}{2},k+\frac{1}{2}) - H_x^{n-\frac{1}{2}}(i,j+\frac{1}{2},k+\frac{1}{2})}{\Delta t} &= \frac{1}{\mu(i,j,k)}\left[\frac{E_y^n(i,j+\frac{1}{2},k+1) - E_y^n(i,j+\frac{1}{2},k)}{\Delta z} - \right. \\ &\left. - \frac{E_z^n(i,j+1,k+\frac{1}{2}) - E_z^n(i,j,k+\frac{1}{2})}{\Delta y}\right] \end{aligned} \tag{2.47}$$

$$\begin{aligned} H_x^{n+\frac{1}{2}}(i,j+\frac{1}{2},k+\frac{1}{2}) &= H_x^{n-\frac{1}{2}}(i,j+\frac{1}{2},k+\frac{1}{2}) + \frac{\Delta t}{\Delta z}[E_y^n(i,j+\frac{1}{2},k+1) - \\ &- E_y^n(i,j+\frac{1}{2},k)] + \frac{\Delta t}{\Delta y}[E_z^n(i,j,k+\frac{1}{2}) - \\ &- E_z^n(i,j+1,k+\frac{1}{2})] \end{aligned} \tag{2.48}$$

The same procedure is realized for the other field components. The components of the current magnetic and electric field intensity, $\vec{H}^{n+\frac{1}{2}}(i,j,k)$ and $\vec{E}^{n+1}(i,j,k)$, can be obtained with the help of past values by the following equation set

$$H_x^{n+\frac{1}{2}}(i,j+\tfrac{1}{2},k+\tfrac{1}{2}) = H_x^{n-\frac{1}{2}}(i,j+\tfrac{1}{2},k+\tfrac{1}{2}) + \frac{\Delta t}{\Delta z}[E_y^n(i,j+\tfrac{1}{2},k+1) - E_y^n(i,j+\tfrac{1}{2},k)] + \\ + \frac{\Delta t}{\Delta y}[E_z^n(i,j,k+\tfrac{1}{2}) - E_z^n(i,j+1,k+\tfrac{1}{2})] \quad (2.49)$$

$$H_y^{n+\frac{1}{2}}(i+\tfrac{1}{2},j,k+\tfrac{1}{2}) = H_y^{n-\frac{1}{2}}(i+\tfrac{1}{2},j,k+\tfrac{1}{2}) + \frac{\Delta t}{\Delta x}[E_z^n(i+1,j,k+\tfrac{1}{2}) - E_z^n(i,j,k+\tfrac{1}{2})] + \\ + \frac{\Delta t}{\Delta z}[E_x^n(i+\frac{1}{2},j,k) - E_x^n(i+\frac{1}{2},j,k+1)] \quad (2.50)$$

$$H_z^{n+\frac{1}{2}}(i+\frac{1}{2},j+\frac{1}{2},k) = H_z^{n-\frac{1}{2}}(i+\frac{1}{2},j+\frac{1}{2},k) + \frac{\Delta t}{\Delta y}[E_x^n(i+\tfrac{1}{2},j+1,k) - E_x^n(i+\tfrac{1}{2},j,k)] + \\ + \frac{\Delta t}{\Delta x}[E_y^n(i,j+\frac{1}{2},k) - E_y^n(i+1,j+\tfrac{1}{2},k)] \quad (2.51)$$

$$E_x^{n+1}(i+\tfrac{1}{2},j,k) = \left[1 - \frac{\sigma(i,j,k)}{\varepsilon(i,j,k)}\right] E_x^n(i+\tfrac{1}{2},j,k) + \frac{\Delta t}{\varepsilon(i,j,k)\Delta y}[H_z^{n+\frac{1}{2}}(i+\tfrac{1}{2},j+\tfrac{1}{2},k) - \\ - H_z^{n+\frac{1}{2}}(i+\tfrac{1}{2},j-\tfrac{1}{2},k)] + \frac{\Delta t}{\varepsilon(i,j,k)\Delta z}[H_y^{n+\frac{1}{2}}(i+\tfrac{1}{2},j,k-\tfrac{1}{2}) - \\ - H_y^{n+\frac{1}{2}}(i+\frac{1}{2},j,k+\frac{1}{2})] \quad (2.52)$$

$$E_y^{n+1}(i,j+\tfrac{1}{2},k) = \left[1 - \frac{\sigma(i,j,k)}{\varepsilon(i,j,k)}\right] E_y^n(i,j+\tfrac{1}{2},k) + \frac{\Delta t}{\varepsilon(i,j,k)\Delta z}[H_x^{n+\frac{1}{2}}(i,j+\tfrac{1}{2},k+\tfrac{1}{2}) - \\ - H_x^{n+\frac{1}{2}}(i,j+\tfrac{1}{2},k-\tfrac{1}{2}] + \frac{\Delta t}{\varepsilon(i,j,k)\Delta x}[H_z^{n+\frac{1}{2}}(i-\tfrac{1}{2},j+\tfrac{1}{2},k) - \\ - H_z^{n+\frac{1}{2}}(i+\tfrac{1}{2},j+\tfrac{1}{2},k)] \quad (2.53)$$

$$E_z^{n+1}(i,j,k+\tfrac{1}{2}) = \left[1 - \frac{\sigma(i,j,k)}{\varepsilon(i,j,k)}\right] E_z^n(i,j,k+\tfrac{1}{2}) + \frac{\Delta t}{\varepsilon(i,j,k)\Delta x}[H_y^{n+\frac{1}{2}}(i+\tfrac{1}{2},j,k+\tfrac{1}{2}) - \\ - H_y^{n+\frac{1}{2}}(i-\tfrac{1}{2},j,k+\tfrac{1}{2})] + \frac{\Delta t}{\varepsilon(i,j,k)\Delta y}[H_x^{n+\frac{1}{2}}(i,j-\tfrac{1}{2},k+\tfrac{1}{2}) - \\ - H_x^{n+\frac{1}{2}}(i,j+\tfrac{1}{2},k+\tfrac{1}{2})] \quad (2.54)$$

From the latter equation set it can be deduced that the electric field components and the ones of the magnetic field are calculated at different time steps. This sequential computing with the help of past values is also known as the *Leapfrog algorithm*.

2.1.2.2 Numerical dispersion and stability condition

According to [5], the numerical dispersion is obtained by introducing a plane and monochromatic discretized wave solution to the by *Yee's* scheme discretized Maxwell Equations of (2.28) and (2.29). After a respective mathematical development, a relation between the numerical wave vector components, the wave frequency, the time-step and the grid space differences is derived. This resulting relation is the numerical dispersion relation.

Therefore, the following compact vector notation where the six components of the electric and magnetic field, $\vec{E}$ and $\vec{H}$, are put together in one equation is used

$$j\nabla \times (\vec{H} + j\vec{E}) = \frac{\partial}{\partial t}(\vec{H} + j\vec{E}) \tag{2.55}$$

or defining a new field vector $\vec{V}(x,y,z)$ that includes the complex vectors for the magnetic and electric field

$$j\nabla \times \vec{V} = \frac{\partial \vec{V}}{\partial t} \qquad with \quad \vec{V}(x,y,z) = \vec{H}(x,y,z) + j\vec{E}(x,y,z) \tag{2.56}$$

By discretizing the vectorial field function $\vec{V}$ after *Yee's* scheme, the following expression is obtained

$$\vec{V}^n(I,J,K) = \vec{\mathrm{V}} e^{\tilde{k}_x I\Delta x + \tilde{k}_y J\Delta x + \tilde{k}_z K\Delta z - \omega N\Delta t} \tag{2.57}$$

In the latter definition, $\vec{\mathrm{V}}$ represents the magnitude of the complex function $\vec{V}$. By introducing this discrete expression into (2.55) and applying *Yee's* central-differenzing discretization on the gradient operator and the time derivative, the following equation is obtained.

$$\begin{pmatrix} \frac{1}{\Delta x}\sin\left(\frac{\tilde{k}_x\Delta x}{2}\right) \\ \frac{1}{\Delta y}\sin\left(\frac{\tilde{k}_y\Delta y}{2}\right) \\ \frac{1}{\Delta z}\sin\left(\frac{\tilde{k}_z\Delta z}{2}\right) \end{pmatrix} \times \vec{V}^n(I,J,K) = \frac{j}{\Delta t}\vec{V}^n(I,J,K)\sin\left(\tfrac{\omega\Delta t}{2}\right) \tag{2.58}$$

Evaluating the cross product generates a vectorial equation, which can be divided in three scalar equations. The numerical dispersion is obtained by calculating the determinant of this vectorial equation and equaling it to zero. The numerical dispersion relation has then the form

$$\left[\frac{1}{\Delta x}\sin\left(\frac{\tilde{k}_x\Delta x}{2}\right)\right]^2 + \left[\frac{1}{\Delta y}\sin\left(\frac{\tilde{k}_y\Delta y}{2}\right)\right]^2 + \left[\frac{1}{\Delta z}\sin\left(\frac{\tilde{k}_z\Delta z}{2}\right)\right]^2 = \left[\frac{1}{c\Delta t}\sin\left(\tfrac{\omega\Delta t}{2}\right)\right]^2 \tag{2.59}$$

By comparing the numerical dispersion with the analytical physical one for a in free space propagating plane wave that has the form

$$\left(\frac{\omega}{c}\right)^2 = k_x^2 + k_y^2 + k_z^2 \tag{2.60}$$

there can not be recognized a strong similitude between both dispersion relations. However, the numerical dispersion converge towards the analytical one for the differences Δx, Δy, Δz and Δt approaching to zero.

From the numerical dispersion expression it can be expected that the choice of the spatial and time differences, Δx, Δy, Δz and Δt can affect the propagation characteristics of numerical waves in *Yee's* spatial grid. That can be explained by the fact, that the FDTD algorithm approximates the electromagnetic wave behaviour by describing the propagating medium with properties very close but not exact to real conditions. This discrepancy generate delays or phase errors that are accumumulated by the numerical waves. These errors affect the propagation characteristics of numerical waves and can lead to non-physical results.

Consequently, the numerical errors have to remain under a certain range giving the system a certain stability and accuracy at the same time. Therefore, a frequency analysis at the numerical dispersion expression in (2.59) is performed: the numercial dispersion relation is manipulated in order to obtain the angular frequency. This results in

$$\omega = \frac{2}{\Delta t}\arcsin\chi \quad \text{with} \quad \chi = c\Delta t\sqrt{\frac{1}{(\Delta x)^2}\sin^2\left(\frac{\tilde{k}_x\Delta x}{2}\right)+\frac{1}{(\Delta y)^2}\sin^2\left(\frac{\tilde{k}_y\Delta y}{2}\right)+\frac{1}{(\Delta z)^2}\sin^2\left(\frac{\tilde{k}_z\Delta z}{2}\right)} \tag{2.61}$$

The argument χ of the inverse sine function can be zero or it maximum value, which is when the sine function arguments become the value of 1. This is

$$0 \leq \chi \leq c\Delta t\sqrt{\frac{1}{\Delta x^2}+\frac{1}{\Delta y^2}+\frac{1}{\Delta z^2}} \tag{2.62}$$

It can be deduced that for values $\chi > 1$ the angular frequency get complex complex values, which would amplify the value of a sinusoidal wave function (e.g. with the form of (2.57)) with every time-step. Hence it would change the near real propagating behaviour of the FDTD wave to a non-physical one and would make the system instable. Thus, in order to obtain real values for the angular frequency and prevail numerical stability, χ must remain in the interval $[0,1]$.

Therefore, the maximum time step value Δt_{max} is derived by using the expression in (2.62) and adjusting $\chi = 1$. The result is

$$\Delta t_{max} = \frac{1}{c\sqrt{\frac{1}{\Delta x^2}+\frac{1}{\Delta y^2}+\frac{1}{\Delta z^2}}} \tag{2.63}$$

For time-step values $\Delta t \geq \Delta t_{max}$ the argument χ of the inverse sinus function in (2.61) has values higher than the value 1. Hence, by using the *Yee algorithm* the time difference Δt must fulfill the following condition for reasons of stability

$$\Delta t \leq \frac{1}{c\sqrt{\frac{1}{\Delta x^2}+\frac{1}{\Delta y^2}+\frac{1}{\Delta z^2}}} \tag{2.64}$$

Moreover, this relation between the spatial and time steps means that they play a decisive role in the accuracy as well as in the stability of this numerical approach.

2.1.3 Finite Integration Technique (FIT)

The Finite Integration Technique (FIT) is proposed by Weiland with his publication [28]. This approach consists in a discretization of Maxwell's equations in integral form, resulting in matrix equations that can be solved. It uses integral balances and thus it permits to check the conservation properties of the discrete fields and the stability of the system before the solving procedure is run.

2.1.3.1 FIT Principle

According to [29], the first step consists in the restriction of the electromagnetic field problem to a simply connected and bounded space region $\Omega \in \mathbf{R}^3$. Like in the FDTD Method, the analysed

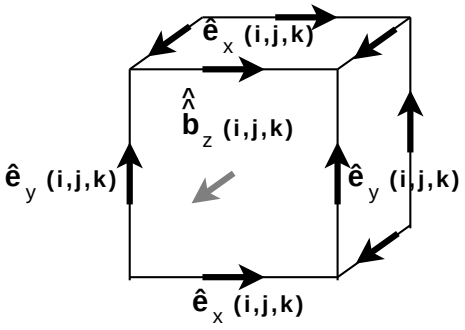

Figure 2.3 : *Discrete cubic cell according to the Finite Integration Technique (FIT)*

medium is discretized into a finite number of volumic cells $V_{i,j,k}$ that fit exactly to each other. This decomposition results in the cells complex G

$$G := \{V_{i,j,k} \in \mathbf{R}^3 | V_{i,j,k} = [x_i, x_{i+1}] \times [y_j, y_{j+1}] \times [z_k, z_{k+1}]\} \qquad \text{for} \quad \begin{matrix} i = 1, \ldots, i_{max} - 1 \\ j = 1, \ldots, j_{max} - 1 \\ k = 1, \ldots, k_{max} - 1 \end{matrix} \tag{2.65}$$

This yields to a total number of nodes $N_p = i_{max} \cdot j_{max} \cdot k_{max}$ that have the form (x_i, y_j, z_k) and to an amount of $N_{cells} = (i_{max} - 1)(j_{max} - 1)(k_{max} - 1)$ cells.

As depicted in figure 2.3, the Maxwell's Equations are discretized and "applied" to each cell of the complex G. For example, for the upper facet $\mathtt{S}_z$ of cell $V_{i,j,k-1}$ (parallel to the x-y-plane) the first Maxwell's Equation (see equation (1.1)) or Faraday's law in integral form becomes

$$\hat{e}_x(i,j,k) + \hat{e}_y(i+1,j,k) - \hat{e}_x(i,j+1,k) - \hat{e}_y(i,j,k) = -\frac{\partial}{\partial t}\hat{\hat{b}}_z(i,j,k) \tag{2.66}$$

$\hat{e}_x(i,j,k)$, $\hat{e}_y(i+1,j,k)$, $\hat{e}_x(i,j+1,k)$ and $\hat{e}_y(i,j,k)$ are the electric voltages along the edge of the surface $\mathtt{S}_z$. The scalar value $\hat{\hat{b}}_z(i,j,k)$ represents the magnetic flux over the facet $\mathtt{S}_z$. These is expressed by

$$\begin{aligned} \hat{e}_x(i,j,k) &= \int_{(x_i,y_j,z_k)}^{(x_{i+1},y_j,z_k)} \vec{E} \cdot d\vec{l} \\ \hat{\hat{b}}_z(i,j,k) &= \iint_{\mathtt{S}_z(i,j,k)} \vec{B} \cdot d\vec{s} \end{aligned} \tag{2.67}$$

Similar is valid for the other components $\hat{e}_y(i+1,j,k)$, $\hat{e}_x(i,j+1,k)$ and $\hat{e}_y(i,j,k)$. Assuming a lexicographical ordering of all voltages $\hat{e}(i,j,k)$ and fluxes $\hat{\hat{b}}(i,j,k)$ in the complex G, two vectors including the node reference like in the following can be defined

$$\begin{aligned} \hat{\mathbf{e}} &= (\hat{e}_{x,n} | \hat{e}_{y,n} | \hat{e}_{z,n})^T_{n=1,\ldots,N_p} \\ \hat{\hat{\mathbf{b}}} &= (\hat{\hat{b}}_{x,n} | \hat{\hat{b}}_{y,n} | \hat{\hat{b}}z,n)^T_{n=1,\ldots,N_p} \end{aligned} \tag{2.68}$$

Consequently, the equations with the form of (2.66) for all the cell facets over the whole complex G can be expressed in matrix form as follows

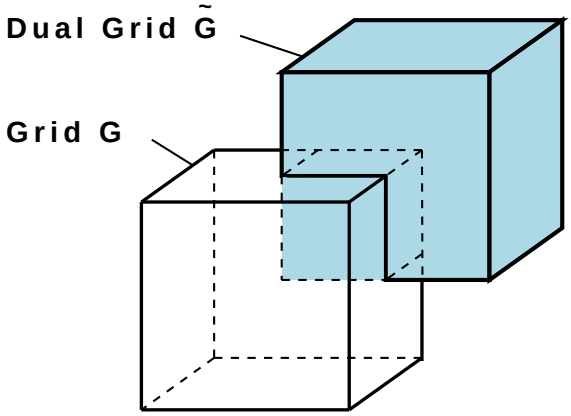

Figure 2.4 : *Discrete cubic cells* G *and* $\widetilde{G}$ *according to FIT*

$$\mathbf{C}\cdot\hat{\mathbf{e}} = -\frac{\partial}{\partial t}\hat{\tilde{\mathbf{b}}} \tag{2.69}$$

The matrix **C** contains topological information on the incidence relation of the cell edges and on their orientation. Thus it has only the values $\{-1,0,1\}$. This can be interpreted as **C** being the curl-operator on the complex *G*.

The same procedure can be applied to the other Maxwell's equations, whereas for equations (1.2) and (1.4) a second cell complex $\widetilde{G}$, which is dual to the primary complex *G*, is required. For it, the dual grid is defined by taking the foci of the cells of *G* as gridpoints for the meshcells of $\widetilde{G}$ as depicted in figure 2.4. In a more general manner, it is possible to take the cell barycenters as boundary vertices [29]. Along the edges of the dual grid cells the magnetic field intensities are applied. On the cell surfaces of $\widetilde{G}$ the dielectric fluxes and the electric currents are allocated in analogy to the quantities allocated on *G*

Therefore, the Maxwell's Equation set in chapter 1 (equations (1.1)-(1.4)) the so-called "Maxwell Grid Equations" (MGE) are obtained. These are

$$\mathbf{C}\hat{\mathbf{e}} = -\frac{\partial}{\partial t}\hat{\tilde{\mathbf{b}}} \tag{2.70}$$

$$\widetilde{\mathbf{C}}\hat{\mathbf{h}} = -\frac{\partial}{\partial t}\hat{\tilde{\mathbf{d}}} + \hat{\tilde{\mathbf{j}}} \tag{2.71}$$

$$\mathbf{S}\hat{\tilde{\mathbf{b}}} = 0 \tag{2.72}$$

$$\widetilde{\mathbf{S}}\hat{\tilde{\mathbf{d}}} = q \tag{2.73}$$

$\hat{\mathbf{e}}$ and $\hat{\mathbf{h}}$ are the electric voltages between grid points and the magnetic voltages between dual grid points, respectively. $\hat{\tilde{\mathbf{d}}}$, $\hat{\tilde{\mathbf{b}}}$ and $\hat{\tilde{\mathbf{j}}}$ are the fluxes over grid or dual grid faces. Following the interpretation made for expression (2.69), the matrix **S** can be seen as discrete divergence matrix applied on *G*. Moreover, the matrix $\widetilde{\mathbf{C}}$ can be interpreted as the dual discrete curl-operator and $\widetilde{\mathbf{S}}$ as the dual discrete divergence on $\widetilde{G}$, respectively

Following the theory in electromagnetics, the constitutive material relations (see chapter 1, equations (1.19) - (1.22)) have to be adequately defined. Therefore, the following discretized material property relations are obtained

$$\hat{\tilde{\mathbf{d}}} = \mathbf{M}_\varepsilon \hat{\mathbf{e}} \tag{2.74}$$

$$\hat{\tilde{\mathbf{b}}} = \mathbf{M}_\mu \hat{\mathbf{h}} \tag{2.75}$$

$$\hat{\tilde{\mathbf{j}}} = \mathbf{M}_\sigma \hat{\mathbf{e}} \tag{2.76}$$

$\mathbf{M}_\varepsilon$, $\mathbf{M}_\mu$ and $\mathbf{M}_\sigma$ are the permittivity matrix, the permeability matrix, and the conductivity matrix, respectively. The elements of these matrices are obtained by using the values of the MGE. For example the calculation of a diagonal element of the conductivity matrix is obtained as result for the coupling of the electric currents and the electric grid voltages like in the following

$$\frac{\iint_{\widetilde{S}_m} \vec{J} \cdot d\vec{s}}{\int_{L_m} \vec{E} \cdot d\vec{l}} = \frac{\iint_{\widetilde{S}_m} \sigma d\vec{s}}{\int_{L_m} d\vec{l}} + O(h^l) \approx \bar{\sigma} \frac{\iint_{\widetilde{S}_m} d\vec{s}}{\int_{L_m} d\vec{l}} = (\mathbf{M}_\sigma)_{m,m} = \frac{\hat{\tilde{j}}_m}{\hat{e}_m} \tag{2.77}$$

The latter is for a corresponding pair of a grid voltage $\hat{e}_m$ along the edge $\mathrm{L}_m \in G$ and the flux $\hat{\tilde{j}}_m$ through the facet $\widetilde{\mathrm{S}}_m$. The error exponent has values of $l = 2$ in the case of non-uniform grid spacing, otherwise $l = 3$. In a similar way the other discrete material matrix elements are obtained. In general the four MGE are an exact representation of Maxwell's Equations and contain only topological information. Consequently, the discretization error of this method is found to be located at the discrete constitutive material equations.

[30], [29] and [31] show the algebraic properties of the discretized fields frequency and time domain. The MGE can be transformed into frequency domain with $\hat{\mathbf{e}}(t) = \mathrm{Re}(\underline{\hat{\mathbf{e}}} e^{j\omega t})$. With the frequential MGE certain wave equations, like the homogeneous wave equation and the Helmholtz equation, can be transformed in eigenvalue problems that can be solved by known techniques. From the analytical version of the latter equation for instance the generalized Helmholtz-grid-equation was derived [29]. The respective expression is

$$\left[\widetilde{\mathbf{C}}\mathbf{M}_\mu \mathbf{C} + \mathbf{D}_1 \widetilde{\mathbf{S}}^T \mathbf{D}_2 \widetilde{\mathbf{S}} \mathbf{D}_1\right] \underline{\hat{\mathbf{e}}} = \omega^2 \mathbf{M}_\varepsilon \underline{\hat{\mathbf{e}}} \tag{2.78}$$

at which $\mathbf{D}_1$ and $\mathbf{D}_2$ are diagonal matrices that when chosen properly allow the discretization of the analytical Helmholtz equation for homogeneous materials. This is necessary due to the definition of two orthogonal vector subspaces, which span the vector space of solutions for the static ($\omega_2 = 0$) and dynamic modes ($\omega \neq 0$); a consequence of the necessity of a real-valued and non-negative system matrix.

According to [31], the time-domain formulation of the discretized equations is equivalent to FDTD. Consequently, the equation set is solved with Yee's algorithm, which leads to an explicit algorithm. For the lossless case this is

$$\mathbf{f}^{i+1} = \mathbf{A}\mathbf{f}^i + \mathbf{s}^i \tag{2.79}$$

with

$$\mathbf{A} = \begin{pmatrix} \mathbf{I} & -\Delta t\mathbf{C} \\ \Delta t\mathbf{M}_{\varepsilon}^{-1}\widetilde{\mathbf{C}}\mathbf{M}_{\mu}^{-1} & \mathbf{I} - \Delta t^2\mathbf{M}_{\varepsilon}^{-1}\widetilde{\mathbf{C}}\mathbf{M}_{\mu}^{-1}\mathbf{C} \end{pmatrix} \tag{2.80}$$

$$\mathbf{f}^i = \begin{pmatrix} \hat{\hat{b}}^i \\ \hat{e}^{i+\frac{1}{2}} \end{pmatrix} \tag{2.81}$$

$$\mathbf{s}^i = \begin{pmatrix} 0 \\ -\Delta t\mathbf{M}_{\varepsilon}^{-1}\hat{\hat{j}}^i \end{pmatrix} \tag{2.82}$$

At the latter equation $\mathbf{I}$ stands for the unitary matrix, Δt is the discretized time step, respectively. The maximum stable time step Δt_{max} is give by the same expression in (2.64) presented in the last section for the FDTD method.

2.1.3.2 Spatial discretization for conformal structures

The FIT method allows to consider all types of coordinates meshes, orthogonal and non-orthogonal meshes. In addition to that, local mesh refinement, also known as "subgridding", including grid line termination techniques can be applied. Other techniques like "triangular filling" or "'tetrahedral filling", which work with geometry approximation and metarial averaging inside the cells, are used to approximate curved boundary surfaces. These techniques enhance the known FIT to the Nonorthogonal Finite Integration Technique (N-FIT). The resulting matrices are symmetric but no longer diagonal. The non-orthogonal algorithm has in its application limitation due to the increase of the numerical cost by its interpolation scheme.

A more efficient approach known as Perfect Boundary Approximation (PBA) can be applied to FIT algorithm. According to [32], it takes the subcellar information into account. Since the lattice generated with this technique is not conformal to the curved boundaries, the PBA algorithm is of second order accuracy for arbitrary shaped boundaries. In particular, the additional preproccesing effort with PBA is slightly higher than without it, avoiding a highly resolved mesh for non-orthogonal shapes.

2.1.4 Additional Techniques

There exist several other numerical methods for handling electromagnetic problems and hence antenna analysis. Among them there are like the Finite Element Method, asymptotic techniques like Uniform Theory of Diffraction, and analytical methods, like the mixed-potential

2.1.4.1 Finite Element Method (FEM)

The finite element method (FEM) is a mathematical approach for finding a solution to partial differential equations (PDEs). This technique is applicable to a wide range of physical and engineering problems, provided it can be expressed as a PDE. The solution approach is based either on eliminating the differential equation completely, this cases are called steady state problems, or rendering the PDE into an approximating system of ordinary differential equations, which are then solved using standard techniques.

A PDE involves a function $f(\tau)$ defined in a certain domain for all its arguments (in the case

here all values for τ) with respect to a given boundary condition. The purpose of the method is to determine an approximation to $f(\tau)$ the solving function. For instance a second order PDE can have following form

$$\frac{\partial^2 f}{\partial \tau^2} + c_0^2 f = g \tag{2.83}$$

at which g is the inhomogeneous part of the differential equation. The PDE can also be regarded as a linear transformation system like in the Method of Moments (equation (2.84)), this is

$$L(f) = g \qquad \text{with} \quad L = \frac{\partial^2}{\partial \tau^2} + c_0^2 \tag{2.84}$$

at which L is the linear operator. The primary challenge while finding the solution for the PDE is to create an equation that approximates the equation to be studied. Therefore, serveral approaches can be used, for instance the Garlekin's method, the Rayleigh-Ritz approach, etc.

2.1.4.1.1 Rayleigh-Ritz Approach The Rayleigh-Ritz ansatz originates from a generalization of the theory of extremum functions. This variational approach is one of the most common used in engineering problems for calculating the solution of the respective PDE. That is for a PDE of second order

$$F(f) = \iiint \left(\frac{\partial^2 f}{\partial \tau^2} + c_0^2 f \right) \cdot f d\tau - \iiint (f \cdot g) d\tau \tag{2.85}$$

where $F(f)$ stands for the primitive function of the function $f(\tau)$. This new function is variated about f and forced to become zero in order to obtain the sought function f like in the following

$$\delta F(f) = 0 \tag{2.86}$$

δ is the variation operator used on the primitive function $F(f)$. The expression in (2.85) can be written in linear system form as well

$$F(f) = \tfrac{1}{2} \langle L(f), f \rangle - \langle f, g \rangle \tag{2.87}$$

at which the expression $\langle , \rangle$ stands for the inner product.

2.1.4.1.2 FEM principle in Electromagnetics The starting PDE to be solved is the vectorial wave equation, which has the following form

$$\nabla \times \frac{1}{\mu} \times \vec{E} - k_0^2 \varepsilon_r \vec{E} = -jkZ_0 \vec{J}^{int} + \nabla \times \frac{1}{\mu} \vec{M}^{int} \tag{2.88}$$

k_0 stands for the free-space wavenumber, Z_0 for the free-space intrinsic impedance, respectively. The traditional Rayleigh-Ritz approach is used to solve the PDE. Therefore, the left side of (2.88) is taken as the linear operator L applied to the electric field $f = \vec{E}$. The inhomogeneous part at the right side of that equation becomes the function *f*. The ansatz results in

$$F(\vec{E}) = \frac{1}{2}\iiint_V \left(\nabla \times \frac{1}{\mu} \times \vec{E} - k_0^2 \varepsilon_r \vec{E}\right) \cdot \vec{E}\, dv + \\ + \iiint_V \vec{E} \cdot \left(jk_0 Z_0 \vec{J}^{int} - \nabla \times \frac{1}{\mu}\vec{M}^{int}\right) dv \tag{2.89}$$

By means of transformations, among them integration rules and curl as well as divergence theorems (see Appendix A), the latter expression becomes

$$F(\vec{E}) = \frac{1}{2}\iiint_V \left(\frac{1}{\mu}(\nabla \times \vec{E}) \cdot (\nabla \times \vec{E}) - k_0^2 \varepsilon_r \vec{E} \cdot \vec{E}\right) dv + \\ + \iiint_V \vec{E} \cdot \left(jk_0 Z_0 \vec{J}^{int} - \nabla \times (\frac{1}{\mu}\vec{M}^{int})\right) dv \\ + jk_0 Z_0 \oiint_S \vec{E} \cdot (\vec{H} \times \hat{\vec{n}}) ds \tag{2.90}$$

with $\vec{H} \times \hat{\vec{n}}$ considered as one of the sources for $\vec{E}$. The sougth field function $\vec{E}$ can be found by enforcing

$$\delta F(\vec{E}) = 0 \tag{2.91}$$

$\delta F(\vec{E})$ stands for the first-order variation of F over E

2.1.4.1.3 Finite Element Discretization In order to calculate the FEM equation on the volume V, the latter has to be discretized. Therefore, its subdivided into a finite number of small volume elements, for instance in rectangular volumic cells, triangular or tetrahedal prisms. The electric field $\vec{E}$ is discretized in a set of basis functions like in the following

$$\vec{E} = \sum_j^J E_j W_j \tag{2.92}$$

The later function expansion is done with the help of vector basis functions W_j, which have to be chosen appropriately like in MoM, and the unknown coefficients E_j. The discretized electric field is introduced to equation (2.90) and the resulting equation is enforced like in equation (2.91). The discretization transforms the analytical integral equation in the matrix equation

$$[A_{ij}][E_j] + [B_{ik}][H_{S,k}] = [C_i] \tag{2.93}$$

with

$$[E_j] = [E_1 \quad E_2 \quad \dots \quad E_J] \qquad [H_{S,k}] = [H_{S,1} \quad H_{S,2} \quad \dots \quad H_{S,K}] \tag{2.94}$$

and

$$A_{ij} = \iiint_V \left(\frac{1}{\mu}(\nabla \times W_i) \cdot (\nabla \times W_j) - k_0^2 \varepsilon_r W_i \cdot W_j \right) dv$$
$$B_{ik} = jk_0 Z_0 \oiint_S W_i \cdot (W_j \times \hat{\vec{n}}) ds$$
$$C_i = \iiint_V W_i \cdot \left(jk_0 Z_0 \vec{J}^{int} - \nabla \times (\frac{1}{\mu}\vec{M}^{int}) \right) dv \tag{2.95}$$

I gives the total number of element edges as well as J. Consequently, $[A_{ij}]$ is a square matrix. K is the total number of element edges residing on the surface S. A similar matrix system is obtained if the wave equation for $\vec{H}$ is used. Consequently, the field $\vec{H}$ is discretized as in (2.92). The obtained matrix equation is solved by simple matrix convertion or other known techniques.

In addition to that, the solving system should be discretized so that the computing process remains numerically stable. The latter means that errors in the input data and intermediate calculations should not accumulate and cause the resulting output to be meaningless. [33], [34], [35] and [38] are cited as main references for the short summary on FEM.

2.1.4.2 Uniform Theory of Diffraction (UTD)

The Geometrical Theory of Diffraction (GTD) and the Uniform GTD (UTD) are asymptotic methods used for approximating solutions to electromagnetic problems at very large frequencies. The GTD, which postulates the existence of "diffracted rays", is an extension of Geometrical Optics (GO). These rays that describe the solutions containing terms of fractional power are no taken into account at the GO. Furthermore, the UTD, whose pioneers were Kouyoumjian and Pathak with their publication [37], generalizes GTD by stating definition formulae for the diffraction coefficients valid also within singularities not reached by GTD. For the following short summary [2], [18] and [8] are main references.

2.1.4.2.1 UTD principle The idea of this method is based on the concept of the GO: to approximate the radiation of high-frequency electromagnetic scenarios by determining wave propagation for incident, reflected and refracted fields. Moreover, it approximates diffraction problems in a more generalized manner than the GTD. Hence UTD models with direct rays the direct wave propagation. Therefore, it uses the expression

$$E(P_{obs}) = E_i(Q_{ref}) \cdot \sqrt{\frac{\rho_1 \rho_2}{(\rho_1 + s)(\rho_2 + s)}} \cdot e^{-jk_0 s} \tag{2.96}$$

at which ρ_1 and ρ_2 are the curvuture radii of the reflected wave-front, s is the distance between the reference and the observing point Q_{ref} and P_{obs}, k_0 the free-space wave constant, and E_i the incident field component at the reference point. The expression under the square root is known as the spatial attenuation, the exponential function represents the phase factor.

The diffracted rays resulting from interaction with obstacles are taken into account by using a similar expression as (2.96) enhanced with a diffraction coefficient. For reasons of convenience the spatial angle is transformed in order to become independent of the reference

point. Consequently, the diffracted field component E_d can be calculated by means of following adapted formula

$$E_d(P_{obs}) = E_i(Q_{ref}) \cdot \mathbf{D} \cdot A(\rho_c, s) \cdot e^{-jk_0 s} \tag{2.97}$$

with $A(\rho_c, s)$ as the spatial attenuation

$$A(\rho_c, s) = \begin{cases} \frac{1}{\sqrt{s}} & & & \text{for plane and conical wave incidences} \\ \frac{1}{\sqrt{\rho}} & \text{, with} & \rho = s\sin\beta_0 & \text{for cylindrical wave incidence} \\ \sqrt{\frac{s'}{s(s+s')}} & \simeq \frac{\sqrt{s'}}{s} & \text{for} \quad s \gg s' & \text{for spherical wave incidence} \end{cases} \tag{2.98}$$

D stands for the diffraction factor, s' is the distance between the source of the incident field and the reference point.

There are diffraction coefficients of first and second order. The former ones model the first diffracted field at the diffraction process. The latter coefficients known as slope diffraction coefficients describe the second order diffraction, which occurs specially for rapid changing fields. The diffraction coefficients depend on the type and geometry location of the canonical form (edge, wedges), but also on their material properties and on the type of the incident wave (planar, spherical). These coefficients are approximated by their asymptotic form defined for canonical forms like edges, wedges. Many studies were realized in order to define diffraction coefficients, for instance for a wedge with impedance faces [36].

According to UTD and GTD as well, the diffracted field is composed by "soft" and "hard" polarized components. The "soft" polarization component is parallel to the propagation plane of the diffracted rays, the "hard" polarization component propagates perpendicular to it. This propagation plane is expanded by the vector along the diffracting border (egde, wedge, etc) and the vector from the reference to the observing point. Respectively there exist for each polarization component its corresponding diffraction coefficient.

The diffracted electric field $\vec{E}_d$ at the observation point P_{obs} is yielded by using the incident field $\vec{E}_i$ at the reference point Q_{ref} in the following formula

$$\vec{E}_d(P_{obs}) = \overline{\overline{\mathbf{D}}} \cdot \vec{E}_i(Q_{ref}) \cdot \sqrt{\frac{\rho_c}{s(\rho_c + s)}} \cdot e^{-jk_0 s} \tag{2.99}$$

at which $\overline{\overline{\mathbf{D}}}$ is the diffraction dyadic, whose elements contain the diffraction and the slope diffraction coefficients, and ρ_c is the distance between the reference point $Q_{ref}(s=0)$ and the edge (also first caustic of the diffracted rays) and the second caustic of the diffracted rays. In a system of a tube of rays the caustics are the lines perpendicular to the propagation direction that connect the references points of the cross-sectional areas. In this equation the spatial attenuation simplifies for the case of the incident field having a planar wave-front as shown in equation (2.98).

The application of UTD and GTD is limited to the frequency of the regarded system. Both methods are usually used in combination with other methods. For instance [52] combines GTD with slot theory and the modal expansion technique for calculating the far field of microstrip

antennas. Another example is the application of the UTD combined with Discrete Fourier Transform (DFT) on arrays [50].

2.2 Approachs for Modeling Conformal Antennas

Due to the increasing popularity of conformal antennas, several approachs for their modeling and simulation have been proposed. These proposals are based more or less on the former presented numerical techniques. This section will summarize these conformal antenna modeling methods giving the reader a general overview.

2.2.1 Application of the Transmission Line Model

Early works creating models for conformal antennas were derived from their planar analogues. For instance Munson in his work [53] makes an analysis of a conformal microstrip antenna using an adapted version of his model for planar antennas based on the Transmission Line Model (TML). The latter model, which can be found in [1] and [14], is the easiest but the less versatile and less accurate way to model a patch antenna and therefore it will not be presented in the present thesis work.

2.2.2 Application of the Cavity Model

The Cavity Model is a method for approximating the behaviour of microstrip patch antennas by assuming the patch antenna to be a cavity. A detailed introduction to this technique can be found in several works like [3], [1] and [2] and [8]. This resonant cavity is described as a dielectric volume enclosed by six rectangular surfaces in the case of a rectangular patch. In the case of a circular patch the boundaries of the cavity are the surfaces of a cylinder: the lateral surface plus the top and bottom caps.

In both cases, the latter two surfaces of the cavity, which correspond to the patch and the ground plane, are assumed to be perfect electrical conductors (PEC's). The other walls of the dielectric loaded cavity are modeled as perfect magnetic conductors (PMC). According to Balanis [1] the current distributions on the patch are related to the modes of the cavity that behaves like a truncated waveguide.

This method has a good accuracy at the resonant frequency but the latter deteriorates outside the resonance region. Nevertheless, it has been used in the present thesis work and hence the method and its implementation will be presented in the next chapter.

2.2.3 Approachs based on methods applied to volume: FDTD, FIT and FEM

Methods that use cubic mesh elements to treat antenna problems, like FDTD and FIT, can not give accurate solutions but approximate the conformity of curved antennas. Additional meshing techniques can enhance the accuracy of the approximations. Consequently, as mentioned in the former section, FIT uses the PBA mesh technique [32]. In reference to the FDTD method, there exist a conformal variant and the latter can be used to model and simulate conformal

antenna behaviour. Holland [25] is one of the pioneers in proposing a generalized FDTD for non-orthogonal coordinates and hence for conformal structures.

The studies made by He and Xu [54], and Kashiwa *et al.* [27], for instance, are based on a conformal FDTD variant. He and Xu use the conformal FDTD in order to obtain the near field and the surface currents on the cylindrical microstrip patch. For it, they assume the cylinder to be infinite and use perfectly matched layers (PML's) to simulate the necessary boundary conditions. Furthermore they calculate the far field radiation by using a modified version of the spectral domain dyadic Green's functions in the arbitrary cylindrically stratified media. The same proceeding is done in [27] with the exception that the far field is calculated from the near field by transforming it using the field equivalence principle.

Due to the fact that FEM uses tetrahedal and triangular prisms as mesh elements, single or doubly curved structures can be discretized with better accuracy than with rectangular bricks. Consequently, in conformal antenna analysis, where FEM-based methods are used as solvers, the FEM technique is used to calculate the electromagnetic fields in the cavity and aperture, which can be used to compute the surface currents of the active antenna zone. Macon *et al.* in [38] and [39] proceed in a similar way. They used the hybrid FE-BI, which models the physical effects of surface curvature by means of a dyadic Green's function. This Green's function, which couples the tangential electric and magnetic fields in the aperture, enforces the boundary conditions on the tangential electric field over the radiating metallic surface. An asymptotic form of the dyadic Green's function is determined by means of UTD in order to avoid complicated time-consuming calculations. stratified layers with UTD. Here the material parameters are assumed to be constant within a finite element but are allowed to vary across elements.

FDTD algorithms are in principle very promising and versatile to describe conformal structures. Nevertheless, the number of nodes used to accurately describe the geometry of an open conformal component grows so that it makes FDTD not convinient for fast analysis purposes. Similar is valid for FIT that despite using mesh techniques it is still necessary a refinement of the mesh, which enhances the number of unknowns. For FEM when applied to conformal antennas, due to a suitable discretization of the air surrounding the antenna and the introduction of absorbing boundary conditions, the number of unknowns increases as well. For instance in [23] the author bridges the modeler of the FEM based software in order to attain suitable meshed surface and so to yield accurate results.

2.2.4 Approachs using the dyadic Green's Function for conformal structures

Approachs to modeling conformal antennas based on the Green's Function integrating equation are limited to the difficulty of obtaining suitable expressions for the Green's function. Moreover, the calculation of the required Green's function is quite effort expensive. Nevertheless, these techniques are the most proposed solution nowadays due to the accuracy of the results. Therefore, a basic step of these proceedings is either to calculate the elements of the dyadic Green's function by means of feasable methods, or to approximate them as good as possible with suitable techniques. In some cases closed-form dyadic Green's functions are found and applied.

For instance, Thiel and Dreher [41] derivate the dyadic Green's function for closed cylindrical and cylindrical sector structures by means of a spectral domain solution known as equivalent-circuit approach . This technique proposed by Dreher [42] creates a hybrid matrix equation that describes the relations between the fields between two medium regions via a two-port representation. This is possible since the differential wave equations for tangential field components become ordinary differential equations, namely transmission lines equations in spectral domain. Moreover, via this port representation the influence of each layer in an stratified media can be taken in account by multiplying its hybrid matrix. By this way, the multilayer Green's Function can be determined.

Consequently, the procedure in [41] starts with the source-free wave equation in spatial domain that is converted into spectral domain. The solution for the wave equation, which is also transformed in frequency domain, is based on modal expansions that are expressed by Fourier Series. The new spectral wave equation solution is limited by the boundary conditions of the dielectric layers on the cylinder. In the following, the solution is introduced to the spectral wave equation and the resulting equations are expressed in circuit equivalents in matrix form. The spectral coefficients of the Dyadic Green's Function are derived so that equation $\tilde{\vec{E}} = \tilde{\tilde{\mathbf{G}}} \cdot \tilde{\vec{J}}$ is valid. For it, the spectral excitation $\tilde{\vec{J}}$ is defined to a unit source. By this way, in the latter equation the spectral Dyadic Green's function $\tilde{\tilde{\mathbf{G}}}$ becomes equivalent to the spectral field $\tilde{\vec{E}}$ and the coefficients for the Dyadic elements can be calculated. Furthermore, this spectral elements of the spectral Green's Function Dyad are transformed with an inverse Fourier Transform and used then to form the respective spatial dyadic Green's Function. At the end, the latter Dyad can be used with a numerical technique like MoM, in order to evaluate the electric field of the conformal antenna.

Another spectral domain approach example for cylindrical antenna using a transmission line analogy is proposed by Biscontini *et al.* [43]. This method starts with the decomposition of the field in TE and TM modes using the electric and the magnetic vector potentials in spectral domain. These spectral potentials are defined as superpositions of with coefficients "weighted" Hankel functions. The coefficients are determined by matching the boundary conditions. Then the harmonic components of the spectral magnetic and electric field are calculated by means of the spectral potentials. In the following, the obtained fields, which are linear combination partial waves, are written in matrix form. Each layer is completely described matching the tangential component at its boundary surfaces. For it the continuity condition for the tangential components at the interfaces are applied.

As next step the analogy with the transmission line is realized by determinating a network by mapping the tangential components of the electric and magnetic fields to voltages and currents at the cylindrical interfaces. The resulting network is normalized in order to make it power conservative. Then every power conservative cylindrical layer is mapped into a power conservative network. In such a representation the electromagnetic boundary conditions are represented by connection between ports. In the following, the discontinuity on the tangential component of the magnetic field is translated into a step current discontinuity represented by a unit current generator. Once that the network is excited, the amplitudes of the modal coefficients can be calculated in the entire network.

2.2.5 Other Techniques

Some techniques for modeling conformal antennas apply directly Maxwell's Equations or their derivative in integral form, like for instance the integral field equations or the mixed potential integral equation (MPIE), in order to find the sought solution. Therefore, the conformal structure, on which the antenna lies, is regarded as an infinite or a finite structure. For the first approach these equations can be solved in a straigthforward way using transformation methods to facilitate the calculation. For the "truncated" structure approach the boundaries have to be taken into account and hence it becomes more difficult.

An example of each one of these approaches is given by Herschlein *et al.* [44]. In this paper two solutions to a patch on a cylindrical bearer are presented. The first is the case of a patch antenna on a cylindrical structure assumed to be infinite. The second case treats the same problem but on a finite structure (a segment). For the infinite structure case they use the spectral domain approach, which consist in dermining with help of the Hankel functions weighted with coefficients the electromagnetic field components for the in cylindrical coordinates give Helmholtz equation in frequency domain. The latter reduces to a Bessel differential equation. The obtained fields in each material can be decomposed into transverse magnetic (TM) and transvers electric (TE) modes. Nevertheless, the modes are coupled due to the interfaces of different dielectrics. The unknown coefficients are determined by means of the boundary conditions. In the end the spatial fields are yield with an inverse Fourier transform.

The solution to the truncated cylinder in [44] is attained by using the Boundary Element Method (BEM). This technique often used for scattering problems reduces in dimension a problem in an unbounded three dimensional domain, in order to determine unknown currents on the surface of the scatterer [45]. In order to facilitate the solution of the boundary integral equations, this surface is discretized by constructing a boundary element mesh consisting of quadrilaterals and triangles. Moreover, this quadrilateral elements are mapped into square master elements, the triangular elements into right, isosceles triangular master elements. The mappings are performed using polynomial Lagrange shape functions. Consequently, BEM does not put restrictions on the geometric complexity of the scatterer.

In order to apply BEM, Herschlein *et al.* divide the problem in two regions: the dielectric between the patch and the ground plane, and the free space. In the following, the vector formulation of the boundary integral equations, namely the electric and magnetic field integral equations (EFIE and MFIE, respectively), are used on both regions. The resulting integral equations are linear equations systems that are coupled and hence they all can be put a matrix equation, that can be solved by known techniques. The necessary integrations are perfomed by Gauss-Legendre quadrature. Consequently, if the field contribution on the surface is known, the field a any arbitrary point can be determined by integration over the surrounding surface. Further information to the derivation for the boundary integral equations can be found in [12].

2.3 Finite Array Analysis Methods

Nowadays, analyses of finite arrays are realized with models for infinite arrays. There exist several solutions for representing an infinite array due to a greater probability to find closed form solutions for the Green functions or more accurate approximations than in the case of finite

arrays. Nevertheless, the infinite periodic array model does not entirely describe the behaviour of finite arrays, even when they are very large, since it omits the important effects resulting from the structure truncation. These effects have an influence on the elements, specially for the ones near the edges of the finite array.

A finite array can be modeled and simulated by using the conventional array element-by-element field summation approach. Herein the aforementioned antenna analysis methods are used. This method is depending on the size of the finite array, which is equivalent to the number of elements, computational effort and time expensive. Consequently, techniques were developed in order to improve the velocity of calculation at element-by-element approach, to use known solutions for infinite arrays by transforming them to solutions for finite arrays, or to add the truncation effects of finite arrays to existing analysis with asymptotic methods. In the next paragraphs three methods coming from these three method groups are presented.

2.3.1 Fast MoM Solution

Array analysis using the normal MoM procedure requires a lot of computation time due to the calculations to be done at a high number of array elements. This comes from the fact that the latter antennas are calculated one by one. In addition, the capacity of storing the required matrices is limited. Consequently, some approaches have been developed to accelarate the calculation. Fasenfest *et al.* [47] present such approach that is applicable to arrays with identical elements and arbitrary boundaries. The method is based on the Adaptive Integral Method (AIM), which projects the solution domain onto a regular grid to enable use of the Fast Fourier Transform (FFT) algorithm.

The difference between AIM and by the author called GIFFT method lies on the choice on radiating basis and testing functions. The AIM procedure uses a neighbouring grid of approximately equivalent monopole sources and the usual Green's function to computed the interactions between the equivalent sources. In the method of Fasenfest *et al.* the Green's function is approximated on an interpolation grid as a sum of separable functions and the basis and testing function integrations are done using the interpolated Green's function in the classical way.

Therefore, the array is described with a mask, which is inside an array boundary, over a bounding box. The array boundary is defined by a closed piecewise linear curve that encloses the matrix. The bounding box is described by a matrix whose row and column dimensions are equal to the number of elements of the planar or linear array. The mask approximates the array boundary by indicating in the bounding box matrix the presence of an element with a 1 or the non-presence with a 0 at the respective index location. For instance, a mask for an array of hexagonal structure is pictured in figure 2.5

From the array mask a matrix mask, which indicates cell index separations $\varsigma - \varsigma'$ between pairs of interacting array elements, is sythesized. The matrix mask determines what sample values of the Green's function are needed to interpolation. A non-zero matrix entry represents coupling between a pair of array elements with the corresponding index separation. Below, the Electric Field Integration Equation (EFIE) is given by

$$\int_S \bar{\bar{\mathbf{G}}}^E(\varsigma - \varsigma', z, z') \bigotimes \vec{J}(\vec{r}')ds' = -\vec{E}^{\text{inc}}_{\tan} \tag{2.100}$$

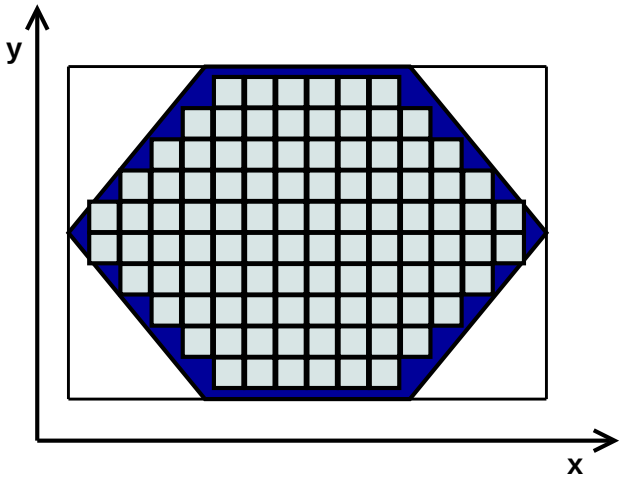

Figure 2.5 : *Mask for hexagonal array form*

is applieed for the MoM procedure like in the following

$$\sum_{p'}\sum_{n=1}^{N} Z_{mn}^{pp'} \cdot I_n^{p'} = V_m^p \qquad \text{with} \quad Z_{mn}^{pp'} = -\langle \Lambda_m^p, \bar{\bar{\mathbf{G}}}^E(\varsigma - \varsigma', z, z'), \Lambda_n^{p'} \rangle \tag{2.101}$$

Here Λ_m^p and $\Lambda_n^{p'}$ are the basis and testing functions and $V_m^p = \langle \Lambda_m^p, \vec{E}^{\text{inc}} \rangle$. The inner product symbol represents the integration over both array source and observation domain. The latter expression can be expanded in the matrix form. Furthermore, the Green's function is approximated by Lagrange interpolation polynomials L_i and L_j resulting in

$$\bar{\bar{\mathbf{G}}}^E(\varsigma - \varsigma', z, z') \cong \sum_{i,i',j,j'} L_i(\varsigma) L_j(z) \bar{\bar{\mathbf{G}}}^E_{i-i',j,j'} L_i(\varsigma') L_j(z') \qquad \text{with} \quad \bar{\bar{\mathbf{G}}}^E_{i-i',j,j'} \equiv \bar{\bar{\mathbf{G}}}^E(\varsigma^i - \varsigma^{i'}, z^j, z^{j'}) \tag{2.102}$$

The Lagrange Green's function interpolation allows the matrix to be filled with fewer inner product calculations than the standard MoM due to the separable nature of the approximated Green's function. The mutual coupling matrix is approximated consequently like in the following

$$Z_{mn}^{pp'} \approx \tilde{Z}_{mn}^{pp'} = -\sum_{i,i',j,j'} \langle \Lambda_m^p, L_i(\varsigma) L_j(z) \rangle \cdot \bar{\bar{\mathbf{G}}}^E_{i-i',j,j'} \cdot \langle L_i(\varsigma') L_j(z'), \Lambda_n^{p'} \rangle \tag{2.103}$$

There are three properties of the latter approximation that contribute on the acceleration of the common MoM approach. The first one is that unless the grid point $\mathbf{i}' = (i_1', i_2')$ is in the cell p' the inner product $\langle \Lambda_m^p, L_i(\varsigma) L_j(z) \rangle$ vanishes. This is so because Lagrange polynomial is non-zero only over the cell containig the interpolation point. The same is valid for the other inner product $\langle L_i(\varsigma') L_j(z'), \Lambda_n^{p'} \rangle$. Second property is related to the inner products too: for each array element they need to be calculated once since both products are identical for each element. Moreover, if the Garlekin's method is used the quantities are equal. The last useful property is that it is necessary to calculate the approximated Green's function only for index pairs $\mathbf{i} = (i_1, i_2)$ appearing within the matrix mask.

The impedance matrix $\tilde{Z}_{mn}^{pp'}$ is inaccurate if the cell separation is not sufficiently large since low order interpolation of the Green's function is inaccurate near the source point. To avoid this inacccuracy the mutual impedance elements and the next-neighbouring element impedances are found by standard MoM. Consequently, the discretized EFIE in matrix form can be written as

$$\left[\Delta Z_{mn}^{pp'}\right]\left[I_n^{p'}\right] + \left[\tilde{Z}_{mn}^{pp'}\right]\left[I_n^{p'}\right] = [V_m^p] \qquad \text{with} \quad \Delta Z_{mn}^{pp'} = Z_{mn}^{pp'} - \tilde{Z}_{mn}^{pp'} \tag{2.104}$$

$[\Delta Z_{mn}^{pp'}]$ is called the Toeplitz Difference matrix. Its element values are taken as zero for elements that satisfy $|\varsigma^i - \varsigma| > 0$. Thus the evaluation of this sparse matrix can be performed quickly. The second matrix $[\tilde{Z}_{mn}^{pp'}]$ is of convolutional form can be evaluated using a two-dimensional FFT, which speeds the evaluation procedure in general.

2.3.2 Fourier Windowing Method

The Fourier Windowing Method is used generally for large finite array analysis in order to avoid rigorous element-by-element analysis, whose optimization for keeping numerical effort reasonable can not be extended indefinitely to larger and larger arrays. This technique assumes the array to be infinite and to have information about the infinite array element. This method is presented in [48] and [49].

In [49] the windowing technique is shown in more general way and for a $N \times N$ grid over a periodic rectangle in scan space wherefrom the quantity samples are taken. It assumes that all elements are to be minimum scattering antennas to a greater or less extent. The infinite array pattern repeats in the scan space with a certain periodicity, hence any sampling of a whole rectangle of these periodic dimensions contains all the information necessary to build up a large finite array. The advantage of the rectangle can be noticed when the array pattern in scan space is transformed back onto the aperture, the points produced are spaced by the array spacings.

According to [49] the procedure starts with retrieving the infinite array immersed element pattern that is then divided by an estimate of the isolated array element. A hypothetical pattern is obtained that enables the transform to the element aperture. The latter step reveals the true excitations on the lattice. In addition to that, the yielded Huygens source pattern is multiplied with the array factor of the finite array before transforming it back to the aperture. This is equivalent as convolving the aperture excitations with forward waves.

One optional advantage of this method is that it can handle array larger than the original size. This is reached by transforming back the Huygens source pattern to the aperture and then by scanning space on a larger grid by padding the dataset with zeros. Back transforming of the multiplication step reveals the true aperture excitations. These are truncated to the size and shape of the finite array.

Furthermore, [48] shows the Fourier Windowing method in detail. It derives first the "finite array Green's function". The derivation is based on the use of Poisson's sum formula in the case of finite sums. Therefore, a finite phased array is described by a $(M+M_i) \times (N+N_i)$ cell structure on the x-y-plane as depicted in 2.6. The current sources of the finite array are defined

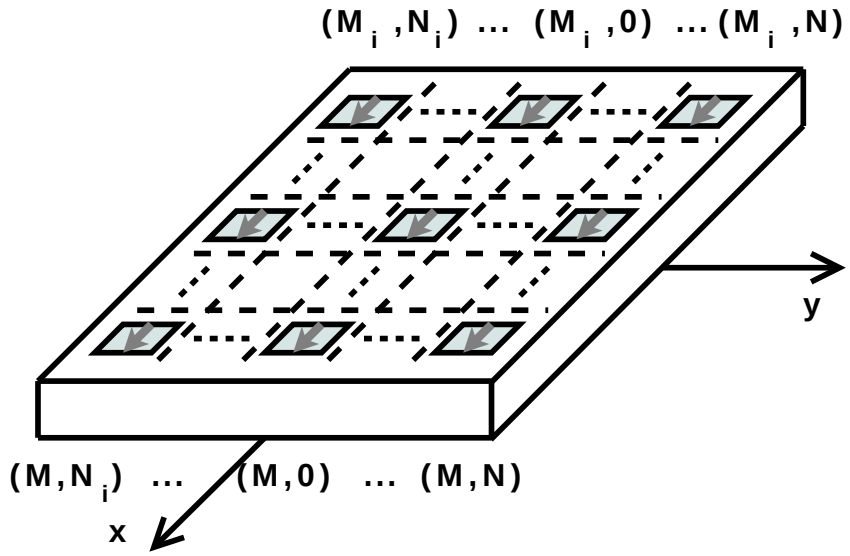

Figure 2.6 : *Finite phased array of microstrip patches*

as excitations having a linear phase shift and amplitude taper.

$$\vec{J}_{mn} = \vec{J}_{00} w(ma,nb) e^{-jk_0(maT_x+nbT_y)} \tag{2.105}$$

with

$$w(ma,nb) = \begin{cases} 1 & \text{if} \quad m=n=0 \\ \text{real} & \text{if} \quad M_i \le m \le M \quad \text{and if} \quad N_i \le n \le N \\ 0 & \text{elsewhere} \end{cases} \tag{2.106}$$

$w(ma,nb)$ is the windowing function. The exponents of the complex exponential replace the angles influence like in the following $T_x = \sin\theta\cos\phi$ and $T_y = \sin\theta\sin\phi$. The excitation amplitude of $\vec{J}_{00}$ at cell (0,0) can be set to unity without loss of generality; in case of elementary current sources $J_{00} = \delta(\vec{r}_{00})$ with $\vec{r}_{00}$ as position vector of that source. The "inferior" borders of the array are defined by $M_i = -M$ or $M_i = -M+1$ and $N_i = -N$ or $N_i = -N+1$ respectively.

By introducing the current distribution in the formula for calculating the far field using the Dyadic Green's function $\overline{\overline{\mathbf{G}}}$ (see chapter 1) and transforming upon other terms with the Poisson's sum formula in the case of finite sums, the following is yielded

$$E_n(\vec{r}_{kl}) = \left\{ \frac{2\pi}{ab} \sum_{m=-\infty}^{\infty} \sum_{n=-\infty}^{\infty} \overline{\overline{\mathbf{G}}}(k_x,k_y) \cdot e^{jk_x(x_k-x'_k)} e^{jk_x(y_k-y'_k)} \right\} * W_{MN}^{kl}(T_x,T_y) \tag{2.107}$$

with

$$W_{MN}^{kl}(T_x,T_y) = \tfrac{1}{2\pi} \tilde{w}_{MN}^{kl}(T_x,T_y) \tag{2.108}$$

$\vec{r}_{kl}$ is the vector that gives the position of the observation point; (k,l) are the subscripts of the coordinates that give the number of cell containing this point. a and b are the dimensions of

the elementary cells. The symbol $\tilde{()}$ stands for the fourier transform and $(*)$ for the convolution product. Consequently, the normalized field E_n of the large finite array is the convolution of the infinite array field with the window function.

The "finite array Green's function" $\bar{\bar{\mathbf{G}}}$ can be expressed with the Dyadic Green's function and the fourier transform of the excitation window. This is given by the following expression where $\vec{r'}_{kl}$ stands for the coordinates vector of the respective source

$$\bar{\bar{\mathbf{G}}}^{kl}_{MN}(\vec{r}_{kl}|\vec{r'}_{kl}) = \left\{ \frac{2\pi}{ab} \sum_{m=-\infty}^{\infty} \sum_{n=-\infty}^{\infty} \tilde{\bar{\bar{\mathbf{G}}}}(k_x,k_y) \cdot e^{jk_x(x_k-x'_k)} e^{jk_x(y_k-y'_k)} \right\} * W^{kl}_{MN}(T_x,T_y) \tag{2.109}$$

Besides, [48] describes the calculation of the active surface current distribution for patch arrays. Therefore, each patch is supposed to have a current as previously defined. An equation that fulfils the boundary condition on the patch surface, which states that on a conductor surface the tangential electric field has become zero, and wherein the surface current is defined as an unknown is set by means of the expression (2.107). The system integral equation is then transformed into a matrix equation by defining the unknown active current function as a set of basis functions. The system is then solved by using the Garlekin procedure and the Method of Moments.

According to [48], this technique gives good results and behaviour predictions for elements embedded in the center of large arrays since it takes automatically into account mutual coupling. Nevertheless, it does not give good predictions for the elements at the borders and corners of the array because edge effects are neglected.

Arbitrary shapes and illumination distributions can be analysed with this method as long as the elements lie at multiples of the infinite array spacing. According to [49], reasonables approximations are yielded even if the elements are relatively complex and - against the initial assumption - if these are not particularly good minimum scatterers.

2.3.3 Asymptotic Approach

The approach presented by Janpugdee and Pathak in [50] is based on UTD. The authors use it in order to analyse a large finite phased array of printed antenna elements. Therefore, a finite rectangular array of $(2N+1)\times(2M+1)$ elements on an infinite grounded material slab is considered. The surface current distribution in all elements are represented in terms of a proper set of basic functions $\vec{f}_i$. Moreover, it is assumed the array elements to have the same set of basic functions. Consequently, the current distribution element $\vec{J}_{nm}$ is approximated like in the following

$$\vec{J}_{nm}(\vec{r'}) = \left(\sum_{L}^{i=1} \vec{f}_i(\vec{r'}) C_{nm,i} \right) e^{-jk_0(\vec{r'}_{nm}\vec{u})} \approx \vec{f}(\vec{r'}) C_{nm} e^{-jk_0(\vec{r'}_{nm}\vec{u})} \tag{2.110}$$

$\vec{r'}$ are the position vectors of the sources, C_{nm} the distribution current coefficients and $\vec{u}$ the unit vector, respectively. Furthermore, the field at an observation point is given by the convolution intergral of the Dyadic Green's function and the current distribution. The resulting field can

be separated in sum components composed of $\vec{E}_{nm}$, which comprend the convolution integrals of the Green's Function with the basis function, and the distribution current coefficients. This is

$$\vec{E} = \sum_{k=-N}^{N} \sum_{l=-M}^{M} \vec{E}_{nm} C_{nm} e^{-jk_0(\vec{r'}_{nm}\vec{u})} \tag{2.111}$$

Due to the form of the latter expression, the current coefficients can be regarded as a Discrete Fourier Transform (DFT) expansion. Consequently, the coefficients can be replaced by its spectral counterparts $\tilde{C}_{kl}$ and the field function becomes

$$\vec{E} = \sum_{k=0}^{2N} \sum_{l=0}^{2M} \tilde{C}_{kl} \vec{E}_{kl} \approx \sum_{k,l \in D} \tilde{C}_{kl} \vec{E}_{kl} \tag{2.112}$$

In addition to that, the DFT expansion allows to take into account the significant DFT terms for the calculation of the field, as expressed with the right-side approximation in the latter equation. This is done by truncating the whole DFT expansion and retaining these relatively few terms. According to [50], the DFT expasion is truncated to approximately 10% to 20% of the total number. Furthermore, the authors convert the finite sums of the field function into infinite Floquet-type modal sums of finite Poisson integrals using the Poisson sum formula.

The asymptotic evaluation of the resulting spectral integrals yields the contribution to the total electric field. It is composed mainly of the following five field contributions: the Floquet wave modal field $\vec{E}^{fw}$, the Floquet edge-diffracted field $\vec{E}^{d,e}$, the Floquet corner-diffracted field $\vec{E}^{d,c}$, the Floquet edge-excited surface and leaky waves (SW / LW) field $\vec{E}^{slw,e}$ and the Floquet corner-excited SW and LW field $\vec{E}^{slw,c}$.

$$\vec{E} \approx \sum_{k,l \in D} \tilde{C}_{kl} [\vec{E}_{kl}^{fw} + \vec{E}_{kl}^{d,e} + \vec{E}_{kl}^{d,c} + \vec{E}_{kl}^{slw,e} + \vec{E}_{kl}^{slw,c}] \tag{2.113}$$

Janpugdee and Pathak attribute the Floquet Waves (FW's) field to the field produced by infinite periodic arrays. This is due to the fact, that FW's exist only in a confined region of space due to the array boundary truncation. Furthermore, they see the FW's ways as the source for the diffracted Floquet edge-diffracted field, which has the form of modal conical waves emanating from the array edges. The FW's diffract at the corners and cause also the Floquet corner-diffracted field. The respective ways of the latter field are of spherical kind and emanated from the corners of the array in all directions.

According to the analysis in [50], more than one SW mode can be excited depending on the thickness and permittivity of the dielectric layer for a given frequency range. While in some configurations the LW can also be excited in addition to the SW. SW's / LW's arosen from diffraction on edges do not spread along the array. The SW's / LW's due to the Floquet modal corner diffraction have cylindrical spreading factor along the surface.

The further alternative of forming array element subgroups, namely subarrays, for calculating the array fields more efficiently is given in [50]. This alternative is benefiting due to the fact that the calculations are realized more efficiently than the conventional brute force array element-by-element field summation. Moreover, the authors remark that non-rectangular periodic array can also be treated as a sum of linear arrays.

The asymptotic ray analysis can not deal with realistic array current distribution, which is in general non-smooth. Thus this method assumes simple, smoth and slowly varying array currents. Moreover, the realistic current distributions can be found by means of the use of numerical techniques. Therefore, the authors recomend accelerated DFT-MoM procedure for finding the currents on the printed antenna elements.

Chapter 3

Development of a hybrid method

The main task of the present thesis work is to perform far field analysis of planar and conformal finite array antennas. Therefore, microstrip patch antennas were chosen as the desired array element, due to their versatily and inherent low profile. In addition to that, these candidates can be designed for wide-band or and multi-band functional tasks. The reader has seen in the latter chapter that there exist already methods for modeling and analysing conformal antennas and arrays. So the question arises: Why the development of a new method although there exist already techniques therefore? To answer this question the following observations about the latter methods have to be given.

Refering to the available techniques for treating finite large array, there exist feasable approachs not for conformal arrays but for planar ones. The reason for this, is that the element radiation in a conformal array is dependant of the geometry and hence it can not be assumed that all elements have in the same radiation behaviour specially in the desired observing direction (θ, ϕ). Contrariwise, for the planar array elements this assumption can be made. However, there exist generally approaches for finite conformal arrays based on the computation expensive element-by-element treatment. Since the objective of the present thesis work is to find a feasable way of modeling, simulating and analysing a curved antenna system, the latter approach proposals can not be used.

Concerning the calculation methods for a conformal antenna, there exist a big number of proposals. These come mainly from the classical methods like FEM, FDTD and MoM with certain modifications or alterations. If these techniques are regarded close, it can be said that FEM and FDTD (and so FIT) analyse more than is required for EM simulations of practical conformal patch antennas: they discretize and calculate the field in the antenna and the space region that surrounds it, analysing in greater scale in comparison to the smaller active radiating region. As aforementioned in the latter chapter, on one side this is promising since it yields good results. On the other side, due to the increasingly high number of unknowns and consequently high computation effort, this is disavantegeous. Consequently, these methods can handle conformal antennas but they are not suitable for fast analysis of conformal arrays.

MoM, which relies on the choice of suitable Green's functions in an integral form, links the positions of equivalent sources on surfaces to the field. This seems to be one of the optimum choices for analyzing curved patch antennas. As MoM deals with surfaces instead of volumes, this gives a substantial savings in terms of the number of unknowns to be solved. Nevertheless,

the involvement of dielectric layers at the analysis of conformal antennas complicate the calculations slowing the analysis process. Furthermore, in the case of finite large conformal arrays, the matrix becomes too big making the calculation of the solution difficult and time consuming. Although there exist some approaches to speed up the calculation for the planar arrays, for instance the technique presented in the latter chapter, these can not be used for the conformal counterparts.

As a consequence of the latter observations and in order to carry out the main task of the present thesis work, a new approach was envisaged. For it, a combination of an efficient and versatile analysis method for the conformal array element, like FDTD, FIT or MoM with an array forming and radiating network was seen as possible solution. This chapter concentrates on the development of such a hybrid method and the respective implementation.

3.1 Method concept

The basic concept of the presented method is to analyse the radiating elements of an array by performing a decomposition of the active radiating region in smaller discrete regions that can be modeled by equivalent sources. These sources are described by electrical currents that are acquired by means of numerical techniques applied to volume, for instance FDTD or FIT, or by means of the cavity model. Furthermore, the method calculates the electromagnetic far field of an antenna array by applying analytical radiation formulae on the obtained active region of the entire array.

For it, conditioned to the availability of input data the method can be initialized by recovering necessary values for the method treatment. In addition, the array structure, including the form of its elements, has to be generated. Furthermore, the array element has to be modeled by means of its radiation characteristics. Besides, it is essential to obtain the current values of the active region of the array elements, namely at the metallic patches. In the following, the array composed by elements, based on the latter modeling, has to be far field analysed. The last step is the implementation of the radiation network giving the desired radiation characteristics for the entire array. Figure 3.1 depicts the latter mentioned stages of the method.

The modeling of the single array element is made by means of elementary dipoles. Like proposed in [11] and [51] the active radiating region, namely the patch, can be decomposed on single elementary dipoles lying on the patch surface. These equivalent sources can be defined in order to take into account the interaction between dielectric and metallic patch. The reason for this is, that in typical cases both the antenna's structure and surrounding region are formed by a relatively small number of homogenous volumes of dielectric material. As a result, the field in such volumes can be represented by equivalent electric and magnetic current densities located at the boundaries of these volumes [23]. The use of such equivalent surface sources minimizes the number of unknowns required to determine both the field inside the antenna structure, as well as in the far field region. The latter approach implies that the current distribution on the active region of the patch antenna should be known. There are two possibilities to obtain these currents values. First option, and possibly the most accurate one, is to calculate the surface current on the patch element with the help of realiable methods like the FDTD, FIT or MoM. Second possibility is to use an approximation model like the cavity model in order to generate

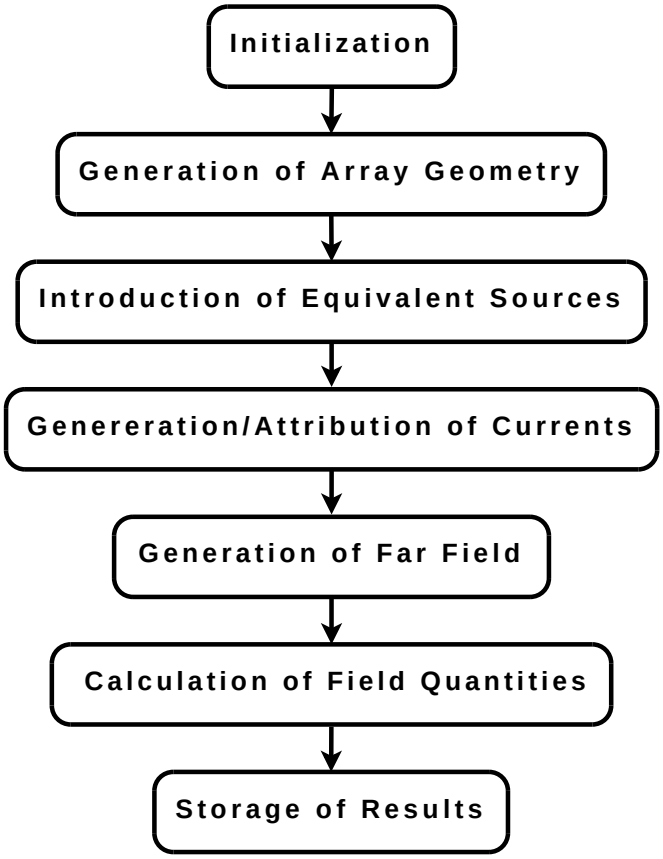

Figure 3.1 : *Structure of the Equivalent Sources Method*

analytic currents on the patch.

Concerning the second stage for the modelling of a non-orthogonal large finite array the conformal structure has to be adequately described. For it, in the proposed approach of the present thesis work, the generation of a large finite array is divided in two realization parts in order to cope efficiently with this task. The first part yields to build from the antenna element a small antenna array, namely a subarray, taking into account the mutual influence between the array elements known as mutual coupling. The second part approaches the realization of the large finite array structure by using the generated subarrays as elements. Furthermore, the option of composing the entire array with array elements is available. The challenge of producing a conformal structure for the antenna array itself can be coped by approximating the conformal array elements with flat array element on a curved structure, as it is proposed by Werner *et al.* in [46] and Allard *et al.* in [77]. Furthermore, this simplification is only possible for a certain moderate degree of curvature as Werner *et al.* [46] imply. Nevertheless, for many problems of practical interest, like an array on a fusilage, sufficient accuracy can be achieved by solving this problem via this approximation. Moreover, this approach simplifies the use and the adaptation of the analytical formulae.

In addition to that, it has to be mentioned that conformal array approximations with planar subarrays [56], [57] and planar elements [77] has been already realized. Moreover, certain techniques that derive from these approximations like Kalinchev's "three segment array" [57] have

been developed. The basic idea of these approaches is to profite from known planar array or element characteristics for further analysis or synthesis. Concerning the procedure for building the conformal array structure in the present thesis work, it has to be added, that unlike the last approaches it is independent of the degree of curvature of the array element. Thus, despite the approximation of the conformal antenna with a planar counterpart in the present thesis work, the construction of the conformal array and the field analysis concept are general.

The last stage of this method concerns the radiation network that calculates the electric far field of the conformal array. Moreover, it computes the radiation pattern and the directivity of the entire antenna system. Besides that, the possibility of performing beam steering is given. Therefore, analytical formulae coming from antenna theory are implemented. Furthermore, modules for the generation of files containing calculated data of far field measure quantities are implemented. In addition to that and for reasons of visualization, additional modules for the generation of pattern and directivity diagrams are implemented. For it, the information stored in the data files is used.

3.2 Algorithm structure and development proceeding

In order to put the approach into practice, an algorithm has been developed. The algorithm development proceeding follows strictly the method concept stages. Consequently, the first development step has the purpose of generating the radiated far field of a single antenna. For that, it is necessary to find a way of modelling the unitary array element. This goal is reached by decomposing the radiating region of this element, namely the patch, in several contributing radiating points. The option of modelling the metallic patch of the microstrip antenna as flat or with a certain degree of curvature is available. The latter is realized by means of a distribution application. From the modelled array element, an array of small size it is built. The already existing distribution application used for positioning the radiating points also allows the modelling of arrays with a conformal shape. The resulting subarray permits the realization of the large array. The last development step is the realization of the far field analysis in order to obtain the desired quantities.

The algorithm structure of the modelling process is based on the afore given method stages. The first stage is the initialization, where the input data defined by the user is retrieved from the respective files. Consequently, by means of this information certain constants and variable values are defined. The next stage starts with the calculation of the array geometry in space using the acquired input data. This comprises the positioning of each array element (and subarray) plus the calculation of the respective normals on the planar or conformal bearer. As next step follows the positioning and normals calculation of the equivalent sources for each array element. This component operates analogue to the former stages. Furthermore, the orientations of each equivalent sources is computed if required. The fourth process component handles the current distribution on all equivalent sources. Therefore, the excitations are retrieved from files with pre-calculated values or they are approximated by means of the cavity model. The next module realizes the calculation of the electric far field. Herein, the computations are done by means of analytical formulae. The sixth component contains a generator of far field quantities such as radiation pattern and directivity. Furthermore, a field conversion between spherical and cartesian coordinates can be here performed. The latter module is the generation of files

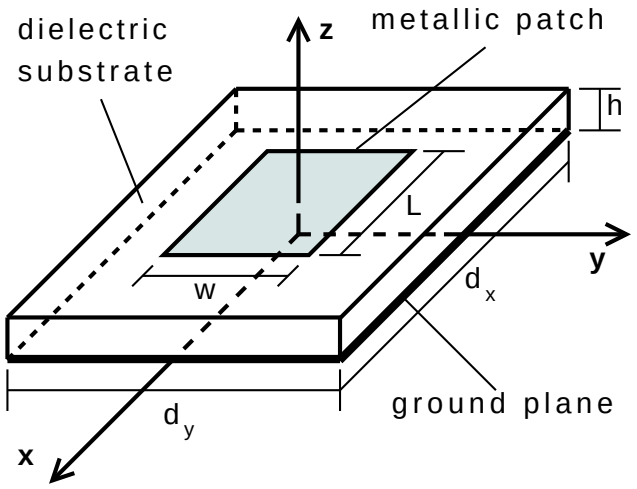

Figure 3.2 : *Single layer patch antenna*

containing all the gained data.

The development of the algorithm in the present thesis work starts, in contrast to its structure, by defining the array element and continues step by step to the desired large array. Consequently, the algorithm will be presented to the reader by going further in detail along the aforementioned development steps.

Moreover, it is necessary for the method and respective algorithm to know the array element to be handled. This element is a planar microstrip antenna and it is described graphically in figure 3.2. The microstrip patch antenna depicted is characterized by a metallic patch of negligible thickness, a dielectric substrate with a certain permittivity ε_r and a ground plane of certain thickness. Furthermore, in this picture L and W give the dimensions of the patch, h the thickness of the substrate, and d_x as well as d_y the cell dimensions, respectively. The antenna array to be modelled can be seen as a composition of element cells. Each of these cells is described then by the latter antenna and consequently the dimensions of the cell are equivalent to the array spacing values.

3.3 Patch antenna modelling by equivalent sources

In order to model the patch array element by means of sources, the *Equivalence Principle* presented in chapter 1 is applied. This principle states that a real and a "ficticious" source are equivalent within a region if both produce the same fields in that region. These "ficticious" sources are described by their electric and magnetic currents. The currents can be obtained from the magnetic and electric tangential fields on the boundary limit. In the analysed case of the present thesis work, this boundary is equivalent to the patch of the microstrip antenna and its entourage. Consequently, the radiating patch can be seen as the sole active radiating region. Therefore, the group of equivalent sources must lie on the latter two dimensional boundary. Furthermore, in order to model the radiating patch with equivalent sources, the metallic patch

surface must be discretized.

The sought radiating field of the microstrip antenna can be determined from these equivalent sources by using analytical formulae for the free space case. In the method developed in the present thesis work, the equivalent sources have only electric currents. These excitations are calculated with the help of the tangential $\vec{H}$ field components at the boundary, namely at the metallic patch level. For it, external software based on FDTD, FIT or MoM can be used. There exist also the possibility of obtaining the required currents by the analytical way. Both approaches are presented in detail later on.

3.3.1 Patch surface discretization

In order to yield the modelling of a microstrip antenna with equivalent sources the patch surface of the antenna has to be discretized in small elements. This is performed by dividing the patch surface in several small surfaces. Each of this small surface elements is then represented by an equivalent source. For carrying out the latter steps, it is necessary to define the patch surface form with discrete points and to attribute the equivalent sources to these points. Furthermore, these discrete points are equivalent to the geometrical centre of the surface elements. The surface definition and the source attribution in the latter procedure steps are performed by a position distribution algorithm. This essential component allows to realize the definition of the array structure as well as the definition of the patch surface form. Three kind of positioning modules have been developed in the present thesis work that perform such a position distribution. They have been conceived with the purpose of defining planar, cylindrical and spherical structures. They are presented to the reader later on. It has to be said that, the microstrip antennas analysed in the present thesis work are supposed to be planar and therefore the planar positioning algorithm has been used.

Independent of the patch shape, the discretization of the radiating surface results in $M \cdot N$ small surface elements. Furthermore, the positioning algorithms yields a $M \times N$ matrix containing all positioning vectors towards the geometrical centre of these discrete surfaces. For each geometrical point described by the resulting position matrix, an equivalent source is defined. The assigned sources have their respective currents and lie equidistant along the patch surface, which is limited by its dimensions. Moreover, depending of the information about the patch geometrical dimensions the points given by the positioning vectors form a rectangular shape or even a square.

3.3.1.1 Mask according to the patch shape

The afore described discretization procedure of the patch surface garantees the layout of a patch shape of rectangular or quadratic kind but it is not suitable for elliptical or circular shapes. Consequently, it is neccessary to give the possibility of conceiving different shapes. This is realized by the introduction of masks. A mask approximates the patch boundary, which is a closed linear curve, by indicating in a mask matrix the presence of an element with a 1 or the non-presence with a 0 at the respective index location. This matrix is later on applied on the position matrix of the equivalent sources in order to activate or deactivate the radiation of certain sources. This means that the resulting group of sources, that radiates, is the equivalent to the radiating patch taking into account its shape.

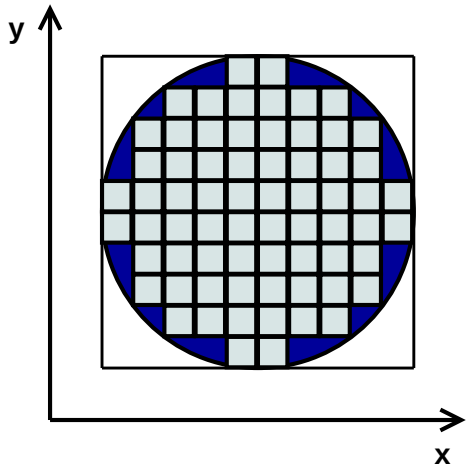

Figure 3.3 : *Mask for circular patch form*

For instance, figure 3.3 shows a possible approximation of the circular patch form by square segments, which contain the equivalent sources. In the present thesis work a mask module for the approximation of circular shape patches has been created. This module is based on the latter approach. For it, the distance of each equivalent source position in reference to the geometrical centre of the patch is compared to the radius of the desired circular shape. The sources outside the circular boundary are deactivate, the other sources contribute to the radiation of the patch. Furthermore, the accuracy of the patch form approximation depends on the number of equivalent sources used: the more sources are used for representation of the patch, the more accurate is the approximation of the curved patch form.

3.3.2 Far field radiation of an equivalent source

As aforementioned, every patch surface element is represented by an equivalent source that is described in the present thesis work by its respective currents. Applying the Equivalence Principle on this model, each patch surface element is characterized by an equivalent electric current. This excitation quantity depends on the difference between the magnetic fields at the boundary, this is, above and below the radiating patch. The equivalent source can be handled as an infinitesimal dipole. Consequently, the radiated electric far field $\vec{E}$ can be calculated by means of the magnetic vector potential $\vec{A}$ as shown in equation (1.73) in chapter 1. Moreover, the vector potential can be obtained knowing the excitation current with the equation (1.72).

Furthermore, both formulae can be simplified by using the far field approximations given in (1.74) in chapter 1. Consequently, the equations (1.76) and (1.77) are obtained. Assuming that the the radiating patch of the microstrip antenna is discretized and approximated by $M \cdot N$ equivalent sources, then the vector potential $\vec{A}_{ij,mn}$ of a surface element (m,n) for the observation point $\vec{r}_{ij}$ in direction (θ_i, ϕ_j) is given by

$$\vec{A}_{ij,mn} \simeq \frac{\mu I_{mn} \vec{l}_{mn}}{4\pi r_{ij}} e^{-\mathrm{j}k_0(r_{ij} - r_{mn}\cos\psi_{ij,mn})} \tag{3.1}$$

$\vec{l}_{mn}$ is the oriented length of the infinitesimal dipole. r_{ij} and r'_{mn} are the magnitudes of

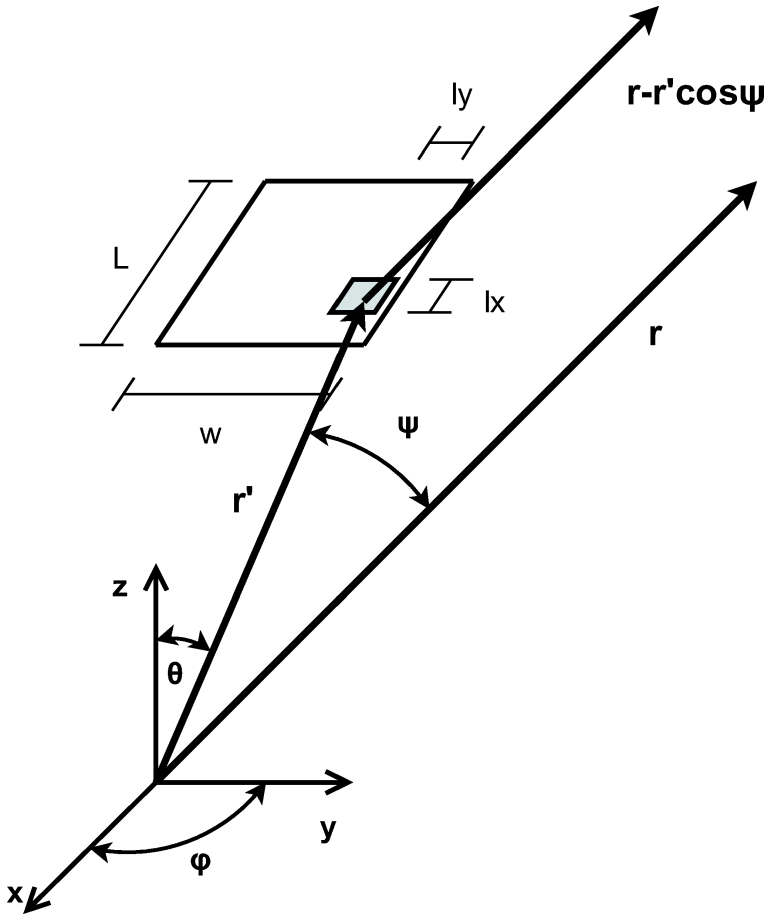

Figure 3.4 : *Patch surface element position for antenna system analysis*

the position vectors towards the observing point $\vec{r}_{ij}$ and towards the source $\vec{r}'_{mn}$, respectively. The spatial angle $\psi_{ij,mn}$ is calculated by means of the aforementioned vectors. Therefore, the relationship between the vectors $\vec{r}_{ij}$ and $\vec{r}'_{mn}$ and the cosine of the angle $\psi_{ij,mn}$ that is enclosed by these vectors is used in the following way

$$\cos\psi_{ij,mn} = \frac{\vec{r}_{ij}\cdot\vec{r}'_{mn}}{|\vec{r}_{ij}||\vec{r}'_{mn}|} \qquad \Longrightarrow \qquad \psi_{ij,mn} = \arccos\left(\frac{\vec{r}_{ij}\cdot\vec{r}'_{mn}}{|\vec{r}_{ij}||\vec{r}'_{mn}|}\right) \tag{3.2}$$

Figure 3.4 depicts an example for a discretized patch. The patch lies parallel to the x-y-plane and is discretized in $M \cdot N$ rectangular surface elements. The reader can observe the position of one of these elements. The observation point lies in the far field hence the vectors between the origin and the surface element are nearby parallel.

In order to handle the discretized elements as infinitesimal dipoles, the magnitude of $\vec{l}_{mn}$ must be infinitesimal small. Technically speaking, this size must be smaller than a tenth of the wavelength. Consequently, this magnitude is limited and hence defined by the wavelength $\lambda = \frac{c_0}{\sqrt{\varepsilon_r} f}$, which depends of the regarded frequency f and the medium's permittivity ε_r, and by the discretization numbers M and N.

In order to simplify the handling of the spatial angles, the analysis of the far field is done

in spherical coordinates. But for reasons of simplicity, it is less difficult to attain the magnetic vector potential using Cartesian coordinates. Therefore, the vector potential is calculated first in Cartesian coordinates and then it is converted by means of a coordinate transformation matrix (see appendix A) into spherical ones. The magnetic vector potential components in spherical coordinates has the following form

$$\begin{aligned} A^{r}_{ij,mn} &= A^{x}_{ij,mn}\sin\theta_i\cos\phi_j + A^{y}_{ij,mn}\sin\theta_i\sin\phi_j + A^{z}_{ij,mn}\cos\theta_i \\ A^{\theta}_{ij,mn} &= A^{x}_{ij,mn}\cos\theta_i\cos\phi_j + A^{y}_{ij,mn}\cos\theta_i\sin\phi_j - A^{z}_{ij,mn}\sin\theta_i \\ A^{\phi}_{ij,mn} &= -A^{x}_{ij,mn}\sin\phi_j + A^{y}_{ij,mn}\cos\phi_j \end{aligned} \tag{3.3}$$

$A^{x}_{ij,mn}$, $A^{y}_{ij,mn}$ and $A^{z}_{ij,mn}$ are the vector potential cartesian components and $A^{r}_{ij,mn}$, $A^{\theta}_{ij,mn}$ and $A^{\phi}_{ij,mn}$ are the spherical counterparts. In the end, the complex components of the electric far field $\vec{E}_{ij,mn}$ from a discretized surface element (m,n) for the observation point $\vec{r}_{ij}$ in direction (θ_i,ϕ_j) can be given by the following equation set

$$E^{r}_{ij,mn} \simeq 0 \tag{3.4}$$

$$E^{\theta}_{ij,mn} \simeq \frac{k_0^2 I_{mn} e^{-\mathrm{j}k_0(r_{ij}-r'_{mn}\cos\psi_{ij,mn})}}{\mathrm{j}2\pi\omega\varepsilon_0 r_{ij}}(l^{x}_{mn}\cos\theta_i\cos\phi_j + l^{y}_{mn}\cos\theta_i\sin\phi_j - l^{z}_{mn}\sin\theta_i) \tag{3.5}$$

$$E^{\phi}_{ij,mn} \simeq \frac{k_0^2 I_{mn} e^{-\mathrm{j}k_0(r_{ij}-r'_{mn}\cos\psi_{ij,mn})}}{\mathrm{j}2\pi\omega\varepsilon_0 r_{ij}}(-l^{x}_{mn}\sin\phi_j + l^{y}_{mn}\cos\phi_j) \tag{3.6}$$

These equations were implemented in form of a FORTRAN code. Therefore, the given expressions were taken directly and translated to FORTRAN equivalent commands. The resulting FORTRAN functions, subroutines and structures were written in different modules and in a main program.

3.3.2.1 Validation: application on dipoles

In order to validate the developed algorithm and respective code, certain cases handling finite length dipoles have been simulated by means of a small program in FORTRAN. Figure 3.5 depicts such a dipole that is characterized by its length L and its orientation. The dipoles are modelled with the help of equivalent sources. Each finite length dipole has been discretized in K small dipole elements, which are represented by respective equivalent sources. The dipole has been fed with a sinousoidal current according to equation (1.78) in chapter 1. According to equation (1.79) the finite length dipole field is the integration of the fields generated by its equivalent sources, namely infinitesimal dipole elements. The discrete form of the latter formula for the field of the finite length dipole $\vec{E}^{dpl}_{ij}$ for an observation point (r,θ_i,ϕ_j) in the far field is

$$\vec{E}^{dpl}_{ij} = \sum_{K}^{k=1} \vec{E}_{ij,k} \tag{3.7}$$

In the latter expression $\vec{E}_{ij,k}$ is the contribution of a discrete small dipole in reference to the observation point (r,θ_i,ϕ_j).

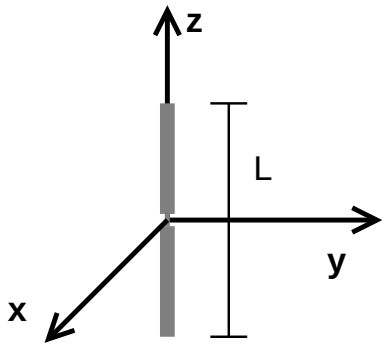

Figure 3.5 : *Geometry of a finite length dipole z-direction oriented*

Moreover, for each finite length dipole case, the coordinates origin has been defined as the dipole's geometrical centre. Consequently, the origin is the reference point for the symmetrical positioning of all equivalent sources. The dipole's length has been defined along one of the axes of the coordinates. Thus, the K positions of the resulting dipole elements have been distributed symmetrically along the chosen axis. The length of each dipole element has been fixed to $\Delta l = \frac{\lambda}{10}$. The number of elements is $K = \frac{L}{\Delta l}$ and hence it depends of the wavelength λ and of the length of the dipole L. The positioning of the dipole elements, and consequently of the equivalent sources, has been done by changing the value of the coordinate of the respective chosen axis. The coordinates of these K sources have been saved in a K-sized vector. Due to the choice of the origin as reference point, these vector is the positioning vector $\vec{r}'_k$ of all dipole elements. Concerning the current values at the sources, they have been calculated using the sinusoidal current distribution presented in expression (1.78) in chapter 1. In this validation case all oriented lengths of the dipole elements are equal. Moreover, the oriented length is related with the orthonormal vector of the axis $\vec{\imath}$, where at the finite dipole expands. Hence $\vec{l}_k = \vec{l} = \Delta l \cdot \vec{\imath}$. For instance, if the finite dipole is aligned to the x-axis, then $\vec{l}$ has only x-components. The other components in y and z-direction have the value zero. The latter, simplifies the calculation procedure of these validation cases.

The contributions $\vec{A}_{ij,k}$ to the magnetic vector potential due to each elementary dipole have been attained by inserting all the aforementioned necessary input values in the expression (3.1). Therein, the equation is adapted by defining $m = k$ and $n = 1$. Furthermore, the for the vector potential calculation indispensable angle $\psi_{ij,k}$ has been obtained applying the position vector $\vec{r}'_k$ and the vector towards the observing point $\vec{r}_{ij}$ on equation (3.2). There are $N_\theta \cdot N_\phi$ observing points and hence $i = 1,\ldots,N_\theta$ and $j = 1,\ldots,N_\phi$. It has to be reported, that a special case take place if the discretized finite dipole expands along the z-axis. Here, the angle values $\psi_{ij,k}$ coincide with the ones of the spatial angle θ for the respective observing points. Consequently, if the observation points are given in spherical coordinates, then the θ values corresponding to the latter points can be taken for the $\psi_{ij,k}$ values saving additional calculation. For the cases, wherein the discretized dipole is positioned along the x or y-axis, the values $\psi_{ij,k}$ and θ_i are related to each other as $\psi_{ij,k} = \frac{\pi}{2} - \theta_i$.

The obtained vector potential contributions in Cartesian coordinates $\vec{A}_{ij,k}$ are then converted into spherical components $\vec{A}^{sph}_{ij,k}$ by using the respective transformation matrix.The electric far

```
Allocation matrix E_{n_θ,n_φ}
Definition θ = 0
Definition φ = 0
Definition rad = 1.0 · 10^4
for i=1,N_θ
    Calculation of θ_i with Δθ and i
    for j=1,N_φ
        Calculation of φ_j with Δφ and j
        Calculation of r⃗_ij with rad, θ_i, φ_j
        Conversion from r⃗_ij into x⃗_ij
        Defintion Δl = λ/K
        Definition E_dipole = 0
        for k=1,K
            Assignation of x⃗'_k and I_k
            Calculation of ψ_ij,k with x⃗_ij and x⃗'_k
            Definition of l⃗_k with value Δl and vector τ⃗
            Calculation of A⃗_ij,k with I_k, l⃗_k and ψ_ij,k
            Conversion from A⃗_ij,k into A⃗^sph_ij,k
            Calculation of E⃗_ij,k with A⃗^sph_ij,k
            Summation of E⃗_ij,k to E⃗^dpl_ij
        end
        Storage of E⃗^dpl_ij in E⃗_i,j
    end
end
```

Table 3.1 : *Code structure for far field calculation of a modelled finite length dipole*

field is then computed according to (1.77) by means of the vector potential results. Furthermore, an observation space in spherical coordinates has been defined for the calculation of the far field. This space is characterized by the respective spherical vector composed of its radial component r and its two angular components, these are, in elevation θ and azimuth ϕ, respectively. Because of the far field calculation, the radial value must be constant for the observing space. Moreover, it has to exhibit a huge value, for instance in this validation case $r = 1.0 \cdot 10^4 m$. The N_θ θ-values and the N_ϕ ϕ-values have been defined and limited by the range $[0^\circ, 360^\circ]$. Table 3.1 shows the code proceeding for the far field analysis of this validation.

For the implementation of the aforementioned algorithm procedure, the respective functions have been embedded in three loop structured code. The code allocates a complex field matrix for the $N_\theta \cdot N_\phi$ far field vectors according to the defined observation space in the beginning. As shown in table 3.1, the loop controled variables θ and ϕ are set to their starting values before any calculation. Two merged loops "scan" the observation space by varying the values of the spatial angles. For it, at each step of the first loop the value of θ is enhanced by a $\Delta\theta$. Similarly, the value of ϕ is increased by a $\Delta\phi$, when the second loop progress. Inside these two loops the spherical vector towards the observing point $\vec{r}_{i,j}$ is defined and transformed by a matrix into a

cartesian vector $\vec{x}_{i,j}$. Furthermore, the field function value $\vec{E}_{ij,k}$ is set to its starting value and the length of the elementary dipoles Δl is computed. Then, the third loop comes into action by assignating the position of the source $\vec{x}'_k$ as well as the current I_k and defining the dipole element orientation $\vec{l}$. In addition to that, the phase $\psi_{ij,k}$ is calculated with the values of $\vec{x}_k$ and $\vec{x}'_k$. By means of all the latter values, the vector potential $\vec{A}_{ij,k}$ and the field contribution $\vec{E}_{ij,k}$ are computed. The third loop is run until the field contribution of the last dipole element is computed. At the end of these loop the attained complex vector value $\vec{E}_{ij}^{dpl}$ for the observation point (θ_i, ϕ_j) is stored as an element of the complex field matrix. At the end of the other two loops this complex matrix is filled with all electric field vectors for the defined observations points.

In order to have a comparison with other results, the analytical function for calculating a dipole oriented along the z-axis derived in [1] and presented in (3.8) in chapter 1 has been implemented by means of a small code in MATLAB. The discretized formula of the respective field function for such a dipole for the $N_\theta \cdot N_\phi$ observing points with the form (θ_i, ϕ_j) has the following form

$$\begin{aligned} E_{ij}^{r} &= 0 \\ E_{ij}^{\theta} &= \mathrm{j}Z_0 \frac{I_0 e^{-\mathrm{j}k_0 r_{ij}}}{2\pi r_{ij}} \cdot \frac{\cos(\frac{k_0 l}{2}\cos\theta_i) - \cos(\frac{k_0 l}{2})}{\sin\theta_i} \\ E_{ij}^{\phi} &= 0 \end{aligned} \tag{3.8}$$

Therein, Z_0 is the intrinsic or wave impedance, k_0 the wavelength, l the dipole length, I_0 the dipole excitation and r_{ij} the distance toward the observation point in direction (θ_i, ϕ_j), respectively. The radiation pattern for both approachs and for several dipole cases has been computed. For each case the three-dimensional pattern is shown by means of cuts in elevation and azimuth direction. Furthermore, it has to be remarked that in the following cases the lengths of the dipoles are given in λ that represents the wavelength. The first case run has been for a $\frac{\lambda}{2}$ dipole. The respective pattern is shown in figure 3.6. In addition to that, the calculation result in form of the radiation pattern for a λ dipole is shown in the figure 3.7.

In diagrams 3.9 and 3.8 the plots give the graphical description of the radiation behaviour of the dipoles of length $\frac{3}{4}\lambda$ and $\frac{3}{2}\lambda$.

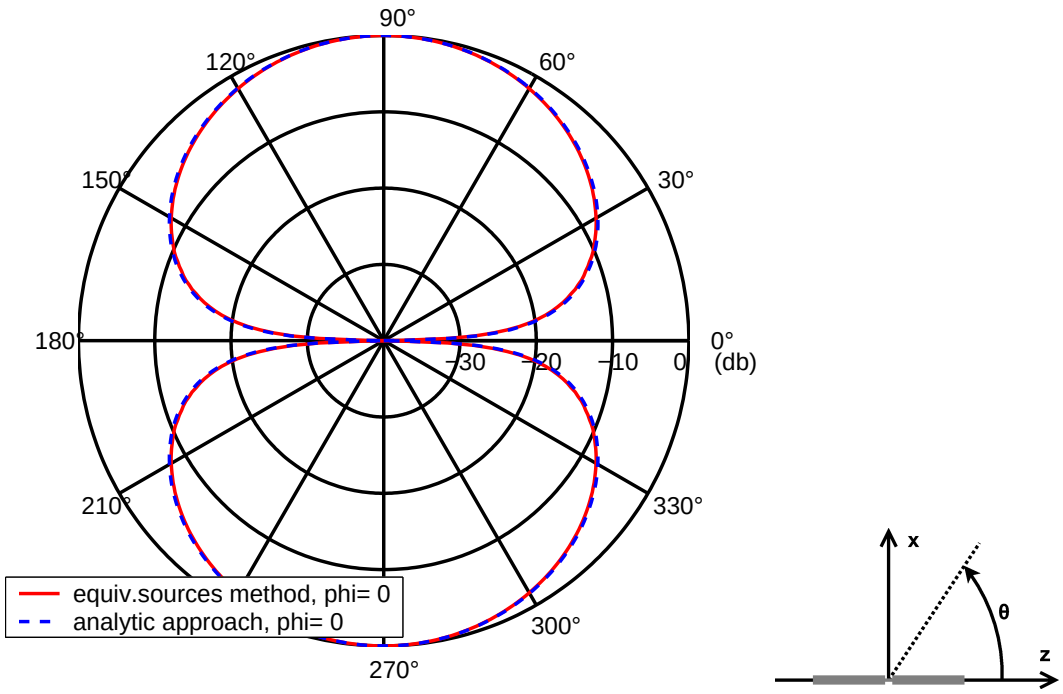

Figure 3.6 : *Pattern comparison for a* $\frac{\lambda}{2}$ *dipole in elevation*

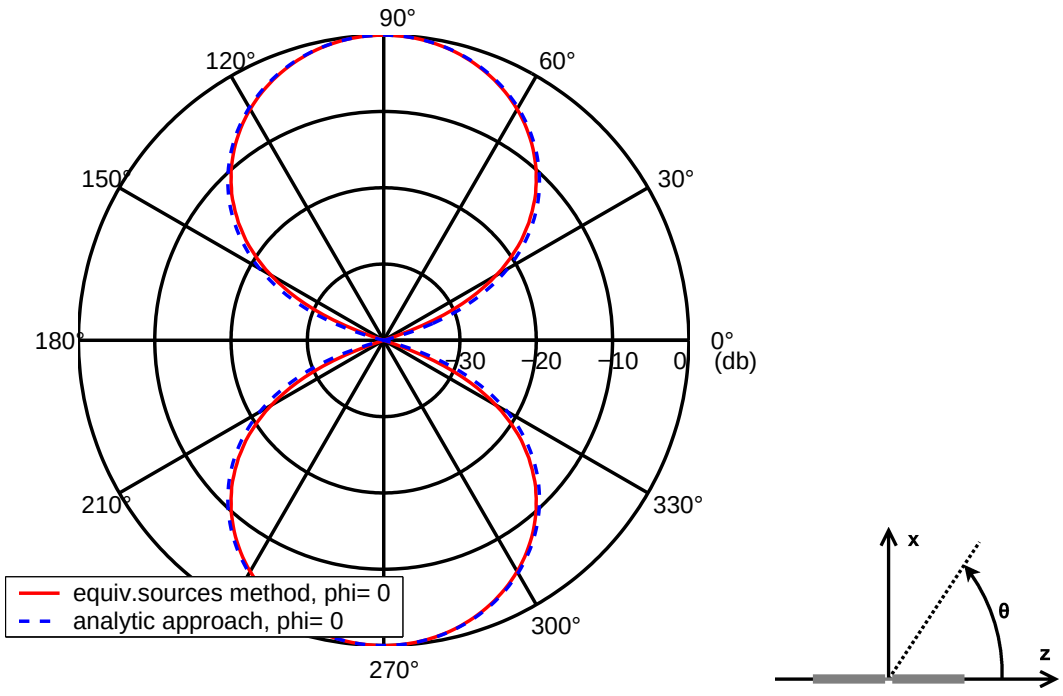

Figure 3.7 : *Pattern comparison for a* λ *dipole in elevation*

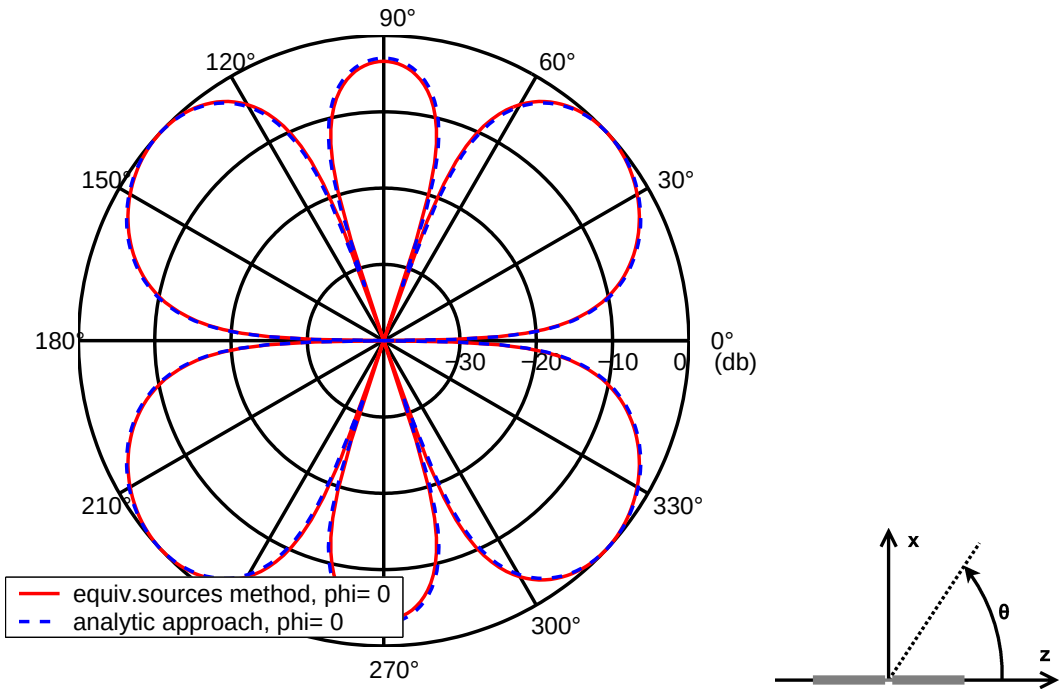

Figure 3.8 : *Pattern comparison for a* $\frac{3}{2}\lambda$ *dipole in elevation*

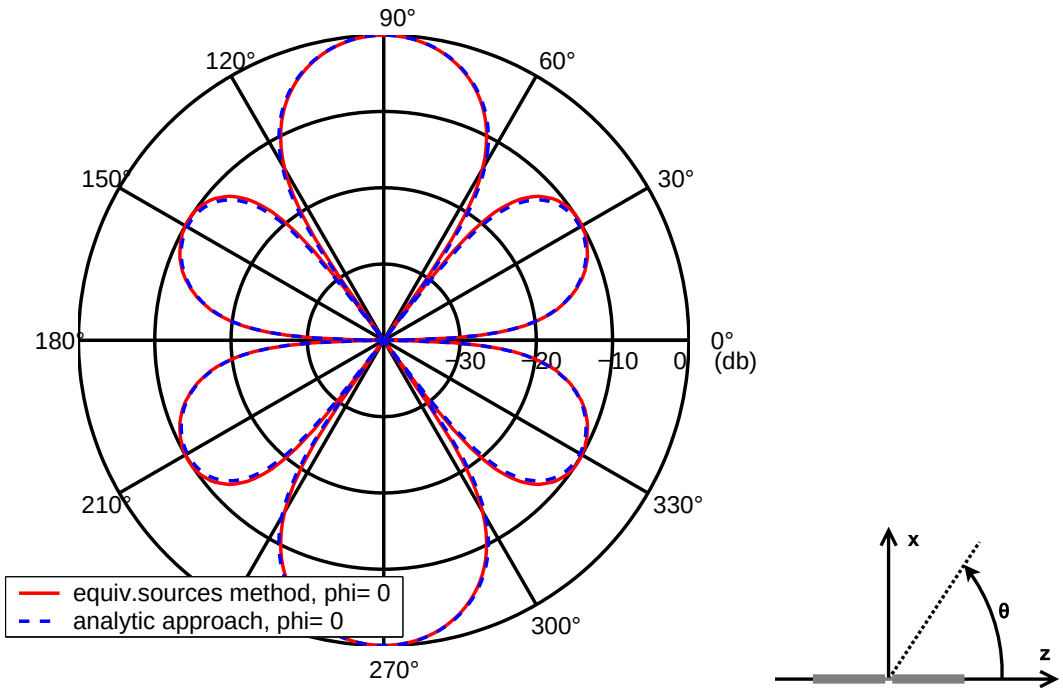

Figure 3.9 : *Pattern comparison for a* $\frac{5}{4}\lambda$ *dipole in elevation*

3.3.3 Effects of the ground plane

A microstrip antenna has in the general case always a ground plane. This metallic plate has an important influence on the antenna radiation. Therefore, it has to be included into the patch antenna model. In chapter 1 the radiation influence an infinite perfect electric conductor (PEC) plate on a simple dipole has been examined. In the respective example, the dipole is positioned parallel to the PEC plane at a certain distance, as it is the case for the equivalent sources used for representing the patch surface of the microstrip antenna. Consequently, the currents of the equivalent sources are oriented parallel to the ground plane. Moreover, equation (1.86) shows that the reflected waves enhances the radiation by a so-called "array factor". Thus, this influence on the antenna radiation can be taken into account by applying such a factor on every equivalent source of the patch antenna model. Consequently, the following "array factor" function, which is dependant on the source regarded, is multiplied to the electric field function of the sources. Furthermore, the values underneath the ground plane have to be nulled. The resulting expression is

$$\vec{E}_{ij,mn}^{GPE} = \begin{cases} \vec{E}_{ij,mn} \cdot 2\mathrm{j}\sin(k_0 h \cos\xi_{ij,mn}) & \text{for} \quad -\frac{\pi}{2} < \xi_{ij,mn} < \frac{\pi}{2} \\ 0 & \text{else} \end{cases} \tag{3.9}$$

at which h is the distance between ground plane and the equivalent source. The spatial angle shift $\xi_{ij,mn}$ is enclosed by the normal vector $\vec{n}_{mn}$ of the patch surface element (m,n) and the distance vector $\Delta\vec{r}_{ij,mn}$ between the source position point and the observing point. Thus, the angle $\xi_{ij,mn}$ can be calculated by the following formula

$$\cos\xi_{ij,mn} = \frac{\Delta\vec{r}_{ij,mn} \cdot \vec{n}_{mn}}{|\Delta\vec{r}_{ij,mn}| \cdot |\vec{n}_{mn}|} \qquad \Longrightarrow \qquad \xi_{ij,mn} = \arccos\left(\frac{\Delta\vec{r}_{ij,mn} \cdot \vec{n}_{mn}}{|\Delta\vec{r}_{ij,mn}| \cdot |\vec{n}_{mn}|}\right) \tag{3.10}$$

The distance vector is defined as $\Delta\vec{r}_{ij,mn} = \vec{r}_{ij} - \vec{r}'_{mn}$. Therein, $\vec{r}'_{mn}$ is the source position vector, $\vec{r}_{ij}$ is the vector towards the observing point in direction (θ_i, ϕ_j), respectively. It has to be remarked that the expression (3.9) is a discretized version of equation (1.86) presented in chapter 1. Furthermore, due to angle $\xi_{ij,mn}$'s dependancy of the normal vector of the metallic ground surface and of the source position vector, expressions (3.9) and (3.10) allow to model an infinite ground plane described by any arbitrary planar surface in space. Moreover, it can be denoted that the normal vector can be retrieved mathematically by doing partial derivatives on the surface function at the required or analysed geometrical point. A more detailed description of this calculation can be found in appendix A. There, the formula for obtaining the normal vector of a tangent plane at a certain point is given.

3.3.3.1 Validation: different dipoles over a ground plane

Certain cases, wherein finite length dipoles are modelled by equivalent sources, have been analysed in order to validate the ground plane effects. Figure 3.10 shows the dimension and the geometrical position of such a dipole. In each validation case the infinite dipole element far field has been calculated by using the field function of the afore given expression (3.9). Furthermore, expression (3.7) has been used in order to calculate the total field of the finite length dipole. The validation of the ground plane modelling has been realized in the same way as the former presented validation of the source modelling. Consequently, the proceeding of the algorithm is the same as for the source modelling algorithm: the dipole is symmetrically modelled

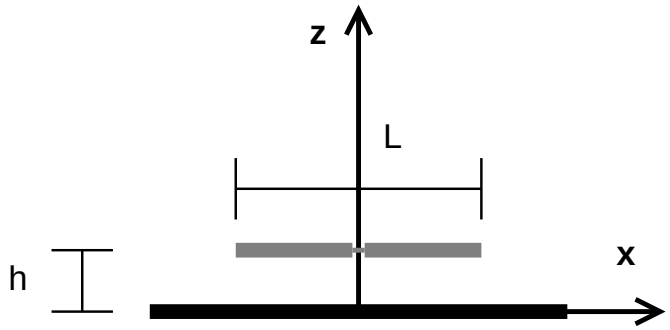

Figure 3.10 : *A x-direction oriented dipole positioned over a PEC layer*

along one of the coordinates axis with the coordinates origin as reference point and by means of K equivalent sources. All sources are treated as elementary dipoles of same length Δl and oriented in $\vec{l} = \Delta l \cdot \vec{\imath}$. The vector potential contribution $A_{ij,k}$ of each dipole element is computed by means of the angle $\psi_{ij,k}$, the excitation I_k, the oriented length $\vec{l}$ and vectors $\vec{r}_{ij}$ and $\vec{r}'_k$ according to (3.1). The latter equation has been adapted to the dipole cases by defining $m = k$ and $n = 1$.

Furthermore, the cartesian $A_{ij,k}$ is transformed into the spherical $A^{sph}_{ij,k}$ that is used to obtain the field contribution $E_{ij,k}$. This field contribution is the required field in equation (3.9) in order to yield the radiated field with the ground plane effect $\vec{E}^{GPE}_{ij,k}$. For it, the angle $\xi_{ij,k}$ has been calculated by means of the vectors $\Delta\vec{r}_{ij,k}$ and $\vec{n}_k$. The first vector has been attained by subducting the source position vector from the vector towards the observation vector, this is $\Delta\vec{r}_{ij,k} = \vec{r}_{ij} - \vec{r}'_k$. Concerning the definition of the normal vector $\vec{n}_k$ for each equivalent source, one of the orthonormal axis vectors, which are orthogonal to the dipoles orientation, has been chosen as respective normal vector. The choice has been done according to the desired placement of the infinite PEC plate. Since all the sources lie on the same axis in a queue and the planar ground surface is infinite, all the K elements have the same normal vector $\vec{n}_k = \vec{n}$. Moreover, a special case takes place if the geometrical location of the discretized dipole is on the x-y-plane and if the dipoles length is small in comparison to the distance towards the observing point. The spatial angle $\xi_{ij,k}$ overlaps with the region of the angle θ_i. Thus, this spatial angle can be obtained by means of the elevation values, fact that diminish the computer calculations. Another special case happens for a placement of the finite dipole along the z-axis: the spatial angle becomes $\xi_{ij,k} = \frac{\pi}{2} - \theta_i$.

Concerning the implementation of the algorithm, the code structure given in table 3.1 has been used, however, the latter has been extended with the calculations of the ground plane's normal vector $\vec{n}_k$, the difference vector $\Delta\vec{r}_{ij,k}$, the angle $\xi_{ij,k}$, and the field contribution with the ground plane effect $\vec{E}^{GPE}_k$. The respective calculation steps have been added to the third loop inside the code structure. Furthermore, the observation space has been defined by $N_\theta \cdot N_\phi$ observing points (r, θ_i, ϕ_j) lying in the far field with $i = 1, \ldots, N_\theta$ and $j = 1, \ldots, N_\phi$ as well as a constant huge-valued radius $r = 1.0 \cdot 10^4$. Consequently, the resulting fields have been stored in a complex $N_\theta \times N_\phi$ matrix. Table 3.2 shows the extended third loop, which replaces the third loop of the previous code structure (table 3.1).

A comparison between the results obtained by the source modelling approach and the ones

```
Definition of start values
...
for i=1,N_θ
        ...
        for j=1,N_ϕ
                ...
                for k=1,K
                        Assignation of x'_k and I_k
                        Calculation of ψ_ij,k with x_ij and x'_k
                        Definition of l_k with value Δl and vector ι
                        Calculation of A_ij,k with I_k, l_k and ψ_ij,k
                        Conversion from A_ij,k into A^sph_ij,k
                        Calculation of E_ij,k with A^sph_ij,k
                        Calculation of n_k with ι
                        Calculation of Δr_ij,k with x_ij and x'_k
                        Calculation of ξ_ij,k with n_k and Δr_ij,k
                        Calculation of E^GPE_ij,k with E_ij,k and ξ_ij,k
                        Summation of E^GPE_ij,k to E^dpl_ij
                end
                Storage of E^dpl_ij in E_i,j
        end
end
```

Table 3.2 : *Part of the code structure for far field calculation of a modelled horizontal dipole*

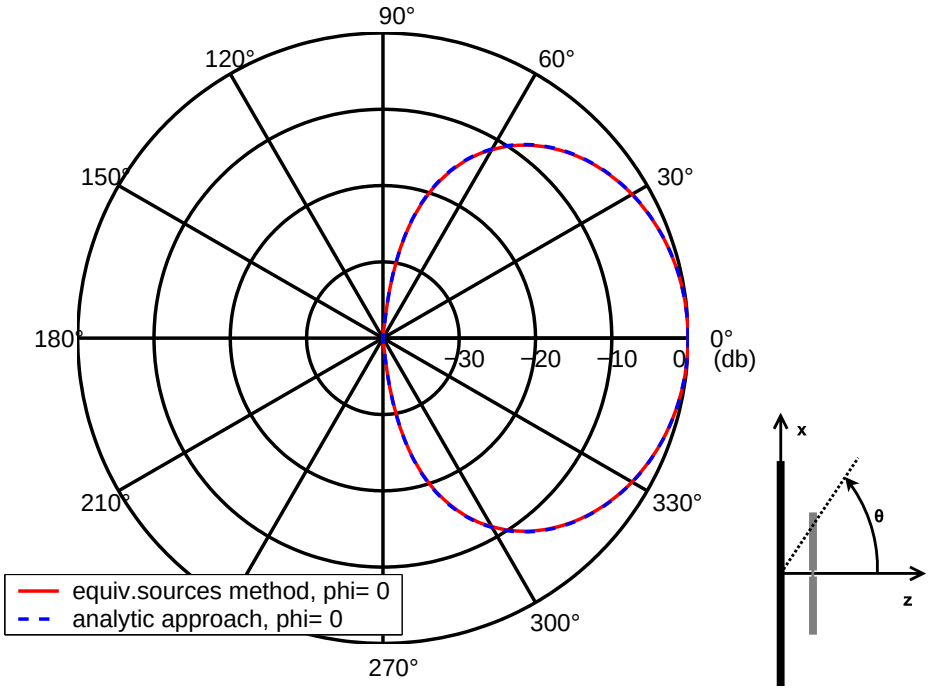

Figure 3.11 : *Pattern comparison for a* $\frac{\lambda}{10}$ *dipole at* $h = \frac{\lambda}{8}$ *over a PEC plane in elevation*

by using straigthforward the analytical functions for the ground plane effect on a dipole has been made. For it, the analytical equation (1.86) of chapter 1 has been evaluated using the previous presented analytical function for computing a dipole oriented along the z-axis in (3.8). Both formulae have been implemented in an MATLAB code. The radiation pattern for the analytical and the source modelling approachs for the case of a $\frac{\lambda}{10}$ elementary dipole.

Furthermore, the influence of the distance *h* between radiation element and PEC layer on a λ finite length dipole is presented in the following figure 3.15. The air-filled region separates with its thickness *h* the metallic ground plane from the radiating dipole. The reflecting metallic layer of infinite size is characterized by a perfect conducting behaviour and by a negligible thickness. As in the validation for the dipole modelling, the dipole of length λ is fed with a sinousoidal current according to equation (1.78) in chapter 1.

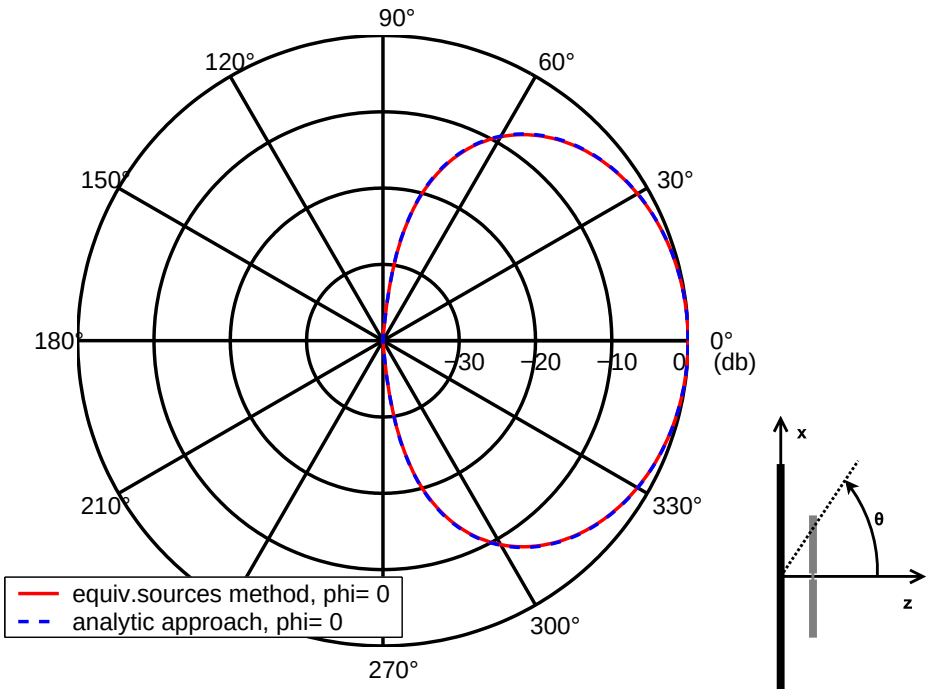

Figure 3.12 : *Pattern comparison for a* $\frac{\lambda}{10}$ *dipole at* $h = \frac{\lambda}{4}$ *over a PEC plane in elevation*

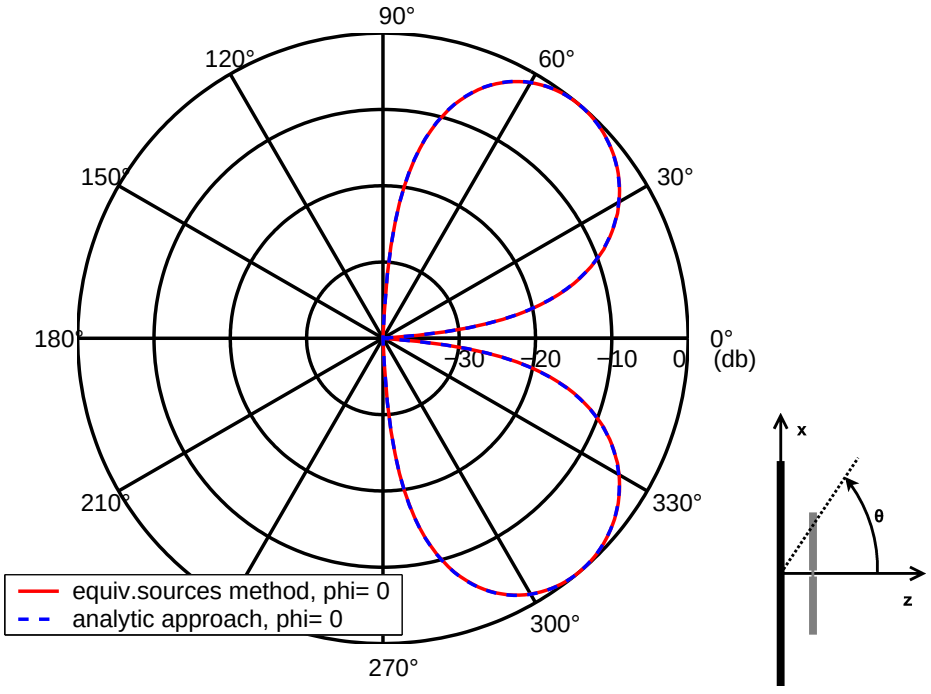

Figure 3.13 : *Pattern comparison for a* $\frac{\lambda}{10}$ *dipole at* $h = \frac{\lambda}{2}$ *over a PEC plane in elevation*

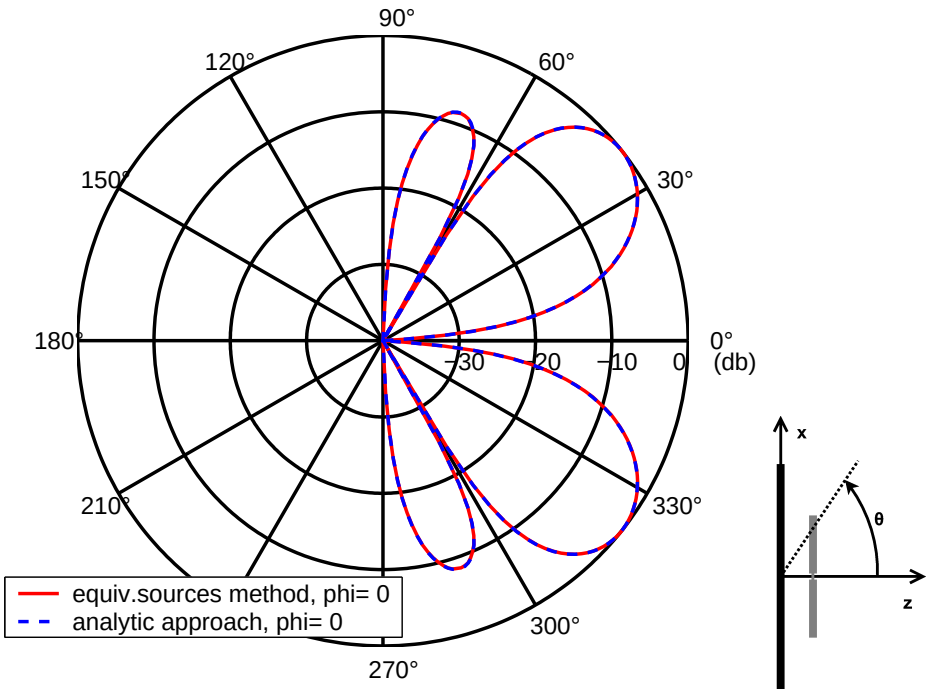

Figure 3.14 : *Pattern comparison for a* $\frac{\lambda}{10}$ *dipole at* $h = \lambda$ *over a PEC plane in elevation*

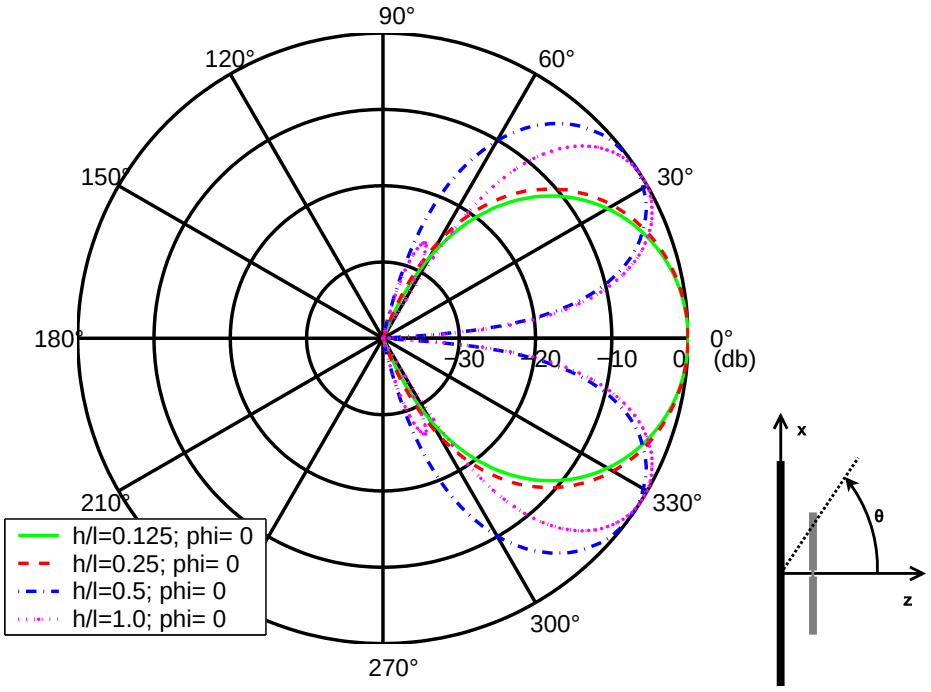

Figure 3.15 : *Pattern in elevation for a finite length dipole over a PEC plane for different heights*

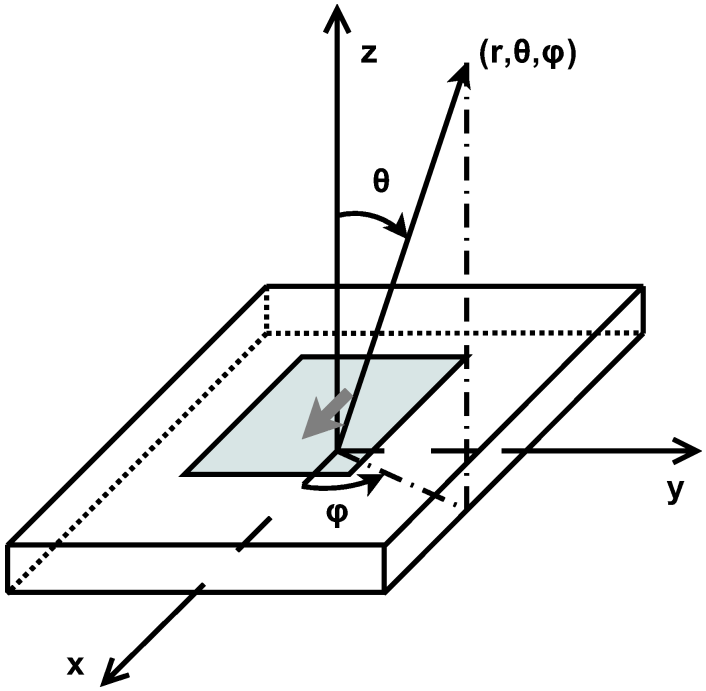

Figure 3.16 : *Geometry of a horizontal electric dipole on an infinite grounded dielectric slab*

3.3.4 Dielectric layer effects

The modelling of a microstrip patch antenna by means of equivalent sources has to take into account the influence of the dielectric layer on the radiation. Therefore, Moini-Mazandarani [11] and Bokhari *et al.* [51] developed additional functions for the far field case in order to apply them directly to the spherical field function. Furthermore, [7] presents dielectric describing functions in order to use them for patch radiation calculation. Reference [11] approachs these functions by analysing and evaluating the potential equations of a Hertztian dipole in air and in the dielectric medium. The necessary integral equations are obtained from the dyadic Green's function. These Sommerfeld integrals are solved by means of Fourier transformation.

In a similar way the second approach in [51] examines and evaluates by means of the Fourier transformation the integral equation obtained from Green's theorem for an elementary dipole that is considered to be an x-directed horizontal electric dipole (HED) on an infinite grounded dielectric slab as depicted in figure 3.16. This infinite expanding medium is limited by a second medium above and a metallic layer underneath. The second medium is composed of air and hence defined by its constant values $\sigma_0 = 0$, $\mu_0 = 1$ and $\varepsilon_0 = 1$. The first medium corresponds to a dielectric substrate described by the following values $\sigma_1 = 0$, $\mu_1 = \mu_0$, $\varepsilon_1 = \varepsilon_0\varepsilon_r$. The last layer is a perfect conducting plate that is characterized by its constant $\sigma_2 = \infty$.

By an application of the volume equivalence theorem, the dielectric layer can be replaced by equivalent volume polarisation currents. Moreover, applying image theory, the infinite ground plane is replaced by images of these currents. Hence, the entire geometry is composed by a set of equivalent currents all radiating in free space. The total field is equivalent to the superposition of all contributions of these sources. The far field $\vec{E}_{diel}^{far}$ due to the polarisation currents $\vec{J}_p$ can be given as

$$\vec{E}^{far}_{diel}(k_x,k_y,k_z) = E_{d0}\int_{-h}^{h} dz \int_{\infty}^{\infty}\int_{\infty}^{\infty} \vec{J}_p \qquad \text{with} \quad E_{d0} = -jk_0 Z_0 \frac{e^{-jk_0 r}}{4\pi r} \tag{3.11}$$

Therein, k_x, k_y and k_z are the Fourier transform variables in the spatial frequency domain, k_0 the free-space wavelength, Z_0 the intrinsic impedance and r the magnitude of the observation vector $\vec{r}$, respectively. For the latter expression, the excitation sources are assumed to be unbounded polarisation currents in the dielecric layer. Nevertheless, the resulting functions are valid for bounded sources and for an observation point outside the source region. The polarisation currents are defined as

$$\vec{J}_p(x,y,z) = \tfrac{jk_0}{Z_0}(\varepsilon_r - 1)\vec{E}^{n}_{diel} \qquad \text{for} \quad |z| \leq h \tag{3.12}$$

where $\vec{E}^{n}_{diel}$ stands for the actual electric field in the dielectric slab caused by the HED. The rectangular components for the latter field can be obtained in closed-form in the two dimensional Fourier transform domain. By introducing them into equation (3.11) and applying the Fourier integral theorem, the expression for $\vec{E}^{far}_{diel}$ reduces to a single integral along z that can be calculated. This approach is called mixed potential integral equation technique (MPIE) by Bokhari *et al.* in [51]. Consequently, the following rectangular components are obtained

$$E^{far}_{diel,x}(\theta,\phi) = j2E_{d0}\left[\frac{T\cos\theta\cos\phi^2}{D^f_{TM}} + \frac{\sin\phi^2}{D^f_{TE}}\right]\cdot(A\cos\theta - TB) \tag{3.13}$$

$$E^{far}_{diel,y}(\theta,\phi) = j2E_{d0}\cos\phi\sin\phi\left[\frac{T\cos\theta}{D^f_{TM}} - \frac{1}{D^f_{TE}}\right]\cdot(A\cos\theta - TB) \tag{3.14}$$

$$E^{far}_{diel,z}(\theta,\phi) = -j2E_{d0}\left[\frac{\cos\theta\cos\phi\sin\theta(TA - B\cos\theta)}{D^f_{TM}}\right] \tag{3.15}$$

with

$$T = \sqrt{\varepsilon_r - \sin\theta^2} \tag{3.16}$$

$$A = \sin(k_0 hT)\cos(k_0 h\cos\theta) \tag{3.17}$$

$$B = \cos(k_0 hT)\sin(k_0 h\cos\theta) \tag{3.18}$$

$$D^f_{TM} = \varepsilon_r\cos\theta\cos(k_0 hT) + jT\sin(k_0 hT) \tag{3.19}$$

$$D^f_{TE} = T\cos(k_0 hT) + j\cos\theta\sin(k_0 hT) \tag{3.20}$$

These far field components can be transformed into the spherical coordinate system by means of a coordinate transformation matrix. Knowing that the radial component of the field vanishes in the far field, only the θ and ϕ components are calculated as in the following

$$E^{far}_{diel,\theta}(\theta,\phi) = E^{far}_{diel,x}\cos\theta\cos\phi + E^{far}_{diel,y}\cos\theta\sin\phi - E^{far}_{diel,z}\sin\theta \tag{3.21}$$

$$E^{far}_{diel,\phi}(\theta,\phi) = -E^{far}_{diel,x}\sin\phi + E^{far}_{diel,y}\cos\phi \tag{3.22}$$

Furthermore, the far field of the x-directed HED and its image due to the infinite ground

plane are given by

$$E^{far}_{HED,\theta}(\theta,\phi) = j2E_{d0}\cos\theta\cos\phi\sin(k_0 h\cos\theta) \quad (3.23)$$

$$E^{far}_{HED,\phi}(\theta,\phi) = -j2E_{d0}\sin\phi\sin(k_0 h\cos\theta) \quad (3.24)$$

As aforementioned the total radiated field is the sum of the latter field contributions. Consequently, the far field of the HED on an infinite grounded dielectric layer is the superposition of the field due to the polarisation currents and the image of the field generated by the HED itself [51]. This can be written as

$$E^{far}_{\theta}(\theta,\phi) = E^{far}_{HED,\theta} + E^{far}_{diel,\theta} = E_{d0}\cdot f_\theta \quad (3.25)$$

$$E^{far}_{\phi}(\theta,\phi) = E^{far}_{HED,\phi} + E^{far}_{diel,\phi} = E_{d0}\cdot f_\phi \quad (3.26)$$

Moreover, due to the fact that the radiation contribution E_{d0} of the HED is the cause of the fields coming from the dielectric slab, this contribution can be factored out, leaving the functions f_θ and f_ϕ that represent all interactions due to the infinite grounded dielectric layer. The yielded functions f_θ and f_ϕ describe the behaviour of electromagnetic waves when they propagate across the layered stack with a structure composed of a single homogene and isotropic dielectric layer. Due to the fact, that equation (3.11) is obtained from Green's theorem and the Green's function, these dielectric effect functions are different if the number of dielectric layers is increased. Consequently, the microstrip antennas defined in the present thesis work are composed of a single dielectric layer.

For the case pictured in figure 3.16, wherein the dielectric layer spreads in the x-y-plane plus the HED is oriented in x - direction and the observing point is (r,θ,ϕ), the far field the dielectric influence functions have the following form

$$f_\theta(\theta) = \frac{2\cos\theta\cdot\sqrt{\varepsilon_r-\sin\theta^2}\cdot e^{\mathrm{j}k_0 h\cos\theta}}{\sqrt{\varepsilon_r-\sin\theta^2}-\mathrm{j}\varepsilon_r\cos\theta\cot(k_0 h\sqrt{\varepsilon_r-\sin\theta^2})} \quad (3.27)$$

$$f_\phi(\theta) = \frac{-2\cos\theta\cdot e^{\mathrm{j}k_0 h\cos\theta}}{\cos\theta-\mathrm{j}\sqrt{\varepsilon_r-\sin\theta^2}\cot(k_0 h\sqrt{\varepsilon_r-\sin\theta^2})} \quad (3.28)$$

Therein, k_0 is the free-space wavelength, ε_r the complex permittivity constant and θ the spatial angle, respectively. Furthermore, Bahl and Bharthia in [7] give the dielectric influence functions for a HED oriented in x and y direction derived by means of the vector potential approach. These are

$$f_\theta(\theta) = \cos\theta\cdot e^{\mathrm{j}k_0 h\cos\theta}\cdot\frac{\cos\theta+\frac{\frac{\varepsilon_r-1}{\varepsilon_r}\sin\theta^2}{\cos\theta+\mathrm{j}\sqrt{\varepsilon_r-\sin\theta^2}\tan(k_0 h\sqrt{\varepsilon_r-\sin\theta^2})}}{\cos\theta-\mathrm{j}\sqrt{\varepsilon_r-\sin\theta^2}\cot(k_0 h\sqrt{\varepsilon_r-\sin\theta^2})} \quad (3.29)$$

$$f_\phi(\theta) = \frac{\cos\theta\cdot e^{\mathrm{j}k_0 h\cos\theta}}{\sqrt{\varepsilon_r-\sin\theta^2}\cot(k_0 h\sqrt{\varepsilon_r-\sin\theta^2})} \quad (3.30)$$

The functions $f_\theta(\theta)$ and $f_\phi(\theta)$ are multiplied to the respective E_θ and E_ϕ component of the electric far field like in the following

$$E_{\theta,\text{diel}} = f_\theta \cdot E_\theta \tag{3.31}$$
$$E_{\phi,\text{diel}} = f_\phi \cdot E_\phi \tag{3.32}$$

From expressions (3.27) until (3.30) it becomes apparent, that functions f_θ and f_ϕ have the spatial angle θ as an essential variable. In the corresponding case the dielectric layer expands along the x-y plane and hence the z-axis becomes the normal vector of the dielectric surface and of the radiating element. Furthermore, this angle gives the inclination between the observation point (r,θ,ϕ) and the z-axis. Consequently, these functions depend geometrically mainly of the angular position of the layer with respect to the cartesian coordinates system. Moreover, this angle depends of the dielectric surface normal and the vector towards the observing point. This means that for the same dielectric layer, but that expands on an arbitrary plane, the functions f_θ and f_ϕ can be adapted with the respective angle.

In addition to that, the reader may have noticed that this angle is equivalent to the afore presented spatial angle ξ used in the ground plane modelling in equation (3.9). The latter case can be interpreted as a special case of the dielectric modelling case, wherein air is the dielectric medium. Consequently, the spatial angle ξ is calculated by the afore given formula in equation (3.10). Moreover, for the case of modelling a radiating patch by means of $M \cdot N$ element (m,n) the functions in equation set (3.32) are matched by replacing the angle θ depending functions by $\xi_{ij,mn}$ depending ones. The new adapted functions, which describe the influence of dielectric layer positioned arbitrarily in space on a source whose current is one-dimensionally directed for an observation point $(r,\theta_i,\phi_j$ in the far field, are

$$f^\theta_{ij,mn} = \frac{2\cos\xi_{ij,mn}\cdot\sqrt{\varepsilon_r-\sin\xi_{ij,mn}{}^2}\cdot e^{\mathrm{j}k_0h\cos\xi_{ij,mn}}}{\sqrt{\varepsilon_r-\sin\xi_{ij,mn}{}^2}-\mathrm{j}\varepsilon_r\cos\xi_{ij,mn}\cot\left(k_0h\sqrt{\varepsilon_r-\sin\xi_{ij,mn}{}^2}\right)} \tag{3.33}$$

$$f^\phi_{ij,mn} = \frac{-2\cos\xi_{ij,mn}\cdot e^{\mathrm{j}k_0h\cos\xi_{ij,mn}}}{\cos\xi_{ij,mn}-\mathrm{j}\sqrt{\varepsilon_r-\sin\xi_{ij,mn}{}^2}\cot\left(k_0h\sqrt{\varepsilon_r-\sin\xi_{ij,mn}{}^2}\right)} \tag{3.34}$$

Furthermore, the new adapted dielectric effect functions for a source with a two-dimensional directed current are

$$f^\theta_{ij,mn} = \cos\xi_{ij,mn}\cdot e^{\mathrm{j}k_0h\cos\xi_{ij,mn}}\cdot \frac{\cos\xi_{ij,mn}+\frac{\frac{\varepsilon_r-1}{\varepsilon_r}\sin\xi_{ij,mn}{}^2}{\cos\xi_{ij,mn}+\mathrm{j}\sqrt{\varepsilon_r-\sin\xi_{ij,mn}{}^2}\tan\left(k_0h\sqrt{\varepsilon_r-\sin\xi_{ij,mn}{}^2}\right)}}{\cos\xi_{ij,mn}-\mathrm{j}\sqrt{\varepsilon_r-\sin\xi_{ij,mn}{}^2}\cot\left(k_0h\sqrt{\varepsilon_r-\sin\xi_{ij,mn}{}^2}\right)} \tag{3.35}$$

$$f^\phi_{ij,mn} = \frac{\cos\xi_{ij,mn}\cdot e^{\mathrm{j}k_0h\cos\xi_{ij,mn}}}{\sqrt{\varepsilon_r-\sin\xi_{ij,mn}{}^2}\cot\left(k_0h\sqrt{\varepsilon_r-\sin\xi_{ij,mn}{}^2}\right)} \tag{3.36}$$

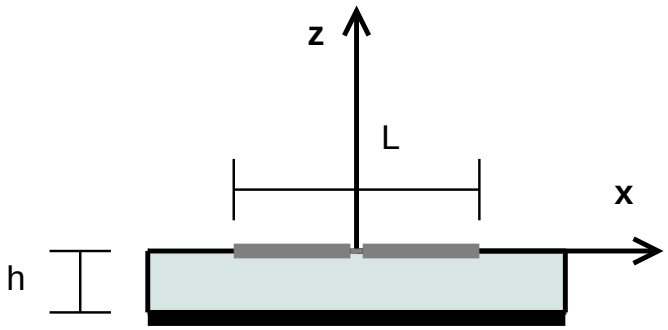

Figure 3.17 : *A x-direction oriented dipole embedded on the top of a grounded substrate*

In the present thesis work the modelled microstrip antennas are assumed to be composed of a dielectric layer surrounded by air such as the afore described structure. Each medium is defined by its electric conductivity σ, its magnetic permeability μ and its dielectric permittivity ε_r. The patch is supposed to be printed on or submerged in the dielectric substrate's upper side. Although dielectric losses can be taken into account, in the present thesis work all dielectric substrates are treated as lossless media.

In addition to that, the finite size of the ground plane is not taken into account. Bokhari *et al.* propose in [51] to use the calculated currents on the patch for the infinite ground plane case in order to scatter the respective radiation on a finite ground plane. For the evaluation of these induced currents the weak conjugate gradient fast Fourier transform (WCG-FFT) technique, which tests the electric field integral equations with roof-top basis functions, is used. Another possible way to include the effect of a finite ground plane is given by Huang in [52]. Therein, the Slot theory or the Modal Expansion Technique combined with GTD is proposed as approach.

3.3.4.1 Validation: Finite length dipole on a grounded substrate

A finite length dipole has been modelled by equivalent sources analysed in order to validate the dielectric effects. The dipole has a length of $L = \frac{\lambda_0}{2}$ and a diameter of negligible size. It is embedded at the top of a grounded dielectric layer that is described by its thickness $h = 0.2\lambda_0$ and its permittivity $\varepsilon_r = 2.35$. The dielectric layer and the ground plane, which is a perfect electrical conductor (PEC) layer, expand along the x-y-plane. Figure 3.17 shows the geometrical position of such a dipole. For this validation case, the effects from the grounded dielectric have been taken into account by applying the dielectric effect functions according to expressions (3.35) and (3.36). Furthermore, the total radiated field of the finite length dipole has been acquired by using equation (3.7) and following the steps of the afore given proceeding for the source modelling algorithm.

Figure 3.18 shows the calculated E-plane and H-plane pattern for the modelled dipole. This validation case have been simulated and analised in [11]. The results using the equivalent sources method yield the same pattern plots presented therein.

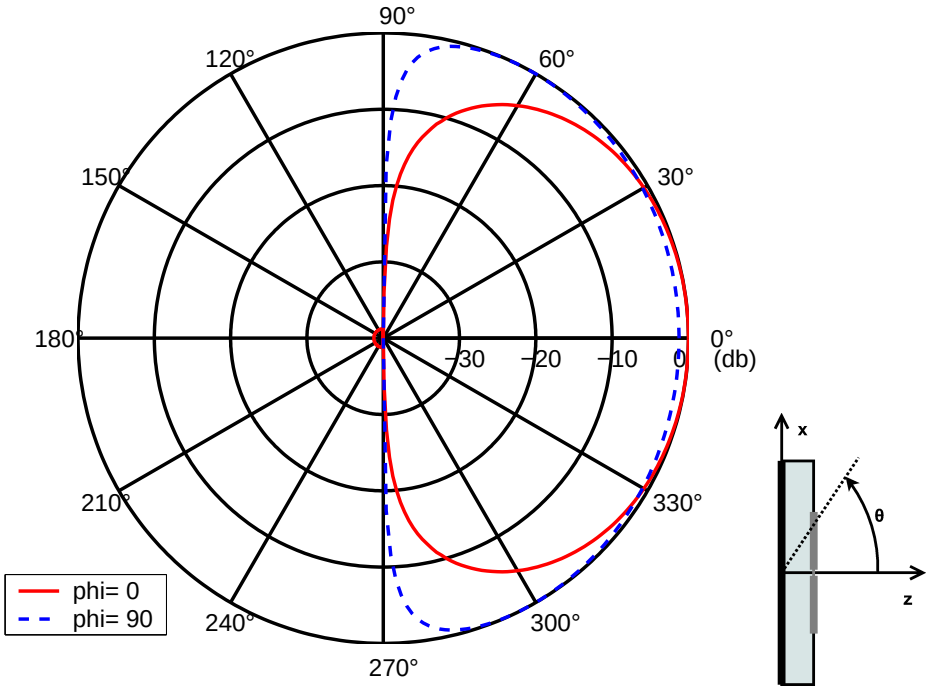

Figure 3.18 : *E-plane and H-plane pattern of a finite length dipole embedded on a grounded substrate*

3.3.5 Far field radiation of a microstrip antenna

According to the basic concept of the approach presented in the present thesis work, the field generated by the radiating region of the microstrip antenna can be seen as a superposition of the field contributions generated by the radiating surface elements that are characterized by equivalent sources. These sources lie equally separated in the region that represents the radiating region of the antenna, namely, the patch surface. This means that all the electric field contributions of the equivalent sources have to be summed up in order to obtain the field of the entire microstrip antenna. Each field of these contributions is yielded with the afore presented far field algorithm conceived for an equivalent source. Consequently, the field of the microstrip antenna $\vec{E}_{ij}^{patch}$ for an observation point (r, θ_i, ϕ_j) in the far field is obtained by using the following formula

$$\vec{E}_{ij}^{patch} = \sum_{m=1}^{M} \sum_{n=1}^{N} \vec{E}_{ij,mn} \tag{3.37}$$

In the latter equation $\vec{E}_{ij,mn}$ stands for the field contributions of an equivalent source assuming the discretization of the radiating surface in $M \cdot N$ small elements. Therefore, the first step in order to obtain the far field radiation of a patch antenna is to discretize the patch surface in small surface elements. Second step is to calculate the position and normal vectors at the geometrical centres of these discrete surfaces. Third step is to obtain or to calculate the current density. Last step is to compute the far field contributions of all discrete surfaces.

The geometrical discretization of the radiating surface is realized by means of different

positioning algorithms developed for the present thesis work. These algorithms distribute the discrete surface elements in space according to the surface real form conceiving a structure that approximates it. Furthermore, the positioning modules yield to obtain all the positions of the surface element centres in space, resulting in a meshed lattice. In all modules the dimension of the distances between the surface element centres are handled so that the discretized surfaces can be represented by equivalent sources, namely infinitesimal dipoles. Consequently, the size for each side of a grid rectangle has been chosen to be smaller than a tenth of the wavelength. These resulting positions are stored in a matrix, whose elements are the position coordinates of the surface elements. Moreover, these elements are the position vectors of the equivalent sources. The positioning procedure at all modules starts from a reference point that can be the geometrical centre of the respective surface. The choice on the positioning algorithm depends on the kind of surface of the modelling patch. The positioning algorithms for planar, cylindrical and spherical surfaces have been developed in this work and these are presented later on.

Assuming the discretization of the radiating surface in $M \cdot N$ small surface elements, the positioning algorithms yields a $M \times N$ matrix containing all positioning vectors towards the geometrical centre of these discrete surfaces. For each geometrical point described by the resulting position matrix, the normal vector of the respective discrete surface at this point is calculated. Depending on the surface structure, the latter can be accomplished by applying the respective analytical function or approximating the normal vector geometrically. The normal vector calculation algorithm generates a matrix with the same size of the position matrix. Both approach are presented together with the positioning algorithm later on. Furthermore, due to the fact that in the present thesis work conformal arrays are approximated by planar patch elements, the normal vectors of all discrete surfaces that belong to a patch element are the same.

Concerning the current densities at the discrete surfaces, an external analysis method in order to retrieve these excitations is used. At the present thesis work, the required currents densities at the patch surface have been calculated by means of FDTD or FIT. Due to the fact that the required grid structure in FDTD or FIT is finer than the discretisation lattice produced by the positioning modules of the present thesis work, the algorithm averages the current densities calculated by the external method into the required excitations for the equivalent sources of the discrete surfaces. This is realized by comparing the grid rectangles of the external method and the internal positioning module: the dimensions L_{int} and W_{int} of the internal grid cell are divided by the dimensions L_{ext} and W_{ext} of the external cell. The acquired values P_1 and P_2 are summed up into P. This resulting value gives the number of external cells that contain one internal mesh cell.

$$\begin{array}{l} P_1 = \frac{L_{int}}{L_{ext}} \\ P_2 = \frac{W_{int}}{W_{ext}} \end{array} \qquad \rightarrow \qquad P = P_1 + P_2 \tag{3.38}$$

Consequently, the current densities $\vec{J}_p^{ext}$ of these external cells are averaged resulting in one current density value $\vec{J}_{eq.s}$ for the internal grid rectangle.

$$\vec{J}_{eq.s} = \frac{1}{P} \cdot \sum_{p=1}^{P} \vec{J}_p^{ext} \tag{3.39}$$

Furthermore, the option of calculating the current densities by means of the cavity model is

given in the present thesis work. Therein, the excitations are approximated by dipole moments that are equivalent to a multiplication of the current distribution at the dielectric layer surface by the orientation length of elementary dipoles. Each oriented length is defined by the orientation vector and the length of the elementary dipole. The orientation vector of a discrete surface is composed of the vectors that stretch the area of the discrete surface. Due to the fact that the present thesis work handles planar patch elements, these vectors are the same for all discrete surfaces. The length of the elementary dipole is equivalent to the minimum size of the internal grid cell sides. It has to be remarked that the algorithm in the present thesis work computes for each arbitrary positioned surface element the required two vectors, which expand the area of the patch surface, by means of the surface normal vector. Moreover, the algorithm steers the contribution of these vectors at the composition of the orientation vector. Consequently, the elementary dipole orientation can be defined by the user.

The computation of the complex field contributions $\vec{E}_{ij,mn}$ of the equivalent sources, which represent the surface elements of a discretized patch surface, is realized by merging the algorithm for the radiation of such a discretized surface element (m,n) in direction (θ_i,ϕ_j) with the algorithms that model the ground plane and dielectric effects. For it, expressions (3.4) - (3.6) and (3.35) - (3.36) have been fusioned yielding the following far field function

$$E^r_{ij,mn} \simeq 0 \tag{3.40}$$

$$E^\theta_{ij,mn} \simeq f^\theta_{ij,mn} \cdot \frac{k_0^2 e^{-\mathrm{j}k_0(r_{ij}-r'_{mn}\cos\psi_{ij,mn})}}{\mathrm{j}2\pi\omega\varepsilon_0 r_{ij}} J^\theta_{ij,mn} \tag{3.41}$$

$$E^\phi_{ij,mn} \simeq f^\phi_{ij,mn} \cdot \frac{k_0^2 e^{-\mathrm{j}k_0(r_{ij}-r'_{mn}\cos\psi_{ij,mn})}}{\mathrm{j}2\pi\omega\varepsilon_0 r_{ij}} J^\phi_{ij,mn} \tag{3.42}$$

Therein, $k_0 = \frac{2\pi}{\lambda}$ is the wave number, $\omega = 2\pi f$ the angular frequency, and ε_0 the free-space permittivity, respectively. In addition, $f^\theta_{ij,mn}$ and $f^\phi_{ij,mn}$ are the dielectric influence functions. Besides that, r_{ij} and r'_{mn} are the magnitudes of the position vectors towards the observing point $\vec{r}_{ij}$ and towards the source $\vec{r}'_{mn}$. Furthermore, the required spatial phase $\psi_{ij,mn}$ enclosed by the latter vectors is obtained using equation (3.2). Moreover, $J^\theta_{ij,mn}$ and $J^\phi_{ij,mn}$ are the spherical components of the surface density $\vec{J}_{ij,mn}$. The latter excitation density is calculated as aforementioned by means of an external module or by using the internal module that applies following equation

$$J^\theta_{ij,mn} = I_{mn}(l^x_{mn}\cos\phi_j + l^y_{mn}\sin\phi_j) \tag{3.43}$$

$$J^\phi_{ij,mn} = I_{mn}(-l^x_{mn}\sin\phi_j + l^y_{mn}\cos\phi_j) \tag{3.44}$$

In the latter expression l^x_{mn}, l^y_{mn} are the cartesian components of the oriented length $\vec{l}_{mn}$. It had to be said, that for a planar patch the component l^z_{mn}, whose direction is parallel to the normal vector of the patch surface, is equivalent to zero due to the fact that the electric currents exist only on the patch surface. Consequently, it does not appear in the latter equation set. Furthermore, I_{mn} is the excitation current of element (m,n). Its value is obtained by using the cavity model approach that is presented in the present thesis work later on. Moreover, the multiplication of the vector $\vec{J}_{ij,mn}$ and the Green's function term $\frac{e^{-\mathrm{j}k_0(r_{ij}-r'_{mn}\cos\psi_{ij,mn})}}{r_{ij}}$ in expressions

(3.40) - (3.42) can be interpreted as the discrete vector potential $A_{ij,mn}$ in spherical coordinates if compared with afore given cartesian expression of the magnetic potential in (3.1).

3.3.5.1 Validation: planar patch antennas with dielectric

Based on the algorithm proceeding used at the validation for an equivalent source and on the afore given function that enhances the equivalent source handling with ground plane and dielectric effects, an algorithm for the far field analysis has been developed. Consequently, the proceeding of this algorithm is similar as for the source modelling: the radiating patch is symmetrically modelled in reference to its geometrical centre by means of $M \cdot N$ equivalent sources. The latter point is defined by a position vector inside a cartesian coordinate system. All sources are treated as elementary dipoles of same length Δl with the same orientation in $\vec{l}_{mn} = \vec{l} = \Delta l \cdot (\vec{\imath}_1 + \vec{\imath}_2)$. $\vec{\imath}_1$ and $\vec{\imath}_2$ are the cartesian tensing vectors of the patch surface. The vector potential contribution $A_{ij,mn}$ in Cartesian coordinates of each surface element (m,n) is computed by means of the angle $\psi_{ij,mn}$, the excitation I_{mn}, the oriented length $\vec{l}$ and vectors $\vec{r}_{ij}$ and $\vec{r}'_{mn}$ according to (3.1). Furthermore, the computation of the spatial angle $\psi_{ij,mn}$ has been realized according to (3.2). Moreover, in case of existing external precalculated current densities $\vec{J}_{ij,mn}$, the cartesian vector potential is obtained by multiplying these excitations with the Green's function term.

Furthermore, the Cartesian vector potential is transformed into spherical form yielding $A^{sph}_{ij,mn}$ that is used in combination with the spherical dielectric effects functions $f^{\theta}_{ij,mn}$ and $f^{\phi}_{ij,mn}$ according to (3.29)-(3.30) and with other constants according to (3.40) - (3.42) in order to obtain the field contribution $E_{ij,mn}$. The resulting field contribution is consequently the radiated field of an equivalent source with the ground plane and dielectric effect. Furthermore, the required angle $\xi_{ij,mn}$ for attaining $f^{\theta}_{ij,mn}$ and $f^{\phi}_{ij,mn}$ has been calculated by means of the vectors $\Delta\vec{r}_{ij,mn} = \vec{r}_{ij} - \vec{r}'_{mn}$ and $\vec{n}_{mn}$ according to (3.10). Besides that, the normal vector $\vec{n}_{mn}$ is for all surface elements the same due to the planar patch surface assumption. Consequently, the normal vector at each source is equivalent to the patch surface normal vector, this is $\vec{n}_{mn} = \vec{n}_{surf}$.

The implementation of the algorithm has been realized with a FORTRAN code whose structure is given in table 3.3. For it, an observation space has been defined by $N_\theta \cdot N_\phi$ observing points with the form (r, θ_i, ϕ_j) lying in the far field with $i = 1, \ldots, N_\theta$ and $j = 1, \ldots, N_\phi$ as well as a constant huge-valued radius $r = 1.0 \cdot 10^4$. The resulting fields have been stored in a complex $N_\theta \times N_\phi$ matrix.

In order to calculate all points of the observing space, two loops are run like in the case for the dipole's simulation. These external loops in the FORTRAN code vary the angles θ_i and ϕ_j in the range of $[0^\circ, 360^\circ]$ starting with values of 0°. Inside these loops the vector towards the observation point $\vec{r}_{i,j}$ defined by the constant radius and the angles θ_i and ϕ_j is converted by a transformation matrix from this spherical into Cartesian coordinates yielding in $\vec{x}_{i,j}$. Then, the field calculation of the patch for this observing point is started. Due to the fact that the equivalent sources model a two dimensional radiating surface, the realization of the required calculations has to be done with the help of two loops. These internal loops steer the variables and functions that contribute to the computation of the patch field. The first step inside these loops is to assign the required information to the respective variables: the position vector $\vec{x}'_{mn}$ of the equivalent source, the normal vector at this point $\vec{n}_{mn} = \vec{n}_{surf}$, the current value I_{mn} plus

Allocation matrix E_{n_θ,n_ϕ}
Definition $\theta = 0$
Definition $\phi = 0$
Definition $rad = 1.0 \cdot 10^4$
Definition of start values
for i=1,N_θ
    Calculation of θ_i with $\Delta\theta$ and i
    for j=1,N_ϕ
        Calculation of ϕ_j with $\Delta\phi$ and j
        Calculation of $\vec{r}_{ij}$ with rad, θ_i, ϕ_j
        Conversion from $\vec{r}_{ij}$ into $\vec{x}_{ij}$
        Definition $E_{patch} = 0$
        for m=1,M
            for n=1,N
                Assignation of $\vec{x}'_{mn}$, I_{mn} plus Δl or $\vec{J}_{ij,mn}$, $\vec{\iota}_1$, $\vec{\iota}_2$ and $\vec{n}_{surf}$
                Calculation of $\psi_{ij,mn}$ with $\vec{x}_{ij}$ and $\vec{x}'_{mn}$
                Definition of $\vec{l}_{mn}$ with value Δl and vectors $\vec{\iota}_1$ and $\vec{\iota}_2$
                Calculation of $\vec{A}_{ij,mn}$ with I_{mn}, $\vec{l}_{mn}$ and $\psi_{ij,mn}$
                    or with $\vec{J}_{ij,mn}$ and $\psi_{ij,mn}$
                Conversion from $\vec{A}_{ij,mn}$ into $A^{sph}_{ij,mn}$
                Assignation of $\vec{n}_{mn}$ with $\vec{n}_{surf}$
                Calculation of $\Delta\vec{r}_{ij,mn}$ with $\vec{x}_{ij}$ and $\vec{x}'_{mn}$
                Calculation of $\xi_{ij,mn}$ with $\vec{n}_{mn}$ and $\Delta\vec{r}_{ij,mn}$
                Calculation of $f^{\theta}_{ij,mn}$ and $f^{\phi}_{ij,mn}$ with $\xi_{ij,mn}$
                Calculation of $\vec{E}_{ij,mn}$ with $A^{sph}_{ij,mn}$
                Summation of $\vec{E}_{ij,mn}$ to $\vec{E}^{patch}_{ij}$
            end
        end
        Storage of $\vec{E}^{patch}_{ij}$ in $\vec{E}_{i,j}$
    end
end

Table 3.3 : *Code structure for field calculation of a modelled microstrip patch antenna*

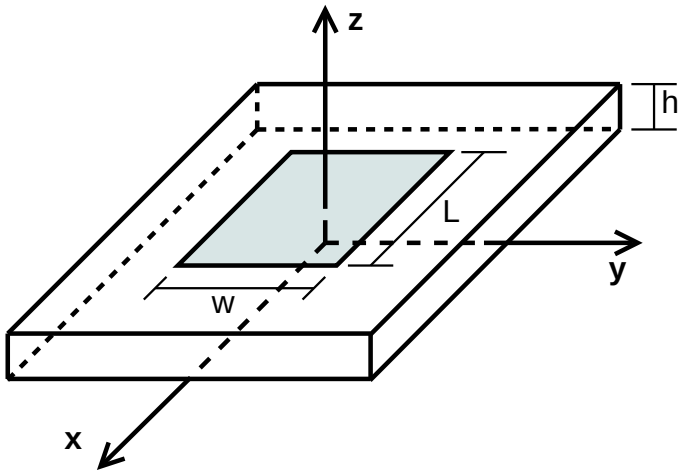

Figure 3.19 : *Geometry of a rectangular microstrip patch antenna*

the elementary dipole length Δl or eventually the current density $\vec{J}_{ij,mn}$ in Cartesian coordinates, and the surface tensing vectors $\vec{\iota}_1$, $\vec{\iota}_2$. As next step, the required geometrical functions like the spatial angles $\psi_{ij,mn}$ and $\xi_{ij,mn}$, and if necessary the dipole orientation $\vec{l}_{mn}$, are calculated with the latter variables. By taking all these required geometrical values in addition to the latter variables, the Cartesian vector potential $\vec{A}_{ij,mn}$ and the dielectric effects functions $f^{\theta}_{ij,mn}$ and $f^{\phi}_{ij,mn}$ are computed. Furthermore, $\vec{A}_{ij,mn}$ is converted in spherical coordinates resulting in $A^{sph}_{ij,mn}$. The forelast step inside the internal loops is to obtain the electric field $\vec{E}_{ij,mn}$ for the element (m,n) by means of the vector potential and the dielectric effects functions. At the end of internal loops the obtained field components $\vec{E}_{ij,mn}$ are summed up in order to define the complex electric far field $\vec{E}^{patch}_{ij}$ for the observation point (r,θ_i,ϕ_j). Moreover, each of the resulting field values is stored as an element of a $N_\theta \times N_\phi$ complex matrix. At the end of the external loops a complex field matrix for the desired observing space is obtained.

Validation cases for the patch modelling have been realized with some examples of microstrip antennas. For it, simulations with the developed code have been performed. Paralell to it, analytical formula has been derived following the same procedure introduced in [7] in order to validate the results. Therein, the patch antennas are modeled as resonant cavities. Furthermore, their radiation behaviour is approximated by dielectric walls that behave like radiating apertures. For the first validation case, the microstrip antenna has a rectangular patch. The geometry of the latter is depicted in figure 3.19. As aforementioned, the result of the method conceived in the present thesis work is compared with the one of an analytical formula. Consequently, the following analytical equation set for the far field of a microstrip antenna lying in the x-y-plane has been derived and implemented

$$
\begin{aligned}
E_{ij}^{r} &\simeq 0 \\
E_{ij}^{\theta} &= -\mathrm{j}\frac{k_0 \mathsf{h} \mathsf{w} I_0 e^{-\mathrm{j}k_0 r_{ij}}}{\pi r_{ij} Z_0} \left\{ \cos\phi_j \frac{\sin\left(\frac{k_0 \mathsf{w}}{2}\sin\theta_i \sin\phi_j\right)}{\frac{k_0 \mathsf{w}}{2}\sin\theta_i \sin\phi_j} \frac{\sin\left(\frac{k_0 \mathsf{h}}{2}\sin\theta_i \cos\phi_j\right)}{\frac{k_0 \mathsf{h}}{2}\sin\theta_i \cos\phi_j} \right\} \cdot \\
&\quad \cdot \cos\left(\frac{k_0 L_{eff}}{2}\sin\theta_i \cos\phi_j\right) \cdot f_\theta(\theta_i) \\
E_{ij}^{\phi} &= -\mathrm{j}\frac{k_0 \mathsf{h} \mathsf{w} I_0 e^{-\mathrm{j}k_0 r_{ij}}}{\pi r_{ij} Z_0} \left\{ \cos\theta_i \sin\phi_j \frac{\sin\left(\frac{k_0 \mathsf{w}}{2}\sin\theta_i \sin\phi_j\right)}{\frac{k_0 \mathsf{w}}{2}\sin\theta_i \sin\phi_j} \frac{\sin\left(\frac{k_0 \mathsf{h}}{2}\sin\theta_i \cos\phi_j\right)}{\frac{k_0 \mathsf{h}}{2}\sin\theta_i \cos\phi_j} \right\} \cdot \\
&\quad \cdot \cos\left(\frac{k_0 L_{eff}}{2}\sin\theta_i \cos\phi_j\right) \cdot f_\phi(\theta_i)
\end{aligned} \tag{3.45}
$$

Therein, L and w are the geometrical size of the patch, h the dielectric thickness, respectively. I_0 is the feeding current, k_0 the free space wave number, Z_0 the intrinsic impedance, respectively. Furthermore, f_θ and f_ϕ are the dielectric effect functions defined in equations 3.27 and 3.28. In addition to that, L_{eff} stands for the effective length, which takes into account the length of the patch L as well as the length $\Delta\mathsf{L}$ of the region where fringing effects take place. The fringing fields let appear the patch electrically longer comparing to its physical dimension. Hence the amount of fringing is a function of the patch length and width. According to [1] the effective length L_{eff} can be defined by the following expression

$$L_{eff} = \mathsf{L} + 2\Delta\mathsf{L} \tag{3.46}$$

The length ΔL that describes the geometrical influence region of the fringing fields, is defined by following relation

$$\frac{\Delta\mathsf{L}}{\mathsf{h}} = 0.412 \frac{\left(\varepsilon_{eff} + 0.3\right)\left(\frac{\mathsf{L}}{\mathsf{h}} + 0.264\right)}{\left(\varepsilon_{eff} - 0.258\right)\left(\frac{\mathsf{L}}{\mathsf{h}} + 0.8\right)} \tag{3.47}$$

The required effective dielectric constant ε_{eff} is defined as in the following formula

$$\varepsilon_{eff} = \frac{\varepsilon_r + 1}{2} + \frac{\varepsilon_r - 1}{2}\left[1 + 12\frac{\mathsf{h}}{\mathsf{W}}\right]^{-\frac{1}{2}} \qquad \frac{\mathsf{W}}{\mathsf{h}} > 1 \tag{3.48}$$

A rectangular patch antenna that resonates at the frequency $f = 10.0$GHz has been taken for further analysis. This single layered microstrip antenna with a dielectric thickness of $\mathsf{h} = 1.588$mm and a permittivity of $\varepsilon_{eff} = 2.2$ has following patch dimensions: $\mathsf{L} = 9.06$mm and $\mathsf{w} = 11.86$mm. The behaviour of the latter patch antenna in form of the radiation pattern has been analysed. In the following diagrams, cuts in elevation of the resulting three-dimensional patterns are shown. These sections are done for $\theta = 45^\circ$ and $\theta = 90^\circ$. Furthermore, additional cuts in azimuth for $\phi = 90^\circ$ and $\phi = 0^\circ$ have been performed. Figures 3.20 and 3.21 show the radiation pattern in E-plane and H-plane for the first validation case. The pattern plots for the analytical formula proceeding and for the method developed in the present thesis work, namely the equivalent source approach, are depicted in the latter figures. The currents used at the equivalent source approach are calculated by means of the cavity model.

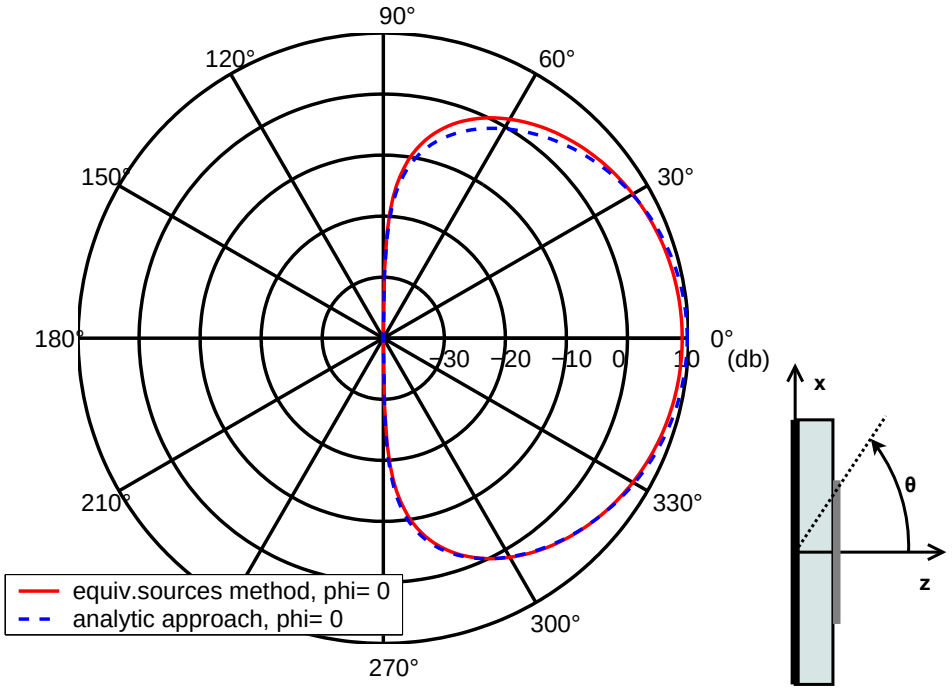

Figure 3.20 : *E-plane directivity of a microstrip antenna with rectangular patch - currents calculated with cavity model*

Furthermore, additional diagrams have been plotted in order to compare the radiation behaviour caused by currents that are obtained by means of the cavity model and by means of the accurate FDTD. These pattern plots are given in appendix D to the reader. The respective figures show that the approximated currents with the help of the cavity model converge towards the FDTD ones and therefore they are acceptable. Moreover, figures 3.22 and 3.23 depict the simulation with the equivalent source approach and the FDTD method. For them, the currents have been calculated with FDTD.

The second validation case embraces a simulation of a microstrip antenna with a circular patch. The geometry of the latter antenna is shown in figure 3.24. The simulation of the method conceived in the present thesis work is compared with an analytical formula. Consequently, the following analytical equation set for the far field components of a microstrip antenna lying in the x-y-plane has been derived and implemented

$$
\begin{aligned}
E_{ij}^{r} &\simeq 0 \\
E_{ij}^{\theta} &= -\mathrm{j}\frac{k_0 h a_{\mathrm{eff}} I_0 e^{-\mathrm{j}k_0 r_{ij}}}{2 r_{ij} Z_0} J_1(k_\rho a_{\mathrm{eff}}) \cos\phi_j \left[J_0(k_0 a_{\mathrm{eff}} \sin\theta_i) - J_2(k_0 a_{\mathrm{eff}} \sin\theta_i)\right] \cdot f_\theta(\theta_i) \\
E_{ij}^{\phi} &= -\mathrm{j}\frac{k_0 h a_{\mathrm{eff}} I_0 e^{-\mathrm{j}k_0 r_{ij}}}{2 r_{ij} Z_0} J_1(k_\rho a_{\mathrm{eff}}) \cos\theta_i \sin\phi_j \cdot \left[J_0(k_0 a_{\mathrm{eff}} \sin\theta_i) + \right. \\
&\quad \left. + J_2(k_0 a_{\mathrm{eff}} \sin\theta_i)\right] \cdot f_\phi(\theta_i)
\end{aligned}
\tag{3.49}
$$

In the latter equations J_0, J_1 and J_2 stand for the first kind Bessel functions of null, first and

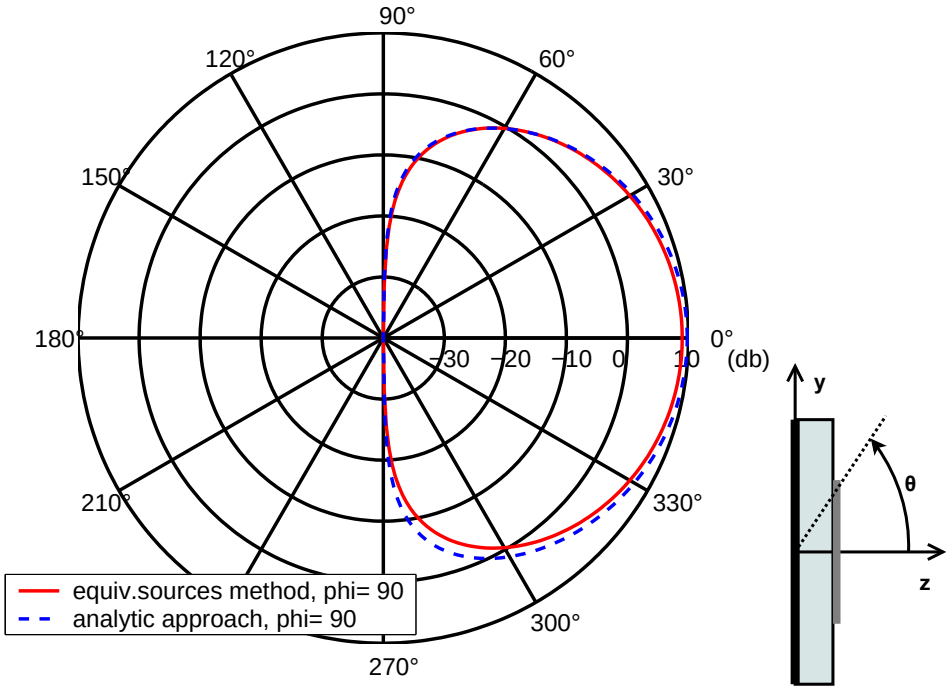

Figure 3.21 : *H-plane directivity of a microstrip antenna with rectangular patch - currents calculated with cavity model*

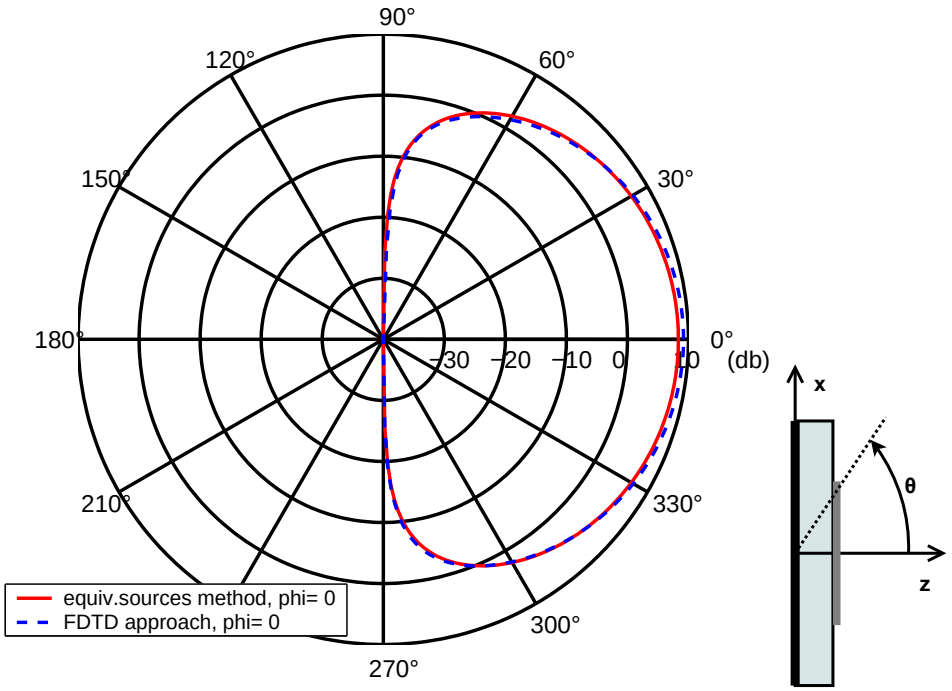

Figure 3.22 : *E-plane directivity of a microstrip antenna with rectangular patch - currents calculated with FDTD*

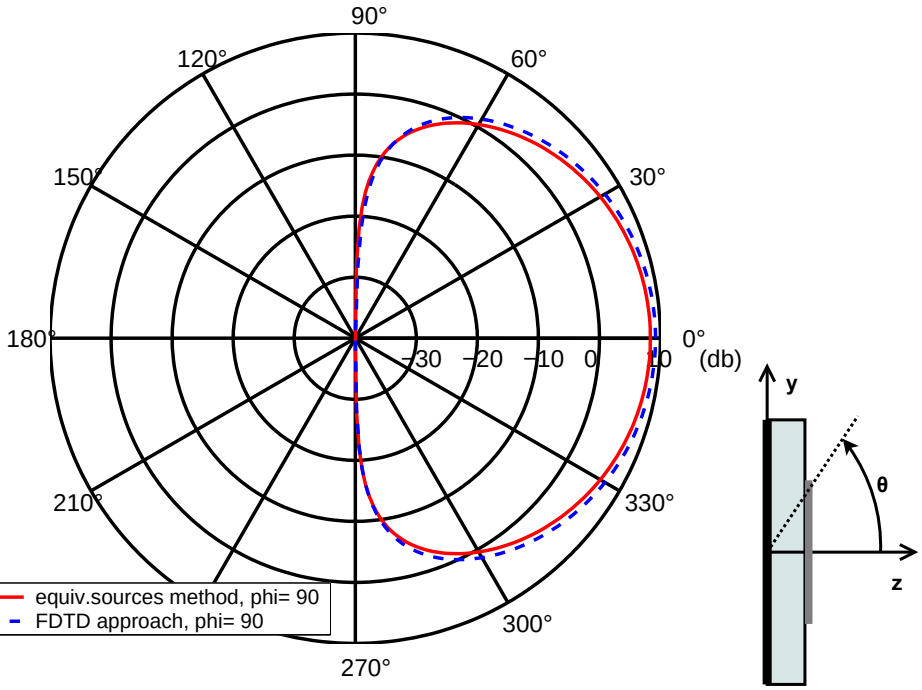

Figure 3.23 : *H-plane directivity of a microstrip antenna with rectangular patch - currents calculated with FDTD*

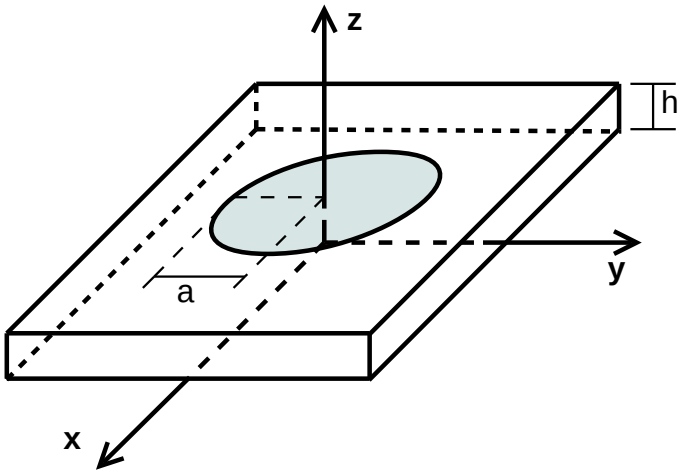

Figure 3.24 : *Geometry of a circular microstrip patch antenna*

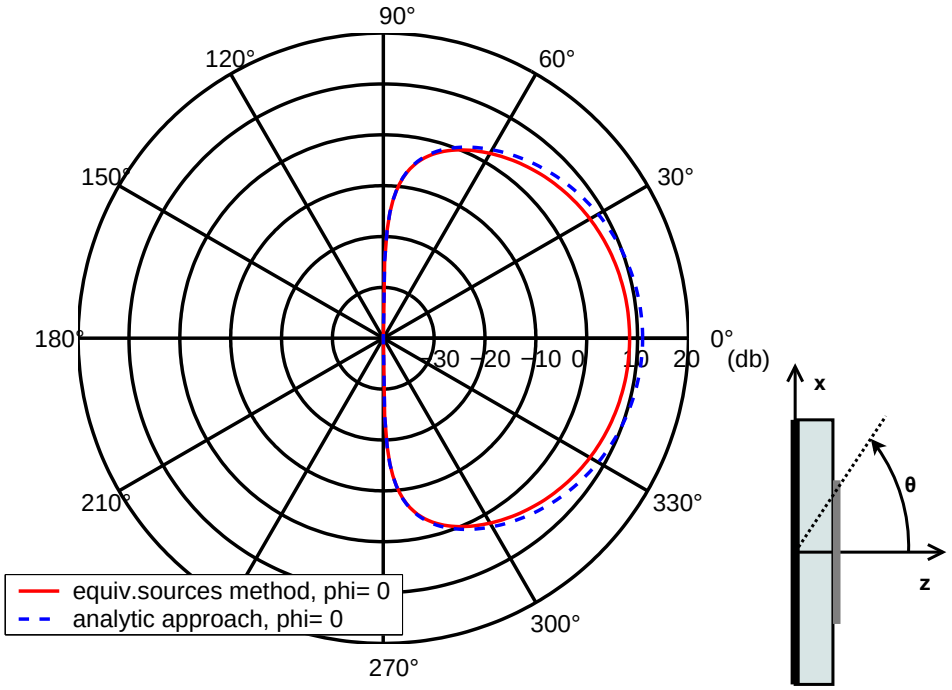

Figure 3.25 : *E-plane directivity pattern of a microstrip antenna with circular patch - currents calculated with cavity model*

second order, respectively. Moreover, k_ρ is the wave number in radial direction, I_0 the feeding current, h the dielectric layer thickness, k_0 the free space wave number, and Z_0 the intrinsic impedance, respectively. Furthermore, f_θ and f_ϕ are the dielectric effect functions defined in equations 3.27 and 3.28. As in the rectangular case patch, the region, wherein fringing effects take place, is taking into account by defining an effective radius a_{eff}. This radius has generally greater values than the actual physical radius a because the fringing fields let appear the patch electrically larger. The effective radius is yielded by means of the following expression

$$a_{eff} = a\left(1 + \frac{2h}{\pi a \varepsilon_r}\left[\ln\left(\frac{\pi a}{2h}\right) + 1.7726\right]\right)^{\frac{1}{2}} \tag{3.50}$$

For the validation, a circular patch antenna with the resonance frequency $f = 10.0\text{GHz}$ has been taken for further analysis. This single layered microstrip antenna with a dielectric thickness of $h = 1.588\text{mm}$ and a permittivity of $\varepsilon_{eff} = 2.2$ has a circular patch described by its physical radius $a = 5.25\text{mm}$. The necessary currents have been acquired by using the cavity model. In order to test the simulation with the analytical formulae, the radiation behaviour has been visualized by means of plots. The respective diagrams are presented in figures 3.25 and 3.26. Additional plots have been realized in order to compare the results with currents by means of the cavity model in contrast to the acquired currents with FDTD. These figures are shown in appendix D to the reader. These plots demonstrate that the approximated currents with the help of the cavity model are acceptable.

As in the other examples the plot lines of both methods are depicted. In these diagrams the curves show the radiation pattern of the microstrip antenna in elevation for $\theta = 45^\circ$ and

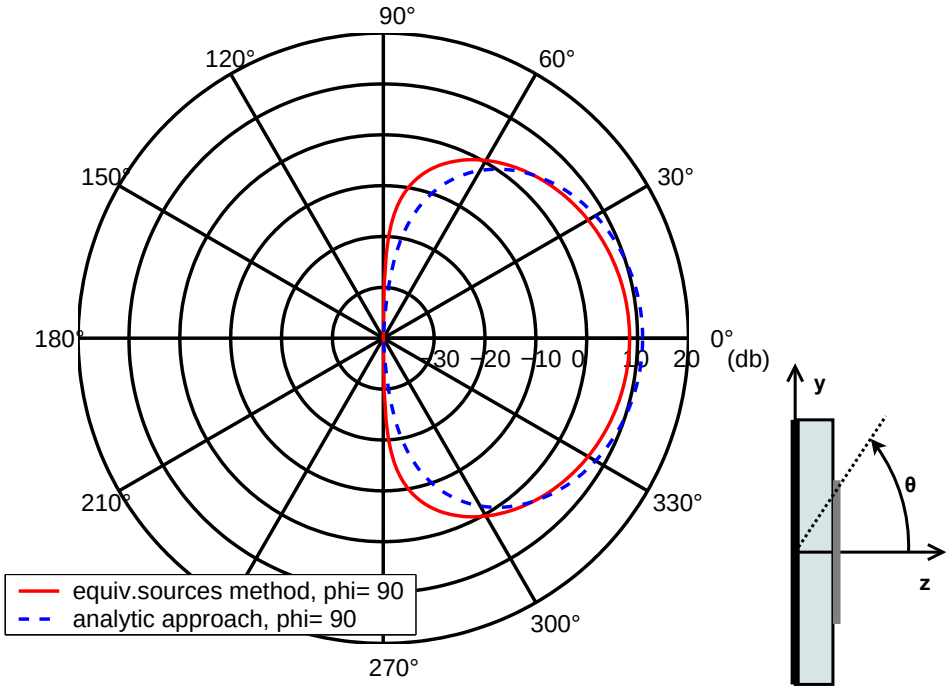

Figure 3.26 : *H-plane directivity pattern of a microstrip antenna with circular patch - currents calculated with cavity model*

for $\theta = 90^\circ$. Furthermore, the pattern in azimuth for $\phi = 90^\circ$ and for $\phi = 0^\circ$ are depicted. In addition to the latter results, a comparison of them with the results using the FDTD method are presented in figure 3.27 and 3.28. Therein, the currents have been calculated with FDTD.

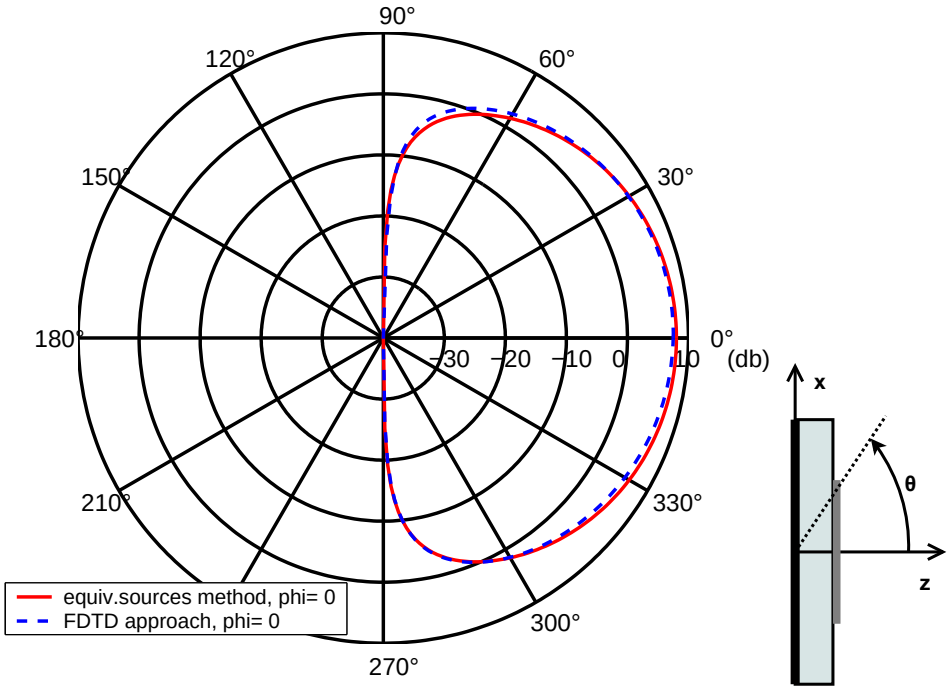

Figure 3.27 : *E-plane directivity pattern of a microstrip antenna with circular patch - currents calculated with FDTD*

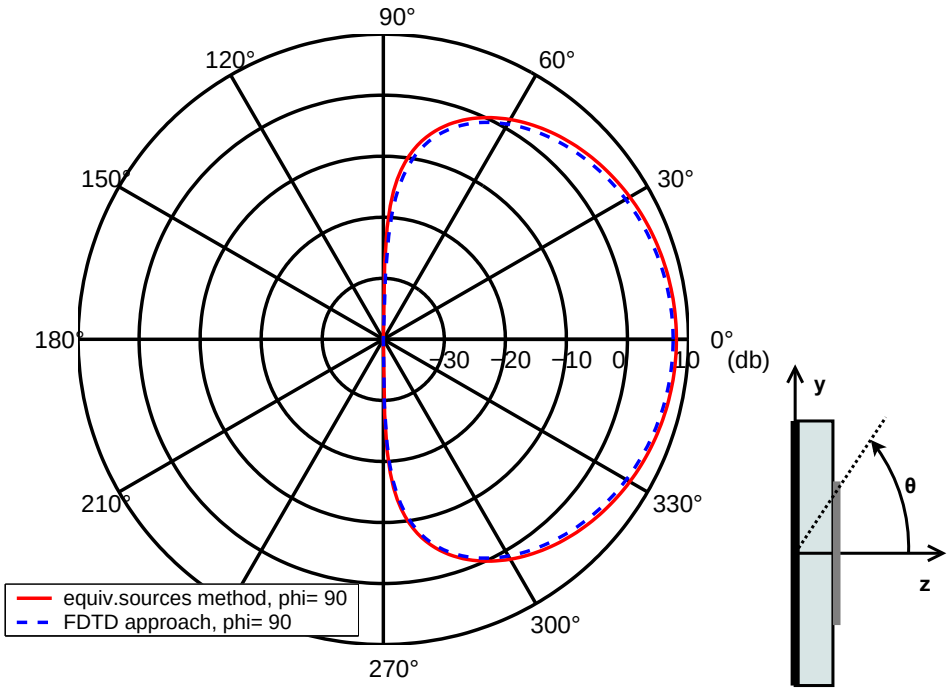

Figure 3.28 : *H-plane directivity pattern of a microstrip antenna with circular patch - currents calculated with FDTD*

3.4 Positioning algorithms

As aforementioned a positioning module has been conceived in the present thesis work. This tool is used to calculate the position of the geometrical centres of the elements on the surface of a planar or conformal array. The position distribution procedure is realized according to the desired spacing values and it starts from a reference point that is the geometrical centre of the surface. The position distribution procedure can be interpreted as a discretization of the handled surface by surface elements whose size is defined by the spacing values. Consequently, the implemented positioning algorithms are used also for the discretization of the patch surface belonging to the microstrip elements of the array. Assuming desired $U \cdot V$ array elements, the positioning algorithms yields a $U \times V$ matrix containing all positioning vectors. The modules in the present thesis work are conceived for planar, cylindrical and spherical positioning.

Furthermore, the concept of these three positioning modules for flat and curved surfaces is based on geometry. Consequently, several mathematical formulae have been applied. Moreover, the geometry dependant concept can be used of any other kind of surface as far as its mathematical form is known or given. The reader has to be informed that the word "distribution" associated with a geometrical context in the present thesis work and specially in this section refers always to the localization of the geometrical positions of points on a certain surface. Moreover, the expressions "position distribution" and "positioning" are equivalent in the present thesis work. In the following, the surface geometrical centre of the patch surface and the discretized surface elements are treated as global and local reference points, respectively. Therefore, the patch surface centre is refered as starting point in the following descriptions of the distribution modules. Besides that, all the distribution modules developed in the present thesis work generate equidistant lying geometrical points on the regarded patch surface.

3.4.1 Planar position distribution

The position distribution module for a planar structure allows to model planar arrays as well as flat patch surfaces for microstrip antennas. For instance, figure 3.29 shows a possible constellation for a planar patch antenna array. A planar surface is described mathematically by two vectors that tense this plane. Each of these vectors belongs to a straight line. Both lines have a common reference point on the tensed surface. The mathematical equation describing a point (u,v) on planar surface is given by the following formula

$$\vec{x}_{uv} = \vec{x}_{ref} + u \cdot s_u \cdot \vec{\imath}_u + v \cdot s_v \cdot \vec{\imath}_v \qquad \text{for} \quad u = 1,\ldots,U \quad \text{and} \quad v = 1,\ldots,V \tag{3.51}$$

$\vec{x}_{uv}$ stands for the position vector of a point that is part of to the plane, $\vec{x}_{ref}$ for the position vector of the reference point on the plane, respectively. Furthermore, $\vec{\imath}_u$ and $\vec{\imath}_v$ are the tensing vectors and s_u and s_v are real-valued shift coefficients. The latter coefficients steer the translation of the position vector $\vec{x}_{ref}$ towards the a point (u,v) by the tensing vectors. This formula is generally applicable and therefore a plane oriented in any direction in space can be described.

The algorithm developed for the planar distribution module is based on the afore given mathematical function. Consequently, the algorithm needs the information about the reference point and then tensing vectors $\vec{\imath}_u$ and $\vec{\imath}_v$. The first requirement is fulfilled by choosing the

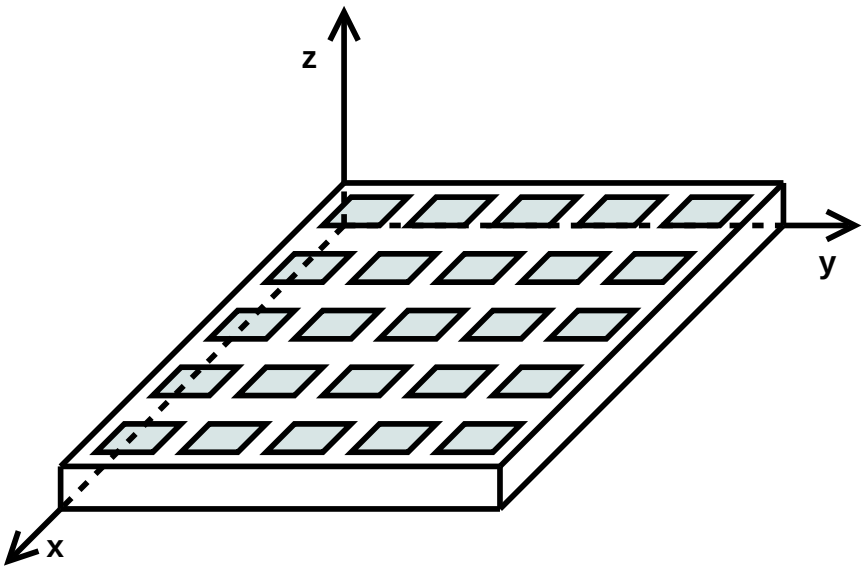

Figure 3.29 : *A planar patch array structure on the* x-y-*plane*

geometrical centre of the patch surface as reference point. The necessary vectors are found by means of the normal vector of the planar surface structure $\vec{n}_{str}$. All three vectors have to build an orthogonal system. Thus, a such vectorial system is built with the information about the normal vector and the position vector of the reference point. This step is entirely of mathematical nature and hence it is presented in the appendix A. In addition to that, it have to be said that, due to the fact that the normal vector on a planar surface is the same for all surface points, the tensing vectors are the same for all these points too. Hence they are calculated only once.

Furthermore, an evaluation on the parity of the values for U and V is performed. This is due to the existance of three constellations depending if U and/or V are even or odd. The first constellation happens for U and V being odd numbers. In this case the surface structure is of point-symmetrical kind and its geometrical centre, which is equivalent to the reference point, belongs to the N_{total} desired points and consequently equation (3.51) can be used straightforward. The second case takes place for U and V being even numbers: the structure is axis-symmetric and therefore the geometrical centre, this is the reference point, is not part of the desired N_{total} points. Consequently, the shift distances s_u and s_v in (3.51) have to be adapted during the distribution. The last case takes place for U being odd and V being even or vice versa: in both situations the reference point is not part of the surface structure. Thus, the shift distance that depends on the even number of elements along the respective tensing vector has to be corrected.

The proceeding of the algorithm begins with calling the planar structure normal vector $\vec{n}_{str}$ and the reference point vector $\vec{x}_{ref}$ values. In addition to that, the algorithm looks for information about the number of desired points U and V along the dimensions of the structure surface and the geometrical shift distances s_u and s_v between them. Consequently, the total number of desired points is $N_{total} = U \cdot V$. Following the latter, the required tensing vectors $\vec{\imath}_u$ and $\vec{\imath}_v$ are calculated. In the following proceeding step, for each desired point (u,v) the algorithm takes the reference point vector $\vec{x}_{ref}$ and shifts it according to (3.51) with the given values for the shift

Recovery of s_u, s_v, $\vec{x}_{ref}$ and $\vec{n}_{str}$
Calculation of $\vec{\imath}_u$ and $\vec{\imath}_v$
Evaluation of U and V on parity
Calculation of correction factor if necessary
Correction of the s_u, s_v if necessary
for u= 1 , U
for v=1,V
Calculation of $\vec{x}_{uv}$ with u, v, s_u, s_v, $\vec{x}_{ref}$, $\vec{\imath}_u$ and $\vec{\imath}_v$
Storage of $\vec{x}_{uv}$
end
end

Table 3.4 : *Code structure for the planar distribution module*

distances including the correction factor. The last step of the proceeding is to store the obtained values for each the distribution point.

Based on the afore described proceeding of the planar distribution algorithm, a module in FORTRAN has been coded. For it, a $U \times V$ matrix for the (u,v) point vectors with $u = 1,\ldots,U$ and $v = 1,\cdots,V$ at the planar structure has been defined. The structure of the resulting code is shown in table 3.4

As observed in the latter presented structure, the developed code uses two loops to perform the entire point distribution on the planar structure. The algorithm steps are practically traduced directly into code functions. Consequently, the necessary input variables s_u, s_v, $\vec{x}_{ref}$ and $\vec{n}_{str}$ are assigned before the loop procedure. In addition to that, the tensing vectors are calculated. Furthermore, the correction factor calculation as well as the respective correction of the shift distances are realized. Inside the loops the calculation of the position vectors $\vec{x}_{uv}$ is performed. For it, the first loop steers distance shifts in direction of tensing vector $\vec{\imath}_u$. The second loop acts the same but in direction of the second tensing vector $\vec{\imath}_v$. The distribution code generates in the end of the procedure a $U \times V$ matrix with the position vectors $\vec{x}_{uv}$ for the points on the surface structure as elements.

The latter developed algorithm and code for the planar structure are used for the construction of a planar array and for the modelling of the planar patch of a microstrip antenna. Thus, the code structure afore given is applied on both cases. In the array case the distribution module asks the user for the values of the normal vector and of a point on the desired planar structure. The normal vector is used in order to calculate the tensing vectors and the given point becomes then the geometrical centre of the array structure. Furthermore, the shift distances, these are the spacing values, are demanded to the user. In the patch modelling case one of the distribution generated points on the array structure is assigned as the geometrical centre of the patch. The required normal vector for the patch surface is the same of the array structure. In the present thesis work the axes of the planar patches and of the planar array structure are aligned. Consequently, the tensing vectors of the patch surface and of the array surface are equal. Concerning the shift distances, the length and width of the patch are discretized by dividing them by

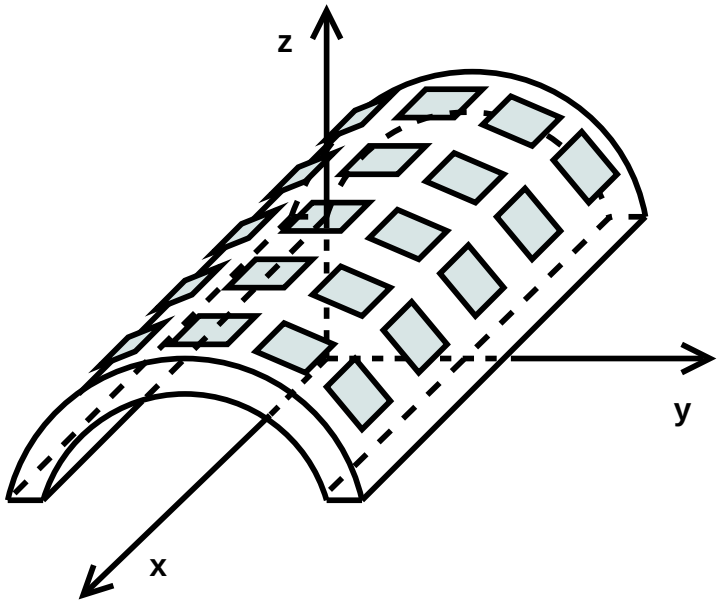

Figure 3.30 : *A patch array on a cylindrical structure along* x*-axis*

the number of discrete elements necessary to approximate the resulting discrete elements with equivalent sources. The resulting discrete elements dimensions are consequently the required shift coefficients for the distribution module.

3.4.2 Cylindrical position distribution

In addition to the afore presented planar distribution module, other distribution modules for non-orthogonal surfaces have been developed. One of them, which is presented in the following, allows to model arrays with a structure that is simply curved with a certain radius. Such a curved surface is equivalent to a section or the entire surface of a cylinder. Figure 3.30 shows the geometry of a patch array on a cylindrical structure. For such array structure, the position vectors of the points belonging to the simply curved surface can be calculated using the mathematical definition of a cylinder. According to [85] for a *x*-axis oriented cylinder, this is

$$\vec{x} = \begin{pmatrix} x\cos\theta \\ r_{cyl}\sin\theta \\ r_{cyl}\cos\theta \end{pmatrix} \qquad (\theta, x) \in [0, 2\pi] \times [0, 1] \tag{3.52}$$

The latter equation shows a vectorial function for a cylinder that expands along the *x*-axis. The latter expression is not a suitable function for the development of a generally applicable distribution algorithm, specially when cases, wherein antenna arrays are integrated in slanted cylindrical structures, have to be simulated. Consequently, a generally applicable approach independent from the direction of the cylinder's longitudinal axis has been developed. For it, the latter equation is analysed. The reader may notice that the *x* component of the position vector $\vec{x}$ along the longitudinal axis of the cylinder remains linear to the changes along this coordinate. Unlike to the latter component, the *y* and *z* components behave according to functions dependant of the angle θ that is defined on the plane build by the *y* and *z* coordinates. Both components

build a circle of radius r_{cyl} on the y-z-plane. Furthermore, the multiplication of the angle dependant harmonic function by the constant radius of the cylinder r_{cyl} at the y and z components can be interpreted as a rotation of a point about the longitudinal axis on the y-z-plane with θ as rotation angle.

Consequently, the main idea used to develope the generally applicable distribution module for a cylindrical surface is to shift a chosen reference point, which should be part of the handled surface, with a certain distance parallel the longitudinal axis of the cylinder and then to rotate it about the latter axis according to a certain rotation angle. Moreover, a condition for this approach is to have information about the longitudinal axis of the cylindrical structure. This axis is obtained by means of the normal vector of the surface structure at the reference point. Based on the the algorithm of the planar distribution and on the latter analysis, which is generally applicable, formulae of following mathematical form have ben derived. These are

$$\vec{x}_{uv} = \vec{x}_{ref} + F_{rot}(u, \nu(s_u, r_{cyl})) \cdot \vec{\imath}_\nu) + v \cdot s_v \cdot \vec{\imath}_v \tag{3.53}$$

or

$$\vec{x}_{uv} = \vec{x}_{ref} + u \cdot s_u \cdot \vec{\imath}_u + F_{rot}(v, \nu(s_v, r_{cyl})) \cdot \vec{\imath}_\nu \tag{3.54}$$

In the latter two equations $\vec{x}_{uv}$ stands for the position vector of the point (u,v) that is part of to the cylindrical surface, $\vec{x}_{ref}$ for the position vector of the reference point on the plane, respectively. Furthermore, $\vec{\imath}_u$ or $\vec{\imath}_v$ and $\vec{\imath}_\nu$ are the vectors that build with the normal vector n_{uv} at the point (u,v) an orthogonal system. Moreover, s_u and s_v are real-valued shift coefficients that steer the translation and the rotation of the position vector $\vec{x}_{ref}$ towards the a point (u,v). Consequently, F_{rot} stands for the rotation function that has the rotation angle ν as argument. The latter required angle is calculated from the cylinder radius r_{cyl} and the arc length s. Besides that, $u = 1,\ldots,U$ and $v = 1,\ldots,V$.

Furthermore, the following relation between the arc length s and the radius r_{cyl} of the cylinder derived from the geometry in figure 3.31 is used for the calculation of the rotation angle ν

$$\nu = \frac{s}{r_{cyl}} \tag{3.55}$$

Moreover, depending of the choice of the longitudinal axis the value for the arc length is $s = s_u$ or $s = s_v$. In order to perform the angular displacement, the rotation function F_{rot} that calculates the rotation angle ν and performs the desired rotation has been developed. F_{rot} is based on the latter expression in order to obtain the rotation angle and on the rotation matrix function that due to its pure mathematical nature is presented in appendix A.

As in the afore presented algorithm for a planar structure, the algorithm proceeding for the cylindrical distribution calculates the positions of the points starting from the reference point. For it, first the normal vector $\vec{n}_{ref}$ at the reference point is obtained by means of $\vec{x}_{ref}$ the reference point and $\vec{x}_{axis}$ a point on the longitudinal axis. Thus, the coordinates of the reference point and a second point that is supposed to be on the longitudinal cylinder axis are demanded from the user. The distance between the longitudinal axis point and the reference point is equivalent to the radius of the cylindrical structure r_{cyl}. Moreover, the respective vector built

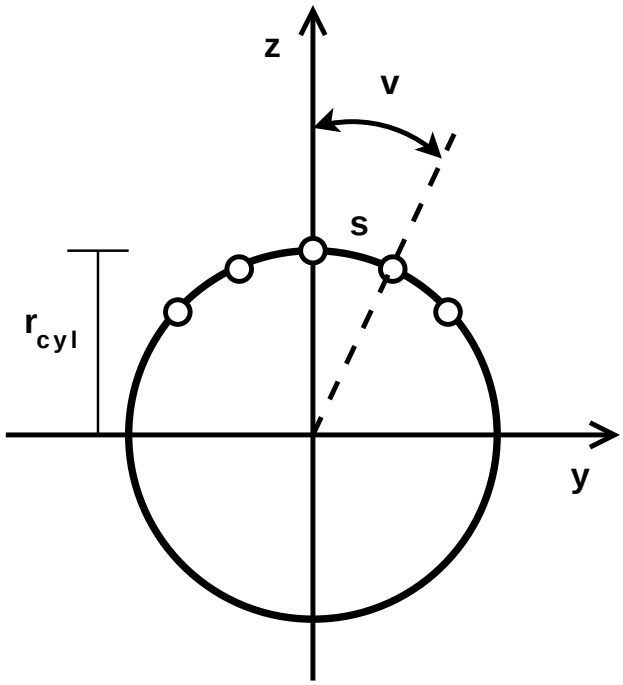

Figure 3.31 : *Geometry of an array on a cylindrical bearer*

by the position vectors towards these points is the normal vector n_{ref} at the reference point. With the information about this vector, the algorithm generates like in the case of the planar distribution an orthonormal system according to appendix A. The latter system is built by $\vec{\imath}_\nu$ plus $\vec{\imath}_u$ or $\vec{\imath}_v$. According to the choice of the user, either $\vec{\imath}_u$ or $\vec{\imath}_v$ becomes the direction vector of the longitudinal axis $\vec{\imath}_{axis}$ that together with the user given point on this axis $\vec{x}_{axis}$ builds the axial straight line.

The next proceeding step is to calculate the rotation angle ν, which depends of the arc length and the cylinder radius, according to expression (3.55). The latter length value, which is equivalent to the spacing between two neighbouring points on the simply curved structure, is s_u or s_v depending on the chosen longitudinal axis. Furthermore, since in the present thesis work the distances between the array elements are supposed to be equidistant, the rotation angle ν is calculated only once. Moreover, the parity evalution of the values for U and V is performed similar to the planar distribution module. In almost the same manner, the correction of the shift coefficients s_u and s_v and consequently of the rotation angle ν for the cases, whereat U and V are even numbers or U is odd and V is even or vice versa, is realized.

The calculation of a vector point $\vec{x}_{uv}$ is performed with all the latter information. Assuming the choice of $\vec{\imath}_v$ as the direction of the longitudinal axis, this is $\vec{\imath}_{axis} = \vec{\imath}_v$, then equation (3.53) is used for the distribution. For it, the reference point is rotated by means of F_{rot} about the latter axis with rotation angle ν in direction $\vec{\imath}_\nu$ and in addition shifted in direction $\vec{\imath}_v$ by the distance s_v. Before a new position is calculated, the normal vector n_{uv} is calculated by means of the position vector for point (u,v) and $\vec{x}'_{axis}$ the point on the longitudinal axis shifted by $v \cdot s_v$ from the reference point $\vec{x}_{axis}$. The direction $\vec{\imath}_\nu$ for the new required rotation is acquired by building a new orthogonal system with n_{uv} and $\vec{\imath}_v$. Following it, the calculation of the new point by the

Recovery of s_u, s_v, r_{cyl}, $\vec{x}_{ref}$ and $\vec{x}_{axis}$
Calculation of $\vec{n}_{ref}$ and r_{cyl}
Calculation of $\vec{\imath}_u$ and $\vec{\imath}_v$
Choice of longitudinal axis vector $\vec{\imath}_{axis}$
Evaluation of U and V on parity
Calculation of correction factor if necessary
Correction of the s_u, s_v if necessary
Choice of the arc length s
Calculation of the rotation angle ν with s and r_{cyl}
for u= 1 , U
for v=1,V
Calculation of F_{rot} with ν and u or v
Calculation of $\vec{x}_{uv}$ with u, v, $\vec{x}_{ref}$, s_u or s_v, $\vec{\imath}_{axis}$, $\vec{\imath}_\nu$ and F_{rot}
Calculation of $\vec{x}'_{axis}$ with $\vec{x}_{axis}$ and $u \cdot s_u$ or $v \cdot s_v$
Calculation of $\vec{n}_{uv}$ and $\vec{\imath}_u$ or $\vec{\imath}_v$
Storage of $\vec{x}_{uv}$
end
end

Table 3.5 : *Code structure for the cylindrical distribution module*

respective rotation and displacement can be done. For the choice of $\vec{\imath}_u$ as the direction of the longitudinal axis, expression (3.54) is used for the distribution. The respective proceeding is performed in the same manner.

The afore described distribution algorithm for a cylindrical structure taking in account the two possible choices of the cylinder axis has been implemented in a FORTRAN code. The resulting distribution module for cylindrical surfaces has the code structure depicted in table 3.5

For the latter code, a $U \times V$ matrix for the (u,v) point vectors with $u = 1,\ldots,U$ and $v = 1,\cdots,V$ at the cylindrical structure has been defined. According to the latter code structure, the required information about the variables s_u, s_v, r_{cyl}, $\vec{x}_{ref}$ and $\vec{x}_{axis}$ is looked for. With them, the code calculates the required orthogonal system composed of $\vec{n}_{ref}$, $\vec{\imath}_u$ and $\vec{\imath}_v$. Furthermore, the choice of the direction of the longitudinal axis allows the value definition of the arclength s and hence the calculation of the rotation angle ν. Moreover the parity check and the respective correction is realized. The code uses two loops to realise the cylindrical distribution. For every element (u,v) the position calculation starts at the reference point $\vec{x}_{ref}$. The code rotates this reference point by a shift angle that is a multiple of the rotation angle ν. The value of the latter multiple depends on how far the new point in reference one is. Furthermore, the code displaces the rotated point by the multiple of the shift distance, whose value is either s_u or s_v depending on the choice of the direction of the longitudinal axis $\vec{\imath}_{axis}$. The code generate a $U \times V$ position matrix, whose elements are the position vectors of the points on the simply curved surface.

3.4.3 Spherical position distribution

The possibility of finding points that belong to a spherical surface by means of a suitable distribution module has been introduced in the present thesis work. For the conception of the latter module an algorithm in order to calculate the position vectors of the points belonging to the doubly curved surface has been derived. Therefore, the mathematical definition of a sphere that according to [85] resembles to the following expression, has been analysed.

$$\vec{x} = \begin{pmatrix} r_{sph}\sin\theta\cos\phi \\ r_{sph}\sin\theta\sin\phi \\ r_{sph}\cos\theta \end{pmatrix} \qquad (\theta,\phi) \in [0,2\pi]\times[0,\pi] \tag{3.56}$$

In the latter equation the position vector $\vec{x}$ depends directly from the spatial angles θ and ϕ and the constant distance r. The latter two angle variables are attached to the local coordinate system. Consequently, the latter expression is not a suitable function for the development of a generally applicable distribution algorithm. Nevertheless, such an approach can been reached by analysing equation (3.56). The reader may notice that the x and y components of the position vector $\vec{x}$ behave according to a multiplication of the constant sphere radius by two harmonic functions dependant of the spatial angle θ and ϕ, respectively. Furthermore, component z is defined by the multiplication of the constant distance by a harmonic function dependant of θ. The relation between the components due to the spatial angles can be interpreted as two rotation procedures about the origin of the local coordinates. The first rotation takes place in x-z-plane and in the y-z-plane with θ as rotation angle. The second rotation happens in x-y-plane and the rotation angle is ϕ. In both rotations a point afar from the origin with the distance $\vec{r}_{sph}$ is displaced.

The algorithm for modelling doubly curved structures developed in the present thesis work is based on the latter analysis. For it, the position vectors of the reference point on the spherical surface and the sphere's centre are required. The algorithm applies the following developed formula

$$\vec{x}_{uv} = \vec{x}_{ref} + F_{rot}(u,\nu_1(s_u,r_{sph}))\cdot\vec{\imath}_{\nu_1} + F_{rot}(v,\nu_2(s_v,r_{sph}))\cdot\vec{\imath}_{\nu_2} \tag{3.57}$$

In the latter equations $\vec{x}_{uv}$ stands for the position vector of the point (u,v) that belongs to the spherical surface, $\vec{x}_{ref}$ for the position vector of the reference point on the plane, respectively. Vectors $\vec{\imath}_u$ and $\vec{\imath}_v$ build with the normal vector n_{uv} at the point (u,v) an orthogonal system. Moreover, s_u and s_v are the values for the arc length in direction $\vec{\imath}_{\nu_1}$ and $\vec{\imath}_{\nu_2}$, respectively. Both real-valued shift coefficients are used to calculate the required rotation angles ν_1 and ν_2 that are arguments of the rotation function of F_{rot}.

Similar to the case of a cylindrical structure, the algorithm proceeding for a doubly curved surface calculates the positions of the points starting from the reference point. Therefore, the normal vector $\vec{n}_{ref}$ at the reference point is acquired with the help of vectors of the reference point $\vec{x}_{ref}$ and of the centre $\vec{x}_{ctr}$. Consequently, the vector values of the latter points are demanded from the user. The distance between the centre and the reference point is equivalent to the radius of the spherical structure r_{sph} and the respective vector built by them is the normal vector n_{ref} at the reference point. With this information the algorithm generates an orthonormal system according to appendix A yielding $\vec{\imath}_{\nu_1}$ and $\vec{\imath}_{\nu_2}$. As next, the rotation angles ν_1 and ν_2, which depend of the arc length values that are s_u and s_v and the sphere radius r_{sph} , are

Recovery of s_u, s_v, r_{cyl}, $\vec{x}_{ref}$ and $\vec{x}_{ctr}$
Calculation of $\vec{n}_{ref}$ and r_{sph}
Calculation of $\vec{\imath}_{\nu_1}$ and $\vec{\imath}_{\nu_2}$
Evaluation of U and V on parity
Calculation of correction factor if necessary
Correction of the s_u, s_v if necessary
Calculation of the rotation angles ν_1 and ν_2 with s_u, s_v and r_{sph}
for u= 1 , U
for v=1,V
Calculation of F_{rot} with ν_1 and u
Calculation of F_{rot} with ν_2 and v
Calculation of $\vec{x}_{uv}$ with $\vec{x}_{ref}$, $\vec{\imath}_{\nu_1}$, $\vec{\imath}_{\nu_2}$, $F_{rot}(u,\nu_1)$ and $F_{rot}(v,\nu_2)$
Storage of $\vec{x}_{uv}$
end
end

Table 3.6 : *Code structure for the spherical distribution module*

obtained using expression (3.55). Furthermore, the rotation angles are calculated once since in the present thesis work the distances between the array elements are supposed to be equidistant. Moreover, the parity evalution of the values for U and V is performed similar to the planar and cylindrical distribution modules. In the same way, the correction of the arc lengths s_u and s_v and consequently of the rotation angles ν_1 and ν_2 for the cases, whereat U and V are even numbers or U is odd and V is even or vice versa, is performed. The calculation of a vector point $\vec{x}_{uv}$ is performed applying equation (3.57). For it, the reference point is rotated by means of F_{rot} about the centre of the sphere first with ν_1 and then with ν_2 in direction $\vec{\imath}_{\nu_1}$ and $\vec{\imath}_{\nu_2}$, respectively. Moreover, as in the cylinder algorithm the rotation function is based on the rotation matrix function that is given in appendix A.

Based on the afore described algorithm a code for finding points on spherical surfaces has been developed in FORTRAN. The code allocates a $U \times V$ matrix for the position vectors of each point (u,v), with $u = 1,\ldots,U$ and $v = 1,\cdots,V$, on the doubly curved structure. These vectors are computed according tho the code structure shown in table 3.6

As in the precedent modules, the code uses two loops to realise the calculation of the point vectors $\vec{x}_{uv}$. Before the loop process starts the required variables according to table 3.6 are retrieved or calculated. Furthermore the evaluation on parity and if necessary the correction of the arc length values are performed. The first loop steers the rotation with the rotation angle ν_1 and hence it displaces the reference point in $\vec{\imath}_{\nu_1}$ direction. In the second loop the similar is done in $\vec{\imath}_{\nu_2}$ direction: the treated point is rotated along the sphere point centre with the rotation angle ν_2. At the end of the procedure, the code fills the $U \times V$ matrix with the respective vector values representing all evaluated surface elements.

3.4.4 Normal vectors at surface points

In the present thesis work certain electromagnetic field and geometrical functions need input information about the normal vectors at the equivalent source positions and at the array element geometrical centres. For instance, the normal vector at the position of an equivalent source is a precondition to calculate its far field. Furthermore, the spatial angles ψ and ξ, which are essential variables in the field functions, depend of the values of the normal vector. Besides that, the geometrical composition of planar and conformal arrays in the present thesis work requires the knowledge on the normal vector. In this section, the approach for calculating the required normal vector is described briefly.

The normal vector at a point that belongs to a surface in space is regarded in a general manner and therefore it is assumed that the analysed field function has the form $z = f(x,y)$. Then according to the formula that is given in detail in appendix A, the normal vector of a function f at point (x_0, y_0, z_0) is

$$\vec{n} = (\nabla f(x,y,z))|_{(x_0,y_0,z_0)} \tag{3.58}$$

The ∇ operator in the latter equation applied on f builds the gradient of this function. Since the partial derivation as itself can not be implemented directly into a code expression in FORTRAN, it is necessary to approximate the gradient components by means of finite difference equations as presented in expression (A.3) until (A.5) in the appendix A.

In the present thesis work a module based on the latter approximation has been developed. The latter module performs the required subtraction and division of the function values. Furthermore, the latter values are obtained using developed distribution modules: the values of the position vector x_{uv} are displaced using the small valued step h for the shift coefficients, this is $s_u = s_v = h$. The same is valid for the cylindrical and spherical distribution modules, due to the fact that the rotation angles in them are calculated with s_u and s_v. Consequently, the point x_{uv} acts like the reference point in the previous described proceeding of the three distribution algorithms. Furthermore, the step value h must be very small in comparison to the mesh cell dimension in the case of handling a patch surface or in comparison to the spacing values in the case of handling an array structure. Moreover, the variation of the position vectors x_{uv} and the resulting variated vectors are limited to $U \times V$ vector elements including x_{uv} with $U = 3$ and $V = 3$.

The latter described approach allows to handle any kind of array structure, nevertheless it is not suitable for the array surfaces analysed in the present thesis work due to the required computational effort. Besides that, it is an approximation whose inaccuracy can perturbate the results of the far field analysis. In order to facilitate the calculation of the normal vector, simple vector arithmetic has been used. As aforementioned, in the case of a planar array or patch, the normal vector is demanded as input information from the user. This normal vector does not change values along the entire extending surface. Consequently, there is no need to compute the normal vector. The latter is not valid for non-orthogonal structures like a cylindrical or spherical surface.

For a spherical structure it is sufficient to create a vector from sphere's centre to the regarded point on the sphere that in the following is normalized. This is

$$\vec{n}_{uv} = \frac{\vec{x}_{uv} - \vec{x}_{ctr}}{|\vec{x}_{uv} - \vec{x}_{ctr}|} \tag{3.59}$$

wherein $\vec{x}_{ctr}$ and $\vec{x}_{uv}$ are the position vectors of the sphere's centre and of the regarded point, respectively. Consequently, the values of the vector $\vec{x}_{ctr}$ are required as input information. It has to be remarked that all the normal vector at each sphere point is different to the others. Besides that, the reader may noticed that the vector arithmetic calculation steps are less than using the gradient module on a spherical surface.

In the case of the cylindrical structure the normal vector is calculated in the same manner: the normalized difference between the position vectors of the regarded point on the structure $\vec{x}_{uv}$ and of a point on the longitudinal cylinder axis $\vec{x}'_{axis}$. This is

$$\vec{n}_{uv} = \frac{\vec{x}_{uv} - \vec{x}_{axis}}{|\vec{x}_{uv} - \vec{x}'_{axis}|} \tag{3.60}$$

Furthermore, the latter axis point must lie perpendicular to the point on the cylinder. The latter condition is guaranteed by obtaining the required values of $\vec{x}'_{axis}$ with the following equation

$$\vec{x}'_{axis} = \vec{x}_{axis} + s \cdot \vec{\imath}_{axis} \tag{3.61}$$

Therein, $\vec{\imath}_{axis}$ is the longitudinal axis vector of the cylinder and s is the shift coefficient that depending on the direction of the latter axis vector is $s = s_u$ or $s = s_v$. It has to be remarked that the normal vectors at the points positioned in direction of the cylinder axis vector do not change and have the same normal values. Different behaviour is found if the points are positioned in angular direction $\vec{\imath}_v$: the normals at these points differ from each other. Besides that, the calculation procedure in this case needs low computational effort than using the gradient module.

Furthermore, it can be said that using the simple vector arithmetic approach yields more accurate values for the normal vectors than the derivative approximation module. Both approachs generate a $U \times V$ matrix with the normal vectors as elements.

3.4.5 Validation of the planar and cylindrical positioning algorithm

In order to test the correctness of the positioning algorithm certain simulations by means of the code developed in the present thesis work and a MoM based solver have been realised. For it, an array composed of 5×5 elementary dipoles oriented in z-direction has been analysed. The $\frac{\lambda}{20}$ dipoles build for the first validation case a planar array that expands on the x-z-plane. The array is defined with a uniform spacing value of $d = 1.0$m and current amplitude $I_0 = 1.0$A. The radiation behaviour in free-space has been calculated by means of the directivity for a frequency of $f = 150$MHz defining the length of the dipoles as $l = 0.1$m. Figure 3.32 shows the resulting plots obtained with the equivalent source method and the MoM approach

In the second validation case the $\frac{\lambda}{20}$ dipoles form a cylindrical array whose curve radius has the value of $r = 2.0$m. The axis of the cylindrical structure expands in direction of the z coordinate. The conformal array is defined with uniform current amplitude $I_0 = 1.0$A and

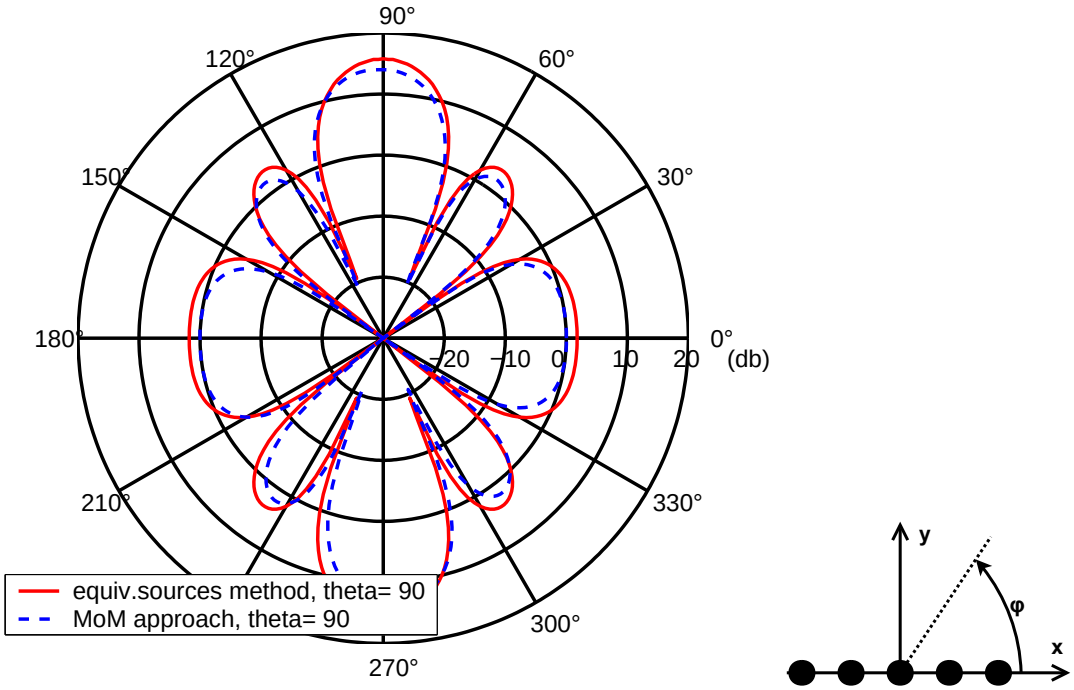

Figure 3.32 : *E-plane directivity of a planar array composed of* 5×5 $\frac{\lambda}{20}$ *dipoles*

with uniform spacing $d = 1.0$m, which is equivalent to a uniform arc length. As in the afore given validation case, the directivity has been simulated for a frequency of $f = 150$MHz with free-space conditions. The respective radiation behaviour is depicted in figure 3.33.

3.5 General array modelling

With the afore described point distribution and patch modelling modules an array of size $U \times V$ can be modelled. The modelling of a planar of conformal array is performed similar to the microstrip patch antenna modelling. The first step is to create the array shape by means of points generated with the developed distribution modules. The conceived array points are the geometrical centres of the array elements. In the second stage these elements are handled as patch antennas. Consequently, they are modelled by means of equivalent sources. For each array element its far field contribution is computed. As third step the far field of the array is calculated by summing up all the latter field contributions.

Concerning the first proceeding step, the geometrical array structure is generated with one of the afore presented distribution modules according to the desired form. The latter tools locate the $N_{elem} = U \cdot V$ points on the array surface. The result of the chosen distribution modules is a matrix containing the position vectors of these points. The distribution procedure starts from a reference point vector whose values are expected to be defined by the user. Furthermore, depending on the desired structure additional information is expected: the normal vector value for a planar array structure, the coordinates of a point on the longitudinal axis in case of a cylindrical array structure or the coordinates of the centre point for a spherical array structure. In

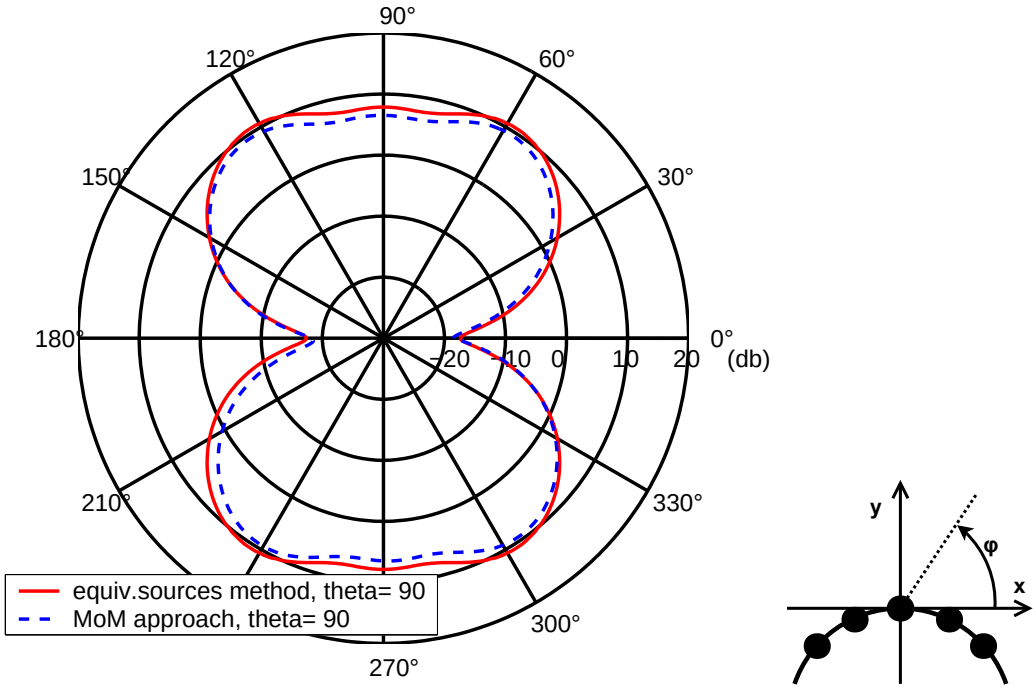

Figure 3.33 : *E-plane directivity of a cylindrical array composed of* 5×5 $\frac{\lambda}{20}$ *dipoles*

addition to the latter, the distances between the neighbouring array elements, the so-called spacing values, and the number of array elements on both expanding directions are expected being part of the input information. The array conception procedure according to the desired form is performed with all the latter required data. In addition, a second matrix with the normal vectors at the yielded array surface points is generated using the afore described vector arithmetic approach.

In the next proceeding step, each resulting position vector of the applied distribution module is attributed to an array element as its geometrical centre. Furthermore, the normal vectors at the latter centre points are given to each array element as input information. Moreover, the information about the geometrical dimensions of the array element and the desired number of discrete points for its discretization are expected from the user. The mesh cell dimensions are calculated with the latter input information: the length and width of the patch are discretized by dividing them by the number of discrete points. As aforementioned, it is necessary that the cells dimension are small enough in order to approximate the discrete elements with equivalent sources. As a general rule, this is guaranteed if each mesh cell side has the size $\Delta l \leq \frac{\lambda}{10}$. The discretization of the patch surface into small surface elements is performed by means of the planar distribution module in the present thesis work. For it, the required shift coefficients are defined by attributing the calculated mesh cell side value to them, this is $s_u = s_v = \Delta l$. Furthermore, the geometrical centre of the patch is defined as reference point for the point distribution and the normal vector values at this geometrical centre are attributed to the discrete surface elements as their normal vectors. Consequently, each array element is discretized with uniform surface elements. After the distribution procedure, the position of all equivalent sources and the respective normal vectors at these positions are obtained for each array element. In

addition to that, the current density values are retrieved from a respective input file generated by external software if the latter file exists. Otherwise the currents are calculated with the information about the excitation amplitudes and phases that are expected from the user. For the latter the cavity model approach, which is presented later on, is used.

The far field contribution generated by each array element is computed by means of the current distribution retrieved or calculated and given to the equivalent sources in addition to the information about the source position and normal vectors. Each field contribution $\vec{E}_{ij,uv}$ is computed according to the afore described algorithm and code for modelling a microstrip antenna. The far field of the entire array $\vec{E}_{ij}^{array}$ is the addition of these fields contributions. The superposition of these fields is realized by means of following equation

$$\vec{E}_{ij}^{array} = \sum_{u}\sum_{v}\vec{E}_{ij,uv} \tag{3.62}$$

It has to be said, that the resulting field is the electric field of the entire array for an observing point (r,θ_i,ϕ_j). This means that in order to obtain the field for a designed space of $N_\theta \cdot N_\phi$ observation points the entire modelling proceeding has to be repeated $N_\theta \cdot N_\phi$ times.

For the realization of the array modelling module a FORTRAN code has been developed based in the afore described proceeding in addition to the required distribution and array element modelling modules. For it, a $N_\theta \times N_\phi$ observation space has been defined composed of observing points with the form (r,θ_i,ϕ_j) with $i = 1,\ldots,N_\theta$ and $j = 1,\ldots,N_\phi$ positioned in the far field. This means that all the observing points are defined by a constant huge-valued radius. In the present thesis work this is $r = 1.0 \cdot 10^4$. The resulting fields have been stored in a complex $N_\theta \times N_\phi$ matrix. The resulting code structure is shown in table 3.7.

The developed code performs first all the necessary procedures in order to obtain and to store the required geometrical information. These procedures are the calculation of the position and normal vectors of the array elements, the computation of the position and normal vectors of the equivalent sources, and the allocation of matrices for storing the geometrical data. Furthermore, the assignment of the current densities to the equivalent sources takes place if a file containing these external calculated excitations exits. In the case that the latter file is missing, the necessary excitation values are computed according to the cavity model and attributed to the equivalent sources. As in the code for modelling the microstrip patch antenna, the implementation of the calculation proceeding of the array far field is performed with two pair of loops. The first two loops control the variation of the spatial angles θ_i and ϕ_j, which define the observation space, in the range of $[0^\circ, 360^\circ]$. The other two loops decide which array element (u,v) is being analysed by steering the control variables u and v that have the values $u = 1,\ldots,U$ and $v = 1,\ldots,V$. The latter means that the field generated by the $U \cdot V$ array elements is calculated for each observation point (r,θ_i,ϕ_j). The internal loops, that indicate which equivalent source is being handled, and the corresponding procedures in table 3.3 are applied in order to obtain the field contribution of a single array element. The resulting field contains all contributions of the modelling equivalent sources for the regarded array element (u,v). Following the latter procedure the fields of all array elements are summed up. The latter step and the array elements loop process are equivalent to the double sum applied on the array elements field in equation (3.62). Moreover, the acquired far field is stored in a matrix as element (i,j). The entire procedure is repeated until the $N_\theta \times N_\phi$ matrix is filled.

```
Allocation matrix E_{n_θ,n_φ}
Definition θ = 0
Definition φ = 0
Definition rad = 1.0 · 10^4
Calculation of the position vectors of the array elements
Calculation of the normal vectors of the array elements
Calculation of the position vectors of the equivalent sources
Calculation of the normal vectors of the equivalent sources
Calculation/Assignment of the current densities for/to the equivalent sources
for i=1,N_θ
    Calculation of θ_i
    for j=1,N_φ
                    Calculation of φ_j
                    Calculation of r⃗_ij with rad, θ_i, φ_j
                    Conversion from r⃗_ij into x⃗_ij
                    Definition E⃗_ij^array = 0
                    for u=1,V
                        for v=1,V
                            Calculation of E⃗_ij,uv with antenna model
                            Summation of E⃗_ij,uv to E⃗_ij^array
                        end
                    end
                    Storage of E⃗_ij^array in E⃗_i,j
    end
end
```

Table 3.7 : *Code structure for the field calculation of a modelled array*

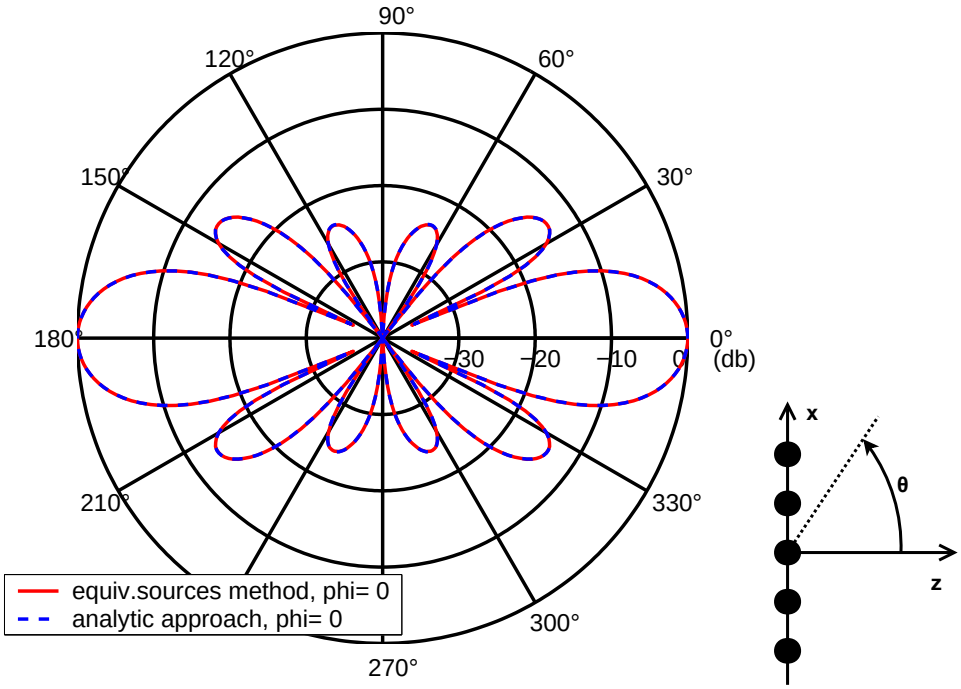

Figure 3.34 : *E-plane pattern for a* 5×5 *array of* $\frac{\lambda}{10}$ *dipoles*

3.5.1 Validation of the general array modelling algorithm

The general array modelling algorithm applied on arrays, that are composed of elementary dipoles, has to yield the results obtained by analytical formulae. Consequently, an array composed of 5×5 infinitesimal dipoles that are oriented in x direction has been analysed. The flat array structure lies parallel to the x-y-plane. The elements of this planar array are positioned with uniform spacing $d = 0.5\lambda_0$ and fed with a uniform current value of $I_0 = 1.0$A. Under the latter conditions the array field has to be equivalent to the multiplication of the element radiated field with the array factor of equation (1.118) in chapter 1. Figures 3.34, 3.35 show the pattern function in E-plane and the H-plane for the approach developed in the present thesis work, the equivalent sources method, compared to the analytical function. Furthermore, the behaviour of the pattern in elevation for $\phi = 45^\circ$ has been compared. All three yielded curves overlap.

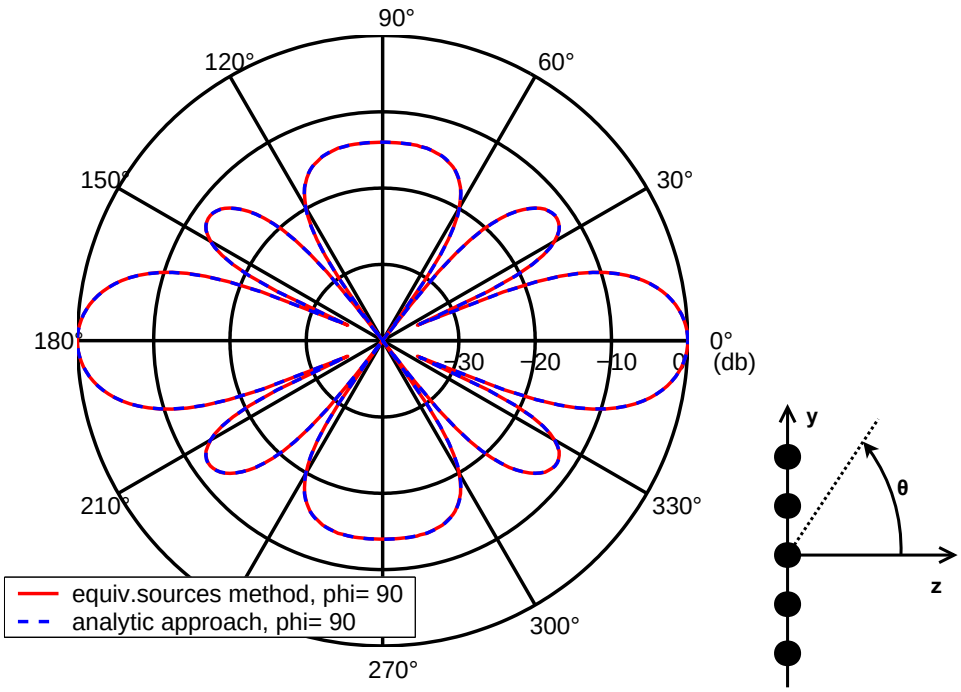

Figure 3.35 : *H-plane pattern for a* 5×5 *array of* $\frac{\lambda}{10}$ *dipoles in elevation*

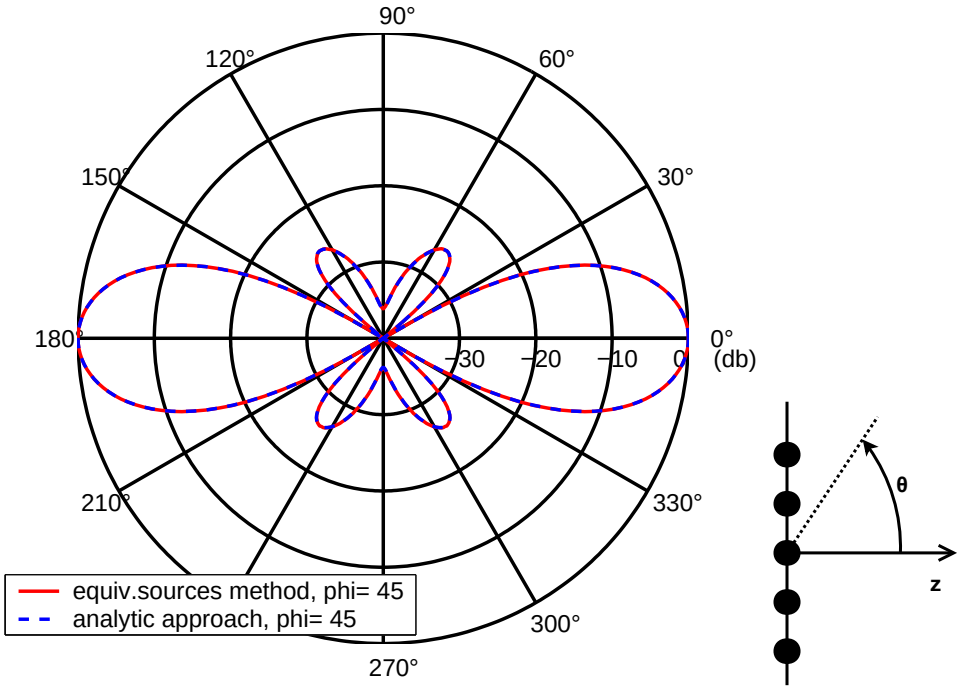

Figure 3.36 : *Pattern for a* 5×5 *array of* $\frac{\lambda}{10}$ *dipoles in elevation*

3.6 Large array modelling by means of subarrays

The radiation behaviour of a finite large array can be modelled by means of the previous described general array modelling approach. Nevertheless, assuming that the analysed array is characterized by uniform spacing, equal planar elements and that it has a periodic structure, it may be possible to model the far field behaviour of an entire array by regarding only a part of the array, namely a subarray. Consequently, some calculation procedures could be simplified and therefore the computational effort reduced. In this section the modelling of a subarray, this is a small array composed of $K \cdot L$ elements e.g. for $K \leq 5$ and $L \leq 5$, is used in order to calculate the entire large finite array.

The principle of this approach is based on the idea that a small group of $K \cdot L$ elements being part of a $U \times V$ uniform spaced periodic array composed of equal planar patch, namely a $K \times L$ subarray, has a certain radiation behaviour that is similar to another $K \times L$ element group of the same array. Furthermore, this periodic array is composed by $N_{sub} = \frac{U}{K} \cdot \frac{V}{L}$ of the latter subarrays. Moreover, the total far field of the array is the sum of the field contributions of the subarrays. Hence it can be decomposed in a multiplication of the subarray radiation by a factor consisting of the sum of the N_{sub} phase terms that correspond to all subarrays. This basic idea originates from the analogue approach developed in order to acquire the theoretical array factor. The respective derivation steps are shown in expressions (1.96) - (1.98) in chapter 1. In these equations the constants and non changing quantities can be factored out of the field sum leaving a sum factor that consist of the non negligible phase terms of the array elements due to their geometrical position. Due to the latter analogy, similar derivations steps can be developed in order to obtain suitable functions for the field calculation by means of subarrays. The following equation shows the resulting mathematical expression for the electric field calculation of an array composed of $N_{sub} = \frac{U}{K} \cdot \frac{V}{L}$ subarrays

$$\vec{E}_{ij}^{\,array} = \sum_{a=1}^{\frac{U}{K}} \sum_{b=1}^{\frac{V}{L}} \vec{E}_{ij,ab}^{\,sub} \cdot e^{\mathrm{j}k\gamma_{ij,ab}} \tag{3.63}$$

At the latter equation $\vec{E}_{ij}^{\,sub}$ is the electric far field of a $K \times L$ subarray and $\gamma_{ij,ab}$ is the non negligible phase due to the geometrical position of subarray a, b. Analogue to the case of the derivation of the array factor, $\vec{E}_{ij}^{\,sub}$ is the radiation of a subarray at the reference point of the large array. In the present thesis work this point is the geometrical centre of the array structure.

The general approach of building an array with the help of its elements implies the knowledge of the positions of these elements. Consequently, in the afore presented algorithm for the general the approach, the geometrical centres of the array structure and of the array elements contribute in building the adequate phase terms required for the far field calculation. Furthermore, these terms contain the information about the relative position of the array elements in reference to the array's geometrical centre that for an odd number of elements is the position of a centre element. Analogue to the latter, the phase $\gamma_{ij,ab}$ should comprise the relative positions of the subarrays in reference to the array centre that for an odd number of elements is the position of the reference subarray. Furthermore, due to the fact that the element modelling equivalent sources contribute to the phase term of the whole subarray, $\gamma_{ij,ab}$ should take into account their influence.

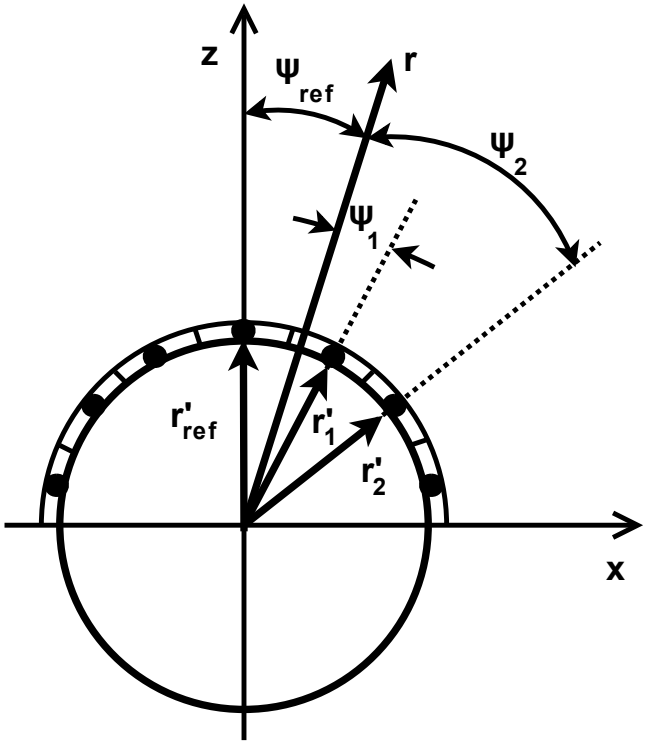

Figure 3.37 : *Geometry for array approximation by means of subarray handling*

Assuming that the subarrays have same radiation behaviour and that they are of small size and hence that the subarray elements are in proximity of the subarray centre, the phase contribution of the entire subarray can be approximated by using the relative position of the subarrays centre. Such positions are shown in figure 3.37 for an array on a cylindrical bearer. In this example there are seven subarrays whose geometrical centre is represented by the dark dots. The subarray in the centre is the reference subarray of the entire array. The required information about the relative positions of the neighbouring subarrays are described by the angles ψ_1, ψ_2, ψ_{ref} and the vectors $\vec{r}'_1$, $\vec{r}'_2$ and $\vec{r}'_{ref}$, respectively. Consequently, a $A \times B$ array can be modelled by N_{sub} $K \times L$ "subarray elements", which are described by their relative position, if the radiated field of a subarray, namely the reference subarray, is known. Since the relative position contains the information about the array structure, this approximation is independent of the form of the structure . Assuming that the phase term of the radiated field of the reference subarray has the form $e^{-jk_0 r'_{ref0}\cos\psi_{ij,ref0}}$, then the phase $\gamma_{ij,ab}$ is calculated by

$$\gamma_{ij,ab} = r'_{ref0}\cos\psi_{ij,ref0} - r'_{ab}\cos\psi_{ij,ab} \tag{3.64}$$

In the latter equation $r'_{ref0} = |\vec{r}'_{ref0}|$ is the magnitude of the position vector towards the geometrical centre of the reference subarray and $r'_{ab} = |\vec{r}'_{ab}|$ stands for the length of the position vector towards the geometrical centre of the subarray (a,b). Furthermore, $\psi_{ij,ref0}$ and $\psi_{ij,ab}$ are the spatial angles enclosed by the vectors $\vec{r}'_{ref0}$, $\vec{r}_{ij}$ and vectors $\vec{r}'_{ab}$, $\vec{r}_{ij}$, respectively. The $\vec{r}_{ij}$ is the position vector of the observation point (r,θ_i,ϕ_j). Using the afore given formula (3.2) for the definition of a spatial angle enclosed by two vectors, the following mathematical expression can be applied in order to acquire the values for $\psi_{ij,ab}$

$$\cos\psi_{ij,ab} = \frac{\vec{r}_{ij}\cdot\vec{r}'_{ab}}{|\vec{r}_{ij}||\vec{r}'_{ab}|} \qquad \Longrightarrow \qquad \psi_{ij,ab} = \arccos\left(\frac{\vec{r}_{ij}\cdot\vec{r}'_{ab}}{|\vec{r}_{ij}||\vec{r}'_{ab}|}\right) \tag{3.65}$$

The other required spatial angle ψ_{ref0} is obtained using the same formula with the vectors $\vec{r}'_{ref0}$, $\vec{r}_{ij}$. This is

$$\cos\psi_{ij,ref0} = \frac{\vec{r}_{ij}\cdot\vec{r}'_{ref0}}{|\vec{r}_{ij}||\vec{r}'_{ref0}|} \qquad \Longrightarrow \qquad \psi_{ij,ref0} = \arccos\left(\frac{\vec{r}_{ij}\cdot\vec{r}'_{ref0}}{|\vec{r}_{ij}||\vec{r}'_{ref0}|}\right) \tag{3.66}$$

Recapitulatory, it can be said that this approximation can be performed if the radiation behaviour of all subarrays are equal. Moreover, if the geometrical centre of the reference subarray is not the origin of the coordinates system, the phase term due to its relative position has to be compensated and taken into account in the phase $\gamma_{ij,ab}$. Besides, in order to obtain the far field of the analysed array it is necessary to calculate the field contribution of the reference subarray and then to convert the obtained contribution into the total far field. The latter conversion is performed by multiplying it with the sum of the phase terms that correspond to the rest of the subarrays. Moreover, in the case of an even number of subarrays, the radiation field for a virtual array is computed and then it is multiplied by the sum of the phase terms. By this mean, the calculation of the far fields of the large finite array is simplified.

The previous described approach is valid for planar as well as conformal structures. The multiplication of the reference subarray field with a single phase term can be interpreted as a translation along the array surface in the planar case. In the cylindrical case the latter phase term multiplication means a translation in direction of the cylinder axis or a rotation transversal to this axis. In the spherical case the phase multiplication is equivalent to a rotation aroung the sphere's centre. Furthermore, the algorithm and the respective approximation can only be realized for certain curvature grades, due to the fact that for high curvature grades the phase contribution of each single array element on the subarray phase term is greater and can not be neglected. Since in general large finite conformal arrays are mainly integrated in structures of aceptable curvature grade, this approximation can be applied.

The afore presented algorithm has been implemented in a FORTRAN module. The structure of the developed code is shown in table 3.8 and it based on the code structure of table 3.7. The code performs all procedures previously explained with the help of some pair of loops: one pair for defining the observing space, another for the field calculation of a subarray and a third for the acquiring of the total field of the entire array. A complex matrix, whose elements contain the electric field values for all observation points, is obtained at the end of the loop procedure.

An observation space composed of N_θ values for θ and N_ϕ for ϕ as well as a constant radius value has been defined. The spatial angles values θ_i and ϕ_j have been limited by the range $[0°, 360°]$. The code performs first the geometrical array structure by calculating the positions and the normals of all equivalent sources. Then, it calculates and assigns the excitations to these source or it assigns the excitations from a current file according to the case. Then, it calculates for each observation point the far field of the reference subarray and the phase term due to the reference subarray geometrical centre. Then, the phase terms due to the positions of the other subarrays are calculated. These terms are used together with the field of the reference subarray and the reference centre phase term for calculating the field contributions of the respective

Allocation matrix E_{n_θ,n_ϕ}
Definition $\theta = 0$
Definition $\phi = 0$
Definition $rad = 1.0 \cdot 10^4$
Calculation of the position vectors of the array elements
Calculation of the normal vectors of the array elements
Calculation of the position vectors of the equivalent sources
Calculation of the normal vectors of the equivalent sources
Calculation/Assignment of the current densities for/to the equivalent sources
for i=1,N_θ
    Calculation of θ_i
    for j=1,N_ϕ
        Calculation of ϕ_j
        Calculation of $\vec{r}_{ij}$ with rad, θ_i, ϕ_j
        Conversion from $\vec{r}_{ij}$ into $\vec{x}_{ij}$
        Definition $\vec{E}_{ij}^{sub} = 0$
        for u=1,K
            for v=1,L
                Calculation of $\vec{E}_{ij,uv}$ with antenna model
                Summation of $\vec{E}_{ij,uv}$ to $\vec{E}_{ij}^{sub}$
            end
        end
        Recovery of $\vec{r}'_{ref0}$
        Calculation of $\psi_{ij,ref0}$ with $\vec{r}'_{ref0}$
        Definition $\vec{E}_{ij}^{array} = 0$
        for a=1,$\frac{U}{K}$
            for b=1,$\frac{V}{L}$
                Recover of $\vec{r}'_{ab}$ and conversion to $\vec{x}'_{ab}$
                Calculation of $\psi_{ij,ab}$ with $\vec{x}'_{ab}$,$\vec{x}_{ij}$
                Calculation of $\gamma_{ij,ab}$ with $\psi_{ij,ab}$, $\psi_{ij,ref0}$
                Calculation of $\vec{E}_{ij,ab}$ with $\gamma_{ij,ab}$, E_{sub}
                Summation of $\vec{E}_{ij,ab}$ to $\vec{E}_{ij}^{array}$
            end
        end
        Storage of $\vec{E}_{ij}^{array}$ in $\vec{E}_{i,j}$
    end
end

Table 3.8 : *Code structure for the field calculation of a large finite array by means of subarrays*

subarrays. In the last step the fields of all subarrays are superposed yielding the far field for an observation point that is stored in a $N_\theta \times N_\phi$ matrix.

Concerning the generation of points that represent the subarrays on the analysed large array structure, it is realized by means of the distribution algorithms presented in this chapter. The distribution procedure starts from a reference point, which is the geometrical centre of the finite large array. Consequently, the geometry of the array structure will be symmetrical to this point. The distances between the neighbouring subarrays are equivalent to the ones between the subarray centres. These distances are defined by the size of the subarrays. The respective length and width values of the subarray are integer multiples of the array spacings and hence they depend of the number of elements that belong to a subarray. As at the patch structure generation procedure there is a parity evaluation and a corresponding shift coefficient correction if necessary.

3.6.1 Validation of the large array modelling algorithm

As validation case for the large array modelling algorithm an array composed of 100×100 elementary dipoles has been modelled and analysed. This algorithm has to generate the same field resulting from the multiplication of the element radiated field with the array factor of equation (1.118) in chapter 1. The latter field generation is performed similar as in the general array modelling algorithm case. The infinitesimal dipoles are oriented in x-direction and are fed with a uniform current value of $I_0 = 1.0$A. Furthermore, the array is uniformly spaced and the spacing value is $d = 0.5\lambda_0$. Furthermore, the subarrays have been defined to be composed of 10×10 elements. Consequently, the large array has 100 "subarray elements". In figures 3.38 and 3.39 the E-plane and H-plane radiation pattern obtained with the approach developed in the present thesis work and with the analytical formulae are plotted. The reader may observe that the curves obtained by means of both approaches overlap.

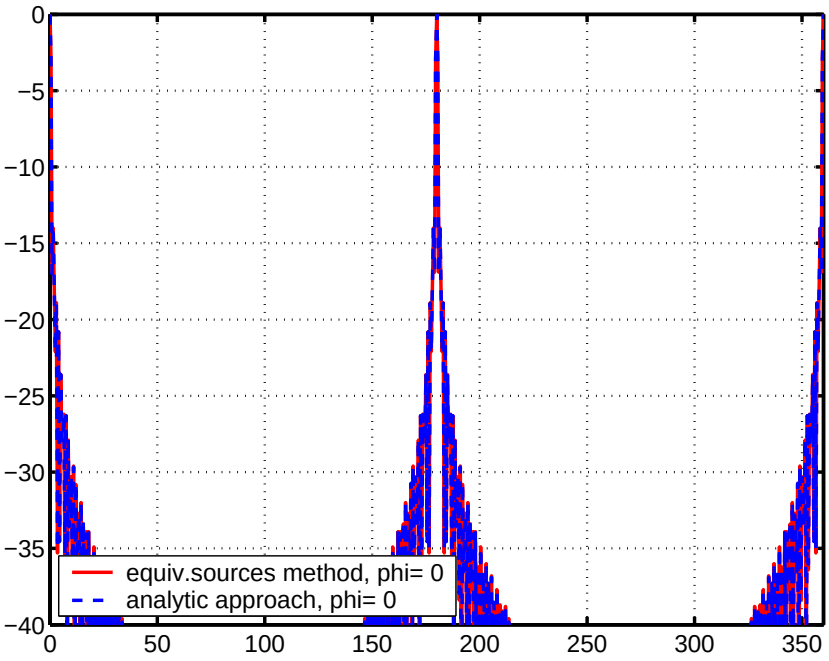

Figure 3.38 : *E-plane pattern of a* 100×100 *array composed of* 10×10 *subarrays of* $\frac{\lambda}{10}$ *dipoles*

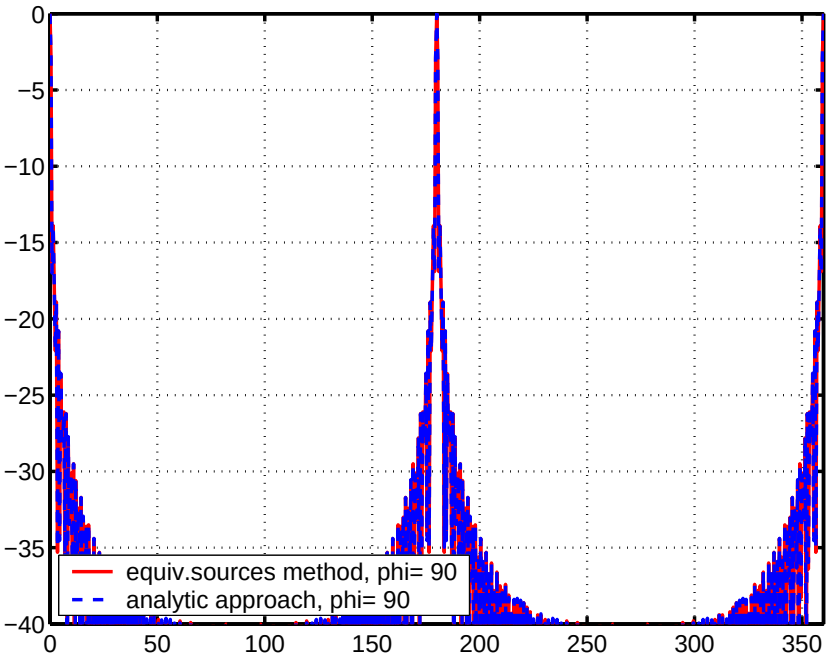

Figure 3.39 : *H-plane pattern of a* 100×100 *array composed of* 10×10 *subarrays of* $\frac{\lambda}{10}$ *dipoles*

3.7 Excitation currents for the sources

The excitation currents are essential variables for the calculation of the array far field. There exist two possibilities in order to obtain these currents on the array elements. The first approach consists in modelling the current distribution on the radiating region of the microstrip antenna by means of the cavity model. For it, the respective analytical formulae, that are presented later on, are applied. The second possibility for attaining the current distribution is to compute them by means of external software. Therefore, codes based on FDTD and FIT has been used. Moreover, it has to be remarked that the acquired currents using the cavity model does not allow to take into account the interactions between neighbouring array elements. Consequently, it models the currents of a single antenna element.

Two aspects of the present thesis work have to be recalled to the reader. The first one is that the field of a conformal array and conformal radiation elements is approximated with planar radiating elements on a conformal structure. Furthermore, these array elements are supposed to be equal shaped and with equal radiation characteristics. Consequently, these antennas imply to have same current distributions. Second aspect is that the code presented in the present thesis work treats the antenna array according to a micro-to-macro approach. This means that the code calculates first for each array element the far field contribution of the equivalent sources and then with them the field contribution of a subarray or the entire field of the array. Therefore, the assignment of the current values must be performed on the equivalent sources. Furthermore, the attribution of the currents must be realized after the conception of the array structure and before the far field calculation procedure.

3.7.1 Currents with the Cavity Model approach

There exist simple models in order to approximate the radiation behaviour of a microstrip antenna, for instance, the Transmission Line model and the Cavity Model. For the generation of the excitation currents certain analytical functions originating from the Cavity Model technique have been used in the present thesis work. Theory concerning the latter approach is presented briefly in the next lines. For this introduction, [1], [2] and [14] have been used as reference. Moreover, [51] and [10] give also a brief description of the model.

3.7.1.0.1 The Cavity Model According to [1] the current distributions on the patch are related to the modes of a rectangular cavity. In this model the patch antenna is described as a dielectric volume enclosed by six rectangular surfaces. The top and the bottom of this cavity, which correspond to the patch and the ground plane, are assumed as perfectly conducting electric walls. The other four walls of the dielectric loaded cavity are modelled as perfect magnetic walls. Furthermore, under the concept of a rectangular cavity a waveguide of finite length, that enclosures a dielectric, is understood. A microstrip antenna resembles to such a cavity with the exception of not having all conductor walls. Consequently, to model more accurately the microstrip patch antenna, the cavity walls around the patch are treated as magnetic walls simulating an open circuit. The assumption, that the cavity current distribution describes very close the distribution of the microstrip antenna, is confirmed by measurements. Therefore, other quantities like resonant frequencies and modes of the cavity compare very well to the ones of the microstrip antenna.

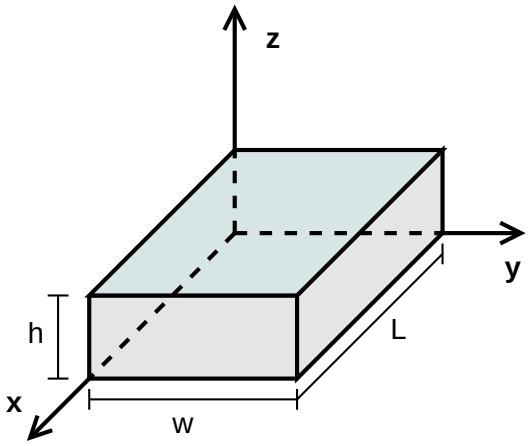

Figure 3.40 : *Cavity model of a rectangular microstrip patch antenna*

Since the thickness of the microstrip is very small, the waves generated within the dielectric substrate undergo extensive reflections causing standings waves. At the same time the field variations along the very small height of the microstrip is considered as constant. The height is usually very small compared to the wavelength of the resonance frequency. The fields underneath the antenna patch, which form standing waves, can be represented by cosinusoidal wave functions. Concerning these wave functions, only transversal magnetic mode TM_{mnp} field configurations are assumed to exist within the cavity in the present thesis work and hence only these configurations are considered. These field configurations can be taken into account by defining the magnetic vector potential function adequately. Furthermore, the vector potential is conceived according to the boundary conditions of the cavity.

For instance, the boundary conditions for a rectangular cavity that expands at the x-y-plane as shown in figure 3.19 are the following

$$\begin{aligned}
E_x(0 \le x \le \mathsf{L}, 0 \le y \le \mathsf{w}, z = 0) &= 0 \\
E_x(0 \le x \le \mathsf{L}, 0 \le y \le \mathsf{w}, z = \mathsf{h}) &= 0 \\
H_x(x = 0, 0 \le y \le \mathsf{w}, 0 \le z \le \mathsf{h}) &= 0 \\
H_x(x = \mathsf{L}, 0 \le y \le \mathsf{w}, 0 \le z \le \mathsf{h}) &= 0 \\
H_y(0 \le x \le \mathsf{L}, y = 0, 0 \le z \le \mathsf{h}) &= 0 \\
H_y(0 \le x \le \mathsf{L}, y = \mathsf{w}, 0 \le z \le \mathsf{h}) &= 0
\end{aligned} \tag{3.67}$$

In the latter equation set h stands for the height of the cavity, L for the length and w for the width of the cavity, respectively. Consequently, the magnetic vector potential must fulfil the latter conditions on these geometrical borders. The function of such a vector potential $\vec{A}$ inside the cavity is given by the following equation set

$$\begin{aligned} A_x &= 0 \\ A_y &= 0 \\ A_z &= A_{coef}\cos(k_x x)\cos(k_y y)\cos(k_z z) \end{aligned} \tag{3.68}$$

In the latter expression A_x, A_y and A_z are the components of the vector potential, A_{coef} the amplitude coefficient, respectively. k_x, k_y and k_z stand for the wave numbers that also have to fulfil the boundary conditions. These wave numbers are calculated by the next formulae

$$\left.\begin{array}{ll} k_x = \frac{\mathsf{m}\pi}{\mathsf{L}} & \mathsf{m} = 0,1,2,\ldots \\ k_y = \frac{\mathsf{n}\pi}{\mathsf{w}} & \mathsf{n} = 0,1,2,\ldots \\ k_z = \frac{\mathsf{p}\pi}{\mathsf{h}} & \mathsf{p} = 0,1,2,\ldots \end{array}\right\} \quad (\mathsf{m},\mathsf{n},\mathsf{p}) \neq (0,0,0) \tag{3.69}$$

In the latter equation set, the variables m, n and p represent the mode numbers that describe the behaviour of the waves in the cavity. These numbers give the quantities of half-cycle filled variations along x, y and z directions. According to the Cavity Model, the yielded vector potential for the cavity is also valid for a microstrip patch antenna that is characterized by the same geometrical values. Consequently, the analysed microstrip antenna has a radiating patch of length L and of width w. Furthermore, the thickness of the dielectric substrate in the antenna is h. Moreover, the transversal magnetic waves TM_{mnp} in basic mode has great influence on the radiation behaviour according to [1]. Consequently, only basic modes are used in order to approximate the vector potential behaviour inside the microstrip antenna structure.

The acquired vector potential function can be used straight forward in order to obtain the the fields enclosed by the dielectric layer of the microstrip antenna. Consequently, it can be used to acquire the current distribution on the radiating antenna. According to equation (1.76) in chapter 1, the vector potential for far field analysis can be approximated by a multiplication between the excitation current, the orientation of the element, the phase term with the position information, and other constants. Thus, assuming the discretization of the radiating patch and according to the equation for a discrete patch surface element in expression (3.1), the amplitude coefficient A_{coef} of the vector potential can be determined. For instance, the vector potential in TM_{mnp} mode underneath a patch surface element is defined as in the following

$$\begin{aligned} A^x_{mn} &= 0 \\ A^y_{mn} &= 0 \\ A^z_{mn} &= A_{coef}\cos(k_x x_{mn})\cos(k_y y_{mn})\cos(k_z \mathsf{h})\frac{\mu I_{mn}}{4\pi} \end{aligned} \tag{3.70}$$

The current distribution on the patch can be obtained using the afore given function for the vector potential in combination with its relation with the magnetic intensity and with the boundary relation. The latter relation results from the use of equivalent sources and is given in chapter 1. Consequently, by applying the latter vector potential function in equation (1.37), the magnetic field $\vec{H}_{mn}$ under the patch surface element (m,n) is obtained. This is

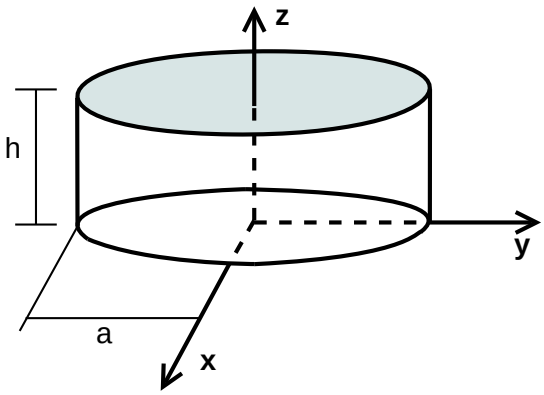

Figure 3.41 : *Cavity model of a circular microstrip patch antenna*

$$\begin{aligned} H_{mn}^{x} &= -\frac{k_z I_0 l_{mn}}{\mu}\cos(k_x x_{mn})\cos(k_y y_{mn})\sin(k_z \mathsf{h}) \\ H_{mn}^{y} &= \frac{k_y I_0 l_{mn}}{\mu}\cos(k_x x_{mn})\sin(k_y y_{mn})\cos(k_z \mathsf{h}) \\ H_{mn}^{z} &= 0 \end{aligned} \tag{3.71}$$

wherein $l_{mn} = \Delta l$ is the size of the mesh cell, I_0 the excitation current of the entire patch antenna and μ the permeability of the dielectric layer, respectively. With the acquired field underneath the metallic patch surface the current distribution according to (1.69) can be acquired. Furthermore, it is assumed that there exist no incident field on the patch surface and consequently the field above the patch surface is zero. Taking into account the latter assumption and adapting the expression (1.69) for a patch discretized in $M \cdot N$ surface elements, the following expression for obtaining the current distribution $\vec{J}_{mn}^{surf}$ on the surface element (m,n) is yielded

$$\vec{J}_{mn}^{surf} = -\vec{n}_{surf} \times \vec{H}_{mn} \tag{3.72}$$

Therein, $\vec{n}_{surf}$ is the normal vector of the regarded surface element that is for all surface elements the same since the patch surface is assumed to be planar. Furthermore, $\vec{H}_{mn}$ is the afore acquired magnetic intensity underneath the surface element (m,n). The latter defined current distribution, which fulfills the boundary conditions given in set (3.73), has been implemented for the a TM_{mnp} in form of a module coded in FORTRAN. In order to obtain a required dominant mode, the wave numbers according to (3.69) have to be determined. The mode with the lowest order resonant frequency is referred to as the dominant mode. According to [1] for all rectangular microstrip patch antennas with $\mathsf{h} \ll \mathsf{L}$ and $\mathsf{h} \ll \mathsf{w}$, the dominant mode is the TM_{010}. For the latter mode, the wave number in y direction becomes $k_y = \frac{\pi}{\mathsf{w}}$ and the wave numbers in x and z direction dissapear for $\mathsf{m} = 0$ and $\mathsf{p} = 0$, respectively.

In addition to the latter, the possibility of calculating the current distribution at a patch of circular form has been implemented. Consequently, the cylindrical patch antenna is modeled by a cylindrical cavity with the geometrical dimension of r and h that are the radius and the height of the cylinder. Furthermore, the required vector potential function in the cavity has to fulfil following boundary conditions

$$\begin{aligned} E_\rho(0 \le \rho \le a, 0 \le \phi \le 2\pi, z = 0) &= 0 \\ E_\rho(0 \le \rho \le a, 0 \le \phi \le 2\pi, z = h) &= 0 \\ H_\phi(\rho = a, 0 \le \phi \le 2\pi, 0 \le z \le h) &= 0 \end{aligned} \tag{3.73}$$

The fields in latter equation set are in cylindrical coordinates. ρ, ϕ and z are the radial component, the azimuthal component and the axial component of the position vector in cylindrical coordinates. These boundary conditions, which characterize the cylindrical cavity, describe the cylinder envelope as a perfect magnetic wall, and the top and bottom of the cylinder as perfect electric walls. A vector potential that fulfils the conditions on the dielectric layer borders is proposed in [1]. This is

$$\begin{aligned} A^\rho_{mn} &= 0 \\ A^\phi_{mn} &= 0 \\ A^z_{mn} &= B_{coef} J_m(k_\rho \rho_{mn})[C_1 \cos(m\phi_{mn}) + C_2 \sin(m\phi_{mn})] \cos(k_z z_{mn}) \end{aligned} \tag{3.74}$$

The latter vector potential equation gives the wave function in the transversal magnetic mode TM_{mnp}. Therein, k_ρ and k_z are the wave numbers in ρ and z direction, and B_{coef}, C_1 and C_2 are coefficients. Furthermore, J_m stands for the Bessel function of first kind of order m. The required wave numbers are defined by

$$\begin{aligned} k_\rho &= \tfrac{\chi_{mn}}{a} \quad m = 0, 1, 2, \ldots \quad \text{and} \quad n = 1, 2, 3, \ldots \\ k_z &= \tfrac{p\pi}{h} \quad p = 0, 1, 2, \ldots \end{aligned} \tag{3.75}$$

In the latter equation, m, n and p stand for the mode numbers that describe the behaviour of the waves in the cavity. Furthermore, χ_{mn} represents the zeros of the derivative of the Bessel function J_m. For most typical microstrip antennas the thickness h of the dielectric layer is typically $h < 0.05\lambda_0$ with λ_0 as the free space wavelength and therefore it is very small. Consequently, the fields along z direction for a patch geometry as in figure 3.24 are essentially constant and are defined by setting $p = 0$. According to [1], the first dominant mode of the TM_{mnp} wave functions is the TM_{110}. The magnetic field due to this vector potential wave function can be calculated by applying equation (1.37). Consequently, the magnetic intensity under the surface element (m,n) chosing a simple cosine variation, this means $C_1 = 1$ and $C_2 = 0$, is given by

$$\begin{aligned} H^\rho_{mn} &= j\tfrac{I_0}{\omega\mu}\frac{1}{a} J_1(k_\rho \rho_{mn}) \sin\phi_{mn} \\ H^\phi_{mn} &= j\tfrac{I_0}{\omega\mu} J_1'(k_\rho \rho_{mn}) \cos\phi_{mn} \\ H^z_{mn} &= 0 \end{aligned} \tag{3.76}$$

In the latter expression ρ_{mn}, ϕ_{mn} together with the z_{mn} give the position of the regarded surface element (m,n) in cylinder coordinates.

It has to be said that the calculated excitations by means of this module, which is based on the latter theoretical concepts of the Cavity Model, do not take into account coupling effects. In order to include this interaction between the array elements additional current functions de-

scribing the dielectric current due to surface and leaky waves and other parasitic currents have to be added.

3.7.2 Currents with external software

The developed module expects as input information the name of the files, wherein the external calculated values are stored, so that it retrieves and assigns them to matrices that are further treated by the code. In the present thesis work, software based on FDTD and FIT has been used for the generation of the values that are stored in the required file format. These applied tools do not furnish the currents on the metallic patch but the fields above and underneath it. Following it, from the acquired field values the module calculates the necessary currents on the radiating metallic surface.

3.7.2.1 Currents on a radiating patch

The currents on the radiating patch have not been acquired directly but with the field values around it. The simulation tools allow the user to calculate the magnetic and electric field in a certain region at or around the analysed element. By using this feasibility and the relation (1.69) of chapter 1 for the magnetic intensity according to the *Equivalence Principle*, the electric currents on the patch can be acquired. Consequently, the first goal of the current gaining process is to obtain the magnetic fields under and on the radiating patch and second to applied them to the following equation in order to compute the necessary currents

$$\vec{J}_{mn}^{surf} = \vec{n}_{surf} \times (\vec{H}_{mn}^{above} - \vec{H}_{mn}^{under}) \tag{3.77}$$

In the latter adapted expression for a patch surface discretized in $M \cdot N$ elements, $\vec{H}_{mn}^{above}$ and $\vec{H}_{mn}^{under}$ are the magnetic intensity above and underneath the surface element (m,n), respectively. Furthermore, $\vec{n}_{surf}$ stands for the normal vector of the regarded surface element that is equivalent to the normal of the patch surface since the microstrip antenna is assumed to be planar. The resulting value is the current density $\vec{J}_{mn}^{surf}$ at the surface element (m,n). These acquired values are stored in a matrix of complex elements.

3.7.2.2 Coupling between array elements

For an antenna array, the coupling effects due to the proximity of neighbouring array elements contribute on the radiation and hence they should not be neglected. Due to the fact that every antenna can receive and send radiated waves, the interaction between neighbouring elements can affect their radiation and hence the far field of the whole array. As mentioned in chapter 1, the mutual coupling effects can be taken into account by introducing a mutual impedance matrix, like [20] and [21] suggest. Another way of calculating the coupling currents is proposed in [9].

In microstrip arrays coupling takes place inside the dielectric layer due to leaky waves and in the proximity space between the neighbouring array elements due to surface waves. Therefore, the coupling influence can be determined by the currents on and under the radiating patches. This conception is the basic idea for modelling the coupling with the help of external software. Furthermore, for the desired large array it is valid that all the inner elements will interact similarly with each other. This means that the currents of an element surrounded by a certain number

of neighbouring elements will contain the coupling information due to its entourage. Consequently, the coupling effects can be taken into account by using the currents of this element for the calculation of the far field. For it, a patch array of small dimension and point-symmetric constellation can be used as model. The excitation on the centre element of this array can be obtained and used for modelling the coupling currents.

The implementation of the afore given procedure has been performed in the following way. An $U \times V$ array with $U = V = 3$ has been conceived and simulated by means of external software. Following it, the fields above and underneath the centre array element have been extracted. The currents values at the centre element patch are acquired by applying equation (3.77). The procedure ends by storing the obtained current values for the further far field calculation. It has to be remarked that the simulation tools based on FDTD and FIT method include all interactions between the discrete meshed volume cells at the field calculations. Therefore the extracted fields enclosed by the dielectric layer will contain the coupling influences of all array elements.

3.7.3 Fringing effects at the array borders

Due to the fact that an array analysis approach should be capable of modelling a finite large array, the effects at the elements at the borders of an array are discussed in the following. Unlike the inner array elements, these fringing elements are influenced by their neighbours and by the abrupt end of the dielectric layer. Consequently, the radiation of these elements will be different and therefore their contribution on the far field should be taken into account.

The modelling of the fringing effects is based on the coupling modelling. The interaction between the array elements and the layer edges takes place mainly inside the dielectric layer and in the upper space. Therefore, the fringing effects can be determined by the currents on and under the radiating array elements similar to the coupling effects. Furthermore, the elements at the border of the array structure have less interaction with the inner array elements.

The fringing effects are considerated by taking the current values of the array elements near the layer edges and by using them for the calculation of the far field with the help of the developed approach in the present thesis work. Thus, a small array analysis similar to the one for the coupling case has to be realized. The currents of the array elements near the corners and edges are acquired and assigned to the counterparts of the finite large array.

The implementation of the fringe effects in the code is similar the one realized for the coupling effects. The difference lies on the atribution of the currents: these are assigned only to the finite large array elements near the layer edges and corners.

3.7.4 The applied software and its solvers

In the present thesis work simulation tools based on FDTD and FIT have been used in order to obtain the field values above and underneath the metallic patch of the analysed microstrip antenna. The simulation of the analysed patch and the small patch array has been performed operating the user interfaces of these tools with the purpose of conceiving the geometrical structure and of running the solvers. Furthermore, two huygen's surfaces above and underneath the

respective cell region, whereat the patch surface resides, have been declared. The field values have been obtained by means of these surfaces and they have been stored in two separete files. These files are expected to be available by the current extracting module that has been devoloped in the present thesis work. Moreover, the software applied are TEMSI, that uses an FDTD solver, and Microwave Studio, that solves with the FIT method.

TEMSI stands for Time Electromagnetic Simulator and is a open source software created at laboratory XLIM (a collaboration between the Centre Nationale de Recherche Scientifique CNRS and the University of Limoges). This simulation tool is based on FDTD and is suitable for handling flat structures of any kind including radiating patch antennas or even small arrays. Since FDTD approximates antenna radiating behaviour very well and therefore it gives a certain reliability to simulation tools based on this method, TEMSI has been used to perform the field calculations of the microstrip antenna. With the help of the computed fields at the dielectric layer, the currents on the radiating zone, namely the patch surface, have been determined.

Microwave Studio is a custom software developed by the entreprise CST. This simulation tool uses the FIT method in time and spectral domain in order to solve electromagnetical problems. For the simulation purposes in the present thesis work the FIT solver in time domain has been selected.

3.8 Implementation of antenna far field quantities

The quantities that describe the far field behaviour of an antenna array in a clearly arranged manner are the directivity and the radiation pattern. Consequently, these quantities have been implemented by developing respective modules in FORTRAN.

3.8.1 Calculation of the radiation pattern

The mathematical function for the radiation pattern presented in equation (1.87) in chapter 1 has been implemented in a respective module. Therefore, the necessary electric far field values $\vec{E}_{i,j}$ in reference to a $N_\theta \times N_\phi$ observation space have been acquired from the complex field matrix. In the following, the absolute magnitude of each electric field value for an observation points has been computed. In addition, the maximum magnitude among the latter values has been selected. With all the latter values the radiation pattern $C_{i,j}$ for an observation point (r, θ_i, ϕ_j) has been acquired by using the following expression

$$C_{i,j} == \frac{|\vec{E}_{i,j}|}{\max_{\forall i,\forall j}\{|\vec{E}_{ij}|\}} \tag{3.78}$$

The latter approach in order to calculate the pattern of an entire array has been used at the development of a code in FORTRAN. The structure of this code is shown in table 3.9. Therein, the brackets [ ] about the respective elements represent the matrix of these elements.

The code reads the stored electric field matrix and transforms the latter matrix in another one that contains the magnitudes of the electric field values. Then, the value with the maximum magnitude is selected from the new matrix. According to the code structure, two loops control the afore presented function in expression (3.78) for the calculation of the radiation pattern

Calculation of $\left[\lvert\vec{E}_{i,j}\rvert\right]$ with $\left[\vec{E}_{i,j}\right]$
Selection of maximum value from $\left[\lvert\vec{E}_{i,j}\rvert\right]$
for i=1,N_θ
for i=1,N_ϕ
Calculation of $C_{i,j}$ with $\lvert\vec{E}_{i,j}\rvert$ and $\max\{\lvert\vec{E}_{i,j}\rvert\}$
end
end

Table 3.9 : *Code structure for the radiation pattern calculation*

Assignment of $\Delta\theta$ and $\Delta\theta$
for i=1,N_θ
Calculation of θ_i
for i=1,N_ϕ
Calculation of $\lvert\vec{E}_{i,j}\rvert^2$ with $\vec{E}_{i,j}$
Storage of $\lvert\vec{E}_{i,j}\rvert^2$ in $\left[\lvert\vec{E}_{i,j}\rvert^2\right]$
Summation of $\lvert\vec{E}_{i,j}\rvert^2 \sin\theta_i \Delta\theta\Delta\phi$ to $\sum_i\sum_j$
end
end
Calculation of $\left[D_{i,j}\right]$ with $\left[\lvert\vec{E}_{i,j}\rvert^2\right]$ and $\sum_i\sum_j$

Table 3.10 : *Code structure for the directivity calculation*

elements. At the end of the loops a matrix containing the pattern values for all combinations of the elevation and the azimuth angles, θ and ϕ, respectively, is obtained.

3.8.2 Calculation of the directivity

The computation of the directivity has been implemented based on the mathematical function given in equation 1.91 in chapter 1. For it, the latter formula has been transformed in a suitable expression given in the following

$$D_{i,j} = \frac{4\pi|\vec{E}_{i,j}|^2}{\sum_{i=1}^{N_\theta}\sum_{j=1}^{N_\phi}|\vec{E}_{i,j}|^2 \sin\theta_i \Delta\theta\Delta\phi} \tag{3.79}$$

For the latter equation the availability of the far field values $\vec{E}_{i,j}$ is a precondition. A module coded in FORTRAN, that performs the latter expression, has been developed. For it, the code analyses the far field values for a defined $N_\theta \times N_\phi$ observation space according to the structure depicted in table 3.10. Therein, the brackets [ ] about the respective elements represent the matrix of these elements

The code performs the necessary functions by means of a pair of loops that control the parameters for reading and filling the respective matrices. The first two steps of the developed code for the calculation of the directivity are similar to the steps of the code for the radiation

pattern. The difference is that, instead of acquiring the magnitude of the elements of the complex far field matrix, their quadrature is computed. The obtained values form as well another matrix of the same size as the far field matrix. Moreover, the summation factor $\sum_i \sum_j$, which represents the denominator of equation (3.79), is calculated at each loop step. Furthermore, after the loop proceeding the directivity matrix is acquired by a simple division of the matrix $\left[|\vec{E}_{i,j}|^2\right]$ by the summation factor $\sum_i \sum_j$. In the end of the code procedure, the matrix with the directivity values for all observing points is obtained.

3.8.3 Visualization

In order to visualize the calculated far field quantities, different diagram modules has been developed in MATLAB. Therefore, the small codes depict the obtained matrices for the radiation pattern and the directivity in form of diagrams. The quantities can be graphically plotted in linear diagrams or polar diagrams. Moreover, the reasons for the choice of MATLAB as programming language for the visualization modules are the simplicity of reading external files and the availability of plot commands.

Chapter 4

Antenna array synthesis and optimization

In certain antenna array design cases it is desired that antenna arrays have extremely low side-lobe and narrow beamwidth patterns. In other cases the conceived array should show a desired distribution or radiate a pattern possesing certain characteristics like nulls in certain directions, dacaying minor lobes, etc. Thus certain pattern forms are of advantage in practice and therefore it is necessary the designed array to yield or at least to approximate the desired pattern in an acceptable way. Such a procedure of designing arrays is refered as "synthesis".

The existing sythesis methods can be divided in three clases or categories. The first one is the synthesis of various sector patterns. The second category embrace the synthesis methods for low-side and narrow-beam patterns. Part of the latter class are the Dolph-Tschebyshev and the Taylor line Source methods. Approaches like the Woodward-Lawson and the Fourier transform techniques belong to the category of beam shaping synthesis methods

Furthermore within the array synthesis, there exist procedures that optimize some array parameters subjected to additional condtions e.g. on the sidelobe level or the existance of noise sources.

4.1 Pattern synthesis methods for linear and planar arrays

All the following methods accomplish the achievement of patterns by means of steering the excitation of the array elements, which can be accurately controlled. These are presented in [6], [1] and [55]; in the first two references in a more detailed manner.

4.1.1 Schelkunov or Polynomial Method

The Schelkunov method allows the design of an array whose pattern possesses nulls in desired directions. Therefore, it uses the polynomial form of the array factor: the number of its elements and their excitation coefficients are derived by means of knowing the number of nulls and their location. In order to derive this polynomial form it is necessary to obtain a general expression for the AF. Therefore, the different current amplitudes I_n and a progressive current phase α for each array element are taken into account. The latter derivation is performed by taking the sum expression from equation (1.98) for the array factor and reshaping it in similar way as in (1.103) with $\beta = k(r_n - r_0) + \alpha$ and $a_n = \frac{I_n}{I_0}$ yielding

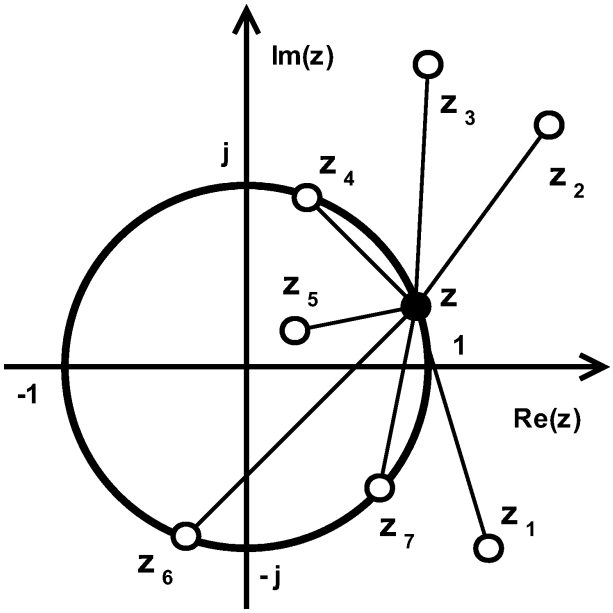

Figure 4.1 : *Unit circle in complex z-space with root locations (white circles)*

$$AF = \sum_{n=0}^{N-1} \frac{I_n}{I_0} e^{jn(k(r_n - r_0)+\alpha)} = \sum_{n=0}^{N-1} a_n e^{jn\beta} \tag{4.1}$$

The phase argument β in the complex expontential function contains the magnitudes of the vectors toward the reference element r_0 and toward the array elements r_n, and the current phase shift α between those two elements. Therefore, it depends of the geometrical position of the array elements and hence of the spacing. The coefficient a_n gives the ratio between the current amplitudes at the n-element and at the reference element. The whole complex exponential function can be substituted by a complex variable like in the following

$$z = e^{j\beta} \tag{4.2}$$

Consequently, the sum of the N-elements at the AF changes to

$$AF(z) = \sum_{n=0}^{N-1} a_n z^n = a_0 + a_1 z + a_2 z^2 + \ldots + a_{N-1} z^{N-1} \tag{4.3}$$

This is the array factor's polynomial form of degree $N-1$. The polynomial has consequently $N-1$ zeros and can be factored as a multiplication of $N-1$ elements in the following way

$$AF(z) = a_{N-1}(z - z_1)(z - z_2)\ldots(z - z_{N-1}) \tag{4.4}$$

In the latter expression the z_n are complex roots and give the $N-1$ zeros of the polynomial. The magnitude of the array factor is given then by

$$|AF(z)| = a_{N-1}|z - z_1||z - z_2|\ldots|z - z_{N-1}| \tag{4.5}$$

The information about the zero locations helps the method to analyse the AF and hence

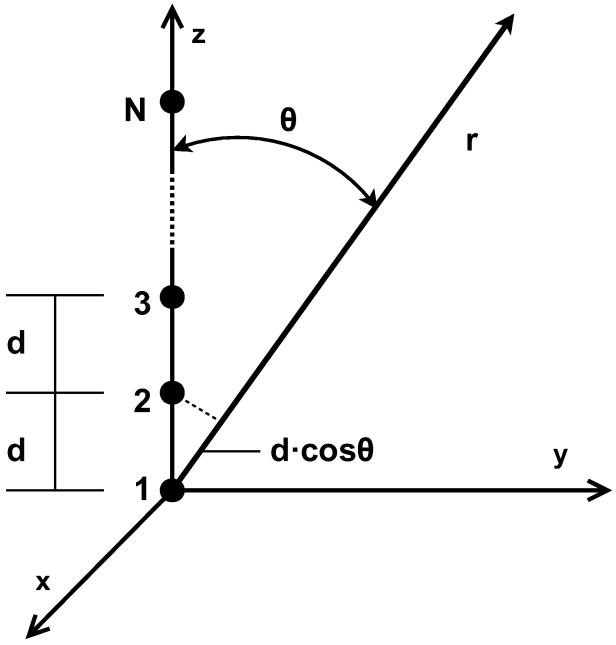

Figure 4.2 : *Linear array of elementary dipoles equally spaced along z axis*

synthesize the array. Therefore, the variable z is plotted on the complex z-space, where $z = Re(z) + jIm(z)$, as depicted in figure 4.1. For any real β the complex variable is on the *unit circle*: each *z's* magnitude amounts to unity and the respective angle depends on β. It can be observed that the product of the lengths of the straight segments joining any point of the unit circle z to the *AF's* roots z_n are equivalent to the *AF's* magnitude.

In order to illustrate the analysis, a linear array of equally spaced elements located along the z-axis with a element spacing of d, as shown in figure 4.2, is regarded. The array factor will have no variation in ϕ, but in θ. Consequently, the phase at the sum expression of (4.1) results in $\beta = \frac{2\pi}{\lambda} d\cos\theta + \alpha$. Furthermore, in the latter analysis case the spacing is defined as $d = \frac{\lambda}{4}$ and $\alpha = 0$. Figure 4.3 shows some possible complex roots at the unit circle for the latter definitions. According to [1] the region where the path of the z values on the unit circle take course is also known as "visible region", the rest of the circle "invisible region", respectively. If all the array factor roots are located in the visible region, then each one corresponds to a null in the pattern of the *AF*. This happens because z changes as the angle θ changes, so that it passes contingently through each of the zeros. While z passes a zero, the length between it and this zero becomes null and the magnitude of *AF* vanishes.

In order to visualize the influence of the progressive current phase, the "visible region" of the last example is depicted in 4.4 for the following case: $d = \frac{\lambda}{4}$ and $\alpha = \frac{\pi}{4}$. Comparing figures 4.3 and 4.4 a rotation counterclockwise of the visible region is perceived for the non-cero α. Plots for different α values show that the visible region rotates a certain amount that is equivalent to the respective phase α.

Combining all the latter observation results the following can be said: In the case that all zeros are not in the visible region, but in the invisible region and/or in a point other than the

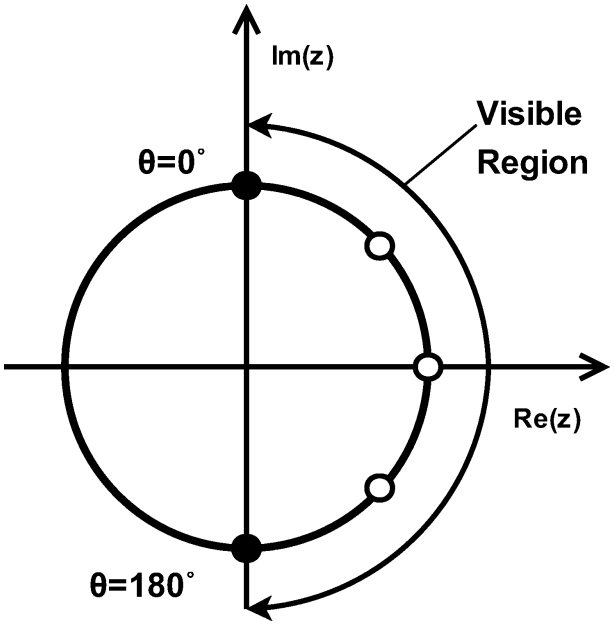

Figure 4.3 : *"Visible region" at unit circle for* $d = \frac{\lambda}{4}$ *and* $\alpha = 0$

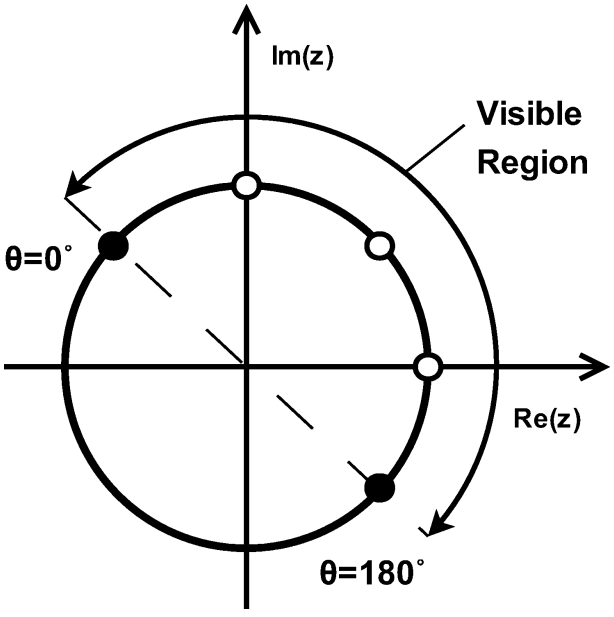

Figure 4.4 : *"Visible region" at unit circle for* $d = \frac{\lambda}{4}$ *and* $\alpha = \frac{\pi}{4}$

circle, then that particular array factor has no nulls for any value of θ. Consequently, only the roots on the visible region will contribute to the *AF*. If a given zero lies in the invisible region, that zero can be included in the pattern by rotating the visible region, namely by changing the current phase α. Hence the *AF* can be "matched" with the zeros to the desired form.

If the array observed is uniform spaced and excited, then the zeros of its *AF* are equally spaced on the unity circle in z-space. For this special case, the polynomial array factor may be described [6] by the following closed form

$$AF(r) = \frac{z^N - 1}{z - 1} \tag{4.6}$$

4.1.2 Fourier Method

The Fourier Method is often used for beam-shaping array synthesis. In this approach the array factor is represented as Fourier series like in the following

$$AF(r) = \sum_{n=-\frac{N-1}{2}}^{\frac{N-1}{2}} a_n e^{jkn\beta(r,d)} \tag{4.7}$$

The Fourier series summation is performed over a symmetrical range. Therefore, the values of *n* depend on the number of the series elements *N*

$$\begin{array}{ll} n = \pm\frac{1}{2}, \pm\frac{3}{2}, \pm\frac{5}{2}, \ldots & \text{for N even} \\ n = 0, \pm 1, \pm 2, \pm 3, \ldots & \text{for N odd} \end{array} \tag{4.8}$$

Consequently, the *AF* is a finite Fourier series that is periodic in *r*-space with the symmetrical interval. If the array factor is known, the excitation coefficients a_n can be found with the help of the following formula that origins from the orthogonality conditions of Fourier series

$$a_n = \frac{d}{\lambda} \int_{-\frac{\lambda}{2d}}^{\frac{\lambda}{2d}} AF(r) e^{-j\frac{2\pi}{\lambda} n\beta(r,d)} dr \tag{4.9}$$

While applying the Fourier Method, a condition for the spacing has to be taken into account. For the spacing $d \geq \frac{\lambda}{2}$ this method yields the least mean squared error approximation of the desired pattern. For the spacing $d \leq \frac{\lambda}{2}$ the definition of the pattern is not unique because the integration domain exceeds the visible region.

4.1.3 Woodward-Lawson Method

The Woodward-Lawson is preferently used for shaping beams. The main idea of this technique is to sample the desired pattern at several discrete points. Each sampled point is related to a harmonic current of uniform amplitude and uniform progressive phase, whose respective radiating field is referred to as a *composing function*. Each current is steered by an excitation coefficient b_m such that its composing function's strength is equal to the amplitude of the desired pattern at its corresponding sampled point. The total current is a finite summation of all harmonic excitations and consequently the synthesized pattern is represented by a finite summation of the

corresponding composing functions.

The number of sampling points is obtained similar to the Shannon sampling theorem: in order to reproduce faithfully the original function, it should be sampled at points separated no more than half the period of the highest frequency. For the pattern sampling case means this that the narrowest pattern possible should be taken as reference in order to calculate the sampling points u_m. The narrowest pattern is achieved by a distance equivalent to the array spacing. Since the length of the array is equivalent to $L = Nd$, there are at least N samples. Hence the m sampling points $u_m = u(m,d)$ for $m = \pm 1, \pm 2, \pm 3, \ldots, \pm\frac{N-1}{2}$ depend of the spacing d and the number of elements N.

Furthermore, the composing function has the following form

$$f_m(d,\alpha) = b_m \frac{\sin\left(\frac{N}{2}\beta(u-u_m)\right)}{\sin\left(\frac{1}{2}\beta(u-u_m)\right)} \tag{4.10}$$

The latter equation is equivalent to the normalized array factor of a uniform excited and spaced array of expression 1.110 in chapter 1 multiplied by the excitation coefficient b_m

The respective radiated field is described by the field contribution of the single array element multiplied by the array factor, which is calculated by means of all composing functions

$$AF(u) = \sum_{m=-\frac{N-1}{2}}^{\frac{N-1}{2}} b_m \frac{\sin\left(\frac{N}{2}\beta(u-u_m)\right)}{\sin\left(\frac{1}{2}\beta(u-u_m)\right)} \tag{4.11}$$

The excitation steering values at the sample points are obtained by

$$b_m = AF(u = u_m) \tag{4.12}$$

The latter means that the excitation coefficients are equal to the value of the desired array factor at the sample points since the composing functions have peak values of unity. Moreover, the normalized excitation coefficient of each array element, which is required to achieve the desired pattern, is given by

$$a_n = \frac{1}{N} \sum_{m=-\frac{N-1}{2}}^{\frac{N-1}{2}} b_m e^{-jk\beta(u=u_m)} \tag{4.13}$$

The implementation procedure looks like in the following. The first composing function generates a radiation pattern, whose placement is defined by the uniform progressive phase. The second composing function produces a similar pattern that according to its respective adjusted progressive phase coincides with the intermost null of the pattern of the first composing function. This results in a kind of controlled filling-in of the null of the first pattern contribution, whose amount is steered by the amplitude of the excitation of the second sample point. In the same way, the uniform progressive phase of the third composing function is adjusted: the maximum of its pattern is placed at the second intermost null of the first composing function allowing also a controlled filling-in. This process continues similarly with the remaining number of composing functions.

The primary advantage of the Woodward-Lawson method are the possibility of using lossless composing functions and its simple implementation. On the other side, it does not control the sidelobe level in the unshaped region of the pattern [66].

4.1.4 Dolph-Tschebyshev Method

The Dolph-Tschebyshev technique allows to narrow the beamwidth sustaining a given sidelobe level. Therefore, it relates the excitation coefficients, which build up the array factor, to Tschebyshev polynomials. The formula for Tschebyshev polynomials of recursive kind is

$$T_m(z) = 2zT_{m-1}(z) - T_{m-2}(z) \tag{4.14}$$

Each polynomial can be also calculated with the help of following expressions

$$T_m(z) = \begin{cases} \cos(m\arccos(z)) & \text{for} \quad |z| \leq 1 \\ \cosh(m\operatorname{arccosh}(z)) & \text{for} \quad |z| \geq 1 \end{cases} \tag{4.15}$$

where $m = 0, 1, 2, \ldots, \frac{N-1}{2}$ and

$$z = z_0 \cos(u) \qquad \text{with} \quad z_0 = \cosh\left(\tfrac{1}{M}\operatorname{arccosh}(R)\right) \tag{4.16}$$

Here R stands for the voltage ratio and u is a function that depends of the spacing d and the number of elements N. The voltage ratio takes positive values for the main beam and negative ones for the side lobes.

The synthesis process starts by calculating the linear value of the voltage ratio $R_{dB} = 20\log_{10}(R)$. Continuously, the AF has to be expanded in its polynomial form. Furthermore, the point $z = z_0$ is determined. Thus, the Tschebyshev polynomial coefficient becomes $T_m(z_0) = R$. For calculating the Tschebyshev polynomials, the array side lobe region is attributed to $|z| \leq 1$ and the major lobe to $|z| \geq 1$. In order to normalize the polynomials, the substitution $\cos(u) = \frac{z}{z_0}$ is realized. Consequently, the pattern has a maximum value of unity at $z = z_0$. Introducing all calculated Tschebishev polynomials, the excitation coefficients a_n can be calculated by equating the Tschebishev polynoms with ones of the AF.

The Tschebyshev method is not adequate for large arrays due to the a gain limitation. For relative small arrays as well as large ones the directivity yields a maximum. This can be explained by the forced constant sidelobes: they take a large part of the power, while the beam becomes narrower as the number of array elements increases.

4.1.5 Taylor Line Source Method

As evoqued in the latter subsection, the Tschebyshev technique possesses deficiencies for large arrays. Taylor analyzed the latter method, examined the limit of a continuous line source and drew the following conclusions about allowed illuminations and pattern far-sidelobe levels. The loss in efficiency of the Tschebyshev method comes from the enforcement of having constant sidelobe heights. In the case of large arrays means this that a huge fraction of energy resides in the sidelobe region. Hence a very large array requires an unrealizable aperture illumination.

Taylor states that the far sidelobes of a given line source are a function only of the line

source edge illumination. According to [6], if the edge illumination for a line source of length $2a$ behaves as in the following

$$(a-|x|)^{\upsilon} \tag{4.17}$$

at which x is measured from the center of the source, then for the so-called "derivative" $\upsilon \geq 0$ the far sidelobe level has the behaviour of the following function $f(z)$

$$f(z) = \begin{cases} \frac{\sin \pi z}{\pi z} & \text{for} \quad \upsilon = 0 \\ \frac{\cos \pi z}{\pi z^2} & \text{for} \quad \upsilon = 1 \\ \frac{\sin \pi z}{\pi z^3} & \text{for} \quad \upsilon = 2 \\ \frac{\cos \pi z}{\pi z^4} & \text{for} \quad \upsilon = 3 \end{cases} \tag{4.18}$$

wherein $z = \frac{uL}{\lambda}$ and u is a function that depends of the spacing d and the number of elements N. The choice of values for the "derivative" of the aperture illumination υ "steers" the behaviour of the far sidelobes, for example if $\upsilon = 0$ for the array leeds to sidelobes with $\frac{\sin(\pi z)}{\pi z}$. A pattern distribution, like the one of the uniform illumination, maintains its efficiency even if the array becomes larger. For the other positive "derivative" values the sidelobes decay faster and have generally lower efficiency.

For "derivative" values $\upsilon \leq 0$ the illuminations are no realizable for the continuous aperture case [6]. Furthermore, the location of the far zeros of the pattern are determined by the edge illumination. The n-th pair of pattern zeros appear as N tends to infinity at the following locations

$$z_n = \pm(n + \tfrac{\upsilon}{2}) \tag{4.19}$$

A particular case is observed when the edge illumination zeros are compared with the Tschebyshev zeros that occur asymptotically at $\pm(n-\frac{1}{2})$: the latter zero locations correspond to $\upsilon = -1$, a not realizable illumination.

Taylor suggested a pattern function with zeros far from the main beam at locations that correspond to the uniform illumination ($\upsilon = 0$). Additionally, the zeros closer to the main beam should be chosen similar to those of the Tschebyshev pattern. Taylor simulated and modified a continuous source with similar features as the Tschebyshev pattern using the following ideal line source pattern SF as substitute

$$SF(z,A) = \begin{cases} \cos\left(\pi(z^2-A^2)^{\frac{1}{2}}\right) & \text{for} \quad z^2 \leq A^2 \\ \cos\left(\pi(A^2-z^2)^{\frac{1}{2}}\right) & \text{for} \quad z^2 \geq A^2 \end{cases} \tag{4.20}$$

where

$$z = \frac{uL}{\lambda} \tag{4.21}$$

The sidelobe ratio is given as the value of SF at $z = 0$

$$R = \cosh(\pi A) \qquad \leftrightarrow \qquad A = \tfrac{1}{\pi}\operatorname{arccosh}(R) \tag{4.22}$$

The resulting pattern correspond to the limiting case of the Tschebyshev array as the number of elements is infinitively increased. Therefore, the locations of the zeros are

$$Z_N = \pm(A^2 + (n - \tfrac{1}{2})^2)^{\frac{1}{2}} \qquad N = 1,2,3,\ldots,\infty \tag{4.23}$$

According to [6], if a new function with near zeros very close to those of the ideal pattern in 4.23 but with more far zeros corresponding to those of the function $\frac{\sin(\pi z)}{\pi z}$ is defined, then the requirement on the near and the far sidelobes can be fulfilled.

Taylor chose to keep all nulls at the integer location for $|u| \geq \bar{N}$, and to move those for $|u| \leq \bar{N}$ near the locations of 4.23. By this way, nearly constant sidelobes near the main beam can be obtained. In order to match these two sets of zeros, the *dilation factor* σ is applied. This factor, which is slightly greater than unity, "dilates" the ideal space factor horizontally by moving the ideal zero locations z_n in a way, that eventually one of the zeros equals the corresponding integer $\bar{N}$. Therefore, the synthesized *AF* pattern in normalized form is given then by

$$AF(z,A,\bar{N}) = \frac{\sin \pi z}{\pi z} \prod_{n=1}^{\bar{N}-1} \frac{1 - \frac{z^2}{z_n^2}}{1 - \frac{z^2}{n^2}} \qquad \text{with} \quad z = u\tfrac{L}{\lambda} \tag{4.24}$$

The zero locations of the synthesized pattern can be calculated by the following expression

$$z_n = \begin{cases} \pm\sigma(A^2 + (n - \frac{1}{2})^2)^{\frac{1}{2}} & \text{for} \quad 1 \leq n \leq \bar{N} \\ \pm n & \text{for} \quad \bar{N} \leq n \leq \infty \end{cases} \tag{4.25}$$

Herein the *dilatation factor* is given by

$$\sigma = \frac{\bar{N}}{(A^2 + (\bar{N} - \frac{1}{2})^2)^{\frac{1}{2}}} \tag{4.26}$$

at which for $n = \bar{N}$ the zero location is $z_n = \bar{N}$. Due to the fact that the *dilation factor* σ stretches the "ideal" space factor in the manner that its zeros are shifted away from the major lobe, the beamwidth of the pattern is increased.

4.2 Pattern synthesis methods for conformal arrays

Building arrays with conformal elements conclude from the advantages that offer conformal antennas. Particularly, they can provide wider range of scanning angles for phased arrays than planar arrays. The challenging problem by using conformal arrays is how to handle the different orientations of its radiating elements, which invalidates the pattern separation principle applicable to linear and planar cases. Thus, it makes the classical array synthesis methods unusable. Therefore, different approaches have been proposed. Among them there are the iterative least square method, adaptive array theory, the weighted inner product method and genetic algorithms.

4.2.1 The Projections Method

The generalized Projection Method (PM) is explained by Bucci *et al.* in [58] in detail. The authors show the application of this technique on an array synthesis case [59]. A reconfigurable array with phase-only control, whose elements lie regularly equidistant in a plane of a cartesian frame, is expressed by a multiplication of the element radiation field E_{elem} and the array factor (AF) in direction (θ,ϕ)

$$AF(\theta,\phi) = \sum_{(n,m)\in I} a_{nm} e^{-jk_0 \vec{r'}_{nm}\vec{u}} \tag{4.27}$$

$\vec{u}$ is the unitary vector, the product $k_0\vec{r'}_{nm}$ the propagation vector, respectively. I is the set of the couples of (n,m) specifying the locations of the array elements. a_{nm} is the excitation magnitude coefficient. The AF is defined over $(-\pi,\pi)\times(-\pi,\pi)$. For the reconfigurable arrays there have to be q AF's radiated by the same array and synthesized at the same time. This set of AF's belongs to $\mathcal{B} \subseteq (\mathcal{L}^2)^q$, where $\mathcal{L}^2$ is the set of all functions square integrable on $(-\pi,\pi)$. Thus, a q-tuple of functions $F_q(\theta,\phi)$, which belong to the set $\mathcal{Y} \subseteq (\mathcal{L}^2)^q$ must to be taken into account.

In addition to that, a set $\mathcal{G}$ of admissible q-tuples including only element satisfying the requirement of $|a_{nm,1}| = \ldots = |a_{nm,q}|$ (phase-only reconfigurable array condition) is sought. This means, $\mathcal{G}$ is a subset of $\mathcal{B}$. The requirements on the pattern are expressed by $M_{down,q} \leq F_q \leq M_{up,q}$, namely the definition of the desired pattern mask. Moreover, they belong to the set $\mathcal{M} \subseteq (\mathcal{L}^2)^q$. Due to the fact that there is no need for a stabilizing functional since the pattern mask is defined for $(-\pi,\pi)\times(-\pi,\pi)$, the fundamental functional reduces to the last term [58]. These all reduces the synthesis problem to the search for a point of the intersection $\mathcal{M}\cap\mathcal{B}$, which can be solved via the iterative process with the projection operators $\mathcal{P}_{\mathcal{M}}$ and $\mathcal{P}_{\mathcal{B}}$ and the respective iterative step

$$F_{n+1} = \mathcal{P}_{\mathcal{M}}\,\mathcal{P}_{\mathcal{B}} F_n \tag{4.28}$$

with the general projection operator definition

$$\mathcal{P}_A : x \in \mathcal{H} \rightarrow \hat{y} \in A : ||x-\hat{y}|| \leq ||x-y||, \quad \forall y \in A \tag{4.29}$$

at which A is a closed subset of the normed space $\mathcal{H}$. Applied this definition to the array synthesis example, the operators can be interpreted in the following form

$$\mathcal{P}_{\mathcal{M},q} F_q = \begin{cases} M_{up,q}\frac{F_q}{|F_q|} & F_q > M_{up,q} \\ F_q & M_{down,q} \leq |F_q| \leq M_{up,q} \\ M_{down,q}\frac{F_q}{|F_q|} & F_q < M_{down,q} \end{cases} \tag{4.30}$$

and

$$\mathcal{P}_{\mathcal{B},q} F_q : \sum_{q=1}^{Q} ||F_q - \bar{F_q}||^2 \rightarrow \min \tag{4.31}$$

In the latter expression, $\bar{F_q}$ is the calculated value for the AF and F_q represents the desired array factor. Furthermore, Bucci *et al.* give an insight into the properties of the limit point (4.28)

of the iterative process. Therefore, the authors observe the behaviour of the distance function

$$D(F_n) = ||\mathcal{P}_{\mathcal{B}} F_n - \mathcal{P}_{\mathcal{B}} \mathcal{P}_{\mathcal{M}} F_n|| \tag{4.32}$$

and explain three possible cases. First, if $D(f_n)$ converges to zero, then the sequence f_n contains a subsequence that converges to the intersection point between $\mathcal{B}$ and $\mathcal{M}$ and hence the sought solution is found. In the case that the distance function converge to a non-zero value D_{min}, there exist no intersection point and a "best" possible solution according to the stated quality criterion is obtained. Moreover, the result can be improved by trimming of the requirements. The last case, wherein $D(f_n)$ converge to a nonzero value $D(f_T)$ and f_T is a part of the antecedent f_n, is called "trap" case. The latter can be only avoided by another choice of the starting point, which should be consistent with the problem at hand.

Furthermore, [60] shows the application of this synthesis method to conformal arrays. The procedure is similar with the difference that is applied to the whole radiation pattern and not only to the AF like in the planar case. The reason for that lies on the different radiation directions of the array element pattern. The projection method is summarized in a more generalized manner in [58]. Therefore, Bucci *et al.* the method is derived mathematically and different application examples are shown.

A variant of the aforementioned projections approach is the Successive Projections method (SP). Like the PM approach, it is an iterative procedure for finding a point in the intersection in a number of sets. It is based on the methods of projections onto convex sets [62]. It is applied for image restoration, filter and antenna design. According to Poulton [61], the method proceeds by finding an estimate of nominal array excitation, which is consistent with all field measurements within a prescribed error. These measurements define a number of intersecting sets of possible array excitations: one set for every field point. A point in the intersection of all sets represents an excitation that satisfies all constraints simultaneously, consequently it is a solution to the problem. The iterative procedure of projecting onto each set in turn can under certain conditions converge to a point in the intersection.

Furthermore, in [72] Elliot gives a description of a possible iterative algorithms based on the PM and SP approach for conformal array analysis. Both algorithms are used in order to realize comparisons between existing array synthesis methods for conformal arrays. An observation from the realized analysis in [72] is that the SP did not converge completely in Elliot's investigated case of conformal arrays and hence it delivered only a local minimum.

4.2.2 The Simulated Annealing Technique

The Simulated Annealing technique (SA) is an iterative mathematical algorithm that was used formerly for optimization problems in informatics (physical design of computers) and econocmis (travelling salesmen problem). Kirkpatrick *et al.* describe the procedure of this algorithm in a general form and uses it for the aforementioned optimization cases [65]. Due to its simplicity and efficacy it was used consequently in electromagnetics. In [64] Farhat and Bai describe its implementation for a phased-array pattern synthesis. Furthermore, Ares *et al.* uses the SA method in order to optimize the pattern of circular arc arrays.

According to [65], the SA describes the procedure of finding the right temperature state for growing a single crystal from a melt by careful annealing. Herein, the subtance is melted first with the highest temperature that is then lowered slowly. The melt spends a long time at temperatures near the freezing point. For the mathematical description of the process, a cost function symbolizing the system and a system variable, that represents the temperature T and is to be optimized, are introduced. The process is initiated at high temperature. In each step of this algorithm, the system variable is given a small displacement and the resulting change in the energy ΔE of the system is calculated. If $\Delta E \leq 0$, the variable changes and its configuration in the system is used as the starting point of the next step. In case of $\Delta E > 0$ the acceptance is weighted. Therefore, the probability by means of Boltzmann probability factor $P(\Delta E) = e^{-\frac{\Delta E}{k_B T}}$ with k_B as the Boltzmann constant is calculated and compared to a random number in the range of $[0,1]$. If the latter is less than the probability factor, then the new configuration is retained. Otherwise, the original configuration is used to start the next step. These steps are repeated until the optimum steady state of the system is reached. Furthermore, the choice of the initial T is curcial for the success of the process.

For an array pattern optimization the SA technique is applied by defining a suitable cost function replacing the energy and a set of parameters being the dynamic variables of the system. In [63] the radiation pattern $C(\theta,\phi)$ of a circular arc array is expressed by the following form

$$C(\theta,\phi) = \sum_{n=1}^{N} I_n e^{j\alpha_n} e^{jk_0 R\cos(\phi-\phi_n)} C_{elem}(\theta,\phi-\phi_n) \tag{4.33}$$

at which R is the radius of the arc, where the elements are positioned. k_0 stands for the free-space wave number and $\phi_n = \frac{2\pi}{n-1}$ the angular spacing between the consecutive elements. At the latter equation, C_{elem} is the element pattern, which has to be taken into account due to the different direction of radiation (θ,ϕ) in contrast to their planar counter parts, where it is not necessary. Considerating a conformal array structure, Ares *et al.* define the magnitudes I_n and phases α_n of the excitations as the dynamic variables and therefore for a fixed geometry a set of starting element excitations are chosen. In addition to that, the cost function has to be determined. This is done in a general way as in the following

$$\text{CostFct} = \sum_{M}^{i=1} a_i(\Upsilon_{desired,i} - \Upsilon_i)^2 + \sum_{N}^{j=1} b_j(\alpha_{start,j} - \alpha_j) \tag{4.34}$$

Here, $\Upsilon_{desired,i}$ and Υ_i are the desired and obtained values for the m sought design parameters, which can be beam-width, side-lobe levels, gain, etc. $\alpha_{start,j}$ and α_j are the starting and the obtained value in each iteration. After defining the system to be optimized, the synthesis is realized following the aforementioned SA process steps.

The advantage of the SA technique is its ability to avoid local minima and generally to converge to the global minimum of the cost function. In addition to that, it has to be said that like in the Dolph-Tschebyshev optimum function, the optimum function given by SA is different for different steering angles. Furthermore, since simulated annealing is an iterative improvement process, it takes a relatively long time to do an optimization problem. Thus, instead of the Boltzmann selection rule, a Cauchy probability selection rule can be used to speed up the whole annealing process [64].

4.2.3 The Least Square Method

The Least Square Method is an approach closely related to local optimization techniques, like Conjugate Gradient method and Newton method, that can be applied only to linear problems. Since the relation between the excitations at the elements of an array and the array's radiated far-field are of linear kind, this method can be applied. The concept of the Least Squares method (LS) is to find the required complex excitation values in order to obtain the desired radiation pattern from the antenna system. Furthermore, using the linearity of the system functions the latter can be written in matrix form as in the following equation

$$(\mathbf{C}_d) = [\mathbf{D}] \cdot (\mathbf{A}) \tag{4.35}$$

where $(\mathbf{C}_d)$ stands for the desired pattern in vector form, $[\mathbf{D}]$ for the geometry dependant system matrix, also called complex element directive pattern matrix [72], and $(\mathbf{A})$ the excitation vector, respectively. Consequently, the latter matrix equation has to be solved in order to yield the sought excitations. For it, there exist different kinds of approach. The simpliest one is to multiply equation 4.35 by the transposed matrix $[\mathbf{D}]^t$ resulting in

$$\left([\mathbf{D}]^t \cdot (\mathbf{C}_d)\right) = \left([\mathbf{D}]^t \cdot [\mathbf{D}]\right) \cdot (\mathbf{A}) \tag{4.36}$$

The resulting matrix equation, whose right side is equivalent to a square matrix, can be solved by standard techniques. Furthermore, if the latter equation is reshaped as in the following

$$(\mathbf{A}) = \left([\mathbf{D}]^t \cdot (\mathbf{C}_d)\right)^{-1} \cdot \left([\mathbf{D}]^t \cdot [\mathbf{D}]\right) \tag{4.37}$$

and if instead of using the transposed matrix the hermitian transpose $[\mathbf{D}]^H$ of the system matrix is applied, then the classical LS approach is derived. Consequently, the solution can be calculated as in the next equation

$$(\mathbf{A}) = \left([\mathbf{D}]^H \cdot [\mathbf{D}]\right)^{-1} \cdot \left([\mathbf{D}]^H \cdot (\mathbf{C}_d)\right) \tag{4.38}$$

The latter equation gives the solution according to the classical LS method. The hermitian transpose $[\mathbf{D}]^H$ is equivalent to the transpose of the complex conjugate of $[\mathbf{D}]$.

Moreover, it would be useful to solve the matrix equation by simplifying the required matrix inversion. For it, there exist some decomposition techniques for invertible matrices in order to reduce the computation effort due to matrix inversion . For instance, the LU decomposition sees the matrix $[\mathbf{D}]$ as a result of the multiplication between a lower and upper triangular matrix, $[\mathbf{L}]$ and $[\mathbf{U}]$, respectively. Hence, the matrix system in (4.35) can be solved by finding the solution for two smaller systems. Furthermore, another decomposition technique is the orthogonal matrix triangularization or QR decomposition method. This approach is more effective since it reduces a (m,n) matrix with $m > n$ and full rank to a much simpler form. Furthermore, it minimizes the approximation error, which is usually expressed by

$$err = (\mathbf{C}_d) - [\mathbf{D}] \cdot (\mathbf{A}) \tag{4.39}$$

The QR method decomposes matrix $[\mathbf{D}]$ in an orthogonal part $[\mathbf{Q}]$ and an upper triangular matrix $[\mathbf{R}]$ like in the following

$$[\mathbf{D}] = [\mathbf{Q}] \cdot [\mathbf{R}] \tag{4.40}$$

Since the suitably chosen orthogonal matrix is unitary and the relation $[\mathbf{I}] = [\mathbf{Q}] \cdot [\mathbf{Q}]^H$, with $[\mathbf{I}]$ as the identity matrix and $[\mathbf{Q}]^H$ as the hermitian conjugate, is valid, then the transpose of matrix $[\mathbf{D}]$ is

$$[\mathbf{D}]^{-1} = [\mathbf{R}]^{-1} \cdot [\mathbf{Q}]^H \tag{4.41}$$

Consequently, the solution for equation (4.35) and therefore the sought excitation vector is

$$(\mathbf{A}) = [\mathbf{R}]^{-1} \cdot [\mathbf{Q}]^H \cdot (\mathbf{C}_d) \tag{4.42}$$

It has to be said that in order to apply the QR method, the linear system in (4.35) is suppossed to be a over-determined.

Another more elegant and efficient way to solve the LS matrix equation is performed with the Single Value Decomposition (SVD). This method presented by Mazzarella in [71] decomposes the complex element directive pattern matrix $[\mathbf{D}]$ in order to find its pseudo-inverse for minimizing

$$||(\mathbf{C}_d) - [\mathbf{D}] \cdot (\mathbf{A})||^2 \tag{4.43}$$

The SVD allows to "split" the matrix $[\mathbf{D}]$ in certain matrix components like in the following equation

$$[\mathbf{D}] = [U] \cdot [\Xi] \cdot [V]^H \qquad \text{with} \quad [\Xi] = \text{diag}(\sigma_1, \ldots, \sigma_N) \tag{4.44}$$

In the latter decomposition, $[U]$ is a unitary matrix containing the left-singular eigenvectors, $[V]^H$ the conjugate hermitian of a unitary matrix composed of right-singular eigenvectors, and Ξ a diagonal matrix that is constituted of the singular values of the $[\mathbf{D}]$. For these Eigenvalues is valid $\sigma_1 \geq \sigma_2 \geq \ldots \geq \sigma_{r+1} = 0$ with $\text{rank}\{[\mathbf{D}]\} = r$. Consequently, the pseudo-inverse $[\mathbf{D}]^+$ of the system matrix is

$$[\mathbf{D}]^+ = [V] \cdot [\Xi]^{-1} \cdot [U]^H \qquad \text{with} \quad [\Xi]^{-1} = \text{diag}(\tfrac{1}{\sigma_1}, \ldots, \tfrac{1}{\sigma_r}, 0, \ldots, 0) \tag{4.45}$$

Mazzarella proposes to apply the acquired pseudo-inverse in equation (4.35) replacing the transpose $[\mathbf{D}]^t$ like in the next equation

$$(\mathbf{A}) = [\mathbf{D}]^+ \cdot (\mathbf{C}_d) \tag{4.46}$$

Moreover, Jorna *et al.* in [70] propose a variant of Mazzarella's approach by truncating the SVD by eleminating certain amplitudes that do not contribute to a significantly better synthesized radiation pattern. The proposal demonstrates an improvement for the LS solution in reference to the radiation beam quality due to a improvement for the tapper efficiency of the conformal array.

In addition to that, it has to be said that Least-Squares optimization gives a solution for the unknown excitation values that is valid for some (guessed) phase values of the goal function but that is not necessarily equivalent to the optimum solution for the synthesized pattern amplitude. For finding the best amplitude fit, Vaskeleinen proposes the iterative LS [67]. Furthermore, the LS optimization is also not directly suitable for phase synthesis, which is a nonlinear optimizing problem [68]. Consequently, the iterative LS method in combination with possible contraint

values is presented in [69] as an efficient solution for this case.

4.2.4 The Virtual Array Method

The basic idea of this approach of Vaskelainen [66] is to minimize the difference between the array factors of the "virtual" array and the array to be optimized. Therefore, an array, the so-called virtual array, is synthesized with a suitable method according to the destination array geometry and later its excitation values found are transformed into the excitation values of the destination array. For it, the radiaton pattern of the virtual array C_v and of the analysed array C are described as follows

$$C(\vec{u}) = \sum_{k=1}^{K} a_k e^{jk_0 \vec{r}_k \vec{u}} \qquad \text{and} \qquad C_v(\vec{u}) = \sum_{p=1}^{K} \alpha_p e^{jk_0 \vec{\rho}_p \vec{u}} \tag{4.47}$$

a_k and $\vec{r}_k$ are the excitation coefficients and the position vector of the k elements of the examined array and their counterparts α_p and $\vec{\rho}_p$ for the p element virtual array. $\vec{u}$ is the unit vector. The error function is given by

$$\delta(\vec{u}) = C(\vec{u}) - C_v(\vec{u}) \tag{4.48}$$

Vaskelainen defines the following integral function from the latter error function for all directions (over the solid angle Ω) in order to derivate a relationship between the excitations of the examined and the virtual array.

$$s = \oint_{\Omega} \delta(\vec{u}) \delta^*(\vec{u}) \tag{4.49}$$

The resulting relationship, which fullfils $\frac{\partial s}{\partial \Re(a_i)}$ and $\frac{\partial s}{\partial \Im(a_i)}$, is

$$\sum_{k=1}^{K} a_k \oint_{\Omega} e^{jk_0(\vec{r}_i - \vec{r}_k)\vec{u}} - \sum_{p=1}^{P} v_p \oint_{\Omega} e^{jk_0(\vec{r}_i - \vec{\rho}_p)\vec{u}} = 0 \qquad \text{for} \quad i = 1, \ldots, K \tag{4.50}$$

The latter expression can be expressed by the following matrix equation

$$\mathbf{S}_{rr}\mathbf{A} = \mathbf{S}_{rv}\mathbf{A}_v \qquad \text{with} \quad \mathbf{A} = [a_1, \ldots, a_K], \quad \mathbf{A}_v = [v_1, \ldots, v_P] \tag{4.51}$$

The elements of matrix $\mathbf{S}_{rr}$ and $\mathbf{S}_{rv}$ are the integral components from equation (4.50), which are evaluated and result in

$$S_{rr}(i,k) 4\pi \frac{\sin(k_0|\vec{r}_i - \vec{r}_k|)}{k_0|\vec{r}_i - \vec{r}_k|} \qquad S_{rv}(i,p) 4\pi \frac{\sin(k_0|\vec{r}_i - \vec{\rho}_p|)}{k_0|\vec{r}_i - \vec{\rho}_p|} \tag{4.52}$$

The virtual array should be a known array in the sense of an easy to evaluate array, for which a known and efficient synthesis method exists. In addition to that, it is advantageous if the virtual array is $1.5 - 3$ times the maximum dimensions of the examined array. The choice of the size of the virtual array has influence on the accuracy of the synthesis: for a large virtual array the analysed array can not reproduce the finest details of the respective array factor. Consequently, the detailed errors are smoothened out in the array factor of the examined array.

According to [66], the latter matrix equation can be used for any array geometry, if one can find a synthesis method for the virtual array. This means that the virtual and the examined array

must have similar geometry. Furthermore, Vaskelainen uses the two-dimensional Woodward Synthesis in order to optimize a planar array.

4.2.5 "Conformal Fourier Method" or Weighted Inner Product Method

Deng and Michalski present in [73] an alternative approach that is based on the inner product and resembles to the Fourier method for planar arrays. They proceed regarding the total far field pattern C_{array} as a summation of the translated versions of the reference element pattern Υ_t.

$$C_{array}(\vec{r}) = \sum_t \sum_p c_{t,p} \Upsilon_{t,p}(\vec{r}) \qquad \text{with} \quad \Upsilon_{t,p} = \Upsilon_t e^{jk\vec{r}\vec{p}} \quad \text{and} \quad \Upsilon_t = (T_t C_{ref})(\vec{r}) \tag{4.53}$$

At the latter expression, T_t stands for the translation operator, C_{ref} for the reference element pattern, respectively. $\vec{p}$, $\vec{t}$ and $\vec{r}$ are the position vector, the orientation vector and the vector of observation direction, respectively. Furthermore, the coefficients $c_{t,p}$ embraces the translation and orientation properties on the reference element pattern. The authors find a strong resemblance with the windowed Fourier transform (WFT) that is a reconstruction formula. In order to yield a desired pattern, the coefficients $c_{t,p}$ are calculated with the help of a weighted inner product that has following general form

$$\langle f, g \rangle = \int \Gamma(\vec{r}) f(\vec{r}) g^*(\vec{r}) dr \tag{4.54}$$

at which the symbol $(*)$ stands for the complex conjugate and Γ for the weight function respectively. In the beam synthesis case the weight function is defined by

$$\Gamma(\vec{r}) = \frac{1}{\sum_t |\Upsilon_t|^2} \tag{4.55}$$

The desired pattern constructing coefficients are calculated by the following equation

$$c_{t,p} = \langle C_{desired}, \Upsilon_{t,p} \rangle \tag{4.56}$$

The latter inner product allows the WFT to construct the sought radiation pattern. The approach applied on planar antennas is equivalent to the Fourier method, hence it can be seen as a conformal version of the Fourier method for planar arrays. The additional capability of this method is to compensate nearby all the translation effect due to the curved structure.

4.2.6 Synthesis with a Genetic Algorithm

The classical synthesis techniques presented at the beginning of this chapter, are thought to be for planar arrays and hence they are not adequate for conformal array structures. Furthermore, some of the methods for antenna array synthesis, coming from the afore presented ones for conformal antennas, can only be applied to arrays with certain conditions on the array shape and on the array elements. In addition to that, approachs like the Successive Projections method tend to converge to local minima. Genetic Algorithms (GA's) have the potential and ability to explore the entire configuration space and eventually reach the global minimum [80]. Consequently, they are used for different optimization problems in electromagnetics as shown in [74] and [75].

Moreover, they have been used for array synthesis [76] and [77]. This optimization method is treated in detail in the next chapter.

Chapter 5

Use of a genetic algorithm for antenna synthesis

Considering the aforementioned synthesis methods, the choice on a feasable and efficient approach for optimizing a conformal array has been persued. In order to overcome the great computational effort of direct analysis approaches due to matrix inversions, and to acquire more accurate methods as iterative methods yield, robust optimization methods like simulated annealing and genetic algorithms are most like to be used. Among both techniques, the most diffused and used one are genetic algorithms. The reason therefore is that GA's are versatile and accurate for easy as well as for complex cases, where other optimizing methods fail. Although it is a time consuming method, the ratio between the time effort and the quality of the results back their use in different engineering domains. Therefore, in this work the application of a genetic algorithm is used as synthesis method.

5.1 About genetic algorithm

A genetic algorithm (GA) is a model of machine learning that is based on natural selection. According to [80] and [74] it derives its mechanisms according to the principle stated by Darwin known as "survival of the fittest". Therein, an initial population is created from a random selection of the parameters in the parameter space. Each parameter set represents the individual's chromosomes. Each individual is ranked after his *fitness*, which is a measure of how well the solution is concordant with the requirements. A new generation emerges from the current generation by creating offsprings from a pair of individuals.

There are three operational functions in a GA with the objective of creating the next generation, these are selection, crossover and mutation. At the beginning, a population composed by a number of individuals is given. These individuals are randomly generated. According to the biological life process, the more fit individuals have a higher chance of finding a mate and reproducing. Conversely, the weak individuals have less chance in mating and hence they die off. This is known as natural selection, which is implemented in a GA in form of the selection function. By favouring the mating of the more fit individuals, the more promising areas of the search space are explored. Analogous to its biological counterpart, the cross-over function in a GA is defined for the children of the selected population. A child's chromosome set is some mix of its mated parent's chromosomes.

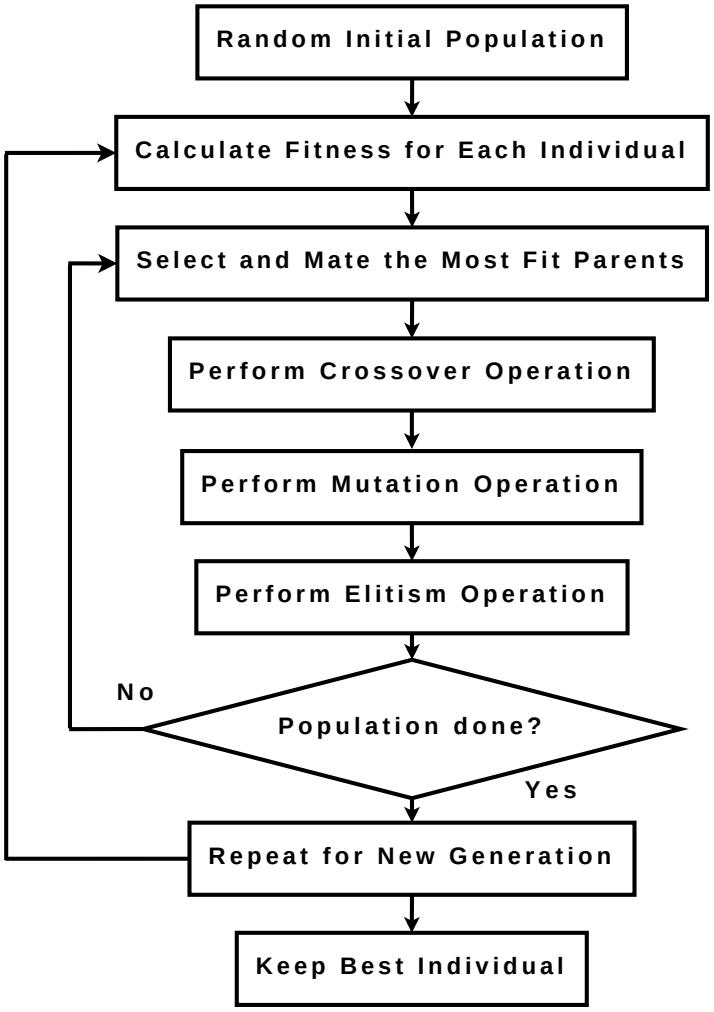

Figure 5.1 : *General flow diagram for a typical genetic algorithm*

Following the cross-over, the mutation function operates in a GA. Like in nature, certain gene's chromosomes are altered or changed by chance, giving additional or taking away certain characteristics of the individual. Furthermore, the fitness of each child is determined and the process of selection, crossover and mutation is repeated. The entire new generation creating process is performed until an entirely new popolation is generated. Practically, the average fitness of the population in the GA tends to increase with every new generation. Consequently, the aforementioned process is successively done until very fit individuals are obtained. Figure 5.1 visualizes by means of a flow diagram the latter described processes in a genetic algorithm.

According to [76], the selection process happens at each iteration step. Herein a certain amount of pairs of parents are chosen by tournament, whereby each parent is selected as the best of a randomly chosen group from the group of candidates. Each of these couples produce a child or more using crossover, which is followed eventually by a mutation. The crossover step refers to the mixing of information from both parents to create the children: from each parent a part of their chromosome set is taken randomly generating a new set of chromosomes for their offspring. The mutation process implies that the chromosome set of an generated individual is modified: one chromosome is altered randomly.

5.1.1 GA process functions and concepts in a Genetic Algorithm

The process functions of the GA and certain additional methods coming from the mathematical implementation are presented in [80], [79] and [78]. These functional steps and concepts are floating point and binary coding, tournament selection, single point and uniform crossover, jump and creep mutation, niching as well as elitism. Therefore, they are presented in the following paragraphs.

Coding is a method for discretizing the individual parameters in a number of possibilities. Analogue to the description of genes in biology, the individual's chromosomes are encoded as a string of values. Therefore, each parameter is represented by its chromosome. The length of each parameter string is called the parameter length. According to the floating point coding, the value of the chromosome is stored as a floating point number. Furthermore, the parameter length is unity since each parameter is represented by a single chromosome in the chromosome length. For binary coding, the chromosome length is based on the total number of possibilities in a binary format. For example, 2^n possibilities would be represented by a string of n binary elements, which can only contain the values of 0 and 1.

Selection in a GA is the function of picking right parents concerning their fitness characteristics for mating. According to [80], there are expected value selection and tournament selection. At the first selection method the expected probability p_i of being selected for an individual is his/her fitness f_i divided by the sum of the fitness of all individuals. This is $p_i = \frac{f_i}{\sum_i f_i}$. Consequently, the expected number of parents with an chromosome set i for the new generation is simply np_i, with n as the population size. Finally, random pairs of the latter attained individuals are chosen for mating. At the tournament selection random pairs from the population are selected and the most fit of each pair is allowed to mate. Each pair of mates create a child or children, which have some mix of the two parents chromosomes according the method of crossover (see next paragraph). This process continues until a new generation with a number of individuals similar to the old generation is repopulated.

Another process function used in a Genetic Algorithm is crossover. There exist single point crossover and uniform crossover. At the first one, a crossover point is randomly chosen in the chromosome set of the first individual. At this point, the part of the first parent set is replaced or overwritten by the one of the second parent set. As an example, let the first parent set be "abcde" and "ABCDE" for the second parent, respectively. Following the single point crossover, a possible child set can be "abcDE". Herein the randomly picked point lies between "c" and "D". The uniform crossover is a crossover process, where each chromosome position has its own probability for a crossover with the one of the second parent. Thus, it is possible to obtain any combination of the two parent chromosomes. Using the latter example a possible chromosome set of the child can be "aBcDe". Comparing both processes, for the single point crossover the possibility that the child inherites the whole chromosome set of one of the parents exists. For the uniform kind, this possibility is not available.

In a GA there exist two kind of mutation: the jump mutation and the creep mutation. The jump mutation produces a chromosome that is randomly chosen from the defined parameter range. Using the example of the crossover methods, the chromosome set of a child can be "abcDM", where "M" is not a chromosome from either parent. The creep mutation method

generates a parameter value that is randomly picked to be larger or smaller than the parents' one. As an example the child chromosome string resembles to "abcDF", where "F" is not a chromosome from either parent but it is only one increment away from the second parent chromosome value of "E".

Niching, also known as sharing, is an effective GA technique for problems in multimodal domain, where each peak can be thought as a niche. The latter means, that there exist more then one possible solution to the optimization task. According to Miller [82], the analogy from nature is that within an environment there are different subspaces (niches) that can support different kind of life (species, or organisms). The number of organisms for a given niche is determined by its fertility and the organism's capacities to exploit this fertility. If there are to many organisms in the niche, there will be not enough food, hence the least efficient organisms will disapear. Conversely, if there are few organisms in a fertile niche, they will quickly reproduce in order to exploit the niche's ability to support life. In a similar manner the GA maintains with the niching function the population diversity of its members in a multimodal domain. This multidimensional sharing scheme is presented by Goldberg in [84].

The elitism function is used frequently in a Genetic Algorithm. This is an operator used for ensuring that the until date generated individual, which has the best chromosome set, procreates offspring. After the population is generated, the GA verifies if the best parent has been replicated. For a negative verification result the algorithm choses a random individual and the chromosome set of the best parent is copied to that individual. This process helps to prevent the random loss of good chromosome strings

5.1.2 The micro-Genetic Algorithm

The micro-genetic algorithm (μGA), as the name 'micro' alludes to, is a small population GA with reinitialization. This approach was derived from some theoretical results obtained by Goldberg, according to which a population size of three is sufficient to converge, regardless of the chromosomic length adopted [81]. Furthermore, Goldberg suggested to start with randomly generated population, then to apply on it the GA process steps aforementioned until reaching nominal convergence. After it, a new population should be generated by transferring the best individuals of the converged population to the new one. The remaining individuals would be randomly created and the process should restart.

Krishnakumar in [83] did the first implementation of the μGA. His algorithm starts with a small random population of five individuals that evolves like a standard GA process but with crossover rate of one and a mutation rate of zero. The elitism step copied the best chromosome string found in the current population to the next generation. The selection step was realized by holding four competitions between strings that were adjacent in the population array, and taking the individual with the highest fitness for the next round. Consequently, at Krishnakumar's μGA the concepts that are used are those of elitism, single point crossover and restart. The mutation concept is not used as aforementioned. Furthermore, Krishnakumar compared his results with the ones of the simple GA and reported a significant improvement: the results converged even on real-world engineering control problems faster. Another advantage found at Krishnakumar's μGA was the avoidance of premature convergence.

5.1.3 Application of a Genetic Algorithm

The GA is applied to a certain process by allowing it to "pilot" the generation or selection of input variables. For example in [77], the genetic algorithm technique is used to select the excitation phases that would produce the closest possible match to a desired array radiation pattern. The input variables will be chosen or created refering to an evaluation of the output quality called "fitness". This fitness evaluation is made by comparing the desired quantity with the calculated one. According to Carroll [78] the fitness can be calculated by

$$\text{fitness}(Q_{calc}, Q_{target}) = \frac{1}{\sum_k^K |Q_{target,k} - Q_{calc,k}|} \tag{5.1}$$

at the latter equation $Q_{target,k}$ is the desired k-th quantity value, $Q_{calc,k}$ the value of the calculated quantity, respectively. The amount of measured and calculated values is for both K. According to [74], to rank the performance of the solutions, it is necessary to calculate the error for a given solution. Therefore, the error value should be calculated by means of an error function, which will reflect the fitness of a solution in a GA. As already seen, the error value is equivalent to the K differences between the calculated quantity value and the desired target value. Consequently, the following equation

$$ErrF(Q_{calc}, Q_{target}) = \sum_k^K |Q_{target,k} - Q_{calc,k}| = \frac{1}{\text{fitness}} \tag{5.2}$$

which is the inverse of the fitness function, gives the total error and is known as the error function. It has to be said, that the afore presented error function is the equivalent to the aforementioned cost function in the Simulated Annealing method. In fact, the term cost function is also used in GA. In the present thesis work cost and error function are synonyms.

Furthermore, it is important that the error function is well designed according to the target requirements. The following equation is an example for a possible error function $ErrF$ proposed by Skaar [74]

$$ErrF(Q_{calc}, Q_{target}) = \sum_k^K (Q_{target,k} - Q_{calc,k})^2 \tag{5.3}$$

The desired quantity values $Q_{target,k}$ can be theoretical values or measurements. In a more general way, the error function can be represented by the following definition, wherein the value differences are weighted with coefficients c_k

$$ErrF_p(Q_{calc}, Q_{target}) = \left[\sum_k^K (c_k |Q_{target,k} - Q_{calc,k}|)^p \right]^{\frac{1}{p}} \tag{5.4}$$

K is the number of target quantity values as well as the number of computed quantity values. The parameter p in the latter equation gives how the large errors are weighted compared to small ones. For example, for $p = 1$ the error function becomes a simple weighted sum of errors, for $p = 2$ the error function is equivalent to a weighted Euclidian metric. For the limit case $p \to \infty$ the error function evolves to

$$ErrF_\infty(Q_{calc}, Q_{target}) = \max_k (c_k |Q_{target,k} - Q_{calc,k}|) \qquad \text{for} \quad p \to \infty \tag{5.5}$$

Therefore, p has to be chosen according to the requirements.

5.2 Implementation of the genetic algorithm

The array synthesis for antenna arrays with a defined structure is done by determining the optimal excitation of the elements. The excitation currents are composed of a complex magnitude (or amplitude) and a complex exponential function with the excitation phase as argument. Generally, the basic concept of the optimization is to determine the best amplitude coefficient and phase coefficient configuration by means of a GA, in order to obtain a desired radiation pattern. In the case of beam-shaping and phased arrays, wherein the excitations amplitudes are pre-determined, the phase coefficient configuration is optimized.

Furthermore as seen in the last paragraphs, the definition of the adequate fitness function is fundamental for the optimizing process of the conformal array. In connection with the fitness comparison, it is essential to define a suitable objective function, or pattern mask, that describes the desired pattern. In addition to that, the GA should be composed of the alternatives for the process functions, which lower the quantity of evaluation operations (this means the GA optimizes fast) and find the optimum solution (this means the GA works efficiently) at the same time. Moreover, the GA's process functions has to be adequately configured in relation to the synthesis of conformal arrays. In addition to that, the initiation and control variables for each GA process step have to be adequately defined.

5.2.1 Structure of the performed GA

The Genetic Algorithm at this work is an adapted version of Carroll's developed GA for the optimization of a chemical oxygene-iodine laser presented in [79]. The reason for this choice is the versatility of Carroll's algorithm, which was previously tested for a source decomposition problem. Besides, being based on the GA theory of Goldberg, it has its own random generator that works more efficient than other tested codes. Consequently, the GA in this work uses binary coding, tournament selection, uniform cross-over, creep mutations, niching, elitism. There exist also the possibility of launching Krishnakumar's μGA. The GA is structured as depicted in figure 5.2.

The GA starts with an initialization stage, wherein the first generation created. Following it, the fitness evaluation step is applied that stores the resulting fitness of the actual generation. Then, the inheritance stage starts, wherein selection and cross-over take place. The latter step leads to the modification stage, whereat if μGA option is note used, mutation is applied. The process continues with the generation of the off-spring, namely the new generation. The last stage of this iteration is the reinitialization. The latter process is run until the designated number of simulations of the GA is reached. The implemented code is analogue to the presented GA structure. The GA process components are explained in the following paragraphs.

5.2.1.1 Initialization

In the initialization stage, the input data containing all values for the GA variables is retrieved from a file. These are the heuristic values, like cross-over and mutation probability, as well

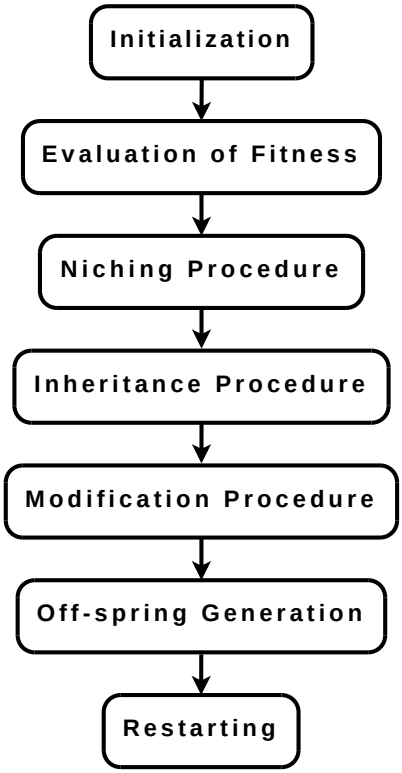

Figure 5.2 : *Structure of the implemented genetic algorithm*

as command values, e.g. if a μGA should be performed. The input file has also information about the population, for instance the amount of generations and parameters to optimize, and about the parameters, namely the element amplitudes and phases. The input data contains also details on the pattern mask that describes the desired pattern function, e.g. beamwidth, steering angle, etc. In the case that the user desires a μGA optimization rather then the standard variant, the values after Krishnakumar, as described in the latter chapter, are set automatically. This is, the population size has the value of five, crossover rate of one and a mutation rate of zero, respectively. Likewise elitism, single-point cross-over and restart are performed.

Furthermore, if it is the first simulation run, the pattern mask function, which is given in detail in the next section, is built according to requirements set by the user. Another significant event, that happens during the first round, is that the population composed of individuals is generated. To these individuals were attributed ramdomly the characteristics given in the input file. Conversely, if it is not the first simulation, the initialization stage reads from a store file the information about an existing optimized generation. Following it, the random values for the amplitudes and phases of the population individuals are coded in strings using coding. This work uses binary coding, since it lowers the size of the population and hence the number on evaluation operations needed for the optimization according to the results obtained in [80]. The coded information about the population is stored in a matrix, which contains in each row each individual and in the columns the properties of each individual. In our case, a rows stands for a solutions and the columns for the parameters, namely the element phases and amplitudes.

5.2.1.2 Evaluation of the fitness

The evaluation of the fitness is the core step of the synthesis process. It performs the analysis of the investigated optimization problem with the regarded population as a posible solution. Therefore, for each generation the evaluation function takes the coded chromosome strings of each individual and then it decodes them using the respective decoder for the binary code. By this way, the phases and amplitudes of all solutions are obtained. Following it, each solution and its respective parameters are transformed in the complex excitation combination applied on all array elements. For each array element, this is multiplying the matching amplitude by the complex exponential function containing the respective phase as argument. Then, the excited array is evaluated on its fitness with the fitness function.

As seen in the latter chapter, the fitness function is the inverse of the error function *ErrF* (equation (5.2)). Consequently, the error and therefore the difference between the pattern mask function values and the calculated values is computed by means of an adequate error function, whose form depends on the optimization case. The construction of a such error function is presented later in this chapter. The radiation pattern is calculated for each solution, this is, the complex excitation combination is applied to the array. The necessary array pattern computation in each case is performed with the hybrid method created in this work. For each proposed excitation combination, an error value is obtained. From all these error results, the lowest value that stands for the highest fitness value is selected and stored.

A distinctive feature of Carroll's GA implemented for this work is the adaptive fitness threshold. The first threshold is set equivalent to the best fitness value obtained at the first run. If a better fitness value is obtained in any random solution during the next rounds, then this value becomes the threshold. The following runs become consequently more discerning and hence the optimization process of higher quality.

5.2.1.3 Niching

Another function that highers the quality of the optimization process is the implemented niche function. The studies made by Carroll in [79] show that the niche technique is only useful for multimodal optimization problems. Consequently, the niching stage is an optional stage and hence it can be switch on or off depending on the problem requirements and, of course, on the user's desire. Furthermore, the niche function is implemented by means of a triangular sharing function according to [84].

5.2.1.4 Inheritance

The inheritance stage consists in elaborating the characteristics of a new generation from the genes or chromosomes of fit individuals of the actual generation. This is realized by the selection and the cross-over functions. The genetic algorithm in this work uses tournament selection, which works efficiently in selecting the fit parents for mating from a relative small sized population. These results are found by Carroll in [78]. He attributes this behaviour to the greater probability to find the mating partner by chance under the constraint of certain selection rules.

For the breeding of a fit generation, the genes of fit partners are combined by means of the cross-over function. Uniform cross-over is used in order to mix up the parents genes as much

as possible. The reason for this choice is found in [79]: the studies effectuated show that the uniform-crossover case converges faster to the optimal solution then the single-point variant. Other studies, like [80], confirm this behaviour.

5.2.1.5 Modification

The modification step stands for the mutation process function. It simulates random changes in the chromosomes. The creep mutation kind is chosen as mutation variant, since apparently this method can slide the gene pool toward the optimal solution rather than just having to jump forwards it [79]. Consequently, the optimum is reached with higher velocity than using the jump mutation method. In the modification stage there exist the option to continue with the process of Krishnakumar's μGA. For it, the mutation function is omitted as aforementioned.

5.2.1.6 Offspring generation

After having all the information required, in the offspring generation stage, as the name implies, a new generation is created with the genes and chromosomes combination from the fittest parents attained by the latter other stages. For it, this stage reuses the created arrays of the parents, giving so place to a new generation. Parallel to it, it also checks if the fittest individual of the parent generation had offspring (elitism). In the end, it codes the gene information in strings with the aforementioned binary code method.

5.2.1.7 Restarting

In the restarting step the gained fittest candidates from the actual generation are stored in a file. The latter file is used in the initialization stage in order to take them as the new parent generation. By this way, the first simulation loop ends and the GA process restarts from the beginning.

5.2.2 Defining the pattern mask

The selection of a suitable objective pattern function to test the fitness of a solution is an essential step for the optimization process. This pattern mask has to depict the characteristics of the desired pattern. Boeringer [76] and Allard [77] propose, based on studies made for pattern approximations, mask functions of cosinusoidal kind. In this work, the following pattern mask function is used

$$F_{mask}(\theta) = \begin{cases} \sqrt{\cos^q\left[\frac{\pi}{2}\frac{\theta-\theta_0}{\delta_{BW,\theta}}\right]} & \text{for} \quad \theta \in [\theta_a, \theta_b] \subseteq [-\frac{\pi}{2}, \frac{\pi}{2}] \\ 0 & \text{elsewhere} \end{cases} \tag{5.6}$$

$\delta_{BW,\theta}$ stands for the angle range of the half-power beamwidth, θ_a and θ_b are the limits of the main beam angular expansion, and θ_0 is the desired steering angle. q is a decimal number that has a different value depending on the antenna kind used as array element. For instance in [77], certain patch antennas are used as array elements and the pattern mask is approximated by means of the latter function with $q = 2$. Furthermore, Boeringer suggests that $q = 1,6$ or $q = 1,5$ approximates the pattern of dipole arrays. The value of q is often chosen to match the half-power beamwidth of the radiating element under consideration [76].

For the two-dimensional array case, if the desired beam should be steered in (θ_0, ϕ_0) direction, expression (5.6) can be expanded by defining the behaviour of the mask pattern in ϕ direction. This can be performed by using the latter equation and replacing the values related to the angle θ with the ones related to ϕ as well as expanding the range for the respective values. This yields to

$$F_{mask}(\phi) = \begin{cases} \sqrt{\cos^q\left[\frac{\pi}{2}\frac{\phi-\phi_0}{\delta_{BW,\phi}}\right]} & \text{for} \quad \phi \in [\phi_a, \phi_b] \subseteq [-\pi, \pi] \\ 0 & \text{elsewhere} \end{cases} \tag{5.7}$$

$\delta_{BW,\phi}$ stands for the half-power beamwidth, this is the range of ϕ values. ϕ_a and ϕ_b are the limits of the main beam angular expansion, and ϕ_0 is the desired steering angle. By combining mask functions (5.6) and (5.7), a three-dimensional pattern mask is obtained for the steering direction (θ_0, ϕ_0)

5.2.3 Building the error function

The error function used in this work has been defined according to the error function given by Baroni *et al.* in [75]. The respective error function is given for a pattern mask values along θ direction. The array pattern synthesis has to take into account the case, whereat the pattern is being steered in direction (θ_0, ϕ_0). Therefore, the error function $ErrF$ has to be extended. This is done by using Skaar and Risvik's proposal in [74]. The error function is composed by two error functions that evaluate the calculated three-dimensional field function regarding one of the two angular dimensions. The sum of both component errors gives the total error. Consequently, the error function $ErrF_\theta$, which evaluates the excitation combination for $\theta = \theta_0$, can be calculated by

$$ErrF_\theta = \left. \frac{\sqrt{\sum_{k=1}^{K} \left\| \vec{E}_k - \vec{\tilde{E}}_k \right\|^2}}{\sqrt{\sum_{k=1}^{K} \|\vec{\tilde{E}}_k\|^2}} \right|_{\theta=\theta_0} \tag{5.8}$$

Similar is valid for the component $ErrF_\phi$ that is obtained with the same equation but with $\phi = \phi_0$ instead of a fixed angle θ.

$$ErrF_\phi = \left. \frac{\sqrt{\sum_{k=1}^{K} \left\| \vec{E}_k - \vec{\tilde{E}}_k \right\|^2}}{\sqrt{\sum_{k=1}^{K} \|\vec{\tilde{E}}_k\|^2}} \right|_{\phi=\phi_0} \tag{5.9}$$

Furthermore, in the calculation of the total error, it can be decided how the synthesis in θ range is weighted in comparison to the synthesis in ϕ range by using a weighting coefficients as shown in [74]. Therefore, the error function is expressed by

$$ErrF = w_{err,1} \cdot ErrF_\theta + w_{err,2} ErrF_\phi \qquad \text{with} \quad w_{err,1} = 1 - w_{err,2} \tag{5.10}$$

$w_{err,1}$ and $w_{err,2}$ ar the weighting coefficients that are linked as shown in the latter expression. Analogue to the error function for the field function values, a function $ErrF^C$ for the calculation of the error regarding the radiation pattern can be expressed by the following equation

$$ErrF^C = w_{err} \cdot ErrF^C_\theta + (1 - w_{err}) ErrF^C_\phi \tag{5.11}$$

The latter statement can be simplified, if instead of the vectorial field values the respective radiation pattern is used. By using the relation between field and pattern given in expression (1.87) of chapter 1 the pattern values for the desired and for the calculated radiation pattern, C_k and $\tilde{C}_k$, are obtained. The error function concerning the radiation pattern is yielded by the respective error components $ErrF^C_\theta$ and $ErrF^C_\phi$ that can be attained in the same way as for the components of $ErrF$. Since the weighting coefficients are linked, the Error function can be calculated only knowing one weighting coefficient. The component $ErrF^C_\phi$ that gives the error in ϕ_0 direction is

$$ErrF^C_\phi = \left. \frac{\sqrt{\sum_{k=1}^{K} (C_k - \tilde{C}_k)^2}}{\sqrt{\sum_{k=1}^{K} \tilde{C}^2}} \right|_{\phi=\phi_0} \tag{5.12}$$

The component for the error function $ErrF^C_\theta$ is calculated with the latter formula but by fixing $\theta = \theta_0$

$$ErrF^C_\theta = \left. \frac{\sqrt{\sum_{k=1}^{K} (C_k - \tilde{C}_k)^2}}{\sqrt{\sum_{k=1}^{K} \tilde{C}^2}} \right|_{\theta=\theta_0} \tag{5.13}$$

5.2.4 Choice on initial values and probabilistic constants

Another important step before the GA optimization process starts is to define the necessary values for all process variables. The heuristic variables are regarded first. According to Carroll in [79], the overall probability of a jump mutation $p_{jump,i}$ and the overall probability of a creep mutation $p_{creep,i}$ ocurring for an individual i are

$$p_{jump,i} = 1 - (1 - P_{jump})^{n_c} \qquad \text{and} \qquad p_{creep,i} = 1 - (1 - P_{creep})^{n_p} \tag{5.14}$$

respectively. n_c stands for the number of chromosomes (bits) in an individual's binary string, n_p for the number of parameters, respectively. Carroll aproximates both probability values with $p_{jump} = \frac{1}{n_{pop}}$ and $p_{creep} = \frac{2}{n_{pop}}$, being n_{pop} the number of parents in the population. This comes from the following tought: if a similar value for the creep and jump probability is desired, then the latter both equations have to be set equal. By using a binomial expansion and by taking into account $P_{jump} \ll 1$, the resulting expression can be approximated as follows

$$P_{creep} = 1 - (1 - P_{jump})^{\frac{n_c}{n_p}} \approx \frac{n_c}{n_p} P_{jump} \tag{5.15}$$

If $p_{jump} = \frac{1}{n_{pop}}$ as stated before and $n_c = 22$ and $n_p = 8$ for instance, then the probabilistic value for creep mutation would be $p_{creep} = \frac{2.75}{n_{pop}}$. Consequently, the approximation is ok, since n_{pop} is not small. The mutation kind and the respective probability are read from the input file.

Furthermore, the popolation size n_{pop} can be determinated by means of following expression

$$n_{pop} = o(mx^k) = o\left(\frac{l}{k}x^k\right) \tag{5.16}$$

k is the size of the schema of interest and l is the length of the chromosome string. Moreover, for the appropiate estimation of n_{pop}, the schema length is assumed to be equal to the average parameter length. In addition to that, $x = 2$ for binary coding. With these approximations the order of the population size can be found. For the optimization process one child per parents has been chosen.

The second part of the preparations is related to the parameters to be optimized. The range of the current amplitudes and phases are given by their maxima and minima extracted from the input file. Moreover, the number of parameters and chromosomes are calculated by means of $n_p = n_{elem}n_{var}$ and $n_c = n_p n_{bits}$. n_{elem} is the number of array elements, n_{var} the number of variables sythesized, respectively. In the case of pattern synthesis, $n_{var} = 2$ due to the sought excitation amplitude and phase for each array element. The values of the other variables are obtained from the input file.

The third part of the preparations concerns the pattern mask. The values for the angle borders in θ and ϕ direction, the half-power beamwidth angle ranges $\delta_{BW,\theta}$ and $\delta_{BW,\phi}$, and the steering direction (θ_0, ϕ_0) are taken from the input file. The pattern mask is built by means of the aforementioned function with $q = 2$.

5.2.5 Pattern optimization examples with the genetic algorithm

The genetic algorithm afore presented has been used for pattern synthesis. For it, the error function and the probabilistic variables have been defined as aforementioned. For reasons of simplicity, linear arrays have been analysed. Furthermore, the array elements are elementary dipoles. Nevertheless, the implemented synthesis method can be applied to any kind of array and any kind of array element as the reader will notice in the next chapter.

Consequently, two optimization cases have been run for a linear array mounted on a flat plane and then on a cylindrical surface. For both cases the GA simulates 500 generations for a population size of 50 members. Furthermore, the probabilistic constant have been defined like in the following: cross-over probability of 50%, mutation probability of 1% and 15bits for each value. Furthermore, the excitation amplitude values of the elements have been limited to the intervall $I_0 \in [0.0, 10.0]$A and the excitation phase value to the intervall $\alpha \in [-180^\circ, 180^\circ]$. Both cases are presented in the following.

5.2.5.1 Source decomposition

The first case realized consists in finding the complex excitation values of a linear array, whose elements are positioned on the x-axis, for a working frequency of $f = 1.0$GHz. The elementary dipoles are oriented in y-direction. The array elements are positioned equidistant with the spacing value of $d = \frac{\lambda_0}{2} \approx 0.15$m. The directivity pattern of the same array for a uniform element excitation with the current amplitude value of $I_0 = 1$A and current phase value of $\alpha = 0^\circ$ has been taken as the goal or mask pattern. The task of the GA is to find out the excitation amplitude and phase, this is the source decomposition, in order to reconstruct the mask pattern. The result

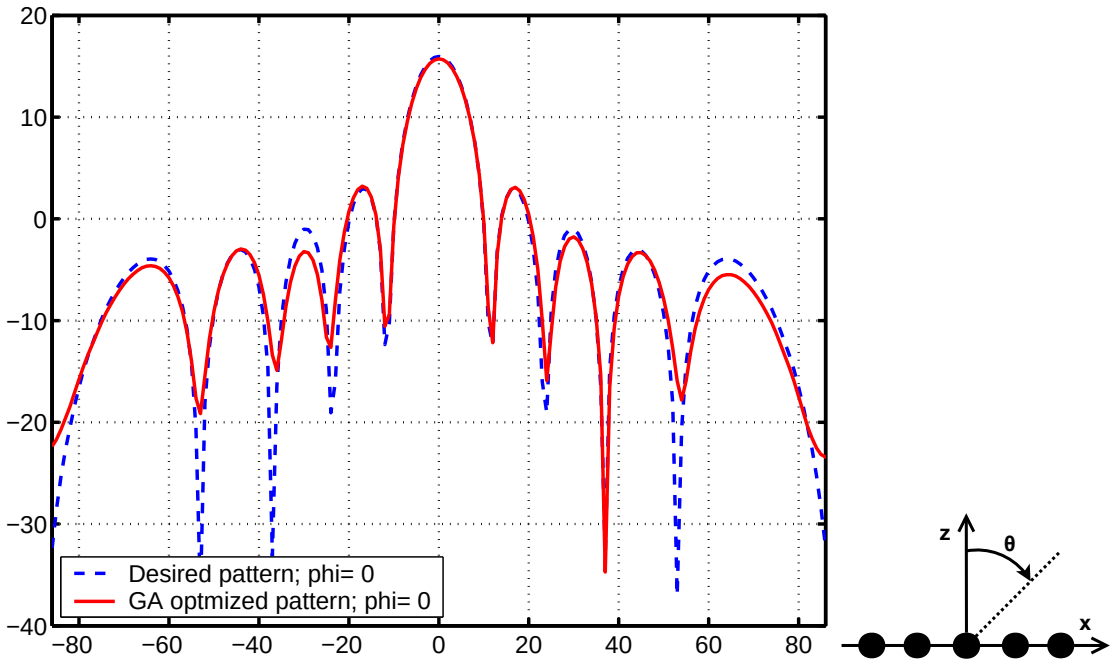

Figure 5.3 : *Pattern Synthesis of a linear array composed of* 10 *dipoles on a planar structure*

of this pattern synthesis is shown in figure 5.3. Therein, the H-plane of the mask pattern and of the reconstructed pattern are depicted for $\theta \in [-90°, 90°]$.

The reader may observe that the obtained excitation produce a directivity pattern that is very similar to the desired one. Due to the fact that the genetic algorithm search for each array element its excitation value independently from the others, the synthesized pattern is not completely symmetrical.

Furthermore, the GA synthesis approach has been tested on the excitation decomposition for a phased array. The pattern of the latter array has been phase shifted causing the main beam to be at $\theta_0 = 40°$. For it, the excitation phase of each 10 elements has been given a respective progressive phase value. Concerning the excitation amplitude values, they have not been modified. The resulting directivity pattern for $f = 1.0$GHz has been taken as mask pattern. The GA synthesis has been applied in order to reconstruct the latter pattern. Figure 5.4 pictures the acquired H-plane directivity pattern with this synthesis approach in addition to the expected pattern function. The resulting pattern approximates the mask pattern very well, specially concerning the main lobe and side lobes maxima.

Moreover, since the directivity pattern of a dipole element and of dipole arrays in free space are symmetrical, the pattern in the θ region of $[-180°, -90°]$ behaves like in the intevall $[-90°, 0°]$. Similar is valid for the interval $[90°, 180°]$: the pattern behaves there like in the region $[0°, 90°]$. Consequently, regions $[-90°, 0°]$ and $[90°, 180°]$ have not been plotted.

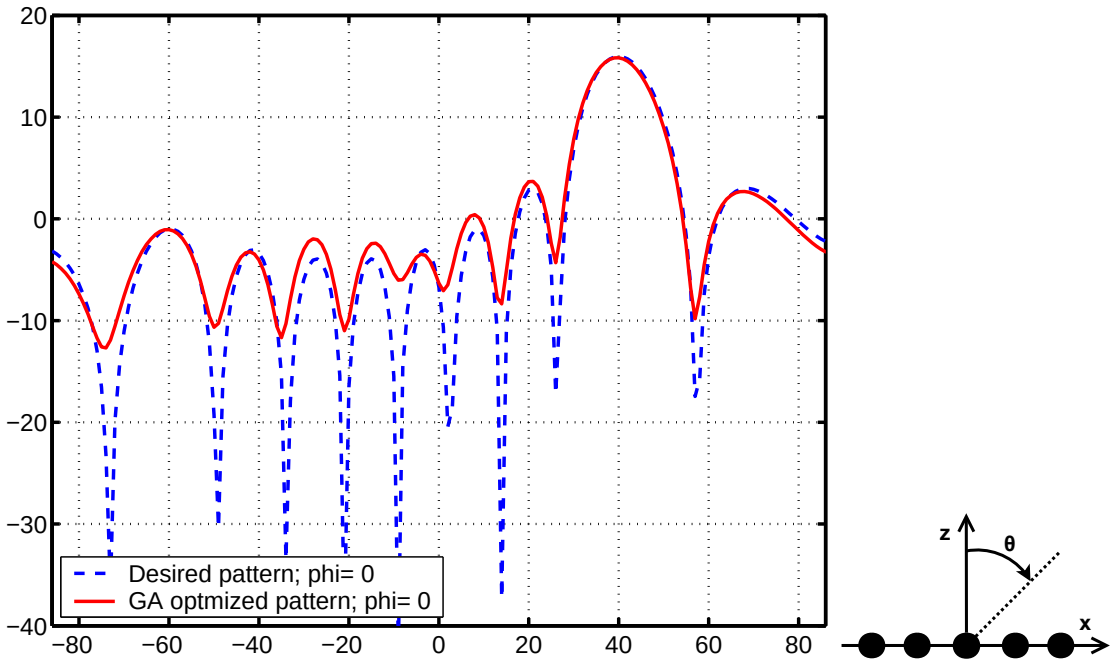

Figure 5.4 : *Pattern synthesis of a linear array composed of* 10 *dipoles on a planar structure with beam steering* $\theta_0 = 40^\circ$

5.2.5.2 Conformal source decomposition

In addition to the afore given synthesis case, the application of the GA approach on conformal array synthesis has been regarded. For it, a linear array, whose elements are positioned along the circumference of a cylindrical structure, has been analysed at a working frequency of $f =$ 1.0GHz. The cylinder has a radius r_{cyl}. Its main axis is oriented in y-direction and therefore the circumference is on the x-z plane. The array elements are positioned equidistant with the spacing value of $d = \frac{\lambda_0}{2} \approx 0.15$m, which defines the arc length between the elements on the circumference. The mask pattern for this case is the directivity of this array for a uniform element excitation with the current amplitude value of $I_0 = 1$A and current phase value of $\alpha = 0^\circ$. Furthermore, the cylinder radius has been given the value of $r_{cyl} = 10.0$m. The task for the GA is to perform the excitation decomposition for a curved linear array in order to yield the mask pattern.

Figure 5.5 shows the synthesis results for $\theta \in [-90^\circ, 90^\circ]$. Therein, the H-plane of the mask pattern and of the reconstructed directivity are presented. The synthesis result approximates the desired pattern with a suitable accuracy. The acquired pattern is not symmetrical but the maxima and almost the entire form of the mask pattern have been found though the influence of the curvature on the radiation.

A second conformal case has been performed in order to analyse the influence of the conformal structure on the pattern synthesis. For it, the same dipole elements as in the latter analysis case have been positioned on a cylindrical structure with a higher degree of curvature. The respective radius of the cylindrical structure becomes then $r_{cyl} = 2.0$m. The pattern to be re-

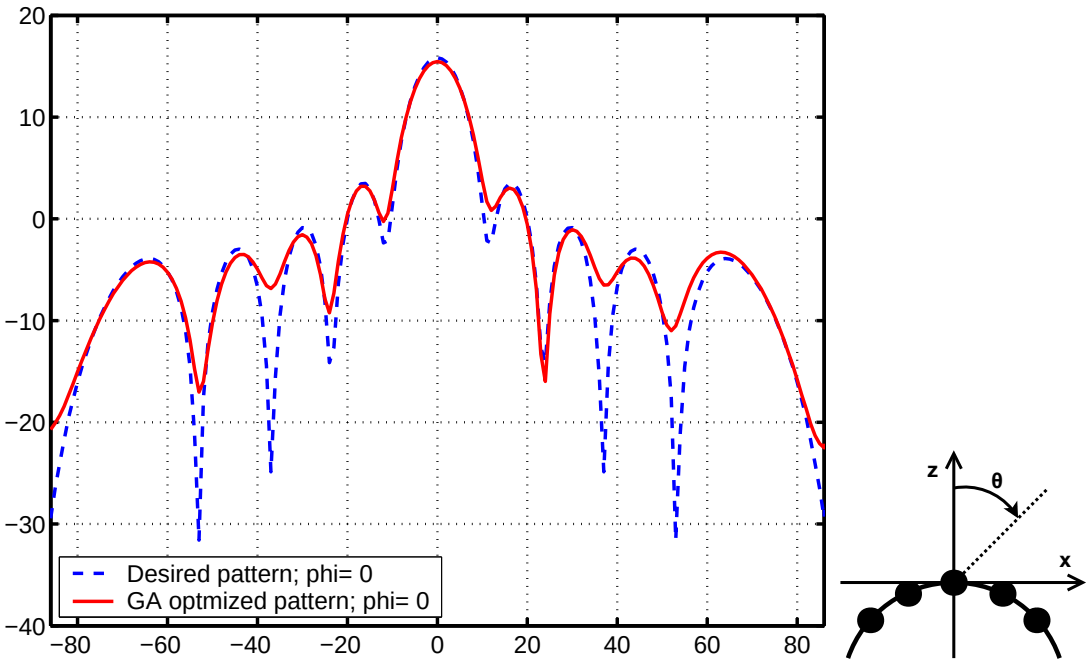

Figure 5.5 : *Pattern Synthesis of a linear array composed of* 10 *dipoles on a cylindrical structure,* $r_{cyl} = 10\text{m}$

constructed is the directivity of the 10 elements array at the frequency of $f = 1.0\text{GHz}$ for a uniform excitation with current amplitude and phase, $I_0 = 1\text{A}$ and $\alpha = 0^\circ$, respectively. The acquired directivity and the mask pattern are depicted in figure 5.6. The reader may notice that the GA synthesis approximates the desired function very well. It finds the proper values for the excitation even for a stronger degree of curvature.

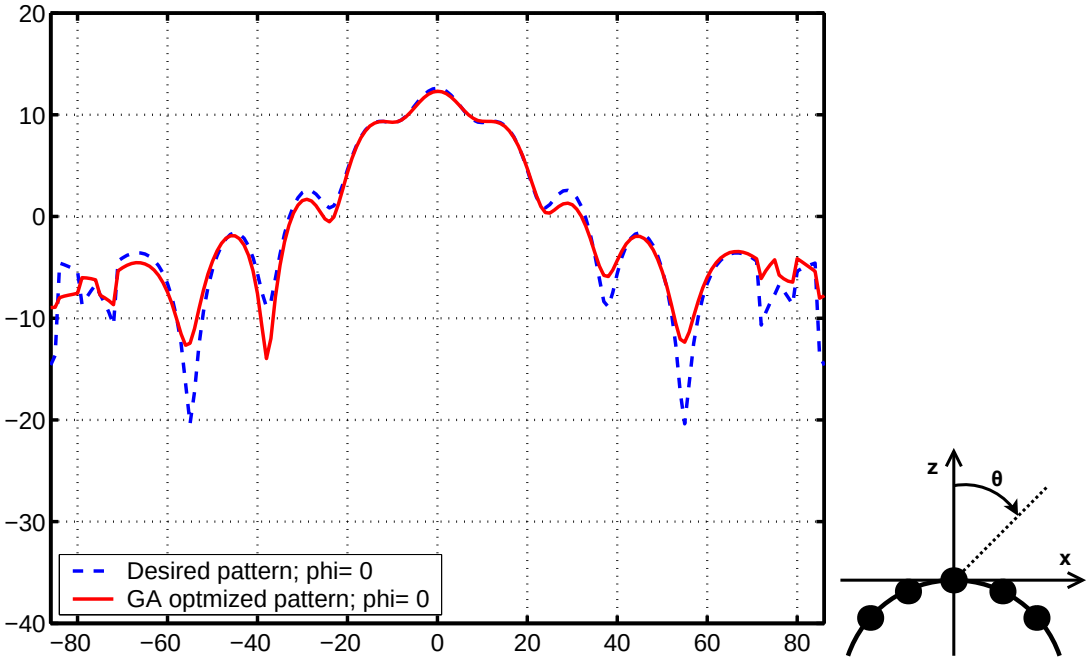

Figure 5.6 : *Pattern Synthesis of a linear array composed of* 10 *dipoles on a cylindrical structure,* $r_{cyl} = 2\text{m}$

Chapter 6

Application of the developed method on antenna arrays

The developed code has been validated by performing the far field analysis of an array that has patch antennas as elements. The antenna array and a single patch element have been modelled and simulated with external software. The solvers of these simulators are based on FDTD and FIT and they have the capability of calculating the radiated field and far field quantities. Therefore, the single patch antenna has been examined with the external software and with the developed method in this work. Subsequently, different planar arrays have been conceived and analysed with the FIT and the equivalent sources approach. The results have been compared. Furthermore, the coupling effects between the array elements are regarded. The behaviour of an array on a cylindrical structure for different degree of curvature is examined. Several pattern optimization cases are performed on planar and conformal arrays by means of the genetic algorithm optimizing approach implemented in this work.

Moreover, the antenna, which is used for the conception of the following arrays, is a circular patch antenna. This microstrip antenna has been proposed by researchers of the research department 'Innovation Works' (IW) that belongs to the European Aerospace Defence and Space company (EADS). The working frequency band of the latter antenna lies in the spectral band used for wireless communication. Consequently, this microstrip antenna can be used in communication systems. Besides that, the research studies on antennas made by IW are focused on the appropiate integration in aircraft fuselage for communication tasks like aircraft-satellite communication.

6.1 Far field analysis of a single array alement

In order to have an idea of the radiation behaviour of an array, the characteristics of a single array element must be known first. Consequently, this section deals with the single antenna analysis concerning its far field behaviour. For it, the proposed microstrip antenna with circular patch form is introduced to the reader. The geometrical measures of the antenna are depicted in figure 6.1. The circular patch antenna resonates at the frequency of $f = 2.4$GHz. This single layered microstrip antenna with a dielectric thickness of $\mathsf{h} = 0.7$mm and a permittivity of $\varepsilon_{eff} = 2.33$ has a circular patch of radius $\mathsf{a} = 2.32$mm. Furthermore, the cell dimensions are defined as $d_x = 60.0$mm and $d_y = 60.0$mm. These dimensions are used later on.

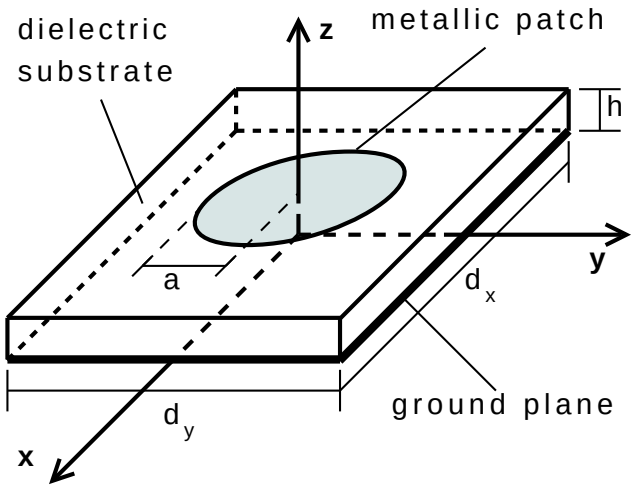

Figure 6.1 : *Single layer microstrip antenna with circular patch*

The far field analysis of the latter antenna has been performed by modelling it with equivalent sources that have been excited with electric currents. The yielded radiated field has been calculated and from it the radiation pattern as well as the directivity. The currents have been retrieved with an internal current generator that calculates them by means of the cavity model. Furthermore, the currents have also been acquired by using external software based on the numerical methods FDTD and FIT. As aforementioned, this software has solvers that calculate the near and the far field generated by the antennas. This possibility has been exploited in order to validate the hybrid method developed in this thesis work. Therefore, several simulations have been run with all three solvers.

Moreover, the currents have been acquired with the internal generator first and then with the help of an external numerical technique. The quantities obtained from the radiated far field caused by the latter excitations have been plotted. In the following diagrams of the resulting three-dimensional patterns, the E-plane pattern refers to the two dimensional cut of the three-dimensional one at $\phi = 0^\circ$, H-plane pattern to the cut at $\phi = 90^\circ$.

6.1.1 Use the of internal current generator

The internal current generator applies the cavity model presented in chapter 3. The equation set in (3.76) is used in combination with equation (3.72) in the generator. According to [1] and [7], the dominant mode in circular patch antenna is the TM_{110}. Therefore, this mode has been chosen and the respective currents have been generated. Subsequently, the far field as well as the directive pattern has been calculated with these excitations. The simulation of the method conceived in this work is compared then with an analytical approach. For it, the analytical equation set (3.49) has been used in for obtaining the far field components of a circular patch antenna. Furthermore, the influence of the dielectric slab has been taken into account by multiplying a correction function that describes the dielectric effects.

The patterns for the analytical formula proceeding and for the hybrid method developed in this thesis work, namely the equivalent source approach, have been computed and pictured.

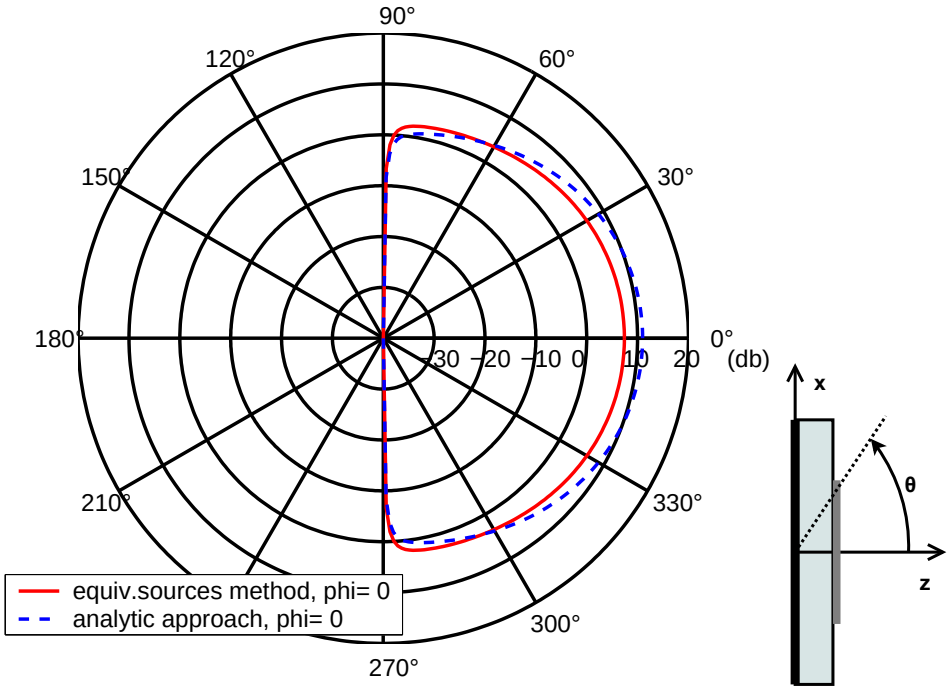

Figure 6.2 : *E-plane directivity of a circular patch antenna - currents calculated with cavity model*

Therefore, figures 6.2 and 6.3 show the radiation pattern in E-plane and H-plane obtained from the far field generated by these currents compared to the pattern acquired with the analytical approach.

6.1.2 Use of external generated currents

For the next analysis results, the currents on the metallic patch of the microstrip antenna have been computed by means of external software. In addition to that, the radiated far field of the circular patch antenna due to these excitations has been calculated with the external solvers in order to perform comparisons. The first current results has been performed with the help of the FIT solver, the second ones with the FDTD solver. The acquired currents by means of the external software have been used to generate the respective radiated electric far field.

6.1.2.1 Currents calculated with FIT

For the simulation with the FIT solver, in order to generate the necessary currents on the active radiating zone of the patch antenna, the antenna element has been defined with the afore given geometrical values. The dielectric substrate has been established as infinite and lossless. The same goes for the ground plane: it is a perfect electric conductor (PEC) layer of infinite extension. The metallic patch has been modelled with a slight thickness of some *mm* and with a very high conductivity value. The antenna has been fed by means of a coax that lies slightly shifted from the geometrical centre of the patch. The feed voltage has been set to $\mathrm{U} = 1.0\mathrm{V}$

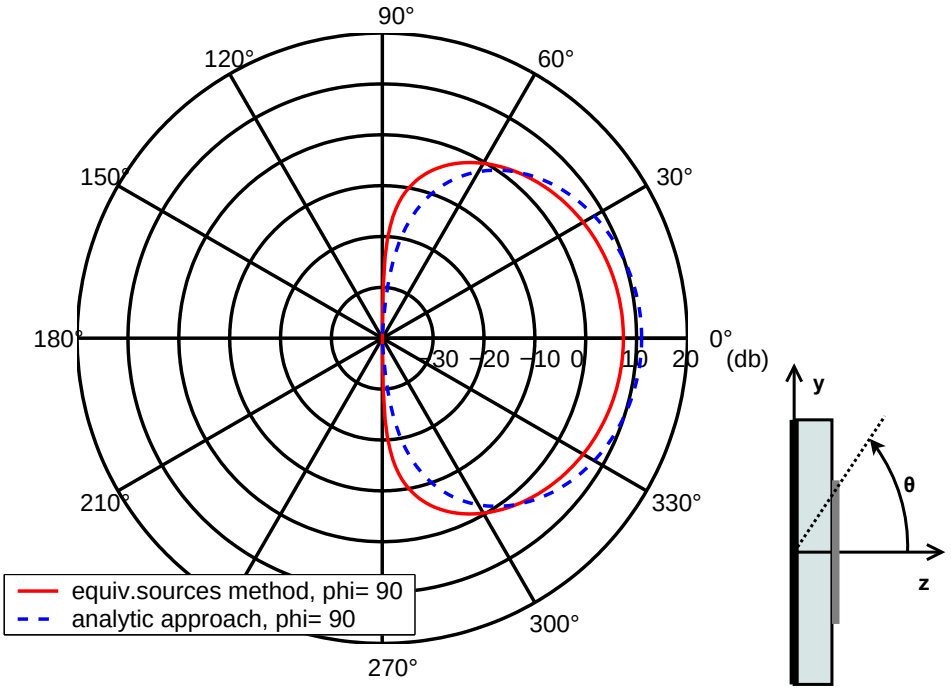

Figure 6.3 : *H-plane directivity of a circular patch antenna - currents calculated with cavity model*

and a well-matched defined input impedance of $Z_{in} = 50\Omega$. The FIT solver calculated the near fields on and under the metallic patch.

The currents in the active region of the microstrip antenna are acquired by giving the calculated near field to the current generation module. Therein, expression (3.77) is applied in combination with the near field as afore described in chapter 3. Continuously, the far field calculation module of the developed method of the present thesis work performs the field generation. Figures 6.4 and 6.5 show the directivity in E-plane and H-plane for external currents that have been calculated with FIT.

The yielded plots show an exact overlap of the calculated pattern by means of the equivalent method approach with the one obtained by means of the FIT based simulation tool. The E-plane plot in particular show the influence of the substrate thickness on the radiation of the patch element: in the θ intervals $[80°, 90°]$ and $[270°, 280°]$ the pattern has still high amplitude values. According to [51], the contributions from the horizontal polarisation currents are very small due to the small dielectric thickness so that they can be neglected. The latter is expressed by the high pattern values at the frontiers between dielectric slab and patch. Furthermore, the results are compared with FDTD results as seen in figures 6.6 and 6.7. There exist a great similarity between both pattern plots. In addition to that, the reader may notice a slight shift between both results. This very small difference that makes the FDTD plot slight asymmetrical might be explained by the influence of the coax fed that is taken into account in a different manner by the FDTD solver. Therefore, the modelling proceeding with the FDTD based simulation tool is explained in the next subsection.

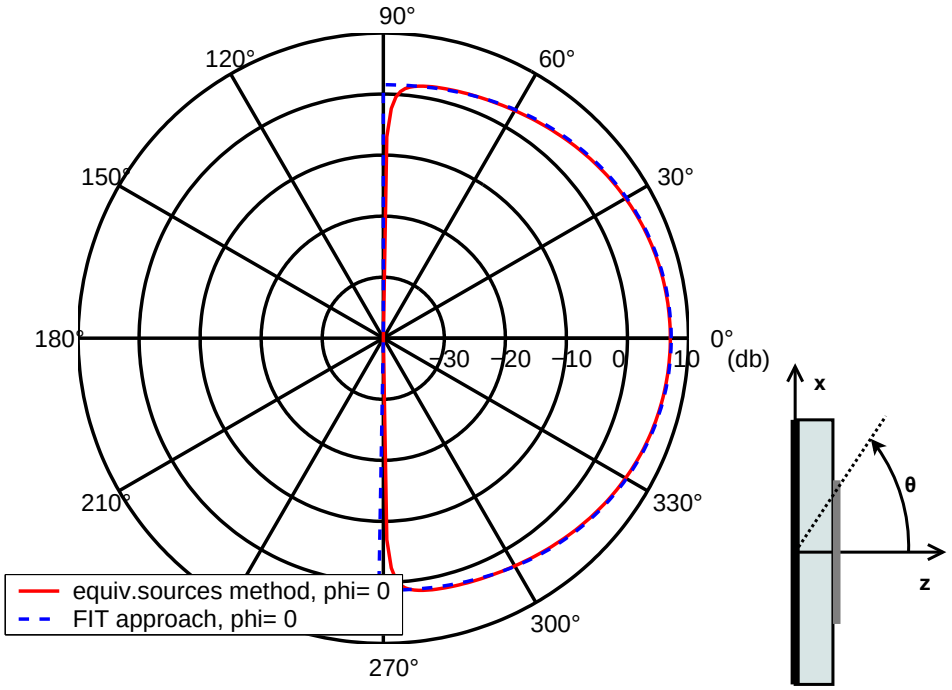

Figure 6.4 : *E-plane directivity of a circular patch antenna - currents calculated with FIT*

6.1.2.2 Currents calculated with FDTD

The current generation with the FDTD simulation tool has been performed in a similar manner as with the FIT solver. This means, that in order to calculate the necessary currents on the metallic patch of the microstrip antenna, this antenna element has to be modelled with the geometrical values afore given at the begin of this section. The dielectric substrate has been also defined as infinite and lossless. The ground plane is established as a PEC layer of infinite extension. In addition to that, the patch has been modelled as a limited metallic layer of negligible thickness with a very high conductivity value. The coax fed has been modelled as a segmented wire slightly shifted from the geometrical centre of the patch. One of the wire segments contains the voltage generator. The feed voltage has been set to $\mathrm{U} = 1.0\mathrm{V}$ as in the FIT case. Furthermore, the fed is set as well-matched with an input impedance of $Z_{in} = 50\Omega$. The FDTD based simulation tool calculated the near fields on and under the metallic patch.

The patch currents of the microstrip antenna are obtained like in the case of the FIT based simulation tool. This is by giving the calculated near field to the current generation module that calculates the required excitations using expression (3.77) in combination with the FDTD generated near field. Subsequently, the far field calculation module of the hybrid method realizes the field generation with the latter currents. Figures 6.8 and 6.9 depict the directive pattern in E-plane and H-plane for external currents that have been calculated with FDTD.

The acquired plot with the equivalent source method converges to the one obtained with FDTD. The reader may notice again the slight difference between both curves. This may confirm the influence of the coax fed modelling concerning the radiation behaviour. This influence is not taken into account at the hybrid method developed in this thesis work. Furthermore, both

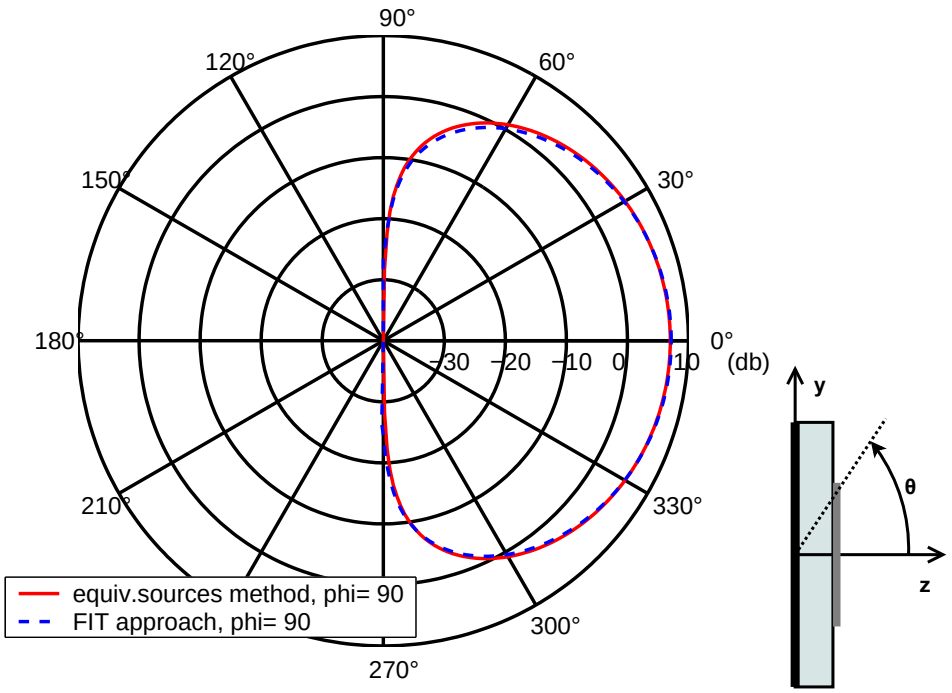

Figure 6.5 : *H-plane directivity of a circular patch antenna - currents calculated with FIT*

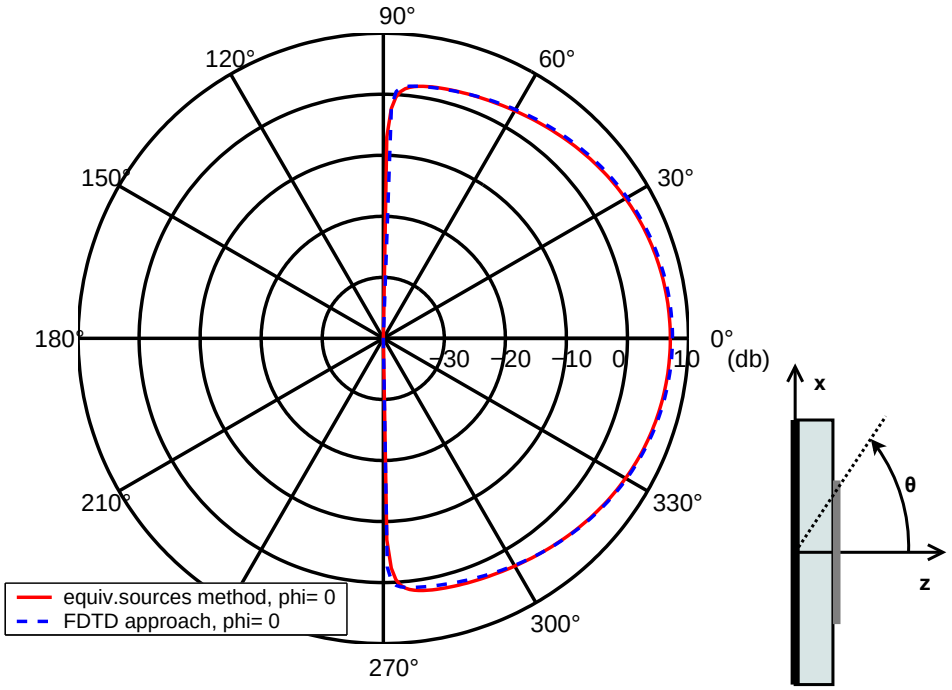

Figure 6.6 : *E-plane directivity of a circular patch antenna - currents calculated with FIT*

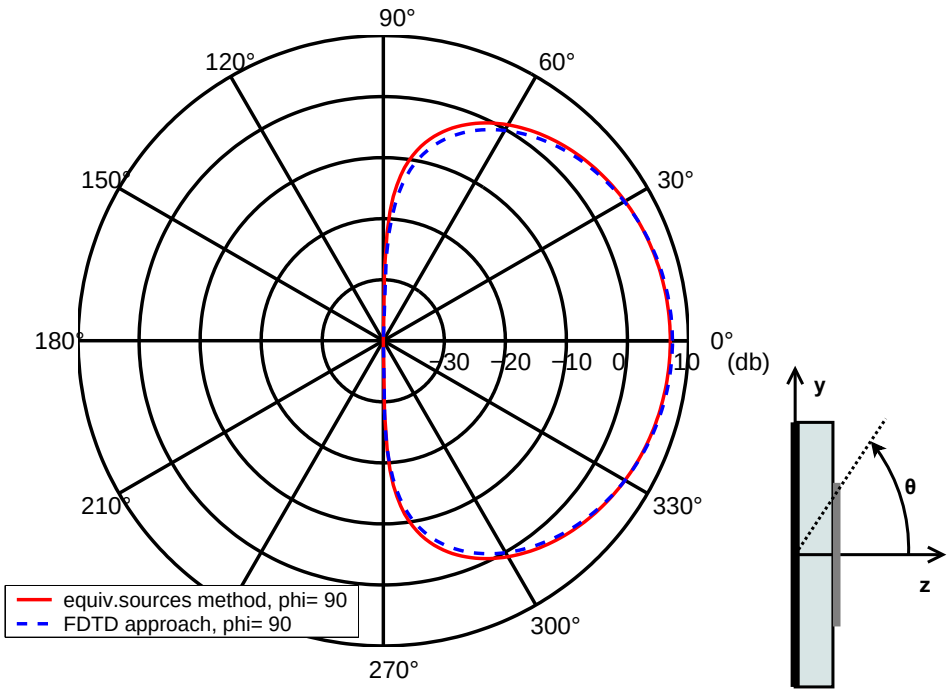

Figure 6.7 : *H-plane directivity of a circular patch antenna - currents calculated with FIT*

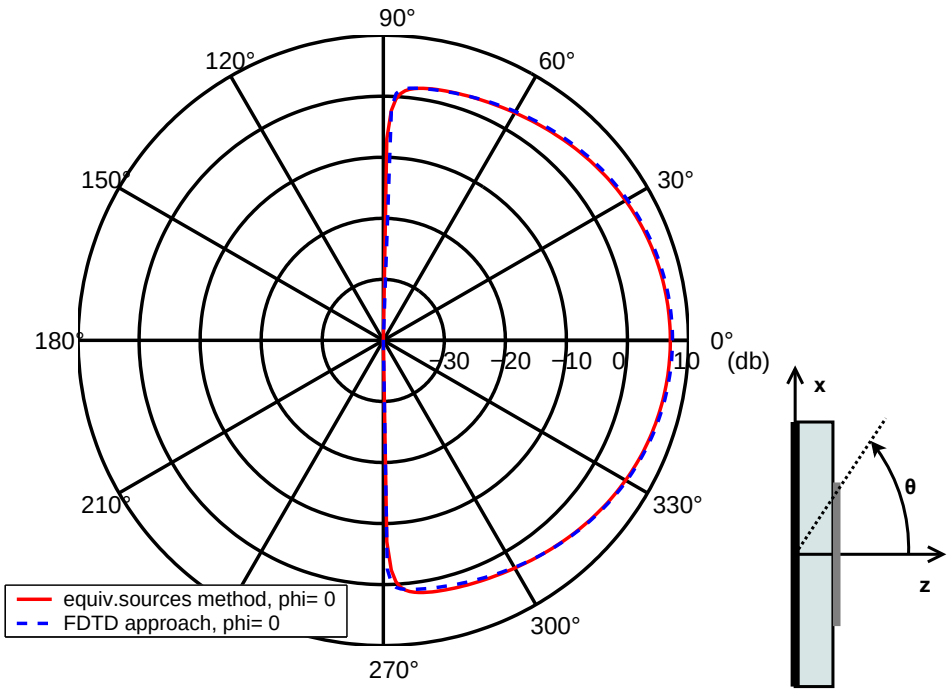

Figure 6.8 : *E-plane directivity of a circular patch antenna - currents calculated with FDTD*

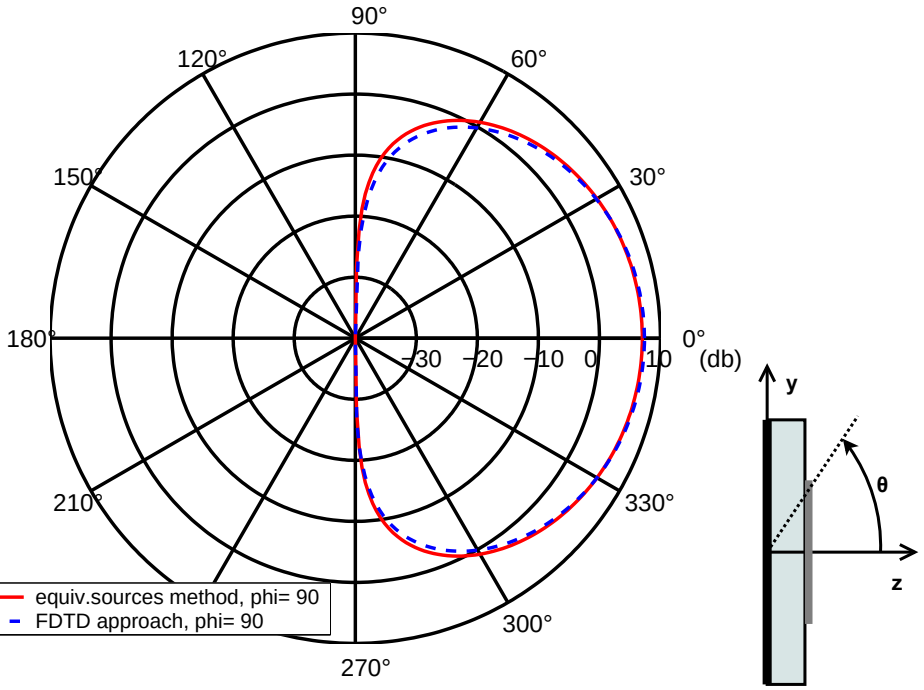

Figure 6.9 : *H-plane directivity of a circular patch antenna - currents calculated with FDTD*

plots show the influence of the very thin dielectric thickness in the E-plane plot. Moreover, the results are compared with the FIT results as shown in figures 6.10 and 6.11. There exist a great similarity between both pattern plots. Furthermore, the exist a negligible difference between the results with the excitation being calculated by means of the FIT solver and the ones by means of the FDTD solver. Consequently, both current values obtained can be used for the following analysis.

6.2 Far field analysis of a microstrip antenna array

After having a certain knowledge about the far field characteristics of a single array element, the radiation characteristics of an array is analysed. For it, the array is built by using the afore presented microstrip antenna. In the following, the interactions between the array elements is regarded. Subsequently, validation examples for the realization of planar arrays are shown. An example concerning beam-steering is given. Furthermore, the influence of the curvature of a conformal array is presented to the reader

6.2.1 Planar arrays

Certain planar arrays have been generated by using the afore validated circular patch antenna. Firstly, planar arrays are analysed. Therefore, the handling with coupling between neighbouring elements are regarded. Then, the far field behaviour of planar arrays defined on the x-y-plane is observed. Three examples have been modelled: a small array composed of 2×2 elements, a

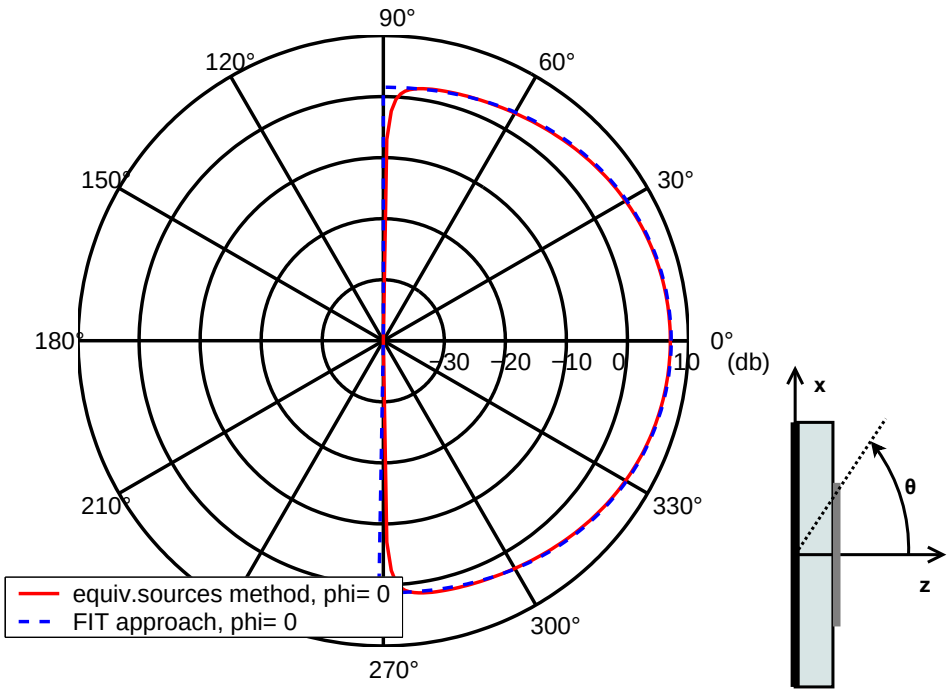

Figure 6.10 : *E-plane directivity of a circular patch antenna - currents calculated with FDTD*

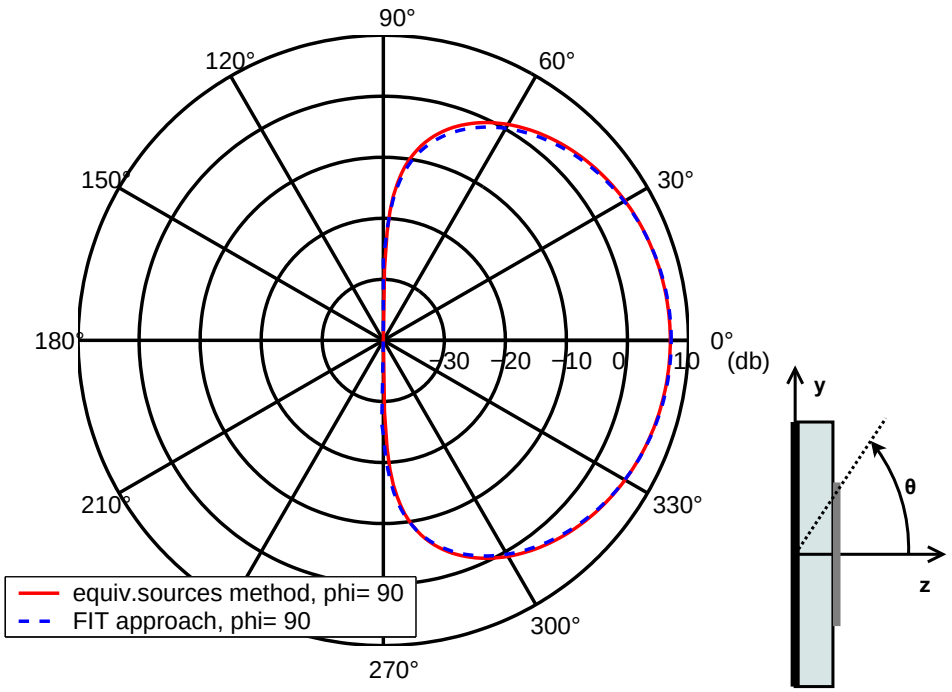

Figure 6.11 : *H-plane directivity of a circular patch antenna - currents calculated with FDTD*

medium array built by 4×4 elements, and a big array conceived by means of 8×8 elements. Furthermore, the cell dimensions d_x and d_y in figure 6.1 are equivalent to the spacing values. These dimensions have been set to $d_x = 60.0$mm and $d_y = 60.0$mm. Consequently, the arrays are defined as uniformly spaced. In addition to that, the array elements are uniformly fed with $U = 1.0$V. The far field and the directivity of the latter arrays has been computed with the hybrid method of this thesis work. Furthermore, these results have been compared with the ones gained by means of the FIT based simulation tool.

6.2.1.1 Consideration of coupling effects

As mentioned in chapter 3, the elements of an array interact between them due to lossy waves, like leaky and surface waves. These waves influence stronger or weaker the radiation characteristics of the elements depending on the proximity between them. Furthermore, the currents of an element, which is surrounded by a certain number of elements, contains in general the coupling information due to its neighbours. Consequently, the coupling effects can be approximated and hence taken into account by analysing such an element and using its currents for the analysis of the entire array. For it, a small array of 3×3 elements has been defined according to the afore defined spacing values. Subsequently, the centre element is analysed. The circular patch antenna studied at the latter subsection has been used as array element. The modelling and the simulation of the array have been performed by means of the FDTD based simulation tool.

For acquiring the currents on the central element, all nine elements have been fed with the same excitation simultaneously. The near field of the excited array has been calculated. The near fields over and underneath the metallic patch of the central element have been extracted. According to expression (1.69) from chapter 1, the currents at the metallic patches, which can be handled as boundaries, can be acquired with these fields. Applying the latter to the calculated near fields yields to the simulation results visualized in figure 6.12. This diagram shows the current magnitude values on the patches of the array elements. Moreover, the near fields over and underneath the metallic patch of the central element have been extracted in order to obtain the currents of this element. The currents contain automatically the mutual coupling coming from the other array elements. These currents are used for modelling the arrays later on.

Furthermore, additional simulation cases have been run in order to observe the coupling effects coming from a single array element. For it, the simulation setting has been modified concerning the feed values for the array elements. Two essential cases are presented in the following. The first case comprises the coupling effects due to the central element. The second treats the mutual coupling due to a corner element. Figure 6.13 depicts the central element case. For this simulation case, the excitation of all array elements with exception of the central element have been set to zero. The reader may notice that the elements right and left of the central element are affected the most by the coupling effects. The occurence of currents in both elements though zero feed values are the highest. Nevertheless, since the values are around -30dB they are probably non perceivable if the elements are excited. Another observation is that the coupling currents magnitudes are distributed likewise at all three patches. It can be assumed that this distribution pattern shows that the coupling currents and the excited ones have the same in-phase or opposite-phase orientation. This would explain also the strong coupling behaviour only in neighbouring elements along the current orientation. Furthermore, the latter

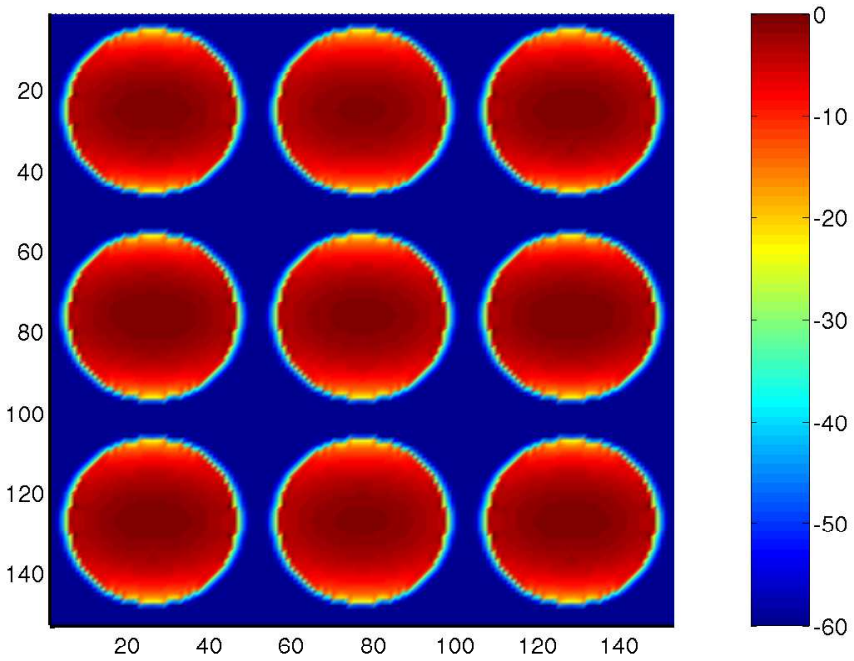

Figure 6.12 : *Magnitude of electric currents at the patches of* 3×3 *array in [dB], all elements fed*

opposite-phase assumption can be supported by the law of induction, that says that induced current flows in a direction to oppose changes due to a magnetic field.

The second case presented handles the coupling effects of the corner element. For it, the simulation settings concerning the excitation have been changed in such a way that only the corner element has been excited, the other elements have been switched off. The resulting current distribution for the entire array in the case of feeding the left upper corner element is depicted in figure 6.14. It can be observed that the corner element causes significant coupling currents mainly on its right hand neighbour. Similar as in the centre element coupling case, the values of the current magnitudes are about -30dB. Hence, it can be pressumed that they are not noticeable if the affected array element is excited. Furthermore, the current distributions on the excited and on the coupling affected patches have a similar pattern and they coincide with the distribution pattern observed in the central element case. This behaviour supports the statement that source and coupled currents are oriented in the same direction but in opposite phase manner.

As aforementioned, the currents found for the centre element of the latter analysed array contain additional coupled currents due to the proximity of neighbouring elements. In order to see the influence of these additional coupling currents on the radiation behaviour of an element, a single element has been fed with the currents of the centre element of the latter array. Subsequently, the far field and the directivity of the excited antenna have been calculated. The results of this simulation have been compared with the results obtained for the single element analysis made in the latter section. The yielded directivities have been plotted together. Consequently, figure 6.15 shows the E-plane of the directive pattern and figure 6.16 the H-plane, respectively.

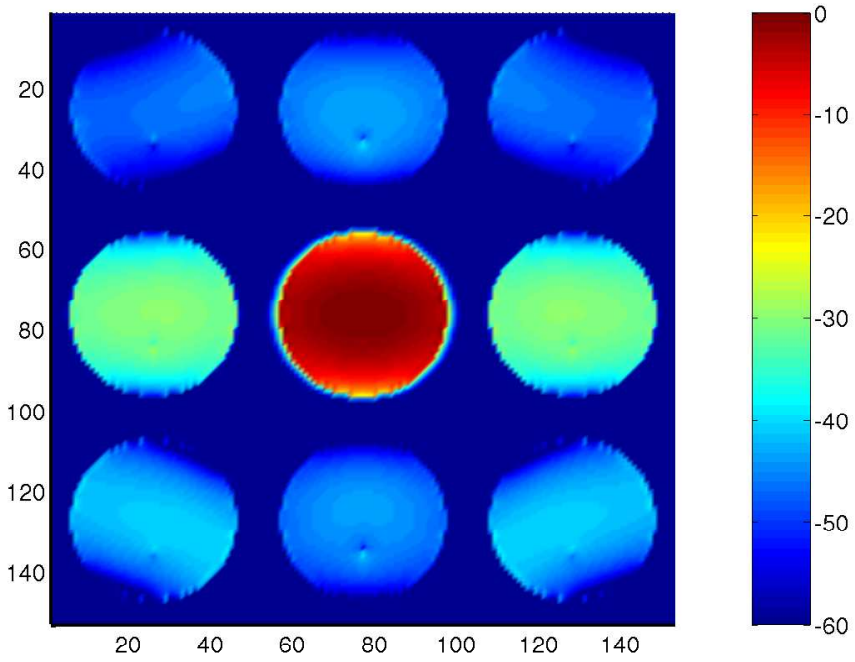

Figure 6.13 : *Magnitude of electric currents at the patches of* 3×3 *array in [dB], central element fed*

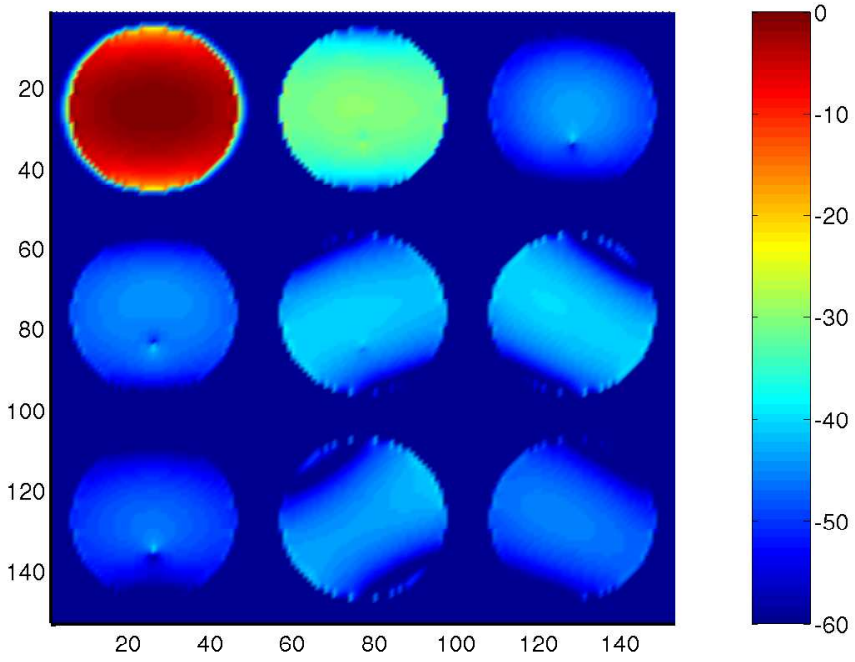

Figure 6.14 : *Magnitude of electric currents at the patches of* 3×3 *array in [dB], corner element fed*

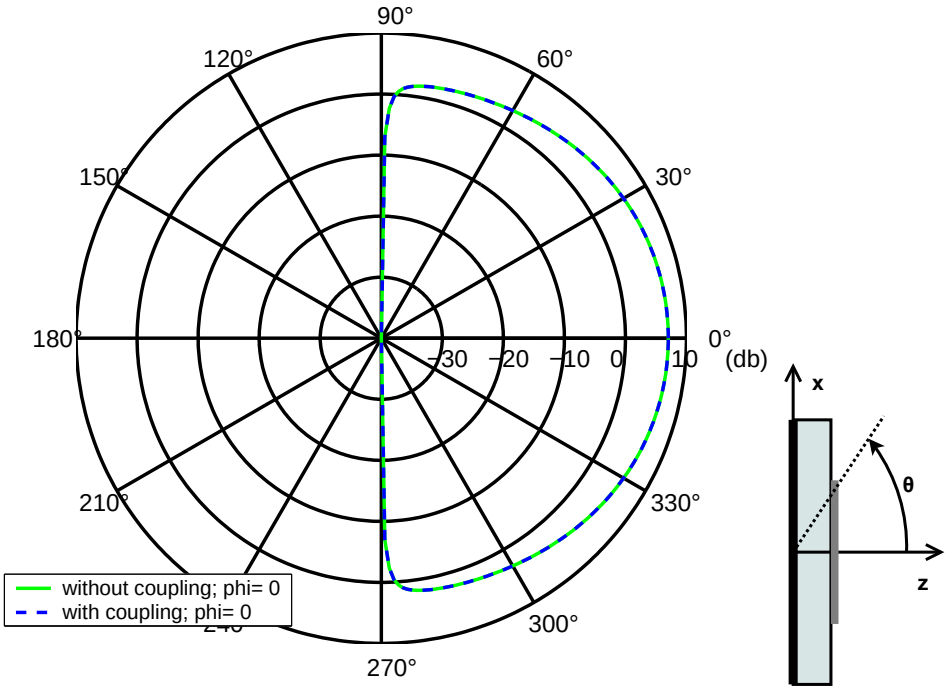

Figure 6.15 : *E-plane directivity of a circular patch antenna - currents with and without coupling*

The reader may observe that the directivities of the single array element and the single antenna coincide entirely. Consequently, it can be said that the coupling effects are apparently minimal in the case of a 3×3 array and therefore negligible. In addition to the latter, it can be said that in a bigger array, for instance 5×5, the centre array element is affected by its neighbours after next, in addition to the next neighbouring elements. Nevertheless, the influence should be minimal, if observing the upper right corner element in figure 6.14. Consequently, the coupling currents can be supposed to come only from next neighbouring elements for this array composed of the circular patch elements afore analysed. Therefore, bigger arrays can be modelled by using the currents obtained for centre element.

Moreover, fringing effects have not been considered in the present thesis work. These effects become noticeable at the border of microstrip antenna arrays, specially for arrays with finite size ground planes. Nevertheless, fringing effects are less perceivable at arrays of big dimensions with directive patterns. Microstrip antenna arrays integrated in aircraft fuselage can be modelled as infinite grounded arrays due to the material characteristics and specially due to the dimensions of the fuselage in comparison to the array. Furthermore, the number of elements of such arrays are of large dimensions and directive patterns are of advantage for communication tasks. Consequently, the fringing effects are neglected in the following analyses.

6.2.1.2 Analysis of an array

Considering the latter examination on the coupling effects between neighbouring array elements, the far field radiation behaviour of a planar array, first taking and then not taking coupling into account, is regarded. The purpose of this simulation is to observe if the coupling

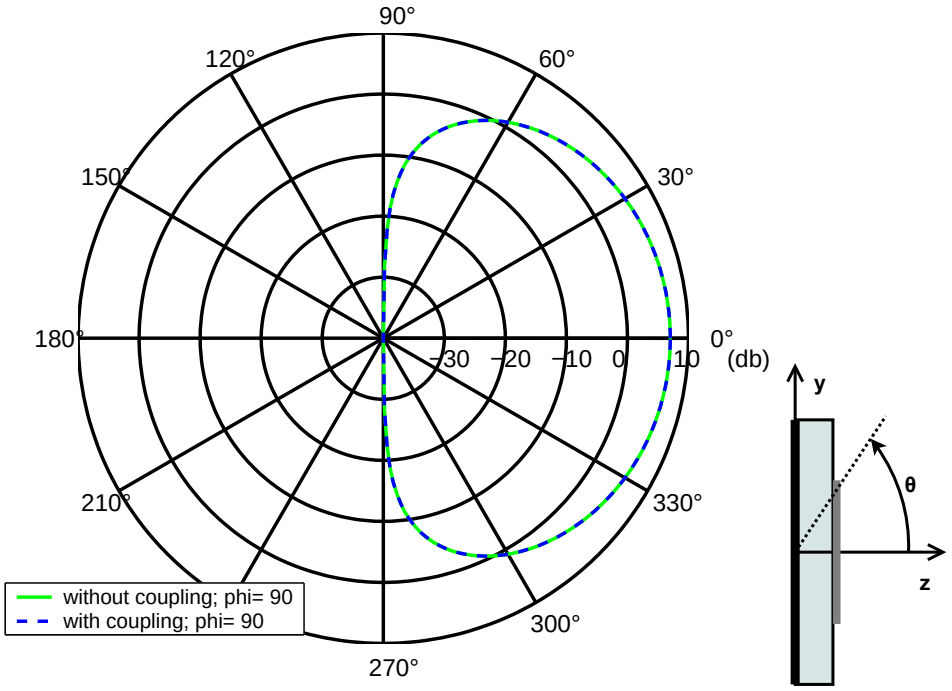

Figure 6.16 : *H-plane directivity of a circular patch antenna - currents with and without coupling*

effects sum themselves up and hence influence the radiation of an array. For it, a planar array has been built with 8×8 circular patch antennas. Therefore, these antenna elements have been positioned on the x-y-plane according to the afore given spacing values. The latter values, which are $d_x = d_y \approx 0.48\frac{\lambda_0}{2}$, fulfill the conditions for avoiding grating lobes and a second main lobe in the end-fire pattern case according to theory (see chapter 1). Furthermore, all array elements have been fed with the same excitation.

The simulations have been run with the hybrid method developed in the present work. For it, the near fields obtained by the analysis of the single patch antenna made with the FDTD solver are given to the current generation module of the hybrid method. The latter module calculates the required excitations that are in the following used in order to generate the far field and the radiation quantities. The same procedure is performed with the near fields acquired by the analysis of the central element of a 3×3 array. The resulting directivity functions are plotted in figures 6.17 and 6.18. The first figure contains the E-plane of the directive pattern, the second figure the H-plane, respectively.

The reader may notice that the results with the currents taking into account coupling and the results without considering them are the same. This means that, the coupling effects due to the next neighbours do not amount to a high noticeable value, if the number of the array elements is enhanced. Consequently, coupling can be neglected in the observed case and the simulations of arrays composed of the circular patch antenna can be performed by means of the excitation currents that do not include the coupling currents.

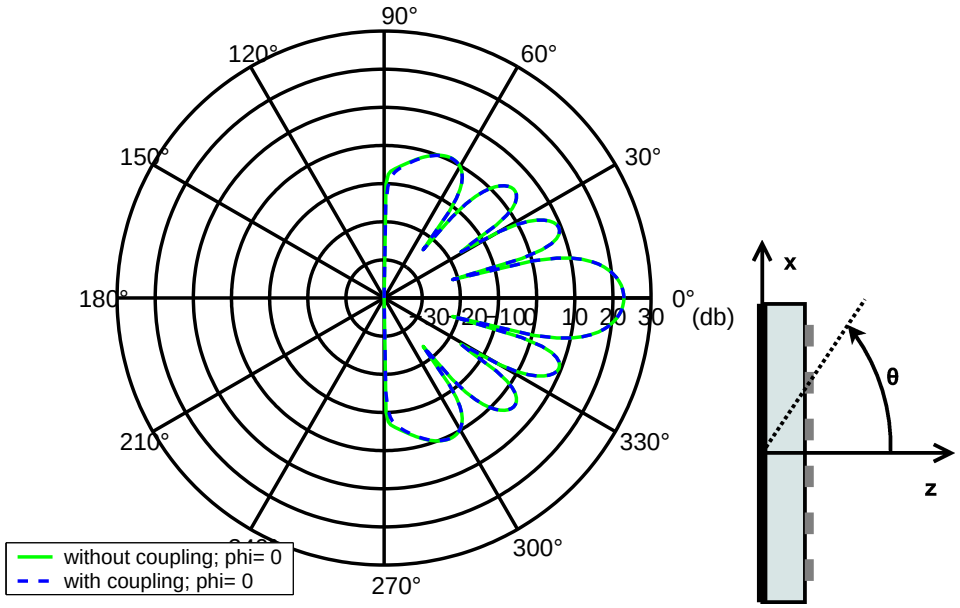

Figure 6.17 : *E-plane directivity of a* 8×8 *circular patch array on a planar structure - currents with and without coupling*

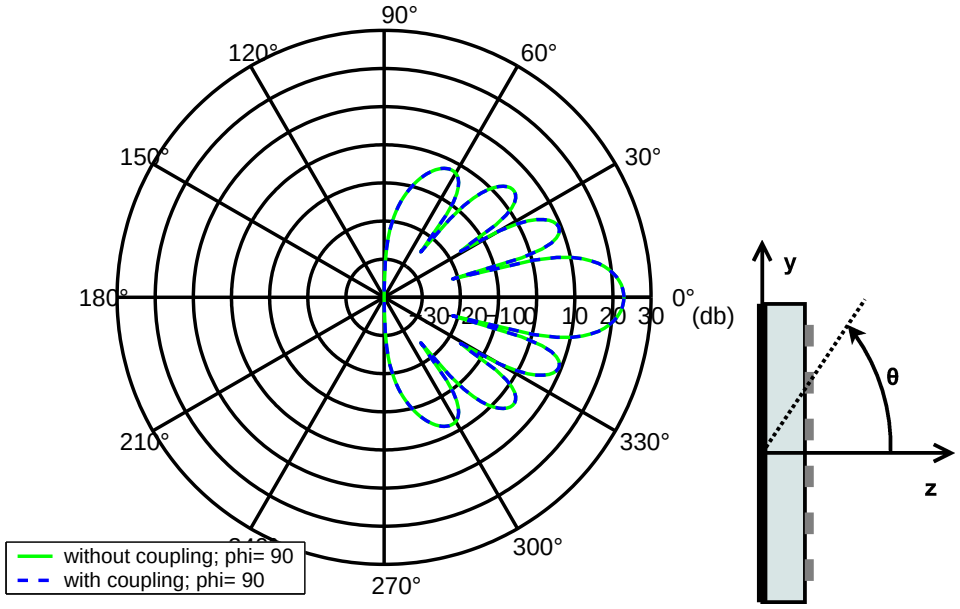

Figure 6.18 : *H-plane directivity of a* 8×8 *circular patch array on a planar structure - currents with and without coupling*

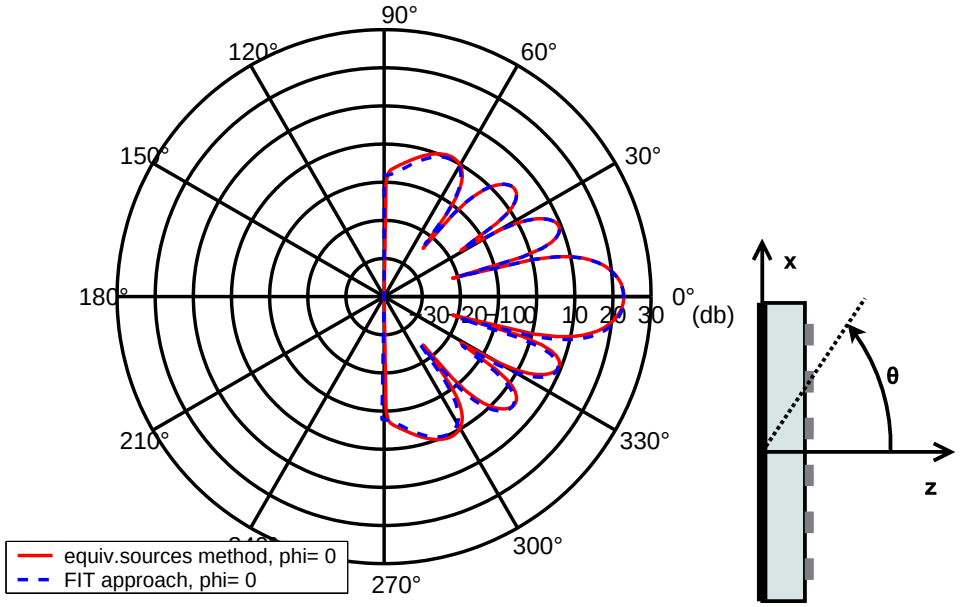

Figure 6.19 : *E-plane directivity of a* 8×8 *circular patch array - currents calculated with FDTD*

For validation reasons, the simulation results of the 8×8 array with the approach developed in this thesis work have been compared to the ones obtained with the FIT-based simulator. The comparison plots are depicted in figures 6.19 and 6.20. Therein, the E and the H-plane of the directive pattern are presented to the reader. The plotted curves show a good agreement between the calculated directivity values generated by the external solver and by the equivalent source method. In addition to that, a low number of side lobes that are noticeable in E and H plane can be discovered. Besides that, the patterns behave symmmetrically in both planes. Furthermore, the directivities in E-plane show the influence of the substrate with a small thickness value that has been encountered in the case of a single patch element. Moreover, the acquired maximum gain has a value of $G_{max} \approx 23$dB according to both simulations.

It has to be remarked that the simulation tools based on FDTD and FIT method include at the field calculations all interactions between the discrete meshed volume cells. Consequently, the near fields over and in the dielectric slab contain the coupling effects of all array elements.

6.2.1.3 Additional planar arrays

In order to give the reader an idea about the radiation characteristics of microstrip antenna arrays, simulations with two array composed of a small number of elements have been performed. The first array analysed is the 2×2 array. The resulting directivity plots are presented in figures 6.21 and 6.22. The first picture depicts the E-plane of the directivities, the second one the H-plane of the latter far field quantities, respectively. In both figures, an overlap between the directivity generated by the hybrid method and the directivity calculated with the FIT method is observed. Furthermore, the reader may notice that the directive pattern of an array composed of four elements is symmetrical and does not have side lobes . Moreover, the influence of the very thin dielectric substrate at the θ intervals $[80°, 90°]$ and $[270°, 280°]$ is perceivable as in the case of the single patch element. The maximal gain according to both simulations is about

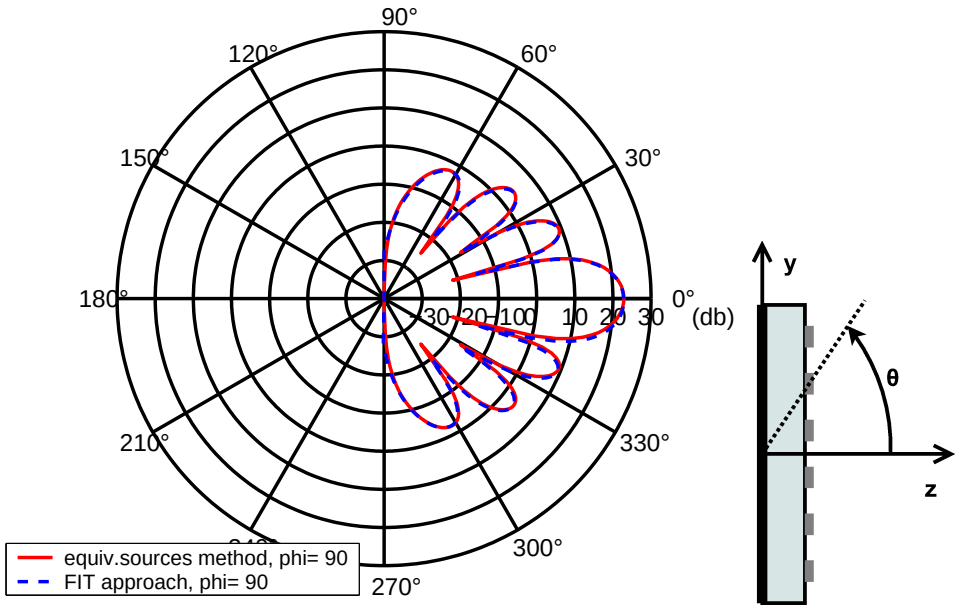

Figure 6.20 : *H-plane directivity of a* 8×8 *circular patch array - currents calculated with FDTD*

$G_{max} \approx 11$dB.

Second example is the simulation of a 4×4 array. The results of this uniform fed and spaced array have been visualized. Figure 6.23 pictures the directive patterns in E-plane, figure 6.24 the directive patterns in H-plane, respectively. The directivities in E-plane show the aforementioned influence of the substrate with a small thickness value, similar as in the case of the 2×2 array and of the single patch element. Furthermore, the rise of two side lobes, which are noticeable in E and H plane, can be discovered. The patterns behave symmmetrically in both planes. Moreover, the directivity results calculated by the approach developed in this thesis work agrees with the one acquired by means of the FIT method. In both simulations the maximal gain amounts to $G_{max} \approx 17$dB.

6.2.1.4 Phased Array

In the following, an example for a phased array is given. For instance, it is desired that the main beam of broadside pattern of the 8×8 planar array afore presented lies the angle $\theta_0 = 60°$. Therefore, the excitation phases are calculated by means of the spatial angles ψ_m and ψ_n (see equation (1.116), chapter 1) that depend of the geometry of the array. These spatial angles must dissappear at the desired direction in order to have the pattern maximum. The progressive shift obtained amounts to $-155,88°$ and the respective multiples are additioned to the array elements in x-direction. The phased array pattern is depicted in figure 6.25. The reader may notice the main beam to be at the desired spatial angle θ_0.

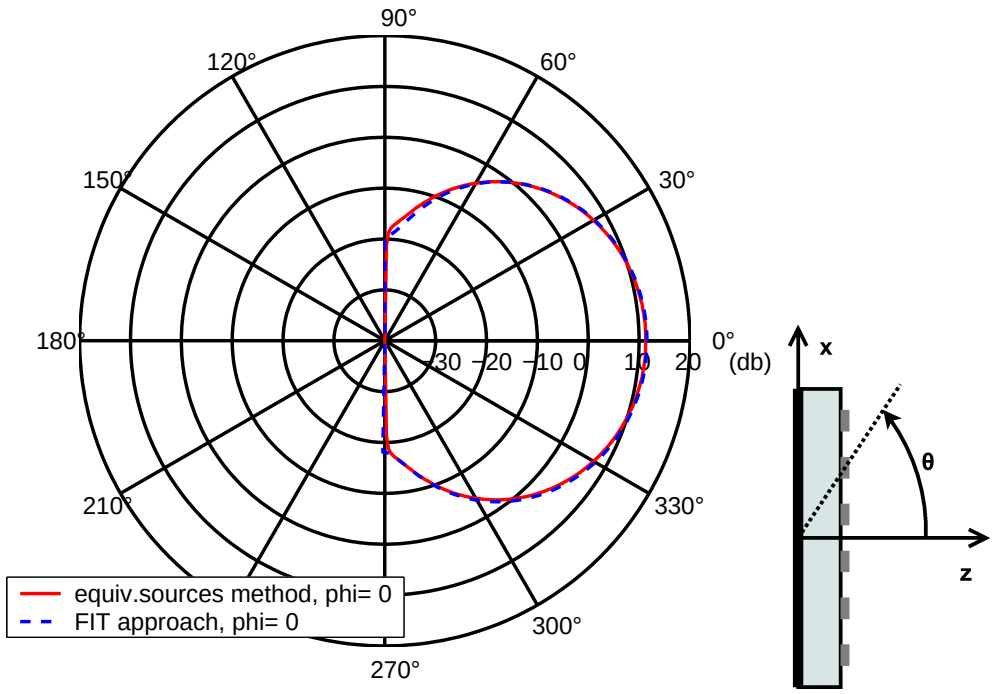

Figure 6.21 : *E-plane directivity of a* 2×2 *circular patch array - currents calculated with FDTD*

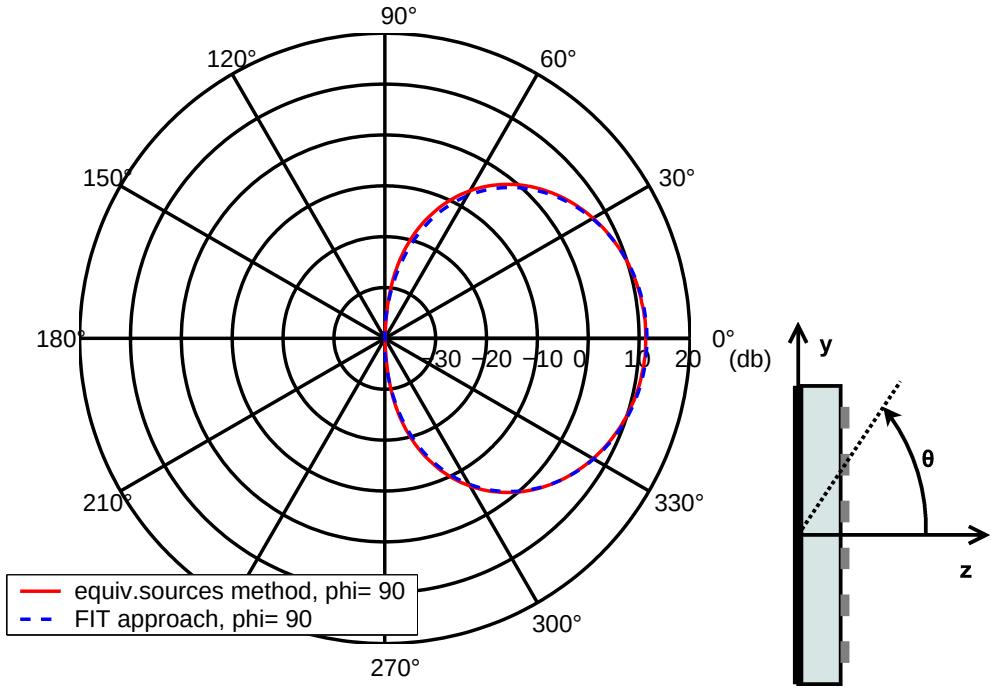

Figure 6.22 : *H-plane directivity of a* 2×2 *circular patch array - currents calculated with FDTD*

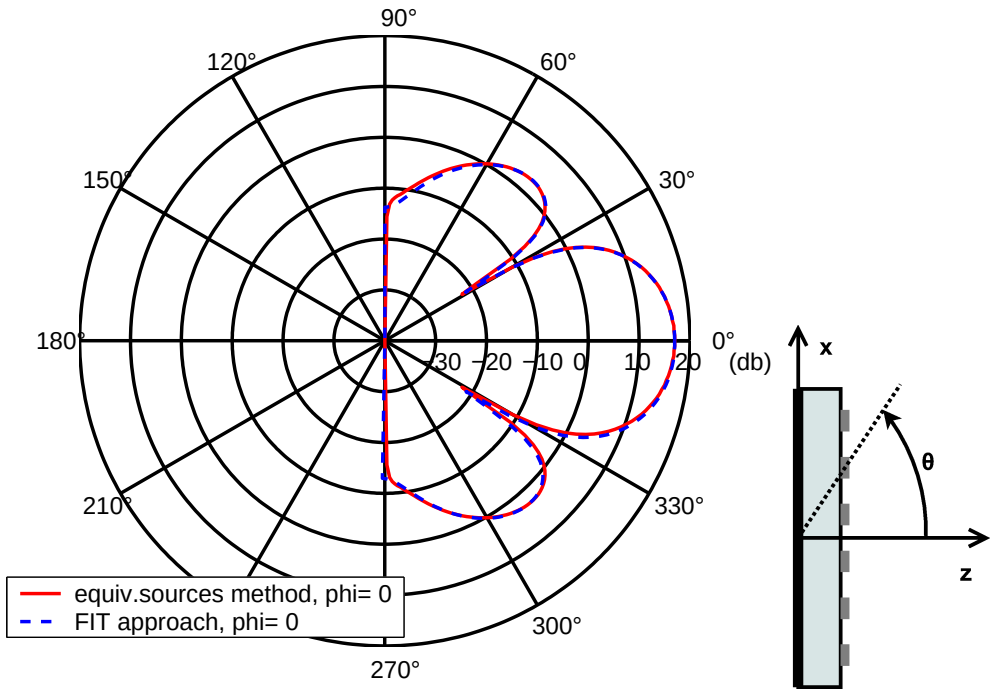

Figure 6.23 : *E-plane directivity of a* 4×4 *circular patch array - currents calculated with FDTD*

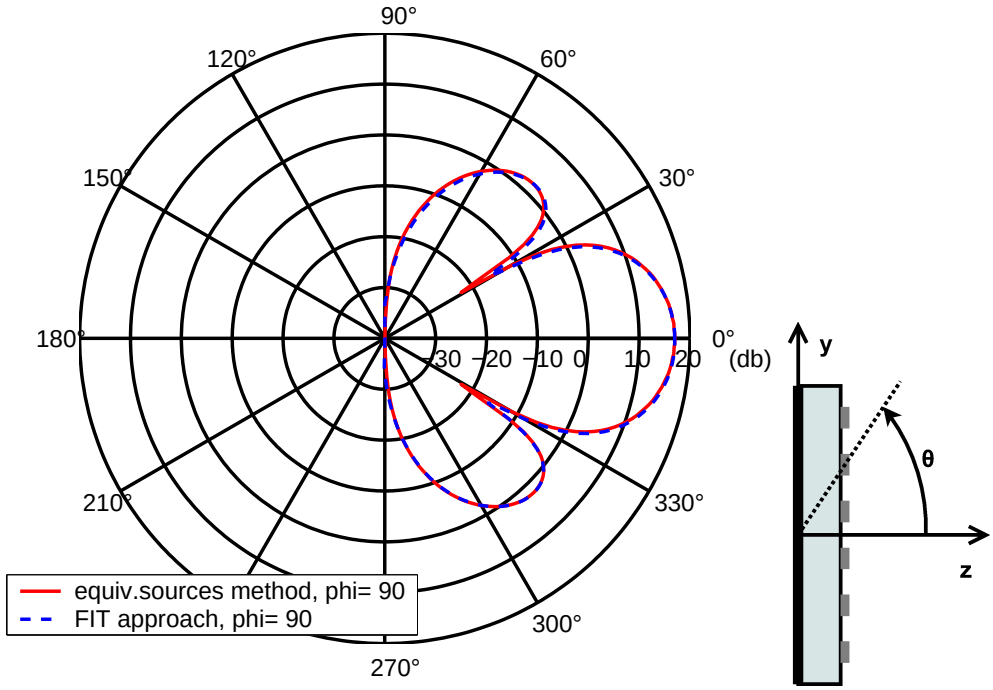

Figure 6.24 : *H-plane directivity of a* 4×4 *circular patch array - currents calculated with FDTD*

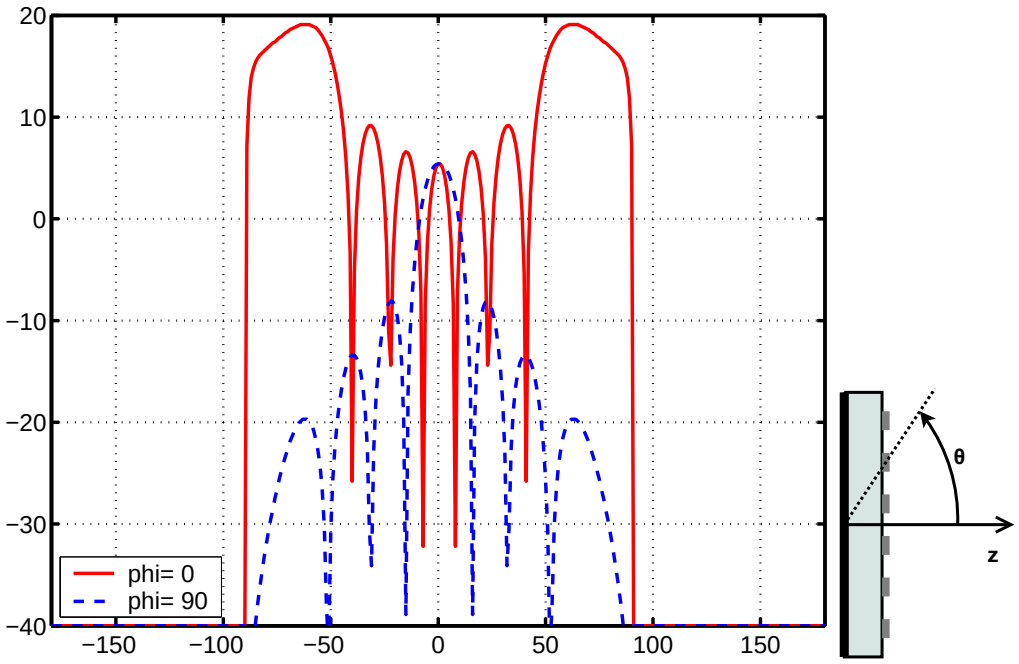

Figure 6.25 : *Phase shifted beam about* $\theta = 60$ *of a* 8×8 *circular patch array on a planar structure*

6.2.2 Conformal arrays for different degree of curvature

The advantage of microstrip antenna arrays is the simpleness of integrating them to conformal structures. Consequently, the behaviour of a conformal array is of great importance and needs to be examined. Therefore, several simulations have been run for an array composed of 8×8 circular patch elements on a cylindrical structure. For it, the centre element currents taken from the afore presented analysis, which include coupling effects, have been used. Proceeding in such a manner means that the coupling effects of the conformal array, which take place on and inside the dielectric slab, are approximated by the coupling effects of the planar counterpart. This approximation can be made for conformal arrays with a slight degree of curvature. For a very curved array structure this approximation is probably not appropiate, due to the fact that the geometry dependant Green's function becomes different.However, the conformal antenna arrays are approximated with flat elements, for whom the coupling effects are valid. Furthermore, since the inner array elements are influenced only by the next neighbour, as observed in the afore presented coupling analysis, the radiation behaviour may approximate the real conformal array.

In order to see the influence of the degree of curvature on the array radiation behaviour, simulations for an 8×8 conformal array have been performed. The conformal array has cylindrical form and is described by the radius r_{cyl} and by its main axis in direction x-axis. Consequently, the spacing value $d_1 = 60$mm is equivalent to the distances between the array elements in x-direction. The spacing value $d_2 = 60$mm is equivalent to the arc lengths between neighbouring elements along the circumference of the cylinder. The afore examinated circular patch antenna is used as array element. Furthermore, the coupling effects are supposed to be the same as in a planar array. Hence, each array element is fed with the currents extracted of the inner element of

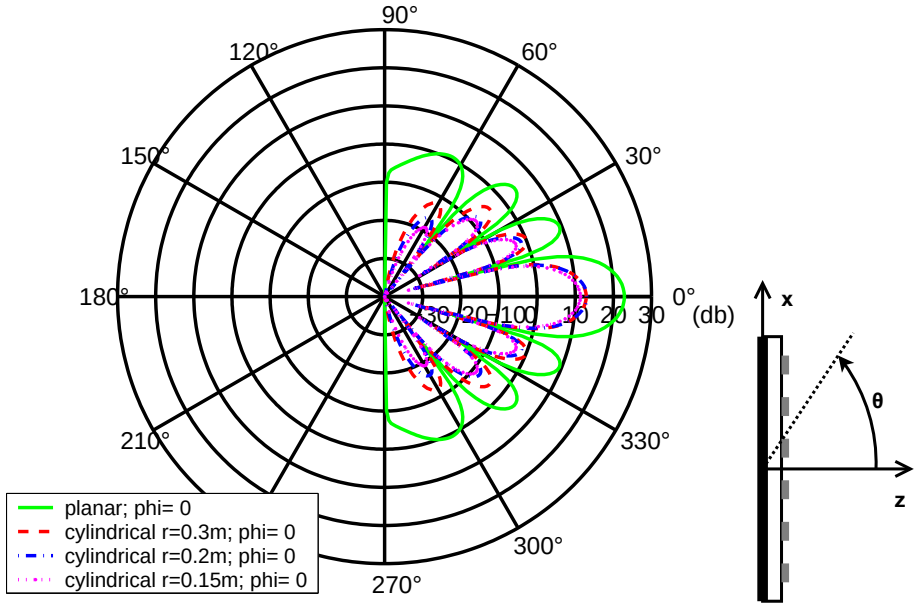

Figure 6.26 : *E-plane directivity of a* 8×8 *circular patch array on a cylindrical structure for different curvature levels - currents calculated with FDTD*

the afore analysed 3×3 array. Figures 6.26 and 6.27 show the directive patterns of conformal arrays with different degree of curvature in comparison to their planar counterpart. The first figure depicts the E-plane of the directivities, the second figure the H-plane, respectively

The H-plane plots show to the reader the influence of the curved structure. The array with $r_{cyl} = 0.15$mm is the conformal array with the strongest curvature degree under the shown ones. The reader may notice that the directive pattern of this array in the H-plane does not show side-lobes but a wide low powered main lobe. This is due to the fact that each array element radiates in different directions. Consequently, a wide angle range is covered but with a small power. The more the degree of curvature is lowered, the more power begins to concentrate in certain regions and hence the more beams begin to rise. The E-plane patterns show a preservation of the main and side lobes but also a reduction of magnitude for the different curved arrays. For the E-plane it is valid too that the stronger the degree of curvature is, the less is the magnitude of the main beam.

6.3 Array optimization

This section comprises the performed validation of the implemented genetic algorithm optimization approach. For it, certain optimization cases taking into account certain industrial aspects have been regarded. The first case treated is source decomposition. The possibility of finding out the optimal excitation for an antenna array under certain geometrical conditions, for instance the integration of the array in a conformal structure, is of advantage for the conception of telecommunication systems in aircraft fuselage.

The second case concerns phase synthesis of a planar or conformal antenna array. This

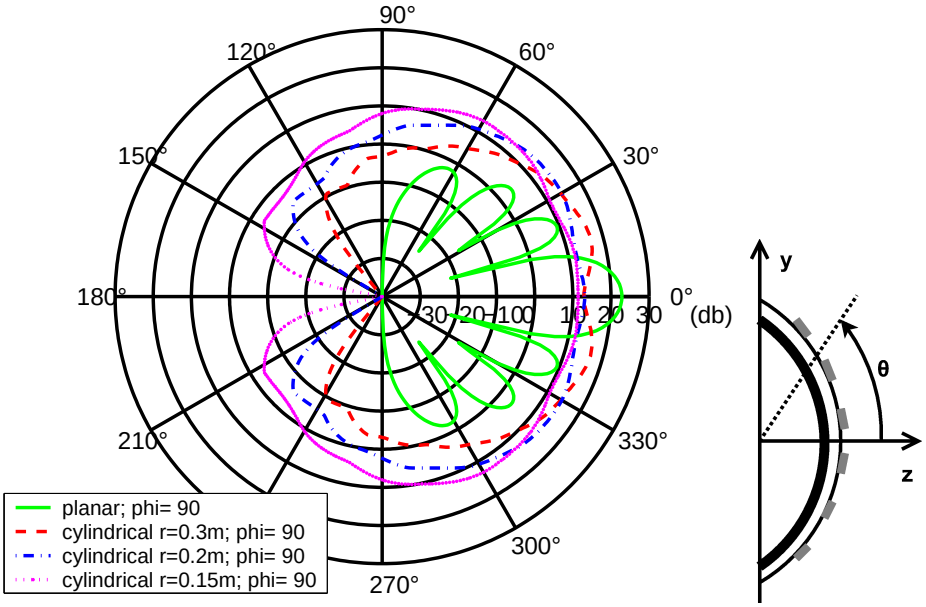

Figure 6.27 : *H-plane directivity of a* 8×8 *circular patch array on a cylindrical structure for different curvature levels- currents calculated with FDTD*

situation may occur, if for example the array of a telecommunication system must concentrate its radiation towards a transmitting station. Then, its main lobe must be shifted at a certain angle. The last example handles the pattern synthesis. For certain applications, for instance satellite-aircraft communication, it is necessary that the antenna array generates a very directive beam. Therefore, the input energy must be distributed in a way that a the biggest fraction of energy goes to the main beam and the rest on the side lobes. For it, the side lobes must be supressed.

It has to be added that in the following optimization simulations realised with the GA the number of iterations, this is the number of generations, is limited to a low value on purpose. This has been realized in order to observe the performance of the optimization method in time limiting and computation effort saving conditions.

6.3.1 Source decomposition with GA

The optimization case in this section consists in finding the complex excitation values of an array composed of 8×8 circular patch elements at the working frequency of $f = 2.4$GHz. The afore validated circular patch antenna is used as array element. The array elements are positioned equidistant with the spacing value of $d = 0.15\text{m} \approx 0.48\lambda_0$. The optimization case is run for an array mounted on a planar structure and then for an array on a cylinder. For both cases the GA simulates 50 generations for a population size of 16 members. Furthermore, the probabilistic constant have been defined like in the following: cross-over probability of 50%, mutation probability of 2.5% and 15bits for each value. Furthermore, the excitation amplitude values for the array elements are limited to the intervall $I_0 \in [10^{-5}, 1.0]$A and the excitation phase value to the intervall $\alpha \in [0^\circ, 360^\circ]$.

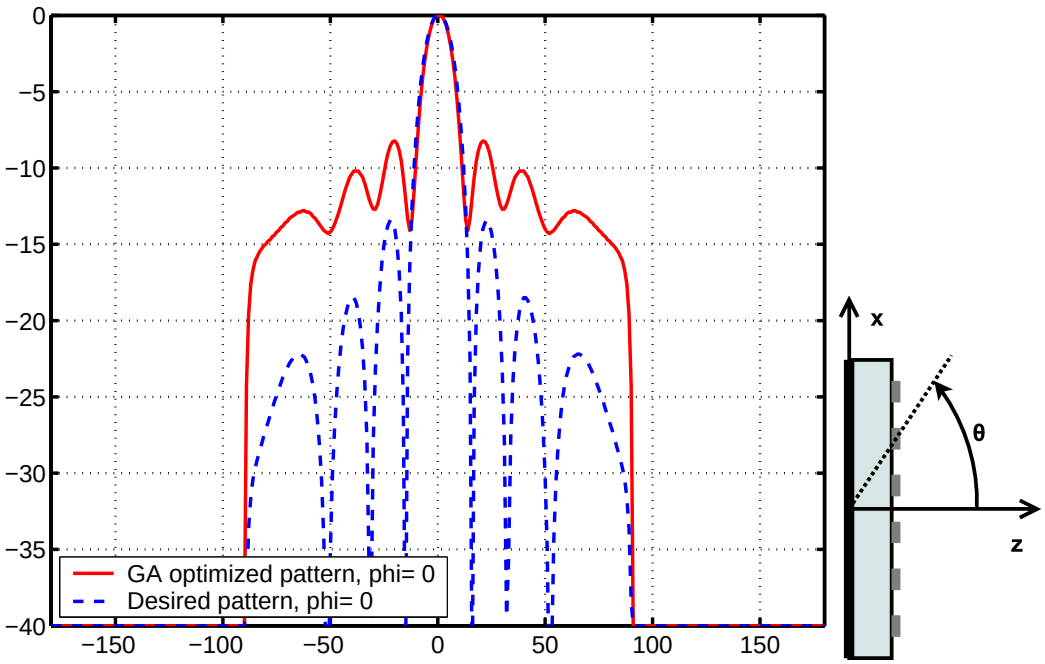

Figure 6.28 : *Source decomposition of a* 8×8 *circular patch array on a planar structure*

The radiation pattern of the conceived planar array for a uniform element excitation with the current amplitude value of $I_0 = 1\text{A}$ and current phase value of $\alpha = 0^\circ$ has been taken as the goal or mask pattern. Subsequently, the GA algorithm has been applied to approximate the excitation amplitude and phase in order to reconstruct the mask pattern. The results of this pattern synthesis is shown in figure 6.28. Therein, the E-plane of the mask pattern and of the reconstructed pattern are depicted. The error between the approximated and the sought pattern amounts to $\text{err} = 0.512$ after all generations. This value reflects mainly the error due to the amplitude difference between the calculated and the desired pattern.

Similar as for the latter planar array synthesis, the radiation pattern used as mask pattern is equivalent to the one generated by all uniformly fed elements with $I_0 = 1\text{A}$ and $\alpha = 0^\circ$. Furthermore, in this conformal source decomposition case, the cylindrical bearer is oriented in z-direction and it has a radius of $r_{cyl} = 0.2\text{m}$. According to the latter values and to the afore given examples, the curvature of the array is very strong. Consequently, a high error value is expected at the end of the generations. The results of this synthesis case are found in figure 6.29.

As expected, the error value is high, it amounts to $\text{err} = 1.7$ after all generations. Nevertheless, the GA optimization method arrives to find all minima and a slight different value for the main lobe amplitude even though the "critical" circumstances.

6.3.2 Phase synthesis with the genetic algorithm

The GA optimization approach has been tested on phase synthesis. For it, the pattern of the planar 8×8 array has been phase shifted causing the main beam to be at $\theta_0 = 60^\circ$. This has been

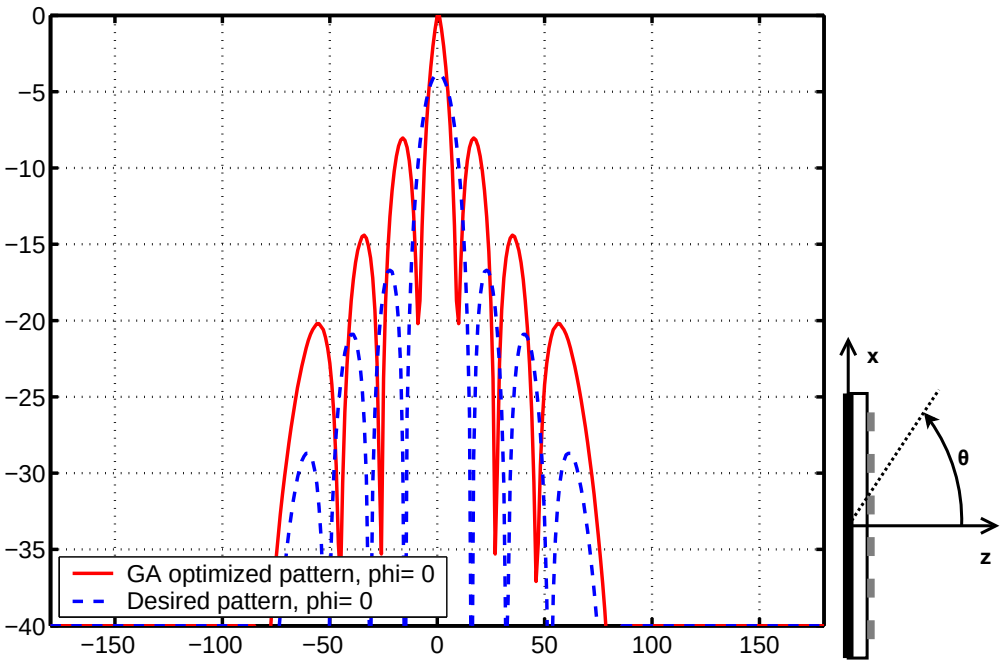

Figure 6.29 : *Source decomposition of a* 8×8 *circular patch array on a cylindrical structure,* $r_{cyl} = 0.2\text{m}$

performed by giving each array element a progressive phase shift of $\alpha = 155.88^\circ$. Concerning the excitation amplitude values, they have been maintained to the value of $I_0 = 1\text{A}$. The resulting radiation pattern for $f = 2.4\text{GHz}$ has been taken as mask pattern. The genetic algorithm has been applied in order to find the right excitations, so that the latter pattern is yielded with the planar array and with its conformal counterpart. The curved array has a cylindrical form with a radius of $r_{cyl} = 0.2\text{m}$. Both cases have been run with the same low number of iterations (50 generations with each generation having 16 members) in order to visualize the influence of the curvature on the optimization. Furthermore, the probabilistic constants have been defined as in the source decomposition example. This is, cross-over probability of 50%, mutation probability of 2.5% and 15bits for each value. In addition to that, the excitation phase values for the elements of the synthesized array have been limited to the intervall $\alpha \in [0^\circ, 360^\circ]$. Furthermore, their excitation amplitude values have been fixed to $I_0 = 1\text{A}$.

The first case performed is the phase synthesis for the 8×8 planar array. Figure 6.30 pictures the acquired E-plane radiation pattern with the GA optimization approach compared to the expected pattern function. The resulting pattern converges towards the desired pattern: the desired phase shift of the main lobes about $\theta_0 = 60^\circ$ have been reached. The error value after the optimization has a value of $\text{err} = 0.494$. This error reflects the differences between the pattern mask and the optimized pattern: it refers to the higher value of the side lobes, specially at $\phi = 0^\circ$, and to the smaller beamwidth.

The second case, the cylindrical case, has been realized similar as for the planar case: the pattern of the planar 8×8 array has been set as mask and the GA optimization algorithm has been applied in order to generate a similar radiation behaviour from the conformal 8×8 array.

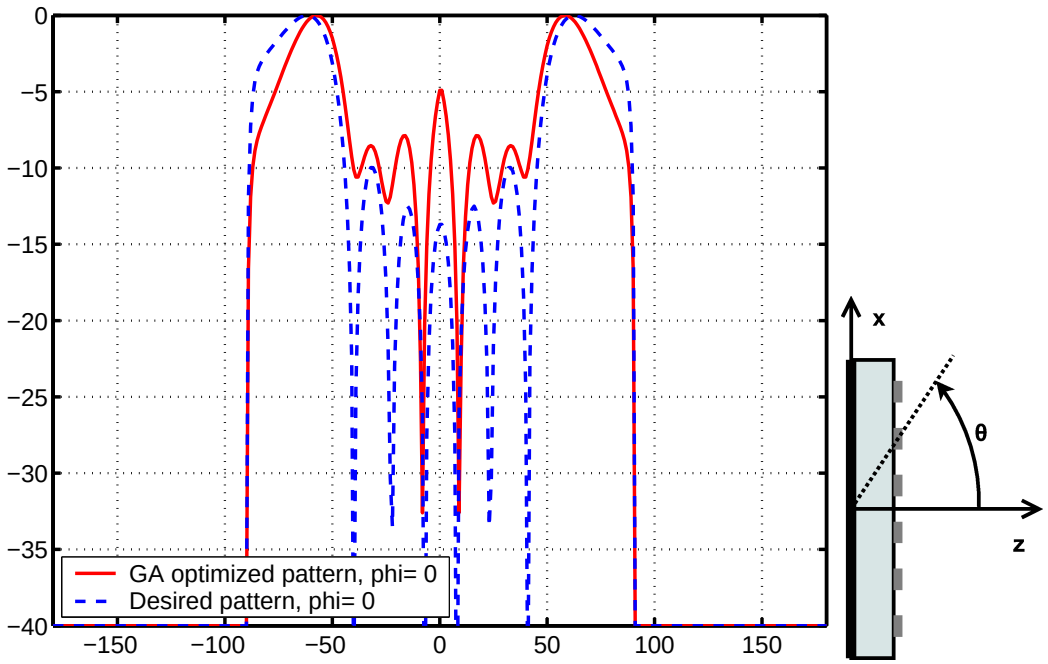

Figure 6.30 : *Phase synthesis of a* 8×8 *circular patch array on a planar structure*

The results are depicted in figure 6.31. Therein, the E-plane of the radiation pattern is plotted for different ϕ values. The yielded error value amounts to err $= 0.885$ after all generations. Since the optimization did not find the required excitation phases in order to attain the desired maxima, the error value is high. The calculated pattern shows respective lobes at the desired angles but these have a smaller amplitude in comparison to the lobe at $\phi = 0°$. This can be explained by the extreme curvature that does not allow all elements to contribute to the radiation in the desired direction. Consequently, the desired beam maxima at $\theta_0 = 60°$ is not reached. Nevertheless, the GA optimization approach "forces" the conformal array to generate lobes in the expected direction.

Furthermore, the reader may have noticed that though the low number of iterations the simulation results approximates the pattern mask, specially in the planar case.

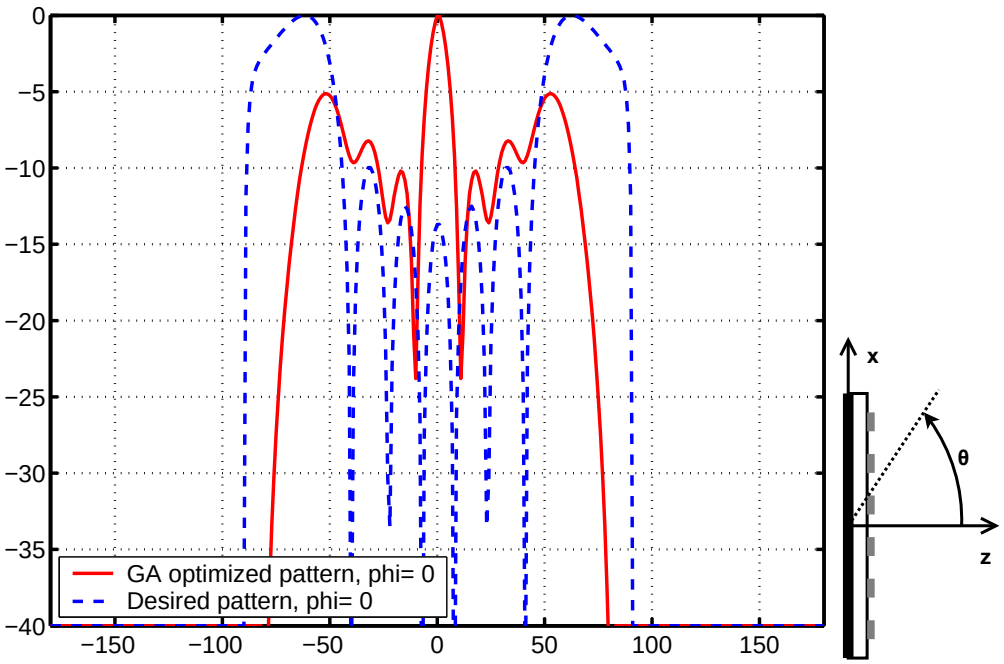

Figure 6.31 : *Phase synthesis of a* 8×8 *circular patch array on a cylindrical structure,* $r_{cyl} = 0.2\text{m}$

6.3.3 Pattern synthesis with the genetic algorithm

The last optimization cases concerns the pattern synthesis. Therefore, a pattern mask according to equation (5.6) of chapter 5 has been defined. The additional values that describe the latter cosinusoidal function are defined like in the following. The half-power beamwidth angle range is $\delta_{BW,\theta} = 20^\circ$ and the main beam angle range is given by $\delta_{MB} = 20^\circ$. The main beam is established to be in direction $(\theta_0, \phi_0) = (0^\circ, 45^\circ)$. Consequently, the main beam range limits are set to $\theta_a = -20^\circ$ and $\theta_b = 20^\circ$. In addition to the latter, the side lobe level has been set to $SLL_{dB} = 30.0\text{dB}$. The mask pattern function determines a certain shape for the beam and an amplitude value for the side lobes.

The GA optimization approach has been used in order to generate a radiation pattern with the characteristics of the pattern mask for a work frequency of $f = 2.4\text{GHz}$. Concerning the probabilistic variables, they have been established as in the latter validation cases (cross-over probability of 50%, mutation probability of 2.5% and 15bits for each value). Furthermore, the excitation phase values for the elements of the tested array have been limited to the intervall $\alpha \in [0^\circ, 360^\circ]$. In addition to that, their excitation amplitude values have been fixed to $I_0 = 1\text{A}$.

Consequently, the main beam of a planar array of 8×8 circular patch elements has been synthesized with the genetic algorithm. The results of this beam-shaping procedure are presented in figure 6.32. Therein, the plots of the pattern mask and of the synthesized pattern are compared. The reader may notice, that the desired beam shape has been nearby completely reached, specially concerning the half-power beamwidth. Nevertheless, the side lobe levels are still at certain small intervals of ϕ over the defined limit. This is recognized by the optimization approach and expressed by the error obtained at the end of the optimization procedure. Its value

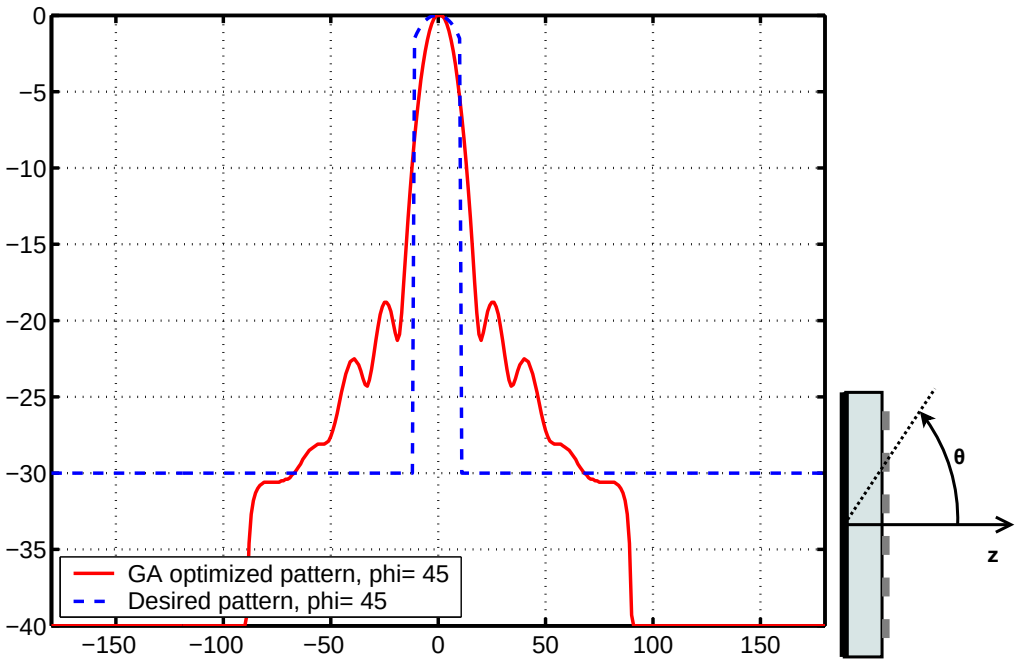

Figure 6.32 : *Pattern synthesis of a* 8×8 *circular patch array on a planar structure*

amounts to err $= 0.327$.

For the next pattern synthesis example, the GA optimization approach has been applied to a conformal antenna composed of 8×8 circular patch elements. As in the afore presented conformal examples, the conformal structure is equivalent to a cylinder of radius $r_{cyl} = 0.2$m. The pattern mask is the same as in the planar pattern synthesis example. The result of the calculated optimization is depicted in figure 6.33 and the produced error has a value of err $=$ 0.464. The computed beam converges toward the desired beam shape, specially concerning the half-power beamwidth, but the side lobe levels are at most parts of the ϕ values range over the desired limit. Consequently, the error obtained at the end of the optimization procedure is high-valued, namely err $= 0.465$.

If the planar pattern synthesis case is compared with the conformal counterpart, it can be said that the optimization of the planar array attains better the desired pattern shape than the cylindrical array. Nevertheless, it has to be added that the conformal array has a strong degree of curvature and therefore the approximation is reasonable.

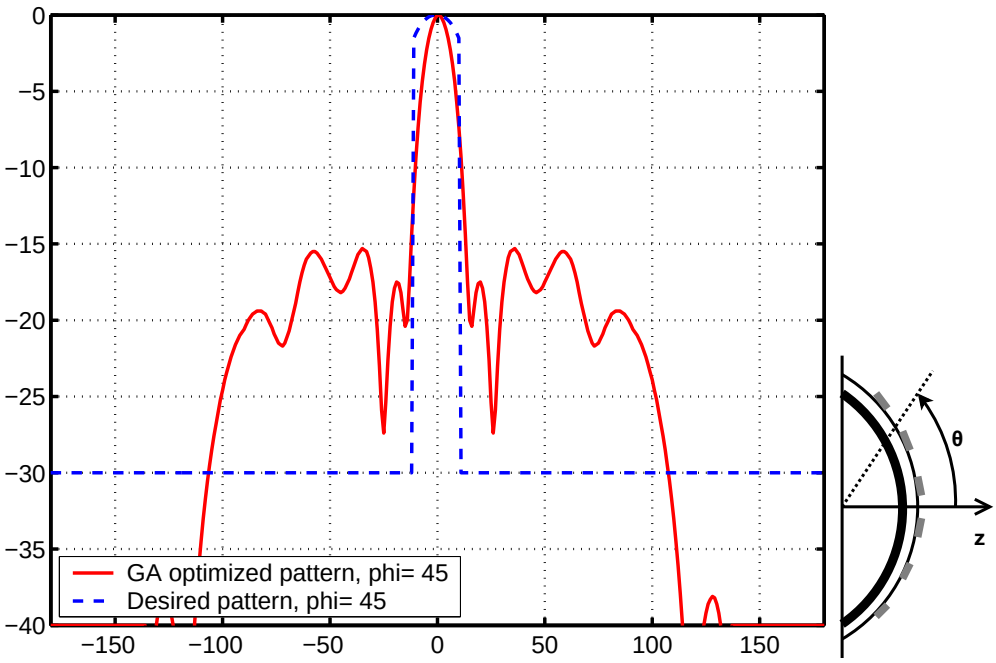

Figure 6.33 : *Pattern synthesis of a* 8×8 *circular patch array on a cylindrical structure,* $r_{cyl} =$ 0.2m

Conclusion

The presented thesis work gives the possibility to realize accurate and fast far field modelling and analysis of planar and conformal arrays in order to support in-depth electromagnetic compatibility analyses. Therefore, an approach for the analysis of arrays has been developed. This developed tool allows the handling of planar and conformal arrays composed of dipole elements or microstrip patch antennas. Due to the combination of the simple modelling approach, that uses equivalent sources with accurate numerical techniques applied to volume for the excitation values, this hybrid method allows the user to produce reliable results with less computational effort. With regard to complex array bearer shapes and large array dimensions, the latter possibility is a big advantage. Moreover, the inner current generator, that approximates the excitation currents with analytical formula and the cavity model, allows this tool to approximate the far field behaviour of antennas and arrays in an acceptable way. The possibility of introducing coupling and fringing effects by means of the currents is another important advantage of the developed analysis approach.

Furthermore, the developed optimization tool offers the possibility of persuing different studies concerning the development and conception of conformal antenna arrays in consideration of aircraft architecture and EMC related thresholds. The implemented pattern optimization approach allows to perform synthesis tasks of different kind. The advantage of the genetic algorithm based optimization tool is that it finds generally a global optimum solution for each synthesis task. Consequently, this synthesis tool generate reliable results. Furthermore, the robustness of a genetic algorithm gives the user the possibility to treat simple and complex synthesis cases. This characterizes this optimization tool as versatile. In addition to that, the implemented synthesis tool in the present work allows to introduce measured or reference data in order to use it as pattern mask. It also allows to define pattern masks that in general reflect the requirements or limitations concerning the far field behaviour of an antenna array.

The examples and cases presented in this thesis manuscript are more of general validating kind and therefore test studies using the developed modelling and analysis tool concerning different EMC applications are required. Besides that, there is the need of reducing computational effort in sophisticated EMC studies that handle the interaction between the antennas radiation characteristics and aircraft architecture. Here, the influence of aircraft structural parts, for instance of the fuselage, wings and/or fin, on the radiation performance of a radiating conformal array can be mentioned as an example. Therefore, the approaches conceived in the present thesis work would be appropiate for the modelling of the conformal arrays.

Moreover, the developed modelling method should be improved concerning the consideration of multilayered microstrip antennas. Therefore, different analyses on the dielectric multilayer effects should be performed. Furthermore, additional studies are required concerning the

mutual coupling effects for conformal arrays. Concerning array synthesis aspects, the performance of the implemented optimization tool should be tested in comparison to other synthesis methods, as for instance the iterative Least Squares approach.

The modelling, analysis and optimization tools presented and implemented in the present thesis work go well beyond of electromagnetic compatibility tasks. They can contribute also to the development of versatile modelling and analysis techniques for the different types of antenna systems. For instance, they can be basic modules for the modelling of finite large arrays.

Appendix A

Geometry Analysis

A.1 Vector transformation

A.1.1 Cartesian to spherical coordinates and vice versa

$$\begin{aligned} v_r &= v_x \sin\theta\cos\phi + v_y \sin\theta\sin\phi + v_z \cos\theta \\ v_\theta &= v_x \cos\theta\cos\phi + v_y \cos\theta\sin\phi - v_z \sin\theta \\ v_\phi &= -v_x \sin\phi + v_y \cos\phi \end{aligned}$$

$$\begin{aligned} v_x &= v_r \sin\theta\cos\phi + v_\theta \cos\theta\cos\phi - v_\phi \sin\phi \\ v_y &= v_r \sin\theta\sin\phi + v_\theta \cos\theta\sin\phi + v_\phi \cos\phi \\ v_z &= -v_r \cos\theta - v_\theta \sin\theta \end{aligned}$$

A.1.2 Cartesian to cylindrical and vice versa

$$\begin{aligned} v_\rho &= v_x \cos\phi + v_y \sin\phi \\ v_\phi &= -v_x \sin\phi + v_y \cos\phi \\ v_z &= v_z \end{aligned}$$

$$\begin{aligned} v_x &= v_\rho \cos\phi - v_\phi \sin\phi \\ v_y &= v_\rho \sin\phi + v_\phi \cos\phi \\ v_z &= v_z \end{aligned}$$

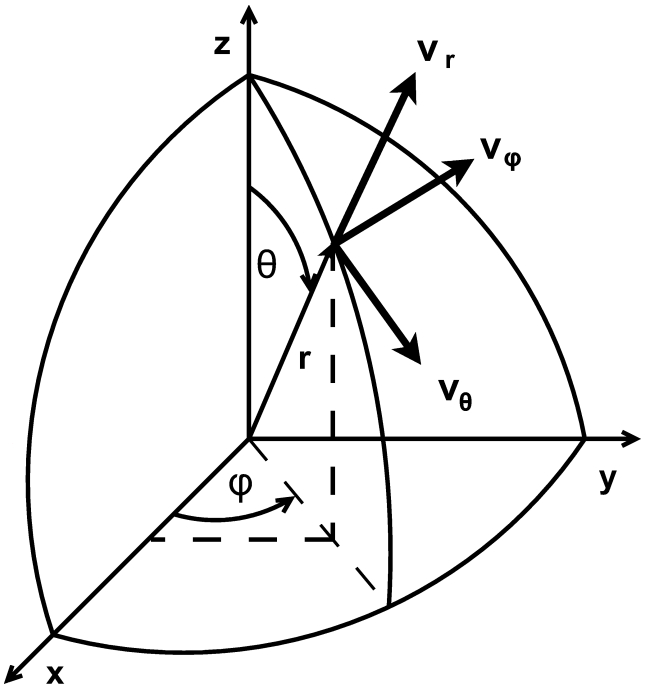

Figure A.1 : *Spherical coordinate system*

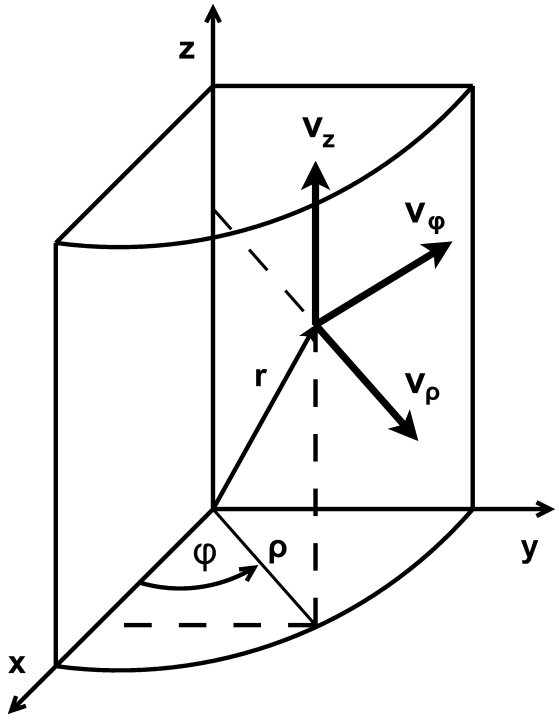

Figure A.2 : *Cylindrical coordinate system*

A.1.3 Cylindrical to spherical and vice versa

$$\begin{aligned} v_r &= v_\rho \sin\theta + v_z \cos\theta \\ v_\theta &= v_\rho \cos\theta - v_z \sin\theta \\ v_\phi &= v_\phi \end{aligned}$$

$$\begin{aligned} v_\rho &= v_r \sin\theta + v_\theta \cos\theta \\ v_\phi &= v_\phi \\ v_z &= v_r \cos\theta - v_\theta \sin\theta \end{aligned}$$

A.2 Spatial Rotation

The rotation function uses the longitudinal axis of the cylinder as reference line in order to shift the desired point by a certain angle without changing the distance between the new point and reference line.

$$\delta(\vec{x}) = (1-\cos\zeta)\vec{a}\vec{x}\cdot\vec{a} + \cos\zeta\cdot\vec{x} + \sin\zeta\cdot(\vec{a}\times\vec{x})$$

$$M(\delta) = (1-\cos\zeta)\cdot\begin{pmatrix} a^2 & ab & ac \\ ab & b^2 & bc \\ ac & bc & c^2 \end{pmatrix} + \cos\zeta\cdot\begin{pmatrix} 1 & 0 & 0 \\ 0 & 1 & 0 \\ 0 & 0 & 1 \end{pmatrix} + \sin\zeta\cdot\begin{pmatrix} 0 & -c & b \\ c & 0 & -a \\ -b & a & 0 \end{pmatrix}$$

A.3 Tangent plane of a surface at a certain point

The mathematical function of the surface is esential for the calculation of the tangent plane normal vector. It has to be known and it has to be differentiable. Depending on the form of the function, it can be in a vectorial form or in form of a scalar equation, the searched vector is calculated with three different solutions. In this work the surface function is supposed to have the following explicit form

$$z = f(x,y) \tag{A.1}$$

The respective method for calculating the tangent plane normal vector uses partial derivation on the surface function $f(x,y,z)$ in order to obtain the normal vector components at the point (x_0,y_0,z_0). The following equation shows which of the partial derivations or gradients are necessary to obtain the desired vector.

$$\vec{n} = (\nabla\cdot f)|_{(x_0,y_0,z_0)} = (\frac{\partial f(x_0,y_0,z_0)}{\partial x}, \frac{\partial f(x_0,y_0,z_0)}{\partial y}, \frac{\partial f(x_0,y_0,z_0)}{\partial z}) \tag{A.2}$$

Furthermore, the following mathematical definition of finite differences can be applied in order to approximate the partial derivatives. This is

$$\frac{\partial f(x_0,y_0,z_0)}{\partial x} = \lim_{h\to 0}\frac{f(x_0+h,y_0,z_0)-f(x_0,y_0,z_0)}{h} \tag{A.3}$$

$$\frac{\partial f(x_0,y_0,z_0)}{\partial y} = \lim_{h\to 0}\frac{f(x_0,y_0+h,z_0)-f(x_0,y_0,z_0)}{h} \tag{A.4}$$

$$\frac{\partial f(x_0,y_0,z_0)}{\partial z} = \lim_{h\to 0}\frac{f(x_0,y_0,z_0+h)-f(x_0,y_0,z_0)}{h} \tag{A.5}$$

wherein h is the infinitesimal variation around the values x_0, y_0 or z_0, respectively. This variation can be approximated by a very small value and hence the accuracy of the partial derivatives depends on how small the value is.

A.4 Vectorial inner product - Angle enclosed by two vectors

$$\vec{a}\cdot\vec{b} = \begin{pmatrix} a_1 \\ a_2 \\ a_3 \end{pmatrix} \cdot \begin{pmatrix} b_1 \\ b_2 \\ b_3 \end{pmatrix} = a_1b_1 + a_2b_2 + a_3b_3$$

$$\cos\angle(\vec{a},\vec{b}) = \frac{\vec{a}\cdot\vec{b}}{|\vec{a}|\cdot|\vec{b}|}$$

A.5 Vectorial cross product

$$\vec{a}\times\vec{b} = \begin{pmatrix} a_1 \\ a_2 \\ a_3 \end{pmatrix} \times \begin{pmatrix} b_1 \\ b_2 \\ b_3 \end{pmatrix} = \begin{pmatrix} a_2b_3 - a_3b_2 \\ a_3b_1 - a_1b_3 \\ a_1b_2 - a_2b_1 \end{pmatrix}$$

$$|\vec{a}\times\vec{b}| = |\vec{a}|\cdot|\vec{b}|\cdot\sin\angle(\vec{a},\vec{b})$$

A.6 Equation of a plane

The latter one is one of the axes vectors of the general coordinate system. The resulting vector is one orthonormal vector that is multiplied with the normal vector again to obtain a second orthonormal one.

$$\vec{x} = \vec{a} + r\cdot\vec{b} + s\cdot\vec{c} \qquad r,s \in \mathbf{R} \tag{A.6}$$

Appendix B

Field Analysis

B.1 Curl and Divergence Theorems

$$
\begin{aligned}
\nabla\cdot(\nabla\times\vec{A}) &= 0\\
\nabla\times\nabla\Psi &= 0\\
\nabla(\Phi+\Psi) &= \nabla\Phi+\nabla\Psi\\
\nabla(\Phi\Psi) &= \Phi\nabla\Psi+\Psi\nabla\Phi\\
\nabla\cdot(\vec{A}+\vec{B}) &= \nabla\cdot\vec{A}+\nabla\cdot\vec{B}\\
\nabla\times(\vec{A}+\vec{B}) &= \nabla\times\vec{A}+\nabla\times\vec{B}\\
\nabla\cdot(\Psi\vec{A}) &= \vec{A}\cdot\nabla\Psi+\Psi\nabla\cdot\vec{A}\\
\nabla\times(\Psi\vec{A}) &= \nabla\Psi\times\vec{A}+\Psi\nabla\times\vec{A}\\
\nabla(\vec{A}\cdot\vec{B}) &= (\vec{A}\cdot\nabla)\vec{B}+(\vec{B}\cdot\nabla)\vec{A}+\vec{A}\times(\nabla\times\vec{B})+\vec{B}\times(\nabla\times\vec{A})\\
\nabla\cdot(\vec{A}\times\vec{B}) &= \vec{B}\cdot\nabla\times\vec{A}-\vec{A}\cdot\nabla\times\vec{B}\\
\nabla\times(\vec{A}\times\vec{B}) &= \vec{A}\nabla\cdot\vec{B}-\vec{B}\nabla\cdot\vec{A}+(\vec{B}\cdot\nabla)\vec{A}-(\vec{A}\cdot\nabla)\vec{B}\\
\nabla\times\nabla\times\vec{A} &= \nabla(\nabla\cdot\vec{A})-\nabla^2\vec{A}
\end{aligned}
$$

B.2 Green's theorems

In Mathematics the statements due to a symmetrical behaviour of two functions are called Green's theorems. These mathematical reprocity theorems exist for scalar as well as for vectorial functions.

The Green's theorem applied to scalars is based on the following mathematical identity wherein ψ and ϕ are scalar functions

$$\nabla\cdot(\Psi\nabla\Phi)=\Psi\nabla^2\Phi+\nabla\Psi\cdot\nabla\Phi \tag{B.1}$$

We obtain *Green's first idendity for scalar functions* shown in B.2 by integrating the last equation throughout a region and applying the divergence theorem on the equation's left side

$$\oiint\Psi\frac{\partial\Phi}{\partial n}ds=\iiint(\Psi\nabla^2\Phi+\nabla\Psi\cdot\nabla\Phi)d\tau \tag{B.2}$$

If we interchange the functions Ψ and Φ in the last statement and subtract the consequently altered equation with the original one, we obtain *Green's second idendity for scalar functions* or mainly known as *Green's theorem*, which is shown in the following

$$\oiint \left(\Psi \frac{\partial \Phi}{\partial n} - \Phi \frac{\partial \Psi}{\partial n} \right) ds = \iiint (\Psi \nabla^2 \Phi - \Phi \nabla^2 \Psi) d\tau \tag{B.3}$$

Analogue to the scalar case, the Green's theorem for vectorial functions is based on the following identity, wherein $\vec{A}$ and $\vec{B}$ are vector field functions

$$\nabla \cdot (\vec{A} \times \nabla \times \vec{B}) = \nabla \times \vec{A} \cdot \nabla \times \vec{B} - \vec{A} \cdot \nabla \times \nabla \times \vec{B} \tag{B.4}$$

In the same way as for the scalar case, an integration throughout a region and the application of the divergence theorem is done. These modifications yield to *Green's first idendity for vector functions* shown in the following

$$\oiint (\vec{A} \times \nabla \times \vec{B}) \cdot ds = \iiint (\nabla \times \vec{A} \cdot \nabla \times \vec{B} - \vec{A} \cdot \nabla \times \nabla \times \vec{B}) d\tau \tag{B.5}$$

Finally, *Green's second idendity for scalar functions* is obtained by interchanging the vector fields $\vec{A}$ and $\vec{B}$ and subtracting the resulting equation from the original one. This identity is also known as the *vector Green's theorem* and it is represented by the following equation

$$\oiint (\vec{A} \times \nabla \times \vec{B} - \vec{B} \times \nabla \times \vec{A}) \cdot ds = \iiint (\vec{B} \cdot \nabla \times \nabla \times \vec{A} - \vec{A} \cdot \nabla \times \nabla \times \vec{B}) d\tau \tag{B.6}$$

B.3 Functional inner product and linearity

inner product for functions

$$\langle f, g \rangle = \int f(t) g(t) dt \tag{B.7}$$

linearity

$$\langle f, g \rangle = \langle g, f \rangle \tag{B.8}$$

$$\langle \alpha f + \beta g, h \rangle = \alpha \langle f, h \rangle + \beta \langle g, h \rangle \tag{B.9}$$

positive definite

$$\langle f^*, f \rangle \begin{cases} > 0 & \text{if} \quad f \neq 0 \\ = 0 & \text{if} \quad f = 0 \end{cases} \tag{B.10}$$

adjoint operator

$$\langle L f, g \rangle = \langle L_a g, f \rangle \tag{B.11}$$

inverse operator

$$f = L^{-1}(g) \tag{B.12}$$

positive definite operator

$$\langle f^*, Lf \rangle > 0 \tag{B.13}$$

B.4 Finite Differences

The function $F(x)$ at the space point $x_i + h$ is approximated with the help of a *Taylor series* about the space point x_i taking in account the difference h. Due to the fact that the components of the series with a grade higher than the second grade are very small, they can be neglected. Thus the function can be represented as follows

$$F(x_i + h) = F(x_i) + h \left.\frac{\partial F(x)}{\partial x}\right|_{x_i} + \frac{h^2}{2} \left.\frac{\partial^2 F(x)}{\partial x^2}\right|_{x_i} + o(h^3) \tag{B.14}$$

In the latter equation, the approximation of the function refering to its spatial dependency is shown. Concerning the time variable of the function: the same approximation is performed in the algorithm. Consequently, the function F can be

$$F(x) = \frac{1}{2}[F(x + \frac{\Delta x}{2}) + F(x - \frac{\Delta x}{2})] + o(\Delta x) \tag{B.15}$$

$$\begin{aligned}
\frac{\partial^2 F(x)}{\partial x^2} &= \frac{F(x + \frac{\Delta x}{2}) + F(x - \frac{\Delta x}{2}) - 2F(x)}{\Delta x^2} && \text{(B.16)} \\
&\approx \frac{1}{\Delta x^2}\left[F(x + \frac{\Delta x}{2}) + F(x - \frac{\Delta x}{2}) - 2\frac{F(x + \frac{\Delta x}{2}) + F(x - \frac{\Delta x}{2})}{2}\right] + o(\Delta x^3) && \text{(B.17)} \\
&\approx 0 && \text{(B.18)}
\end{aligned}$$

$$F(x) = \frac{1}{2}[F(x + \frac{\Delta x}{2}) + F(x - \frac{\Delta x}{2})] + \Delta x \frac{F(x + \frac{\Delta x}{2}) - F(x)}{\Delta x} + o(\Delta x^3) \tag{B.19}$$

B.4.1 Leapfrog algorithm

The leapfrog algorithm is a modified version of the *Verlet algorithm*. The Verlet algorithm uses the positions and accelerations at the time t and the positions at the time $t - \Delta t$ to predict the positions at the time $t + \Delta t$, where Δt is the integration step. The leapfrog algorithm is computationally less expensive than other approaches, for example the Predictor-Corrector, and requires less storage. This is an important advantage in the case of large scale calculations. Moreover, the conservation of energy is respected, even at large time steps. Therefore, the computation time can be greatly decreased, if this algorithm is used. However, it has its limits, if more accurate velocities and positions are needed.

Appendix C

Simulation Results Dipoles

C.1 Simulation of different dipoles

C.1.1 Radiation pattern of different finite length dipoles

The following diagrams give the graphical description of the radiation behaviour several dipoles analysed in the present thesis work.

In addition to the latter, the radiation patter in azimuth, which is the same for the z-directed dipole of different length, is depicted in figure C.3

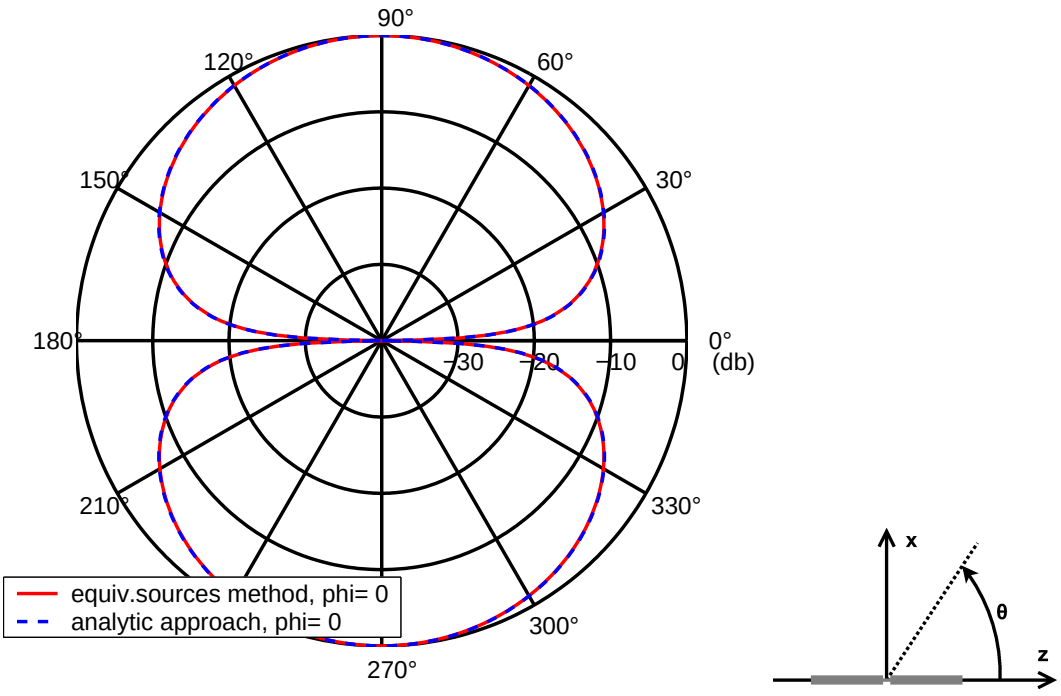

Figure C.1 : *Pattern comparison for a* $\frac{1}{4}\lambda$ *dipole in elevation*

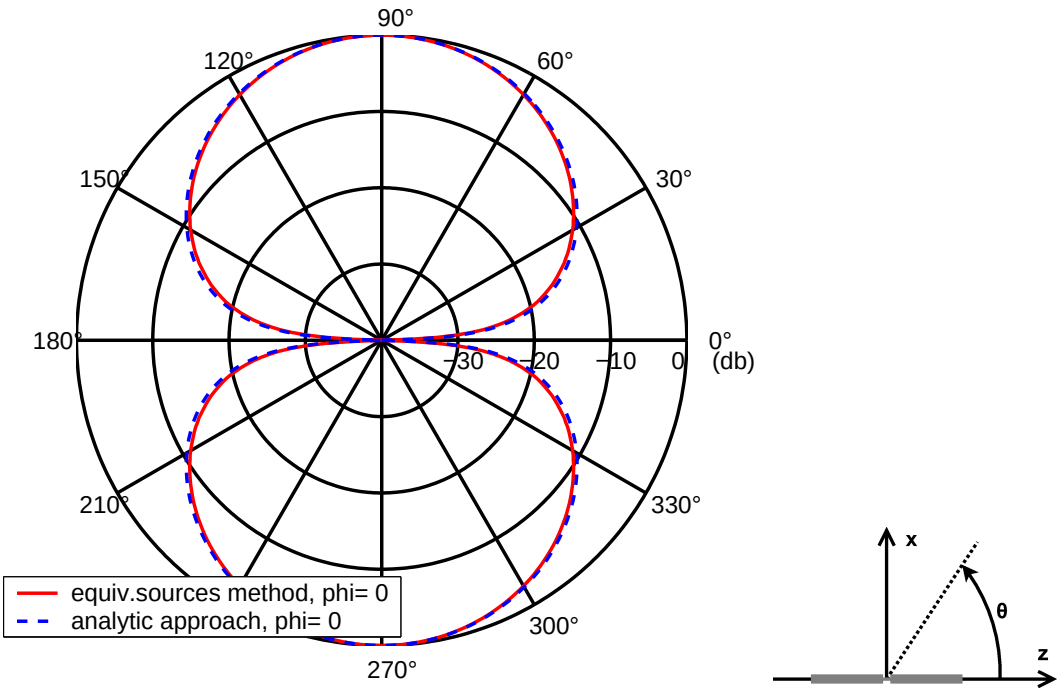

Figure C.2 : *Pattern comparison for a* $\frac{3}{4}\lambda$ *dipole in elevation*

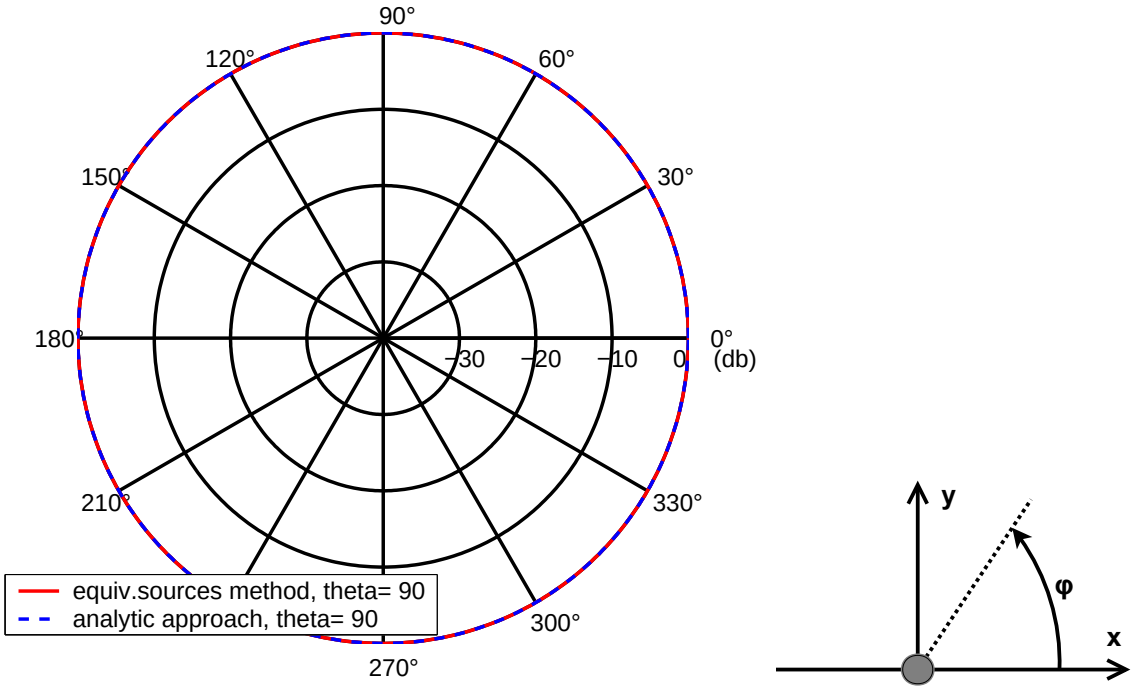

Figure C.3 : *Pattern comparison for a* $\frac{\lambda}{2}$ *dipole in azimuth*

C.1.2 Radiation pattern of arrays of elementary dipoles

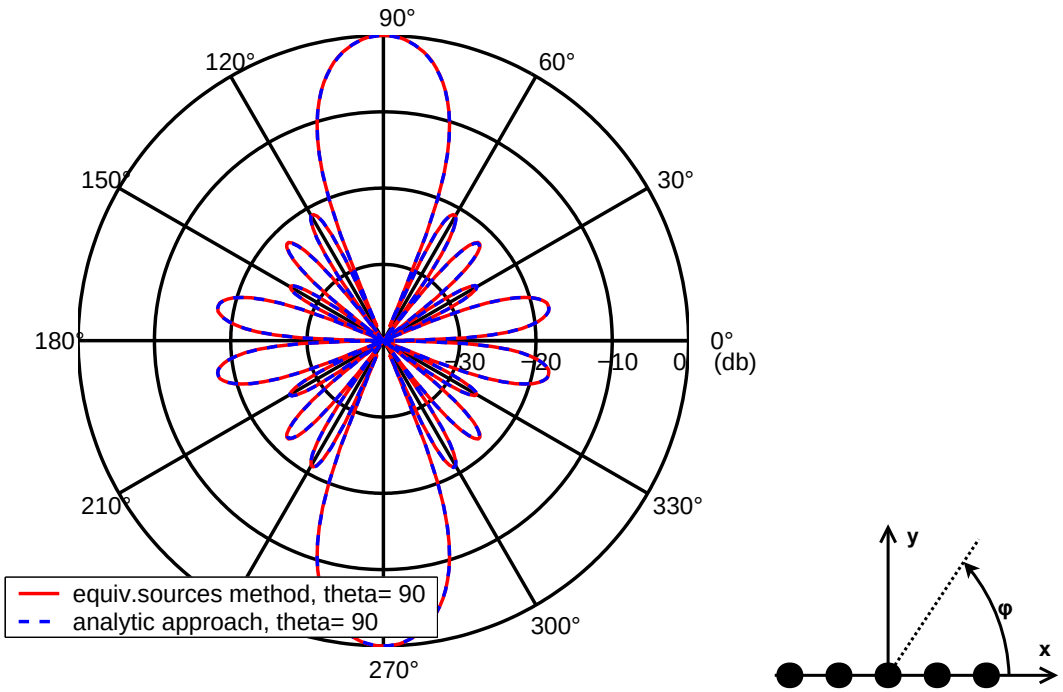

Figure C.4 : *Pattern comparison for a* 5×5 *array of* $\frac{\lambda}{10}$ *dipoles in azimuth*

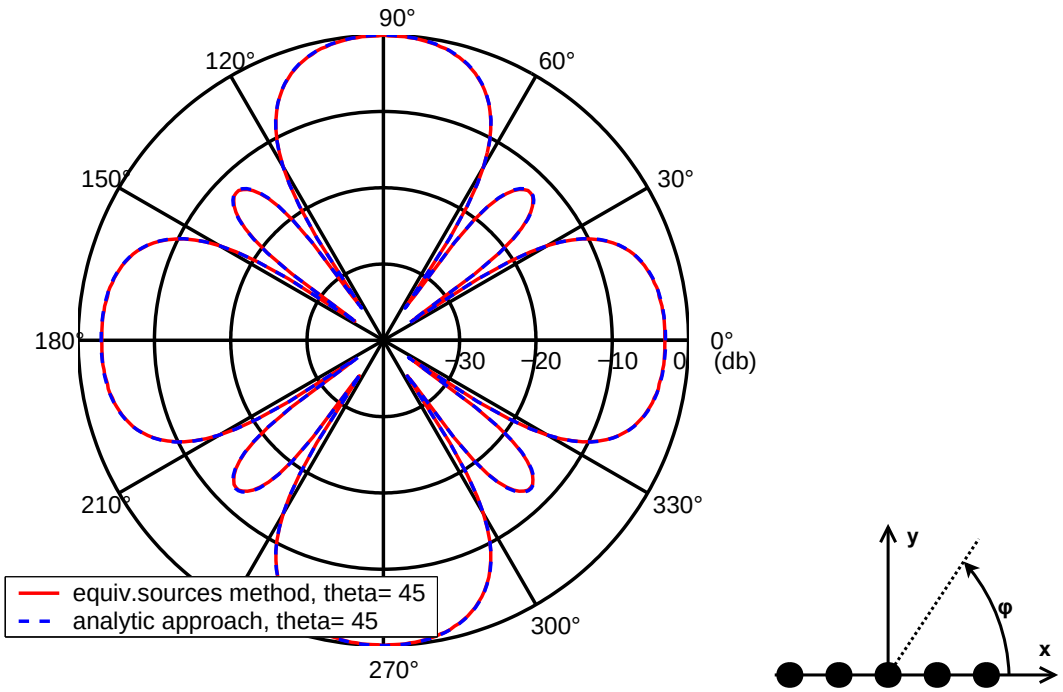

Figure C.5 : *Pattern comparison for a* 5×5 *array of* $\frac{\lambda}{10}$ *dipoles in azimuth*

Appendix D

Simulation Results Patch Antennas

D.1 Simulation of different patch antennas

The directivity and radiation patterns in the next figures describe the radiation behaviour in elevation and azimuth for a patch antenna with a dielectric permittivity $\varepsilon_r = 2.0$. As in the afore given examples, the plot lines for analytical formula approach and the method conceived in the present thesis work are pictured.

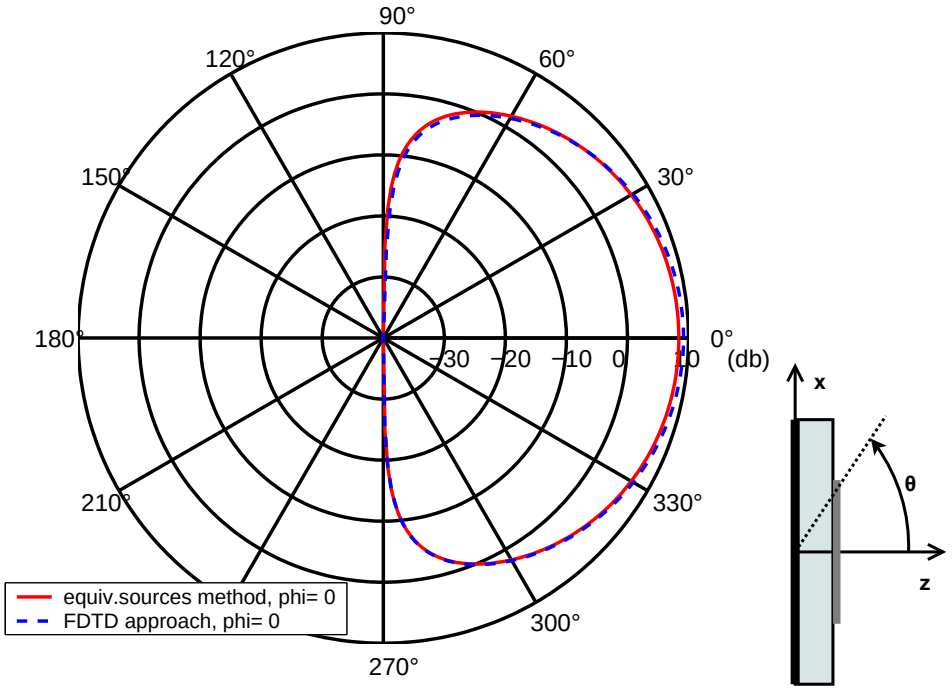

Figure D.1 : *E-plane directivity of a rectangular patch antenna - currents calculated with cavity model*

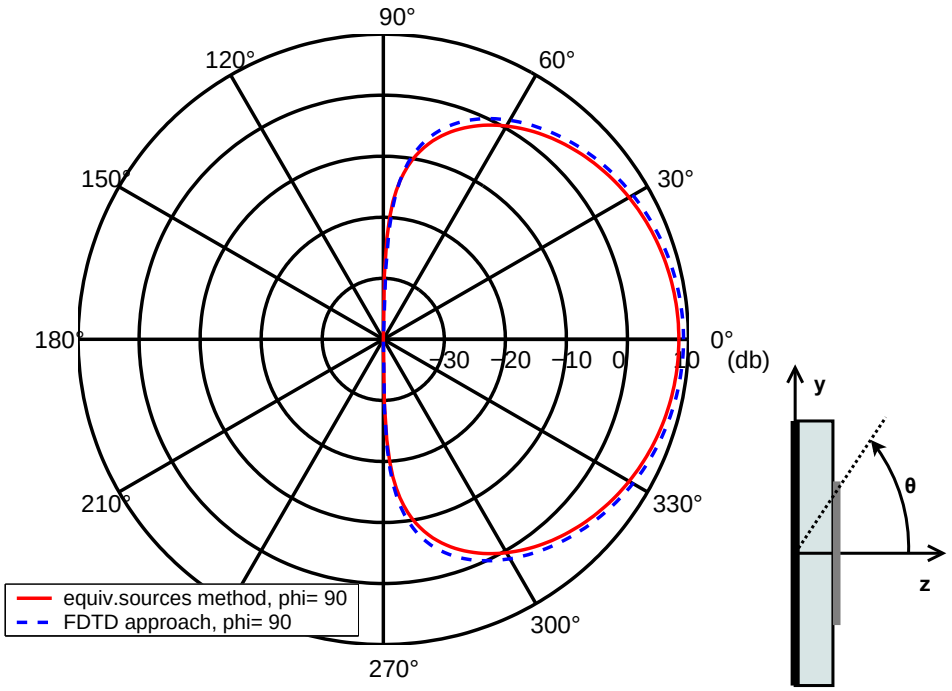

Figure D.2 : *H-plane directivity of a rectangular patch antenna - currents calculated with cavity model*

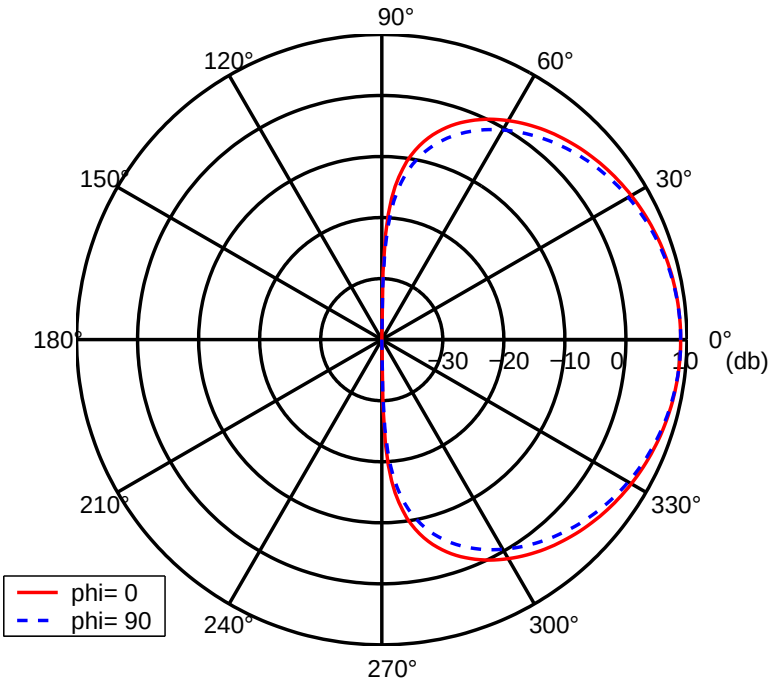

Figure D.3 : *Directivity of a rectangular patch antenna in E- and H-plane - currents calculated with FDTD*

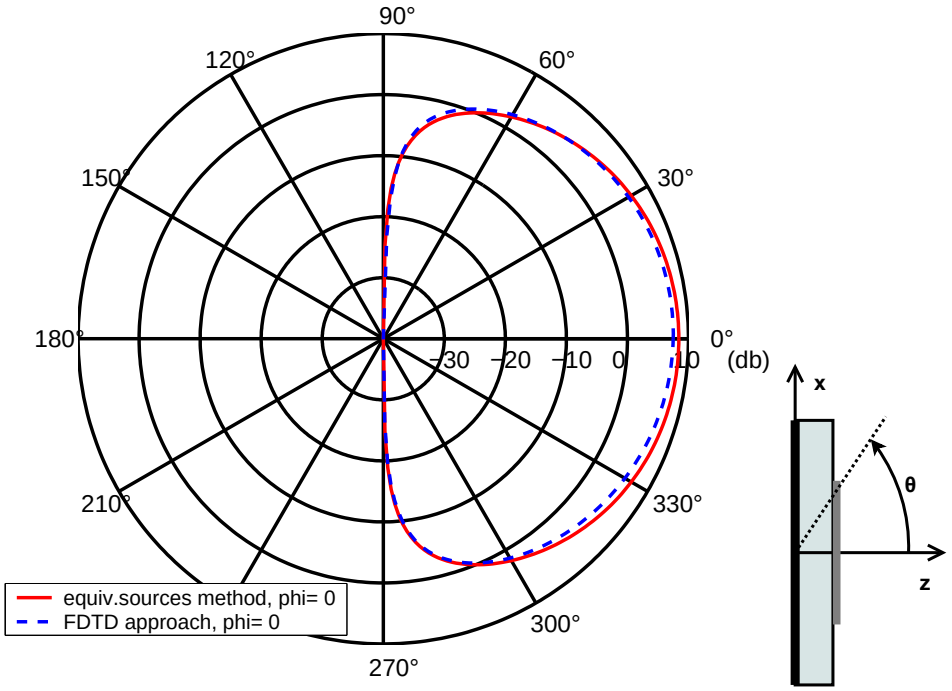

Figure D.4 : *E-plane directivity of circular patch antenna - currents calculated with cavity model*

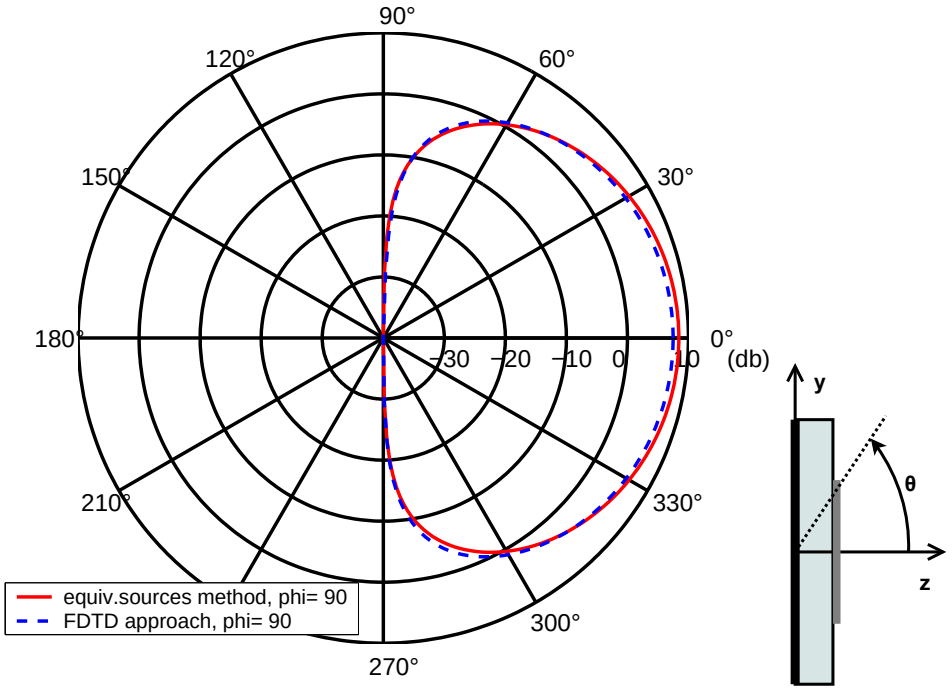

Figure D.5 : *H-plane directivity of circular patch antenna - currents calculated with cavity model*

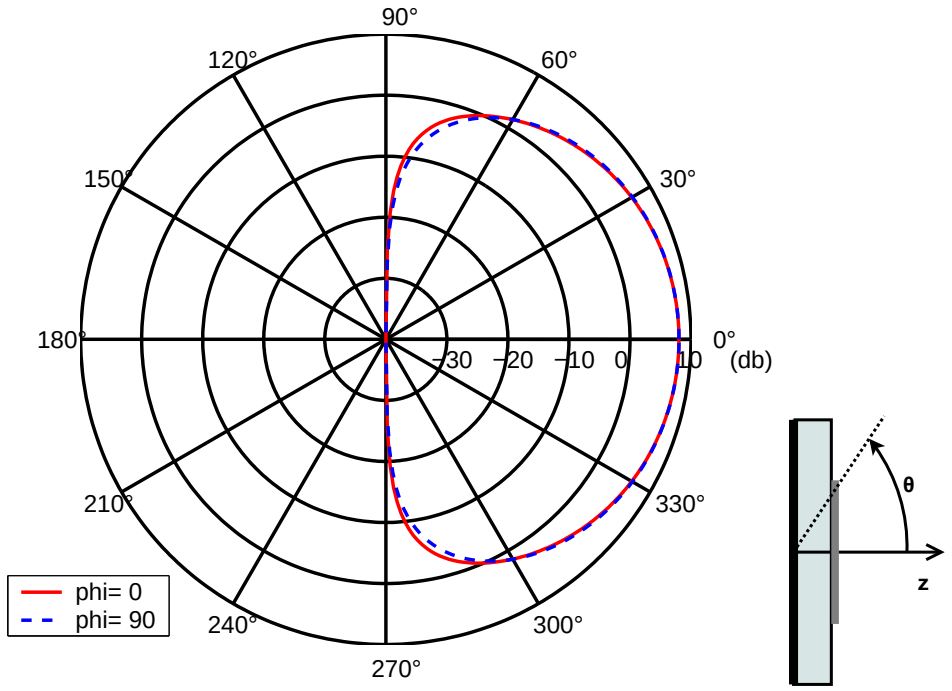

Figure D.6 : *Directivity of a of circular patch antenna in E- and H-plane - currents calculated with FDTD*

Bibliography

[1] C. A. Balanis, Antenna theory: Analisis and Design, *John Wiley & Sons, Inc.*, 2nd Ed., 1997

[2] C. A. Balanis, Advanced Engineering Electromagnetics, *John Wiley & Sons, Inc.*, 1989

[3] R. F. Harrington, Time-harmonic Eletromagnetic Fields, *McGraw-Hill, Inc.*, 1961

[4] R. F. Harrington, Field Computation by Moment Methods, *IEEE PRESS*, 1993

[5] A. Taflove, S. C. Hagness, Computational Electrodynamics: The Finite-Difference Time-Domain Method, *Artech House, Inc.*, 3rd Edition, 2005

[6] R. J. Mailloux, Phased Array Antenna Handbook, *Artech House, Inc.*, 2nd Edition, 2005

[7] I. J. Bahl, P. Bhartia, Microstrip Antennas, *Artech House, Inc.*, 1980

[8] S. J. Orfanidis, Electromagnetic Waves and Antennas, *Rutgers University*, 2007

[9] B.D. Steinberg, Principles of Aperture and Arrays System Design including Random and Adaptive Arrays, *John Wiley & Sons, Inc.*, 1976

[10] J-F. Zürcher, F. E. Gardiol, Broadband Patch Antennas, *Artech House, Inc.*, 1995

[11] R. Moini-Mazandarani, Analyse de l'influence des ondes de surface sur les caracteristiques des antennes microruban, *Faculte de Sciences, Universite de Limoges*, PhD Thesis, 1988

[12] A. Herschlein, Entwicklung numerischer Verfahren zur Feldberechnung konformer Antennen auf Oberflächen oberer Ordnung, *Institut für Hochfrequenztechnik und Elektronik, Universität Karlsruhe*, PhD Thesis, 2002

[13] C. Guiffaut, Contribution a la methode FDTD pour l'etude d'antennes et de la diffraction d'objects enfouis, *Universite Rennes I*, PhD Thesis, 2000

[14] W. Wiesbeck, M. Younis, J. von Hagen, Introduction to microstrip antennas, *Institut für Hochfrequenztechnik und Elektronik, Universität Karlsruhe*, Lecture notes, 2001.

[15] W. Wiesbeck, A. Herschlein, D. Löffler, C. Fischer, Antennen und Antennensysteme, *Institut für Hochfrequenztechnik und Elektronik, Universität Karlsruhe*, Lecture notes, 2000

[16] W. Wiesbeck, R. Schertlen, J. Haala, Hochfrequenztechnik, *Institut für Hochfrequenztechnik und Elektronik, Universität Karlsruhe*, Lecture notes, 2000

[17] W. Wiesbeck, Grundlagen der Hochfrequenztechnik, *Institut für Hochfrequenztechnik und Elektronik, Universität Karlsruhe*, Lecture notes, 5th Edition, 1999

[18] N. Geng, Plannungsmethoden für die Mobile Funkkommunikation, *Institut für Hochfrequenztechnik und Elektronik, Universität Karlsruhe*, Lecture notes, 1996

[19] I.V. Lindel, Huygens' Principle in Electromagnetics, *Proceedings - Science, Measurement and Technology*, IEE 1996, Vol. 143, Nro. 2

[20] D. R. Jackson, W. F. Richards, A. Ali-Khan, Series Expansions for the Mutual Coupling in Microstrip Patch Arrays, *Transactions on Antennas and Propagation*, IEEE 1989, Vol. 37, Nro. 3

[21] A. J. Sangster, R. T. Jacobs, Mutual Coupling in Conformal Microstrip Patch Antenna Arrays, *Proceedings in Microwaves, Antennas and Propagation*, IEE 2003, Vol. 150, Nro. 4

[22] B.M. Notaros, B.D. Popovic, J.P. Weem, R. A. Brown, Z. Popovic, Efficient Large-Domain MoM Solutions to Electrically Large Practical EM Problems, *Transactions on Microwave Theory and Techniques*, IEEE 2001, Vol. 49, Nro. 1

[23] B.R. Piper, M.E. Bialkowski, Electromagnetic Modeling of Conformal Wideband and Multi-Band Patch Antennas by Bridging a Solid-Object Modeler with MoM Software, *Antennas and Propagation Magazine*, IEEE 2004, Vol. 46, Nro. 5

[24] K.S. Yee, Numerical Solution to Initial Boundary Value Problems Involving Maxwell's Equations in Isotropic Media, *Transactions on Antennas and Propagation*, IEEE 1966, Vol. AP-14, pp. 302-307

[25] R. Holland, V. P. Cable, L. C. Wilson, Finite Volume Time-Domain (FVTD) Techniques for EM Scattering, *Transactions on Electromagnetic Compatibility*, IEEE 1991, Vol. 33, Nro. 4

[26] A. Reineix, B. Jecko, Analysis of Microstrip Patch Antennas Using Finite Difference Time Domain Method, *Transactions on Antennas and Propagation*, IEEE 1989, Vol. 37, Nro. 11

[27] T. Kashiwa, T. Onishi, I. Fukai, Analysis of Microstrip Antennas on a Curved Surface Using the Conformal Grids FDTD Method, *Transactions on Antennas and Propagation*, IEEE 1994, Vol. 42, Nro. 3

[28] T. Weiland, A discretization method for the solution of Maxwell's equations for six-component Fields, *Electronics and Communications*, AEÜ 1977, Vol. 31, Nro. 3, pp. 116-120

[29] M. Clemens, T. Weiland, Discrete Electromagnetism with the Finite Integration Technique, *Journal of Electromagnetic Waves and Propagation - Progress In Electromagnetics Research*, 2001, PIER 32, pp. 65-87

[30] R. Schuhman, T. Weiland Conservation of Discrete Energy and Related Laws in the Finite Integration Technique, *Journal of Electromagnetic Waves and Propagation - Progress In Electromagnetics Research*, 2001, PIER 32, pp. 301-316

[31] R. Ehmann, S. Gutschling, B. Trapp, T. Weiland, Numerical Modelling of Mobile Phone Equipment, *Proceedings of the 14th International Wroclaw Symposium and Exhibition on Electromagnetic Compatibility*, EMC 1998, pp. 334-338

[32] B. Krietenstein, R. Schuhmann, P. Thoma, T. Weiland, The Perfect Boundary Approximation Technique facing the big challenge of High Precission Field Computation, *Proceedings of the XIX International Linear Accelerator Conference*, LINAC 1998, pp. 860-862

[33] J-M. Jin, J. L. Volakis, J. D. Collins, A Finite-Element-Boundary-Integral Method for Scattering and Radiation by Two- and Three-Dimensional Structures, *Antennas and Propagation Magazine*, IEEE 1991, Vol. 33, Nro. 3

[34] J. Gong, J. L. Volakis, A. C. Woo, H. T. G. Wang, A Hybrid Finite Element-Boundary Integral for the Analysis of Cavity Backed Antennas of Arbitrary Shape, *Final Report for NASA Project*, University of Michigan, 1993

[35] T. F. Eiber, J. L. Volakis, Adaptive Integral Method for Hybrid FE-BI Modelling of 3-D Doubly Periodic Structures, *Proceedings in Microwaves, Antennas and Propagation*, IEE 1999, Vol. 146, Nro. 1

[36] R. Tiberio, G. Pelosi, G. Manara, A Uniform GTD Formulation for the Diffraction by a Wedge with Impedance Faces, *Transactions on Antennas and Propagation*, IEEE 1985, Vol. AP-33

[37] R. G. Kouyoumjian, P. H. Pathak, A Uniform Geometrical Theory of Diffraction for an Edge in a Perfectly Conducting Surface, *Proceedings of the IEEE*, IEEE 1974, Vol. 62, pp. 1448-1481

[38] C.A. Macon, K.D. Trott, L.C. Kempel, A Practical Approach to Modeling Doubly Curved Conformal Microstrip Antennas, *Journal of Electromagnetic Waves and Propagation - Progress In Electromagnetics Research*, 2003, PIER 40, pp. 295-314

[39] C.A. Macon, L.C. Kempel, S.W. Schneider, K.D. Trott, Modeling Conformal Antennas on Metallic Porlate Spheroid Surfaces Using a Hybrid Finite Element Method, *Transactions on Antennas and Propagation*, IEEE 2004, Vol. 52, Nro. 3

[40] A. Alu, F. Bilotti, L. Vegni, Method of Lines Numerical Analysis of Conformal Antennas, *Transactions on Antennas and Propagation*, IEEE 2004, Vol. 52, Nro. 6

[41] M. Thiel, A. Dreher, Dyadic Green's Function of Multilayer Cylindrical Closed and Sector Structures for Waveguide, Microstrip-Antenna, and Network Analysis, *Transactions on Microwave Theory and Techniques*, IEEE 2002, Vol. 50, Nro. 11

[42] A. Dreher, A New Approach to Dyadic Green's Function in Spectral Domain, *Transactions on Antennas and Propagation*, IEEE 1995, Vol. 43, Nro. 11

[43] B. Biscontini, M. Burger, F. Demmel, P. Russer, Dyadic Green's Function for Conformal Antennas in Multi Layered Cylindrical Structures Using Generalized Transmission Lines, *34th European Microwave Conference, Amsterdam*, 2004

[44] A. Herschlein, G. Gottwald, W. Wiesbeck, Patch Antennas on Finite and Infinite Cylindrical Surface Structures, *Proceedings of the IEEE International Symposium on Phased Array Systems and Technology, Boston-Massachussets*, IEEE 1996, pp. 168-170

[45] M. S. Ingber, R. H. Ott, An Application of the Boundary Element Method to the Magnetic Field Integral Equation, *Transactions on Antennas and Propagation*, IEEE 1991, Vol. 39, Nro. 5

[46] D.H. Werner, R.J. Allard, R. A. Martin, R. Mittra, A Reciprocity Approach for Calculating Radiation Patterns of Arbitrarily Shaped Microstrip Antennas Mounted on Circularly Cylindrical Platforms, *Transactions on Antennas and Propagation*, IEEE 2003, Vol. 51, Nro. 4

[47] B.J. Fasenfest, F. Capolino, D.R. Wilton, D.R. Jackson, N.J. Champagne, A Fast MoM Solution for Large Arrays: Green's Function Interpolation with FFT, *Antenna and Wireless Propagation Letters*, IEEE 2004, Vol. 3

[48] A.K. Skrivervik, J.R. Mosig, Analysis of Finite Phase Arrays of Microstrip Patches, *Transactions on Antennas and Propagation*, IEEE 1993, Vol. 41, Nro. 8

[49] A.J. Roscoe, R.A. Perrot, Large Finite Array Analysis Using Infinite Array Data, *Transactions on Antennas and Propagation*, IEEE 1994, Vol. 42, Nro. 7

[50] P. Janpugdee, P. H. Pathak, A DFT-Based UTD Ray Analysis of Large Finite Phased Arrays on Grounded Substrate, *Transactions on Antennas and Propagation*, IEEE 2006, Vol. 54, Nro. 4

[51] S.A. Bokhari, J.R. Mosig, F.E. Gardiol, Radiation Pattern Computation of Microstrip Antennas on Finite Size Ground Planes, *Proceedings-H*, IEE 1992, Vol. 139, Nro. 3

[52] J. Huang, The Finite Ground Plane Effect on the Microstrip Antenna Radiation Patterns, *Transactions on Antennas and Propagation*, IEEE 1983, Vol. AP-31, Nro. 4, pp. 649-653

[53] R. E. Munson, Conformal Microstrip Antennas and Microstrip Phased Arrays, *Transactions on Antennas and Propagation*, IEEE 1974, Vol. AP-22, pp. 74-78

[54] M. He, X. Xu, Full-Wave Analysis and Wide-Band Design of Probe-Fed Multilayered Cylindrical-Rectangular Microstrip Antennas, *Transactions on Antennas and Propagation*, IEEE 2004, Vol. 52, Nro. 7

[55] W. H. Kummer, Basic Array Theory, *Proceedings of the IEEE*, IEEE 1992, Vol. 80, Nro. 1

[56] J. K. Hsiao, A. G. Cha, Pattern and Polarizations of Simultaneously Excited Planar Arrays on a Conformal Surface, *Transactions on Antennas and Propagation*, IEEE 1974, Nro. 1

[57] V. Kalinichev, Analysis of Beam-Steering and Directive Characteristics of Adaptive Antenna Arrays for Mobile Communications, *Antennas and Propagation Magazine*, IEEE 2001, Vol. 43, Nro. 3

[58] O. M. Bucci, G. D'Ellia, G. Mazzarella, G. Panariello Antenna Array Synthesis: A New General Approach, *Proceedings of the IEEE*, IEEE 1994, Vol. 82, Nro. 3

[59] O. M. Bucci, G. Mazzarella, G. Panariello Reconfigurable by Phase-Only Control, *Proceedings of the IEEE*, IEEE 1991, Vol. 39, Nro. 7

[60] O. M. Bucci, G. D'Elia, G. Romito, Optimal Synthesis of Reconfigurable Conformal Arrays with Phase-Only Control, *Antennas and Propagation Society International Symposium*, IEE 1996. AP-S. Vol. 2, pp. 810-813

[61] G. T. Poulton, Array Pattern Estimation from Amplitude Measurements on Arbitrary Near-Field Surfaces, *International Conference on Acoustics, Speech, and Signal Processing (ICASSP-94)*, IEEE 1994, Vol 4., pp. 241-244

[62] A. K. Brodzik, J. M. Mooney A New Iterative Algorithm for Restoration of Chromotomographic Images, *SPIE IV Conference on Imaging Spectometry*, SPIE 1998, Vol. 3438

[63] F. Ares, S. R. Rengarajan, J. A. Fereira, A. Trastoy, Synthesis of Antenna Patterns of Circular Arc Arrays, *Antennas and Propagation Society International Symposium*, IEEE 1997, Vol. 4, pp. 2248 - 2251

[64] N. H. Farhat, B. Bai, Phased-Array Antenna Pattern Synthesis by Simulated Annealing, *Proceedings of the IEEE*, IEEE 1987, Vol. 75, Nro. 6

[65] S. Kirkpatrick, C. D. Gelatt, M. P. Vecchi, Optimization by Simulated Annealing, *Science*, 1983, Vol. 220, Nro. 4598

[66] L.I. Vaskelainen, Virtual Array Synthesis Method for Planar Array Antennas, *Transactions on Antennas and Propagation*, IEEE 1998, Vol. 46, Nro. 3

[67] L.I. Vaskelainen, Iterative Least-Squares Synthesis Methods for Conformal Array Antennas with Optimized Polarisation and Frequency properties, *Transactions on Antennas and Propagation*, IEEE 1997, Vol. 45, Nro. 7

[68] L.I. Vaskelainen, Phase Synthesis of Conformal Array Antennas, *Transactions on Antennas and Propagation*, IEEE 2000, Vol. 48, Nro. 6

[69] L.I. Vaskelainen, Constrained Least-Squares Optimization in Conformal Array Antenna Synthesis, *Transactions on Antennas and Propagation*, IEEE 2007, Vol. 55, Nro. 3

[70] P. Jorna, H. Schippers, J. Verpoorte, Beam Synthesis for Conformal Array Antennas with Efficient Tapering, *National Aerospace Laboratory (NLR)*, 2007

[71] G. Mazzarella, Pattern Synthesis of Conformal Array, *Antennas and Propagation Society International Symposium*, IEEE 1993, AP-S. Vol. 2, pp. 1054 - 1057

[72] P.G. Elliot, Conformal Array Beam Synthesis and Taper Efficiency Comparisons, *Proceedings - Antennas, Radar and Wave Propagation*, ARP 2005

[73] Z. Deng, K. A. Michalski, Synthesis Method of Conformal Arrays Using a Weighted Inner Product, *Transactions on Antennas and Propagation*, IEEE 2002

[74] J. Skaar, K.M. Risvik, A Genetic Algorithm for the Inverse Problem in Synthesis of Fiber Gratings, *Journal of Lightwave Technology*, IEEE 1998, Vol. 16, Nro. 10

[75] M. Baroni, M. B. Margari, F. Marliani, Source Decompsition by Genetic Algorithm for Space Applications, *Electromagnetic Research Symposium 2004, Pisa-Italy*, March 2004

[76] D.W. Boeringer, D.H. Werner, D.W. Machuga, A Simultaneous Parameter Adaption Scheme for Genetic Algorithms with Application to Phased Array Synthesis, *Transactions on Antennas and Propagation*, IEEE 2005, Vol. 53, Nro. 1

[77] R.J. Allard, D.H. Werner, P.L. Werner, Radiation Pattern Synthesis for Arrays of Conformal Antennas mounted on Arbitrarily-Shaped Three-Dimensional Platforms Using Genetic Algorithms, *Transactions on Antennas and Propagation*, IEEE 2003, Vol. 51, Nro. 5

[78] D.L. Carroll, Chemical Laser Modeling with Genetic Algorithm, *American Institute of Aeronautics and Astronautics Journal*, AIAA 1996, Vol. 34, Nro. 2

[79] D.L. Carroll, Genetic Algorithm and Optimizing chemical Oxygen-Iodine Lasers, *Developement in Theoretical and Applied Mechanics*, School of Engineering, University of Alabama, 1996, Vol. 18, pp. 411-424

[80] G. Yang, L.E. Reinstein, Z. Xu, D.L. Carroll, A Genetic Algorithm Technique in Optimization of permanent prostate implants, *Medical Physics*, Am. Assoc. Phys. Med. 1998, Vol. 25, Nro. 12

[81] C. A. Coello Coello, G. Toscano Pulido, Multiobjective Structural Optimization using a Micro-Genetic Algorithm, *Structural and Multidisciplinary Optimization*, 2005, Vol. 30, No. 5, pp. 388-403

[82] B. L. Miller, M. J. Shaw, Genetic Algorithm with Dynamic Niche Sharing for Multimodal Function Optimization, *Proceedings of International conference on Evolutionary Computation*, IEEE 1996, pp. 786 - 791

[83] K. Krishnakumar, Micro-Genetic Algorithms for Stationary and Non-stationary Function Optimization, *Proceedings in Intelligent Control and Adaptive Systems*, SPIE 1989, Vol. 1196

[84] D.E. Goldberg, J.Richardson, Genetic Algorithms with Sharing for Multimodal Function Optimization, *Genetic algorithms and their application: Proceedings of the Second International Conference on Genetic Algorithms*, Massachussetts Institute of Technology, July 1987, pp. 41-49

[85] G. Merzinger, T. Wirth, Repetitorium der Höheren Mathematik, *Binomi Verlag*, 3rd Edition, 1995